Synthesis and Characterization of Mo, Se and Their Co-Doped Barium Strontium Titanate Dielectric Materials for Capacitor Application

By

Kiflom Gebremedhn Kelele

A Dissertation Submitted to

The Department of Applied Chemistry

School of Applied Natural Sciences

Presented in Partial Fulfilment of the Requirement for the Degree of Doctor of Philosophy in Material Chemistry

Office of Graduate Studies

Adama Science and Technology University

June, 2023

Adama, Ethiopia

Synthesis and Characterization of Mo, Se and Their Co-Doped Doped Barium Strontium Titanate Dielectric Materials for Capacitor Application

By:

Kiflom Gebremedhn Kelele

Supervisors:

Dr. H C Ananda Murthy (Main Supervisor)

Prof. Balachandran Ruthramurthy (Co-Supervisor)

Dr. Aschalew Tadesse (Co-Supervisor)

A Dissertation Submitted to

The Department of Applied Chemistry

School of Applied Natural Science

Presented in Partial Fulfilment of the Requirement for the Degree of Doctor of Philosophy in Material Chemistry

Office of Graduate Studies

Adama Science and Technology University

June, 2023

Adama, Ethiopia

Declaration

I hereby declare that this Dissertation entitled '**Synthesis and Characterization of Mo, Se and Their Co-Doped Doped Barium Strontium Titanate Dielectric Materials for Capacitor Application'** is my original work. It has not been submitted for the award of any academic degree, diploma or certificate in any other university. All sources of materials used for this thesis have been duly acknowledged through appropriate citations.

Kiflom Gebremedhn Kelele	_____	_____
Name of Student	Signature	Date

Recommendation of Supervisors

We, the supervisors of this dissertation, hereby certify that we have read and revised the dissertation entitled '**Synthesis and Characterization of Mo, Se and Their Co-Doped Doped Barium Strontium Titanate Dielectric Materials for Capacitor Application**' prepared under our guidance by Kiflom Gebremedhn Kelele submitted in partial fulfilment of the requirements for the degree of Doctor of Philosophy in Material Chemistry. Therefore, we recommend the submission of the dissertation to the Department for further review and defence.

Dr. H C Ananda Murthy _	_____	_____
Major supervisor	Signature	date
Prof. Balachandran Ruthramurthy	_____	_____
Co-supervisor	Signature	date
Dr. Aschalew Taddesse _	_____	_____
Co-supervisor	Signature	date

Approval Page of Ph.D. Dissertation

This is to certify that the recommendations and suggestions made by the board of examiners are appropriately incorporated into the final version of the dissertation entitled '**Synthesis and Characterization of Mo, Se and Their Co-Doped Doped Barium Strontium Titanate Dielectric Materials for Capacitor Application**' by Kiflom Gebremedhn Kelele.

Dr. H C Ananda Murthy	_____	_____
Major supervisor	Signature	date
Prof. Balachandran Ruthramurthy	_____	_____
Co-supervisor	Signature	date
Dr. Aschalew Taddesse	_____	_____
Co-supervisor	Signature	date

We, the undersigned, members of the Board of Examiners of the dissertation for the open defence by Kiflom Gebremedhn Kelele have read and evaluated the dissertation entitled '**Synthesis and Characterization of Mo, Se and Their Co-Doped Doped Barium Strontium Titanate Dielectric Materials for Capacitor Application'** and examined the candidate during open defence. This is, therefore, to certify that the dissertation is accepted for partial fulfilment of the requirement of the degree of Doctor of Philosophy in Material Chemistry.

_____	_____	_____
Chairperson	Signature	Date
_____	_____	_____
Internal Examiner 1	Signature	Date
_____	_____	_____
Internal Examiner 2	Signature	Date
_____	_____	_____
External Examiner 1	Signature	Date
_____	_____	_____
External Examiner 2	Signature	Date

Finally, approval and acceptance of the dissertation is contingent upon submission of its final copy to the Office of Postgraduate Studies (OPGS) through the candidate's Department Graduate Council (DGC) and School Graduate Committee (SGC).

_____	_____	_____
Department Head	Signature	Date
_____	_____	_____
School Dean	Signature	Date
_____	_____	_____
Office of Postgraduate Studies, Dean	Signature	Date

ACKNOWLEDGEMENTS

First of all, my deepest gratitude goes to my advisors, Dr. H C Ananda Murthy, Prof. Balachandran Ruthramurthy and Dr. Aschalew Taddesse for their all rounded and unhindered guidance as well as mentorship from the beginning to the end of the work.

I would like to acknowledge the Ethiopian Ministry of Education (MoE), Adama Science and Technology University and Woldia University for their financial support.

I would like to thank the Department of Applied Chemistry and Department of Material Science and Engineering of Adama Science and Technology University for the XRD measurement and muffle furnace access.

My appreciation goes to Bahir Dar University for the TGA-DSC, FT-IR and BET measurements provided.

Furthermore, I would like to give my greatest appreciation to Dr. Lemma Teshome Tufa and Dr. Jaebeom Lee along with their laboratory staff for characterizing my samples using SEM, EDS, TEM and XPS at the Department of Chemistry, Chemistry Engineering and Applied Chemistry, Chungnam National University, Daejeon 34134, Republic of Korea. Thank you for your help.

I am so grateful to my friend Dr. Yosef Nikodimos for his support in determining the morphological and microstructural properties of the samples through SEM-EDX, Raman spectroscopy and XRD at Department of Chemical Engineering, National Taiwan University of Science and Technology, Taipei City 106, Taiwan.

I am so thankful to Dr. Kar Ban Tan who helped the Impedance Analyzer meter measurements of the BST samples so as to explore their respective dielectric parameters for capacitive application at the Department of Chemistry, Faculty of Science, Universiti Putra Malaysia, Serdang, Malaysia.

Besides, I appreciate all academic and research assistances of Department of Applied Chemistry, School of Natural Science, Adama Science and Technology University for their continued and friendly assistance throughout my work.

Last but not least, I would happily like to thank my family members who have been helping me financially and mentally all time around. I thank my girlfriend, Sister Maru, for her unconditional support, determination and love. I would like to thank my sister Menberey Gebremedhn and My brother Hailay Gebremeskel who have been backing me up in every of my work.

TABLE OF CONTENTS

CONTENTS **PAGE**

LIST OF TABLES

TABLE **PAGE**

LIST OF FIGURES AND ILLUSTRATIONS

LIST OF ABBREIVATIONS AND ACRONYMS

AC	Alternative Current
BET	Bruner-Emmett-Teller
BST	Barium strontium titanate
dc / DC	Direct Current
DRAM	Dynamic Random Access Memories
DSC	Differential Scanning Calorimetric
EDS	Energy Dispersive Spectroscopy
FFT	Fast Fourier Transform
FT-IR	Fourier Transform Infrared Spectroscopy
FWHM	Full Width at Half Maximum
HR-TEM	High Resolution Transmission Electron Microscopy
MCM	Magnetic Core Memory
MMIC	Monolithic Microwave Integrated Circuit
NLDFT	Non-Local Density Function Theory
SAED	Selected Area Electron Diffraction
SD	Standard Deviation
SEM	Scanning Electron Microscopy
SSA	Specific Surface Area
STP	Standard Temperature and Pressure
TEM	Transmission Electron Microscopy
TGA	Thermal Gravimetric Analyser
TTIP	Titanium(IV)isopropoxide
XPS	X-ray Photoelectron Spectroscopy
XRD	X-ray Diffraction

ABSTRACT

Barium strontium titanate (BST) is a suitable dielectric material for a capacitor application. In this work, BST was doped with Mo, Se and their composites through slow rate injection sol-gel method to study their effect on the capacitive application of BST. The existence of atoms and ions of the BST samples were confirmed by the Energy Dispersive Spectroscopy (EDS) and X-ray Photoelectron Spectroscopy (XPS). The XRD confirmed the formation of the tetragonal shaped $Ba_{0.77}Sr_{0.23}TiO_3$ *(BST-0.7) and cubic shaped* $Ba_{0.6}Sr_{0.4}TiO_3$ *(BST-0.6) samples. The insertion of Mo to* $Ba_{0.77}Sr_{0.23}TiO_3$ *resulted in lowering of the average crystal size from 23.97 nm to 14.46 nm and average grain size from 40.13 nm to 23.35 nm of BST where 0.04 mol Mo-doped BST-0.7 possessed an average particle size of 24.60 nm. The 0.06 mol Mo-doped BST-0.6 possessed a lower crystal size of 15.17 nm as compared to that of BST-0.6 (19.35 nm). Likewise, the average grain size of BST-0.6 decreased from 26.02 nm to 16.40 nm when 0.06 mol* Mo^{6+} *was added to BST-0.6. 0.04 mol Mo-doped BST-0.6 with composed of particles with an average particle size of 20.92 nm. Meanwhile, the 0.06 mol Se dopant caused reduction of average crystal size from 23.97 nm to 18.89 nm for BST-0.6 as well as elevation of average crystal size from 19.41 nm to 30.03 nm for BST-0.7 accompanied by the respective decreasing from 40.13 nm to 12.43 nm and increasing from 26.02 nm to 35.45 nm of the average grain size of the BST-0.7 samples. The 0.04 mol Se-doped BST-0.6 and 0.04 mol Se-doped BST-0.7 acquired average particle sizes of 27.08 nm and 28.34 nm, respectively. The composite dopant of 0.06 mol Mo and 0.06 mol Se have shown higher average crystal size, from 23.97 nm to 28.36 nm, as well as elevated average grain size from 40.13 nm to 62.51 nm of BST-0.6. The 0.04 mol (Mo, Se) co-doped BST-0.6 nanopowder was found with an average particle size of 20.22 nm. The dopants generated more space polarization and oxygen vacancies. At the same time, they neutralized extra electrons. Such changes ultimately led to the enhancement of capacitive application of BST-0.6 by increasing the dielectric constant (*ε_r*) from 233.80 to a maximum of 980.60 for the Mo-doped BST-0.6 calcined at 900* ^oC*, from 248.80 to 1101.40 for the Se-doped BST-0.6 calcined at 800* ^oC *and from 248.80 to 1200.20 for the (Mo, Se) co-doped BST-0.6 calcined at 800* ^oC*, at a frequency of 1 MHz. The doping of Mo and Se resulted in the lowering of dielectric loss of BST-0.6 calcined at 900* ^oC *from 0.15576 to 0.0243 (Mo-doped BST-0.6), 0.1614 to 0.0233 (Se-doped BST-0.6, calcined at 800* ^oC*) and 0.1614 to 0.0182 for the (Mo, Se) co-doped BST-0.6 calcined at 800* ^oC*. The Mo, Se and their co-doped BST were effectively synthesized through a sol-gel method and the dopants improved the capacitive application of the BST-0.6 base material.*

Keywords: Barium strontium titanate, Mo and Se doping, Capacitance, Dielectric constant, Dielectric loss

CHAPTER 1. INTRODUCTION

1.1 Background of the Study

The high-level consumption of the traditional fuel energy and the on-going increase of demands for the energy became a big concern leading a way to develop environmentally-friendly energy sources and the storing mechanisms (Bao et al., 2017; Han et al., 2015; Tong et al., 2013). Energy is continually moving from one form to another in most processes. Examples include how living systems synthesise food using carbon dioxide and water during photosynthesis, transforming solar energy into chemical energy. Additionally, a generator can transform the mechanical energy of a cascade into electromagnetic energy. The potential chemical energy in petrol is converted by an internal combustion engine into heat, which is ultimately converted into the kinetic energy that propels a vehicle. Solar radiation is transformed by a solar cell into electrical energy, which is then used to power a bulb or computer (Goswami & Kreith, 2007). Hence, the studies on renewable energy initiate the development of efficient energy conversion and the energy accumulating devices such as the batteries as well as capacitors (Mohammadian, Moshaii, Alizadeh, Gharibzadeh, and Mohammadpour (2016); Wu et al., 2019). A capacitor is an electrochemical energy storage material with higher power as well as energy quantity having a lengthy lifecycle along with the quick charging/discharging capacity (Abdel Maksoud et al., 2021). As a result of constant charge in reverse to an electrochemical reaction, capacitors accumulate energy. A capacitor gets charged when a potential differential (voltage) is applied on the opposite sides of plates (Z. S. Iro et al, 2016).

The microelectronic industry is in continuous demand to reduce the dimensions of capacitor components. On the other hand, materials with higher dielectric constant have been utilized in the electronic devices industry to a larger extent. Perovskite, ABO_3, such as $BaTiO_3$, $SrTiO_3$ and barium strontium titanate (BST) have suitable properties which make them to be perfect candidates for many semiconductor applications (S. Kongtaweelert et al, 2006).

Materials belonging to the perovskites family have the formula ABX_3. The anion "X" is on the unit cell faces, whereas the cations "A" and "B" are found in the cell's centre and corner positions, respectively. This family includes perovskite materials made of oxides and halides. Ferroelectric $BaTiO_3$ and $PbTiO_3$, dielectric $(Ba,Sr)TiO_3$, piezoelectric $Pb(Zr,Ti)O_3$, electro-strictive $Pb(Mg,Nb)O_3$, magneto-resistant $(La,Ca)MnO_3$, and multiferroic $BiFeO_3$ are a few examples of oxides (Kostopoulou et al, 2019). Hence, BST as a member of the perovskite family is definitely applied in the preparation of electronic devices such as capacitors, piezoelectric sensors and microwave phase shifters because of its desirable ferroelectric and dielectric properties. BST

possess a lower dielectric loss and an enhanced charge accumulation capacity which make it to be the right material for a capacitor (J. D. Baniecki et al., 2001; Leese et al., 2022).

For the effectiveness of BST application in a variety of electronic fields, its dielectric properties need to be modified. Modification is usually executed through the addition of dopants. The dopants to be added must be chosen based on their dielectric strength, ionic radius and electronegativity where dopants with higher dielectric constant values have been preferably used to prepare dielectric materials of a higher capacitance (S. Khardazi et al., 2022; X. Liu et al, 2022). Here, donor and acceptor ions of the dopants occupy the A and B - sites of the perovskite (ABO_3) structure which result in the development of a single-phase arrangement as well as in the formation of the oxygen vacancies and lattice defects. Hence, the dielectric behaviour of the doped BST became more significant compared to the undoped BST (J. Liu, Wei, Zhao, & Zhang, 2011; Novianty, Seminar, Irzaman, & Budiastra, 2018).

A variety of doped BST samples have been studied for their improved dielectric parameters as compared to the BST base material. For instance, Pb-doped BST (Zeng et al, 2006), Ca-doped BST (Yun et al, 2007), Cr-doped BST (Kim & Kim, 2005) and La/Co co-doped BST (Y. Zhang et al., 2009) were reported where relatively small increase in dielectric constant and capacitance as well as less lowering of dielectric loss were observed. Hence, increasing the efficiency of a capacitor to a higher extent was an open task.

However, to the best of my knowledge, the effect of Mo, Se and (Mo + Se) on the capacitance and dielectric properties of BST was not studied to the best of my knowledge. These dopants have been selected due to their higher dielectric constant values and their ionic radii similar to the ions of the BST base material. Both the Se^{4+} and Mo^{6+} ions possess atomic radius values similar to the Ti^{4+} ion. This similarity in atomic radii relatively is beneficial to predict the extent of effective doping and the dopant's solubility in the base material. But, ***t - factor*** is taken as a major factor for an effective doping to happen where its value should be in between 0.77 to 1.1 (Assadi et al, 2013; Libin Gao et al., 2019).

On the other hand, many synthesis methods utilized for the preparation of the doped BST resulted in less uniformly distributed particles which affect its properties and effectiveness towards its applications. Hence, this work was supposed to have its own contribution in enhancing the performance of the BST capacitor by doping it through a slow rate injection *sol-gel* method. This is a *sol-gel* method which employs a slower addition of the precursors using a syringe with 2-3 drops of samples in a minute. It was supposed to be resulted in BST samples of more uniformly distributed particles which enhanced the capacitive application of the BST materials.

Therefore, the main task of this work was synthesizing the pristine BST and doped BST samples through slow rate injection *sol-gel* technique for capacitor application so as to evaluate the effect the dopants on the capacitive application of BST. All the synthesized materials were characterized by Thermal Gravimetric Analyser/Differential Scanning Calorimetry (TGA/DSC), Fourier Transform Infrared Spectroscopy (FT-IR), Raman spectroscopy, X-ray Diffraction (XRD), X-ray photoelectron spectroscopy (XPS), Scanning Electron Microscopy (SEM), Energy Dispersive Spectroscopy (EDS), Transmission Electron Microscopy (TEM), and Brunauer-Emmett-Teller method (BET) for the thermal, compositional information, crystal structure, surface morphology, and textural data. The dielectric properties (capacitance, dielectric loss and dielectric constant) of both undoped and doped BST samples were performed using Impedance Analyzer measurement technique.

1.2 Statement of the Problem

BST doped with Mg, Ni, Fe, Mn, Co, Al, Cr, La, Er, Ta, K, Bi, etc., have been reported where the BST has been used as a dielectric material in capacitors. Almost all of the reported works so far have shown that there was improvement in the dielectric properties and capacitive application of BST by increasing the stored charges and lowering the voltage needed for the charge generation. But the door was open for further enhancement of the dielectric properties of BST to be used as a capacitor by using high dielectric constant dopants. The capacitance and dielectric constant of BST needed to be increased more, while the dielectric loss is in demand to be reduced to smaller values for the effectiveness and improvement of the capacitive performance of BST and needs to be done continuously. Meanwhile, Mo and Se acquire higher dielectric constant values indicating that they are easily polarizable elements. They have also been used as dopants for perovskites other than BST where enhanced capacitive performance of the perovskites was resulted. Despite their relatively higher dielectric nature, no work has been reported about their impact on the capacitive application of BST. Besides, most of the doped BST samples have been mainly synthesized by methods including solid state reaction technique, hydrothermal, metal oxide deposition, *sol-gel* techniques, etc. These methods result in BST samples of relatively large size with varied sized distribution and non-uniform morphology. Therefore to minimize these problems, slow injection *sol-gel* technique has been chosen in this research work where uniform distribution of particles was expected to occur.

1.3 Objective of the Study

1.3.1 General objective

The general objective attributed to this research work was to synthesize the Mo, Se, and (Mo + Se) doped BST dielectric materials through a slow injection *sol–gel* method for a capacitor application.

1.3.2 Specific objectives

The specific objectives of this dissertation work included;

- to synthesize the pristine BST and doped BST nanomaterials using slow-injection *sol-gel* method
- to characterize the pristine BST and doped BST nanomaterials using TGA/DSC, XRD, FT-IR, Raman spectroscopy, SEM, EDS, XPS, TEM, and BET for their thermal, microstructural, compositional, morphological and textural properties
- to explore the differences in the microstructural and morphological properties of the undoped BST and doped BST samples
- to determine the dielectric constant, dielectric loss and capacitance of both the undoped and doped BST samples using impedance analyzer and
- to examine the effect of varying the calcination temperature from 800 ^{o}C to 900 ^{o}C and changing the sintering temperature from 1000 ^{o}C to 1100 ^{o}C on the dielectric constant, dielectric loss and capacitance of the doped BST samples.

1.4 Significance of the Study

Effective accomplishment of this research work was expected to come up with an improved and confirmed insight on the capacitive application of the Mo, Se and their composite doped BST. It was also expected to introduce new dopants which can be possibly used to increase the dielectric constant and capacitance of BST and reduce the dielectric loss. This was expected to be a useful investigation for the research community and electronic industries. Hence, a doped BST containing capacitor with improved capacitance was supposed to have its own contribution on the availability of varied dielectric materials as capacitors.

1.5 Scope of the Study

This work covered a slow injection *sol-gel* synthesis of pristine BST and BST doped with (0.02, 0.04, 0.06) mol Mo, Se, and their composites. The synthesized samples were characterized through TGA/DSC, FT-IR, Raman spectroscopy XRD, SEM, EDS, XPS, TEM/HR-TEM and BET for their thermal, compositional, microstructural, morphological and textural properties. This study also included testing of BST and doped BST materials for their capacitive performance using impedance

analyzer. It explored what happened to the capacitance, dielectric constant and dielectric loss of BST when doped with Mo, Se and their composites at calcination temperatures of 800 ^{o}C and 900 ^{o}C as well as sintering temperatures of 1000 ^{o}C and 1100 ^{o}C. However, this work didn't focus on the measurement of the leakage current density, dielectric strength, and optimization of the amount of dopants, the calcination temperatures as well as sintering temperatures.

CHAPTER 2. LITERATURE REVIEW

2.1 Dielectric Materials

The high level consumption of traditional fuel energy and the ongoing demands for energy have become a big concern that require a way of developing environmentally friendly energy sources and storing energies once generated (Han et al., 2015; N. Liu, Liang, Zhou, & Dong, 2018; Tong et al., 2013). Hence studies on sustainable energy initiated the preparation of energy storage materials such as batteries and electrochemical capacitors (Mohammadian et al., 2016; Shkuratov & Lynch, 2022; Wu et al., 2019).

The performance of a charge and energy storage system is affected by two factors; namely the amount of energy that is stored in a system (volumetric energy density or specific energy) and the speed where energy is either added or released from it (power density or specific power) (Miller & Burke, 2008). Different materials possess a variety of energy and power storing capacity due to variable techniques of energy accumulation as well as charging/discharging processes (Wei et al., 2019). For instance, batteries possess elevated energy accumulating capacity and comparatively lower power density due to the delayed flow of charge transporters at the time of charging/discharging step (Yuan et al., 2018). On the other hand, electrochemical capacitors possess enhanced power density but have longer charging/discharging time (in seconds) and long cycling lifetime during their utilization (Figure 2.1) (Wei et al., 2019).

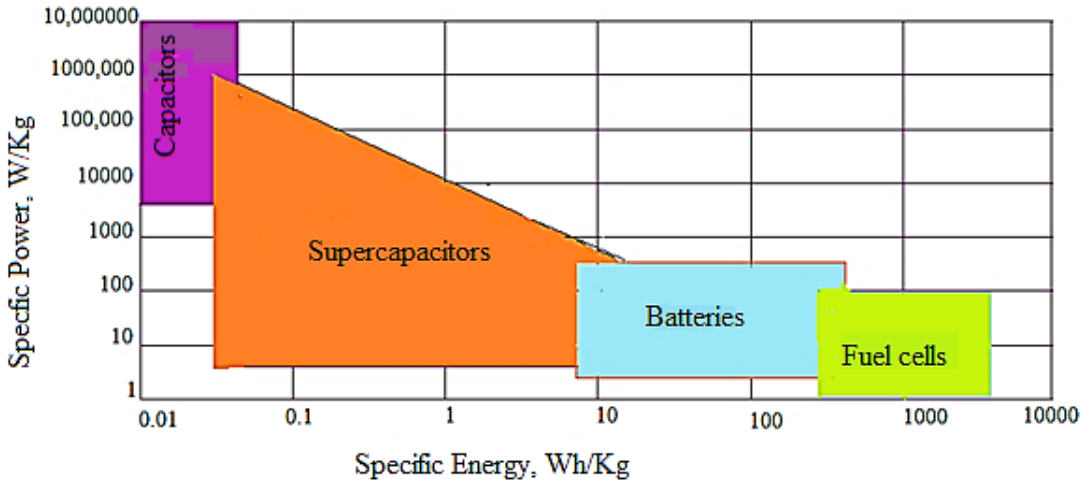

FIGURE 2.1 Specific power and energy of different energy storage devices (Wei et al., 2019)

Batteries are being used as the highly applied as well as favoured energy storing material because of their elevated energy and power derivation ability. But, for a massive energy production along with enlarged power, capacitors are the preferable devices. Even though they are utilized in the current environment, the batteries along with capacitors show inefficient capacity of accumulating enhanced energy as well as power needed as efficient accumulators of recyclable energy (Wei et al.,

2019). On the other hand, nanotechnology was introduced and utilized for the fabrication of electrical devices and enhanced accumulation capacity materials. It deals with particles having a size in the range of 1 - 100 nm, called nanostructures. Hence capacitors at the nanoscale are the preferable energy storing materials (Miller & Simon, 2008; K. Zhang et al., 2022).

Capacitors consist of dielectric materials sandwiched in between their two conducting plates. A dielectric material is a material with an electrical insulation property that is polarizable while an external force is exerted on it. It includes the ferroelectric, pyroelectric, and pizoelectric materials which are polarizable due to electric filed, temperature change, and mechanical pressure, respectively. Dielectric properties of the dielectric materials describe the amount of electrostatic flow of a sample during the application of electrical potential. The amount of polarization of the dielectric material is expressed as dielectric constant. It is affected by content, growth steps and the crystal arrangement of the sample. Dielectric constant is the ratio of electrostatic energy accumulated around a unit volume per unit potential rise (equation 2.1) (C. ZHANG & Y.-f. QU, 2012).

$$\varepsilon_r = \frac{Cd}{\varepsilon_0 A} \quad \text{.....2. 1}$$

where, ε_r is dielectric constant, C is capacitance in F, d belongs to thickness in m while A (m^2) and ε_o are the surface area of the material and permittivity of free space (8.852×10^{-12} F/m) respectively.

Capacitors are classified in to three, namely electrostatic capacitors, electrolytic capacitors and supercapacitors. Electrostatic capacitor possesses a dry separator, extremely less capacitance which is primarily applied in changing radio frequencies and filtering. It encompasses a size range of pico-farads (pF) to low microfarad (μF). The electrolytic capacitor has elevated capacitance as compared to the electrostatic one where its accumulating capacity is at the microfarads (μF) range. It has a watery separator which is utilized as filtering, buffering and signal coupling. Supercapacitors are capacitors with a storing capacity greater than microfarads (μF). Supercapacitors are applied in energy storage which frequently involves charge and discharge periods at elevated current along with lower duration. They are also electrochemical materials that store energy with elevated power as well as energy accumulation having an elongated life cycle. They have mixed properties of both capacitors and batteries in a device. They have the unique advantage of enhanced power density and durability, small mass, higher heat scope of - 40 °C to 70 °C, and are also simple in binding (Miller & Simon, 2008; Pohl et al., 2013). Three types of supercapacitors are distinguished: double-layer capacitors with electrostatic charge storage, pseudocapacitors with electrochemical charge storage, and hybrid supercapacitors with both electrostatic and electrochemical charge storage (K. Sharma,

Arora, & Tripathi, 2019).

The energy, *E,* accumulated at a capacitor is directly related to the capacitance. That is;

$$E = {}^{1}/_{2}\, CV^{2} \ldots\ldots\ldots\ldots\ldots\ldots\ldots\ldots\ldots\ldots\ldots\ldots 2.2$$

In which, *C* represents the capacitance while *V* refers to an applied voltage.

As a general fact, power is also the ratio of energy spent to unit time. The internal parts of capacitors such as the current collector, electrodes, and dielectric material affect the resistance that is determined together with the equivalent series resistance (ESR). A voltage obtained during discharging is calculated by such resistances. At a fitting impedance (R = ESR) the maximum power, Pmax of a capacitor is expressed through the equation;

$$P = {}^{V}/_{4} \times ESR \ldots\ldots\ldots\ldots\ldots\ldots\ldots\ldots\ldots\ldots\ldots\ldots 2.3$$

Where, ESR controls the maximum power of a capacitor (Chu & Braatz, 2002; Pandolfo & Hollenkamp, 2006).

2.2 Working Principle of Capacitors

Capacitors are composed of an electrolyte, two electrodes as well as a separator (dielectrics) that isolates the electrodes electrically by inserting it in between the electrodes (Figure 2.2) (Iro et al., 2016; Masrul et al., 2019; Mustikasari et al, 2018; Sawitri et al., 2019). Opposite charges accumulate on the surface of each electrode as the voltage is applied to the capacitor. The dielectric keeps the charges separated, by creating an electric field that allows the capacitors to store energy. The dielectric material should be ion-permeable, so as to let the ionic charge transfer. It has high electrical resistance, high ionic conductance, and low thickness in order to achieve the best performance (Sharma & Bhatti, 2010). Such capacitors have been used in fuel cell automobiles, hybrid vehicles of less-emission, electric automobiles, forklifts, weight cranes etc (Nan, Hu, & Tian, 2019).

When sufficient amount of voltage is applied, charges are generated and stored in the capacitor. The amount of charge accumulated in a capacitor (Q) is expressed via equation 2.4;

$$Q = C \times V \ldots\ldots\ldots\ldots\ldots\ldots\ldots\ldots\ldots\ldots\ldots\ldots 2.4$$

Where C is the capacitance, V is the applied voltage

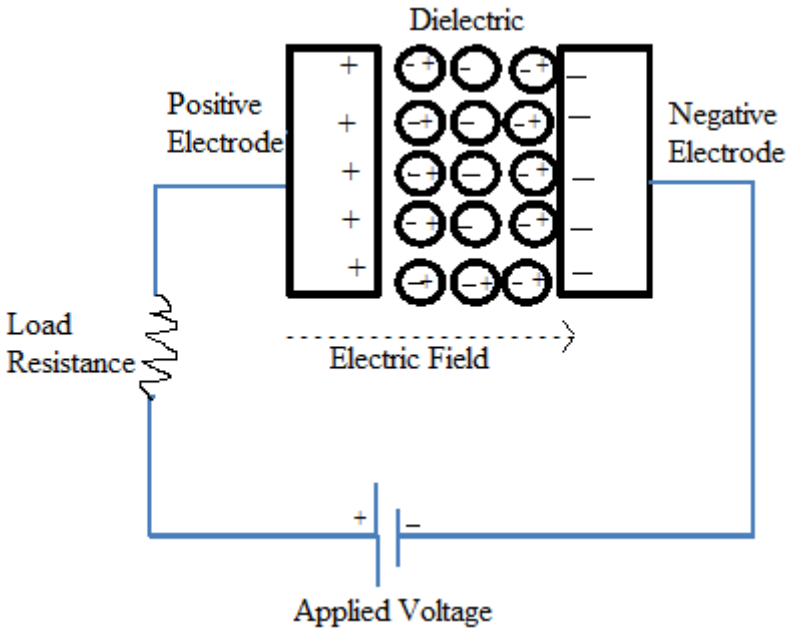

FIGURE 2.2 Structure of a capacitor (Nan, Hu, & Tian, 2019)

The capacitive performance of a dielectric material is usually expressed by a variety of parameters including dielectric constant, capacitance, and dielectric loss (Shalu et al., 2022). Hence, the capacitance for a parallel plate capacitor is expressed in equation 2.5 that is derived from equation 2.1;

$$C = \frac{\varepsilon_0 \varepsilon_r A}{d} \quad \ldots\ldots\ldots\ldots\ldots\ldots\ldots\ldots\ldots\ldots\ldots\ldots 2.5$$

where ε_0 is the permittivity of the free space (8.854 x 10^{-12} (F/m), C is the capacitance (F), ε_r is the dielectric constant, A is the cross-sectional area of the plate (m^2), and d is the thickness of the dielectric layer in the capacitor (m) (Jacob, Nair, & Isac, 2015).

Dielectric loss (D) is another dielectric property of a dielectric material that represents the respective dissipation of electromagnetic energy. It is a loss of electrical energy in the form of heat which is caused by the electrical conduction as well as directional polarization of a sample (Rallapalli et al., 2022). The dielectric loss, D, is determined from the capacitance and resistance of parallel plate capacitors using equation 2.6;

$$D = tan\ \delta = 1/2\pi f C_P R_P \ldots\ldots\ldots\ldots\ldots\ldots\ldots\ldots\ldots\ldots\ldots\ldots 2.6$$

Where δ is the loss angle in *radian*, δ is the phase angle in *radian*, f is the frequency in *Hz*, R_p is the equivalent parallel resistance in *ohm*, and C_p is the equivalent parallel capacitance in F (Rallapalli et al., 2022).

2.3 Barium Strontium Titanate (BST)

To elevate the charge storage capacity of a capacitor, capacitance of the material needs to be increased. One of the methods to increase the capacitance is by simply decreasing the dielectric thickness. However, the loss of electrical charges via an unintended path, known as leakage current, increases when the dielectric thickness of the dielectric material is reduced. The other possibility is increasing the cross sectional area of the capacitor. However, it is difficult to fabricate such structures because of dimensional issues, *i.e.* enormous size. The ultimate option is therefore using material with a higher dielectric constant (Zaharaddeen S Iro et al., 2016).

Materials with higher dielectric constant have been utilized in the electronic devices industry to a larger extent. Meanwhile, perovskite oxides possess elevated dielectric constant. They are being used during the preparation of capacitors intercalated with anions. Perovskites such as $BaTiO_3$, $SrTiO_3$, and $BaSrTiO_3$ have suitable properties which make them to be perfect candidates for such applications (Mikolajick et al., 2018).

$BaSrTiO_3$ (BST) is a metal oxide dielectric substantial material where more focus has been given to it as a result of small dielectric loss, elevated dielectric constant, good thermal stability and adjustable Curie temperature properties. Hence, BST as a member of the perovskite family has been widely used in the preparation of electronic devices such as capacitors, dynamic random access memories (DRAM), piezoelectric sensors, voltage controlled oscillators, microwave state changers, and tunable filters. This is because of the necessary ferroelectric properties along with dielectric properties it possesses (Balachandran et al., 2011; Baniecki et al., 2001).

BST has a typical perovskite arrangement of atoms (Figure 2.3). It has an ABO_3 perovskite structure such that ‘‘A’’ and ‘‘B’’ are sites of cations while ‘‘O’’ is anion site. BST contains both Ba and Sr at the A site and Ti at B site. It has a general formula of $Ba_xSr_{1-x}TiO_3$ ($x \geq 0$) (Ahmed et al., 2015; Jiang et al., 2022; Y. Liu et al., 2000; Moon et al., 2005).

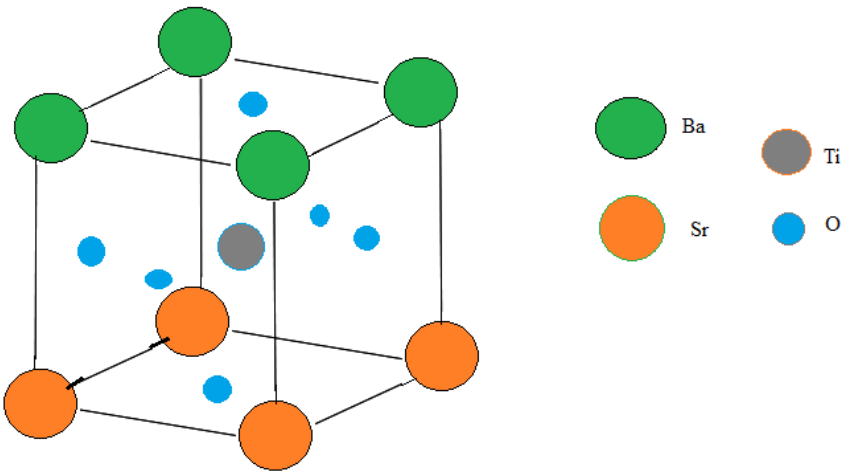

FIGURE 2.3 Non-polar structure of BST at room temperature (Baniecki et al., 2001)

Previously reported studies have shown that the dielectric property values of BST can be changed by varying the mol ratio of Ba and Sr based on the required BST empirical formula. It is found that many BST applications prefer the mol ratio of Ba and Sr to be 0.6:0.4, 0.77:0.23 and 0.5:0.5 so as to generate improved dielectric parameters. These compositions provide elevated dielectric constant, lower aging and smaller dielectric loss. The 0.6:0.4 and 0.77:0.23 ratios contain higher amount of Ba which could enable the BST samples to have a larger unit cell, thus giving rise to better structural flexibility for the dopants (Carlson et al., 2000; Puli et al., 2017). Even though higher mol ratio results in BST with higher dielectric constant, it is not usually chosen since it results in elevated temperature coefficient which required high cost. Temperature coefficient is a coefficient that describes how a change in a physical property and the resulting change in temperature are related (Carlson et al., 2000).

As compared to the conventional charge storage samples like Ta_2O_5 and SiO_2 which possess smaller effective oxide thickness (EOT) as well as elevated current leakage, BST acquire enhanced EOT that provide high charge storage capacity. EOT is the thickness of a capacitor which detects maximum electrical performance of the dielectric material. Hence, BST is then on the verge of completely replacing the conventional dielectrics materials. BST has enhanced charge accumulation capacity as well as smaller dielectric loss value that ultimately results in a minimum refreshing time or charging time of 1 - 10 seconds (Reisinger & Stengl, 2000). Thus, BST is being broadly studied in search of its application as a capacitor because of its improved energy accumulation capacity as well as performance (S. Kongtaweelert et al., 2006).

2.4 Doping Mechanism

Doping is the intentional introduction of impurities into an intrinsic semiconductor for the purpose of enhancing its electrical, optical, thermal, and structural properties. It is a process of modifying the characteristics of materials through introduction of dopants in the parent system (Capsoni et al., 2004; Sharma & Singh, 2013). Dopants are the foreign atoms introduced to the host material. There are two types of doping, p-type and n-type. In n-type doping, dopants involve addition of atoms with a greater number of valence electrons resulting in the formation of free electrons. Such dopants are also called as donor dopants. On the other hand, in the p-type doping, the dopant involves addition of an atom with one fewer valence electron where electron deficiencies are created, also called acceptor dopants. Moreover, doping is also one of the modification methods used as an effective way to enhance the ferroelectric and dielectric properties of BST materials. The wide range of cations A and B substitutions in the perovskite structure, along with the anions and variations in ionic size and tiny atom displacements, cause structural deformation. The octahedral structure of perovskites are bonded together when the structure is deformed, which results in an

extremely strong polarisation. Since the crystallographic dimensions of the barium titanate lattice alter with temperature, this happens particularly with BST. The substitution of small amounts of the A and B - site ions, the microstructure, and the grain size are also highly important factors that affect the dielectric properties of barium titanate ceramics with regard to temperature, electric field strength, and ageing (Petrov et al., 2020).

The A - site and B - site of BST materials can be replaced by different ions using ***t-factor***, electronegativity and ionic radius as determining factors. ***t-factor*** is one of the methods employed to determine whether a dopant is suited for a material or not by predicting the crystal stability of the perovskite (Assadi et al., 2013; Libin Gao et al., 2019). It is determined using equation 2.7;

$$0.77 < t = \frac{r_A + r_O}{\sqrt{2(r_B + r_O)}} < 1.10 \quad \text{.....2. 7}$$

Where r_A (Å) is the radius of ions on the A - site, r_B (Å) is the radius on the B - site, r_O(Å) is the radius of O^{2-} ion and ***t*** is the allowance tolerance factor.

The atoms of dopants can replace the atoms on the A - site or B - site to form a continuous solid solution if the tolerance factors of dopants are located in the range of 0.77 - 1.10. Ionic radius and electrical neutrality (electronegativity) are also the other major criteria considered during selection of dopants where dopant and host material should have comparable ion radius and electronegativity for an effective doping to occur (Assadi et al., 2013; Libin Gao et al., 2019).

2.5 Effect of Doping on Dielectric Properties of BST

The dielectric behaviour of BST can be modified in two ways. The first possible way involves varying and managing the ratio of Ba to Sr during synthesis, while the second method is doping. According to reports, dopants have the ability to change microstructural arrangement of particles of a sample by replacing ions and introducing a new environment around the host particles. This leads to the change of mechanical, electrical, thermal, optical and dielectric properties of the samples. Hence, incorporation of acceptor/donor dopants to the BST structure effectively changes its properties (Godara et al., 2021; Kathait et al., 2017; Xu et al., 2013). Acceptors ions usually substitute Ti at the B - site where a one phase arrangement is formed. This leads to the extra ionization of dopants and formation of oxygen vacancies and lattice irregularities. On the other hand, donor ions usually replace the A - site of BST and increase the number of free electrons leading to increased dielectric constant. Besides, the reduction of Ti^{4+} to Ti^{3+} by the electrons causes additional oxygen vacancies to appear. As a result, increased dielectric loss is obtained which diminishes dielectric parameters of dielectrics and hinders the application of the BST nanomaterial devices. This problem is usually solved through ion substitution. Hence, the charge-compensating

heterovalent replacement of Ti^{4+} ions of BST leads to the development of complex defects which subsequently trap the electrons in a motion. This invites lowering of dielectric loss as well as elevation of dielectric constant. Therefore, complex-defect design is utilized in enhancing the dielectric constant and capacitance of a capacitor. Therefore, doping is selected as one of the effective means of improving the capacitive property of BST (Itoh et al., 1993; Liu et al., 2022).

Previous works have reported the utilization of a variety of metal dopants such as Ni^{2+}, Mg^{2+}, Fe^{2+}, Fe^{3+}, Mn^{2+}, Mn^{3+}, Al^{3+}, Co^{2+} ions etc. revealing modification of the perovskite structure of BST by reducing the dielectric loss and enhancing the dielectric constant (Hofman et al., 1997; Liang et al., 2003). There have been many suggestions given for the mechanism of how the dopant ions affect the microstructural and dielectric characteristics and the changes happened to BST.

For instance, Mn doping involves trapping of electrons which lowers the dielectric loss being an acceptor - class impurity located on the grain boundaries (Cole et al., 2000; Liang et al., 2003). A report by San-Yuan Chen et al. has shown that adding Mg, La, along with Nb dopants in to BST has resulted in the substantial increase of dielectric loss but has been sharply lowered when the amounts of Mg, La, and Nb were elevated. Attar et al. have reported a work on dielectric characteristics of BST nanopowder doped with Bi prepared through *sol-gel* technique. Dielectric constant has been observed increasing up to 1040 at a temperature of 80 ^{o}C during elevation of the calcination temperatures and was then lowered above the Curie temperature. The dielectric loss was lowered during the rise of Bi concentration (Attar et al., 2017). A report by Eswaramoorthi et al. explored the effect of Ga on the electrical properties of BST where the dielectric constant as well as dielectric loss of BST decreased as Ga concentration was increased to 1 mol %. The reduction in dielectric constant was due to the reason that dipoles hardly pursue an enforced field as well as lowering of grain size of BST thin films when doped with Ga. Introduction of Ga resulted in the lowering of dielectric loss as the Ga^{3+} attracted and neutralized the bouncing electrons after Ga^{3+} (0.62 Å) replaced the Ti^{4+} (0.61 Å) (Eswaramoorthi et al., 2015). $Ba_{0.77}Sr_{0.23}TiO_3$ in the form of ceramics doped with Ni and synthesized through slow - injection *sol-gel* technique resulted in a minimum dielectric loss of 0.02 and maximum dielectric constant of 1603. The dopant Ni^{2+} substituted Ti^{4+} after which oxygen vacancies were formed and dielectric loss of BST was reduced. Increase in sintering and calcination temperature is also another driving force for the lowering of the dielectric loss. The dielectric constant of BST elevated following the addition of Ni to it due to the formation of conduction state around grain edges (Shahid et al., 2017).

In contradiction to many reports, doping $Ba_{0.6}Sr_{0.4}TiO_3$ BST with Fe has resulted in lower dielectric constant value as compared to the BST, but no adequate reason and explanation have been given to this unusual result (Jacob et al., 2015). Meanwhile, another report on the Fe doped $Ba_{0.5}Sr_{0.5}TiO_3$

BST synthesized through slow rate injection *sol-gel* has shown expected results where the dielectric constant value of 824.57 for doped BST elevated to 1453.69 as a result of increment in Fe concentration, starting at 0.1 to 1 mol % while sintering temperature was increased. This is mainly due to the formation of oxygen vacancies at elevated sintering temperature and appearance of space charge polarization in response to the applied electric potential (Saeed et al., 2015).

A report, on the impact of gold over some properties of BST, by Wang et al. has explored the improved properties of BST. Increased crystallization and enhanced dielectric constants have been observed as a result of doping of the BST with gold. When the dopant gold was introduced to BST, it catalysed nucleation of the BST particles and enhances its crystallinity. This came up with elevation of the grain size which resulted in higher dielectric constants as compared to the BST (Wang et al., 2005).

From the above works, it is possible to summarize the mechanisms of how dopants affect the performance of a BST based capacitor. Most obviously, dielectric constant is enhanced due to the elevation of polarization as the result of the formation of oxygen vacancies, the occurrence of defects, the generation of free electrons and development of conduction state at the grain edges. Meanwhile, following the incorporation of dopants to BST, electrons and holes are pinned, and the bouncing electrons found at the crystal are trapped as well as neutralized. All these phenomena ultimately resulted in lowering of the dielectric loss. Furthermore, the oxygen vacancies formed after substitution act as donor, and then the ionization of the oxygen vacancies forms conduction electrons that might be bound to Ti^{4+}, resulting in the formation of Ti^{3+}. Then electrons are bound by fully ionized oxygen vacancies, resulting in the formation of a high electron defect-dipole. This ultimately lowers the dielectric loss (Alkathy et al., 2021). Therefore, using suitable dopants on BST is a means of preparing a BST capacitor with improved storing capacity performance.

2.6 The Dopants Mo and Se

Molybdenum (Mo) is a d-block element where molybdenum trioxide (MoO_3) is its most stable form. It is a semi-conductive material with a wide band gap that has been utilized in a variety of semiconductor applications (Arita et al., 2012). MoO_3 films and nanocrystals have been utilized in the development of sensors, lubricants, and solid state micro batteries (Ramana et al., 2007). Reports have also shown that samples have been doped with Mo so as to improve their properties. For instance, a decrease in grain size was observed when ZnO was doped with Mo through a simple ball-milling method (Nandanwar et al., 2020). In another report, the dielectric constant of $CaWO_4$ ceramics increased slightly when it was doped with 6 mol % Mo through solid-state reaction route (Xiao et al., 2017). Moreover, perovskites doped with Mo have shown improved electrical and

electrochemical performances after doping due to the formation of oxygen vacancies and stabilization of the 3D arrangement of the perovskite (Aguadero et al., 2012; Sun et al., 2016; Van Hest et al., 2006). It has been reported that incorporation of Mo to perovskites increased the dielectric constant and capacitance of the perovskites significantly (Padmini et al., 2019; Tomar et al., 2018). Hence, using Mo as a dopant for BST was expected to be effective in enhancing the dielectric properties of BST so as to be applied in capacitors.

Selenium (Se) is a p-block element with non-metallic classification. It has been used as a dopant which affects the structure, shape, magnetic and dielectric properties of samples. In a report, Se forced the shape of $BiFeO_3$ nanoparticles to be changed from needle-like to the nanosheets and then to the self-growth flower-like structure which improved the magnetic properties of $BiFeO_3$ (Rizwan, Umar, Babar, Awan, & ur Rehman, 2019). Se was also used as a dopant for glasses which gradually increases the permittivity and dielectric strength of glass (Deb & Ghosh, 2012). Moreover, Se has been utilized as a dopant and increased the dielectric properties of many perovskites (Auromun & Choudhary, 2020; Chinnathambi et al., 2021; Gaabour, 2020; Susarla et al., 2021).

Mo and Se have common properties which made them more stable composites and hence to be applied for the effective doping. They are of high dielectric materials whose parameters' values are listed in Table 2.1.

Table 2.1 - The average dielectric constant, ionic radius and electronegativity of ions of BST and the dopants

Ions	Minimum Dielectric constant	Electronegativity	Ionic radius (Å)	Reference
Ba^{2+}	130	0.89	1.35	(Barrett, 1962; Gao et al., 2019; Shannon, 1976)
Sr^{2+}		0.95	1.18	
Ti^{4+}		1.54	0.63	
Mo^{6+}	18	2.16	0.59	(Barrett, 1962; Datta et al., 2017; Shannon, 1976)
Se^{4+}	11	2.55	0.5	(Barrett, 1962; Behrens et al., 1974; Shannon, 1976)

It was believed that the tetravalent Se^{4+} ion was expected to replace the divalent Sr^{2+} ions with excess positive charges (charge compensation) since the ***t-factor*** is closer to 1.1. Moreover, there

might be a possibility where Se^{4+} ions replace the Ti^{4+} ions due to the similarity in ionic radius. To maintain the electrical neutrality, conductive electrons arose with contents equivalent to those of the donor ions. Besides, the valence of Ti was waited to be altered from Ti^{4+} to Ti^{3+} following the development of oxygen vacancies which would be resulted in increased polarization leading to enhanced capacitance and dielectric constant. On the other hand, Mo^{6+} ions were supposed to be attracted by the B-site of BST acting as an acceptor dopant whereas the oxygen vacancy was believed to act as a donor and as a result more ionization of the vacancy and Mo was expected to happen. As the result, electrons would be completely surrounded and their movement would be limited. Hence, lower dielectric loss was expected to be resulted. These all were supposed to enhance the capacitive application of BST.

2.7 Preparation of BST Nanopowders

A variety of methods have been employed to synthesize BST nanostructure powders both in undoped and doped form. These methods include conventional solid state reaction technique (Lv et al., 2022), hydrothermal (Ćirković et al., 2015), ultrasonic-driven polycondensation non-aqueous precipitation method (Jiang et al., 2022) and *sol–gel* technique (Eswaramoorthi et al., 2015; Khardazi et al., 2022). Selecting a suitable synthesis method has a positive impact on the dielectric properties of material such as dielectric constant as well as dielectric loss. Most of the methods resulted in BST samples with particles of less homogenised and less effective incorporation of the dopants to the octahedral structure of the perovskite. Out of the many, *sol-gel* method is the preferred one since it gives extra advantages over other techniques. This is due to its important properties such as ease, small cost, superb composition management, elevated molecular uniformity, enhanced purity, small processing temperature, higher crystallization rate of the final product, and smaller polluting extent. It is simple for doping and to obtain uniform products. Therefore, the *sol–gel* method becomes the right technique to be utilized by researchers even though it has a disadvantage of a porous structure as a result of the removal of organic substance and gases while drying. (Eswaramoorthi et al., 2015; Giridharan et al., 2001). *Sol-gel* method involves mixing and stirring of all the precursors with the solvents like acetic acid to form *sol* followed by further stirring so as to obtain the respective *gel*. It is dried to form the crystalline nanopowder (Eswaramoorthi et al., 2015).

2.8 Characterization Techniques of BST samples

2.8.1 Thermal studies of the BST samples

Thermal Gravimetric Analyser (TGA) is a thermal investigation method that determines weight variation of the BST samples due to temperature and time change, in a managed environment. It helps in studying the thermal balance of the BST samples and inquires about property variation at variable atmospheres. It involves heating a mixed sample to an elevated temperature until its contents break down to form gases. Knowing the unreacted amount of the BST sample, percentage by mass is calculated from the mass of the remaining sample as well as the starting mass. On the other hand, mass of the unreacted sample, total mass of impurities released during heating, as well as the stoichiometric ratio are applied in determining the percentage by mass of the BST sample. Thermal studies determine chemical and physical properties of samples as a function of temperature. It is ultimately used to specify the calcination temperature at which the unnecessary solvents found in all the BST samples were removed. It is also applied in determining phase diagram, phase transition, thermal decomposition and solid state reaction. A graph of weight loss against temperature is plotted (Balachandran, Ong, Wong, Tan, & Rasat, 2012; Eswaramoorthi et al., 2015; Shahzad et al., 2017). For instance, a Bi-doped BST nanopowder has been synthesized where an initial weight loss of ~ 6% indicated the removal of water and another peak at about 27% represented the decomposition of organic along with $BaCO_3$ components of the BST sample. At last, a 7% weight loss revealed the evolution of the perovskite structure (Attar et al., 2017).

Differential Scanning Calorimetry (DSC) is used to determine the temperature of the BST sample as compared to that of an inert material under a controlled change of temperature. Any process involving change in enthalpy is detected in the DSC. In general, the temperature of a material and the reference is made to remain constant until the sample temperature is either lower (endothermic change) or higher (exothermic change) than the reference temperature (Balachandran et al., 2012; Eswaramoorthi et al., 2015; Shahzad et al., 2017; Van Erp & Martens, 2011). In a report by Attar, Bi-doped BST nanopowder was synthesized at a calcination temperature of 850 ^{o}C. This temperature was obtained from the exothermic peak at 800 ^{o}C where it was considered as an indicator of the polymorphism stage of the Bi-doped BST sample (Attar et al., 2017).

2.8.2 Compositional studies of the BST samples

Fourier Transform Infrared Spectroscopy (FT-IR) is a technique which is normally used to identify the functional groups of the BST samples by measuring the amount of transmitted light. It depends on the respective infrared spectrum of absorption, emission, and photoconductivity of the sample. Specific functional groups with the respective infrared absorption frequency in the range 400 - 4000

cm^{-1} are usually clarified using the spectrum data (Shameer & Nishath, 2019). The existence of carbonates and C-O-C bond containing impurities obtained from the solvents and the chelating agent used along with the metal-oxygen bonds of a Mn-doped BST nanopowder was revealed from the FT-IR spectrum of the sample according to a report by Shalu et al (Shalu et al., 2022).

Raman spectroscopy is an analytical method in which a scattered light is utilized to determine the vibrational energy modes of the BST samples. Its name came from an Indian physicist C. V. Raman who discovered the effects of Raman scattering in 1928. It gives the chemical along with structural data of a sample. This helps to assign the typical Raman 'fingerprint'. Raman spectroscopy reveals information by measuring the Raman scattering of the sample. An incident light (wavelength = 750 - 850 nm) removes surface molecules of a sample where a light is reflected in a variety of wavelengths. The respective wavelength belongs to a specific component of a sample (Synetos & Tousoulis, 2018). B. Li et al. used Raman spectroscopy to confirm the formation of a (Fe, La, Mn) co-doped BST thin film using a variety of Raman bands such ~170 cm^{-1}, ~223 cm^{-1}, 520 cm^{-1}, ~303 cm^{-1} and ~720 cm^{-1} (Li et al., 2017).

Energy Dispersive Spectroscopy (EDS) is a technique applied in exploring the composition of a sample. It is the X-ray emitted from the ejected electrons and gives information on the type of elements found at the surface of a sample. EDS spectrum is analysed to look for the elements found at the surface of a sample that are preferably identified. The EDS works along with an associated feature of SEM. (Abd Mutalib et al., 2017). Thus, a report by Shalu and Dasgupta Ghosh indicated that the EDS spectrum has been used to explore the existence of Ba, Sr, Zr, Ti, and O in Zr-doped BST nanopowder synthesized through a *sol–gel* route at a calcination temperature of 800 ^{o}C and there were no extra elements identified within the sample. This has shown that a pure Zr-doped BST nanopowder was obtained (Shalu & Ghosh, 2019).

X-ray photoelectron spectroscopy (XPS) is a method utilized for detecting the elemental composition and the binding states of elements of a sample. It is operated to identify the structure of molecules and their interactions with metal centres using the respective binding energy (eV) values. The binding energy corresponds to a specific atom in an orbital with its own spin. Thus, it is mainly utilized to identify ions of a sample (Mather, 2009). Alkathy and co-workers reported that the existence of all the ions of (Bi, Li) co-doped BST nanopowder has been confirmed through the detection of the Ba$3d_{5/2}$, Sr$3d_{5/2}$, Ti$2p_{3/2}$, O$1s$, Bi$4f_{7/2}$, and Li$1s$ at the respective binding energies of 778.19 eV, 131.59 eV, 456.64 eV, 529.73 eV, 157.43 eV, and 60.06 eV, respectively (Alkathy et al., 2021).

2.8.3 Microstructural and morphological studies of the BST samples

X-ray Diffraction (XRD) is a method where X-ray beams coming from a source interfere with one another when they get released from the crystal system due to atomic planes of the crystal. It is utilized to resolve the orientation of a single crystal, crystal structure and crystallite size of the BST materials. XRD pattern is a graph of intensity of the diffraction signal versus the diffraction angle 2θ. X-rays interact with sample and forms secondary "diffracted" beams using the equation called "Bragg's Law" (Equation 2.8);

$$n\lambda = 2d \sin\theta \quad \ldots\ldots\ldots\ldots\ldots\ldots\ldots\ldots\ldots\ldots\ldots\ldots\ldots\ldots 2.8$$

where n is an integer; λ is the wavelength in m; d is the inter-planar spacing in m and θ is the diffraction angle in *radian* (Raval et al., 2019).

Scherrer's equation (Equation 2.9) is used to calculate the crystallite size of samples using Full Width Half Maximum (FWHM) obtained from XRD patterns.

$$\text{Crystallite size } (D) = \frac{K x\lambda}{FWHM\, x\, \cos\theta} \quad \ldots\ldots\ldots\ldots\ldots\ldots\ldots\ldots\ldots\ldots\ldots\ldots\ldots 2.9$$

Where K is the shape factor (0.9) and λ is the wavelength in m.

The locations where peaks are found at the diffraction pattern are determined by the crystal arrangements (shape as well as size) of the substance. On the other hand, the amount of peaks is highly affected by the symmetry of the crystal. The width of an individual peak, called full width at half the maximum height, is utilized for the determination of crystallite size as well as confirmation of the presence or absence of lattice defects. Match software is used to relate the standard JCPDS/ICDD data with the practically obtained data for agreement as well as identification of a species (Raval et al., 2019). For instance, the evolution of a tetragonal (P4mm) shaped Sn-doped BST nanopowder with a JCPDS card number of 00-044-0093 and an average crystal size of 45 nm has been confirmed by the XRD data (S Khardazi et al., 2022).

Scanning Electron Microscopy (SEM) is one form of electron microscopes applied for generating surface images of enhanced resolution. It is used to study the surface appearance, topography, composition and microstructure, homogeneity, necking, grain boundary, grain size and porosity of samples. The images are obtained when electrons in the form of a beam skim the surface of a sample. Secondary electrons ejected from a sample surface show the image of the sample surface. For instance, the SEM photographs of Mg-BST nanopowder displayed that incorporation of MgO dopant to BST resulted in elevated grain size (Farahani et al., 2018)

Transmission Electron Microscopy (TEM) associates the passage or penetration of electrons inside thin layer of the BST samples. It is a method used to determine dislocations and other

crystallographic defects and for an objective of chemical analysis of a sample. It also enables us to determine the particle size as well as size distribution. TEM contains a series of three or more lenses which results in high magnification and hence perfectly characterizes a sample. Electrons produced by a filament (cathode) are accelerated at 100 keV or higher. This helps electrons to be transmitted through thin samples. Electrons reaching the sample will be diffracted in different directions. This diffraction will give information on the orientation of particles of the sample understudy (Ianculescu et al., 2016). Furthermore, high resolution transmission electron microscopy (HR-TEM) - selected area electron diffraction (SAED) is usually utilized to investigate the microstructure of crystals. For such a process to undertake, a small amount of sample will be dispersed in ethanol for about 15 min ultra-sonication. An image of high resolution is expected to be obtained as compared to a TEM image since the imaging electrons interact with the sample independently and involves imaging of the crystallographic structure of a sample at an atomic scale (Ianculescu et al., 2016). For instance, TEM-HRTEM images described the detail microstructure of the Mn-doped BST particles. The lattice fringes of a specific region of the HR-TEM image displayed the evolution of a polycrystalline arrangement while the FFT images revealed the occurrence of the crystal planes (1 0 0) along with (2 0 0) (Fan et al., 2010).

Solid materials have their own textural properties which are usually determined by porosity, surface area, pore volume, and pore size. This are usually obtained from the Brunauer-Emmett-Teller analysis (BET) measurement. Porous solids exist in different forms of pores such as cavities, channels, or interstices. Porosity is obtained by dividing the comprehensive volume of the pore to probable volume of the particles in the BST sample, where pore volume corresponds to the volume of pores in a sample while pore size is the length of separation of two oppositely positioned sides of the pore. Porosity is determined through studies of the amount of gas adsorbed at the surface of a sample. Gas adsorbed at the surface of the sample enables exploration of the parameters like total volume of pore, pore size distribution and specific surface area. Usually, free gas and an absorbed gas do exist in dynamic equilibrium, where the amount of surface covered is determined using the pressure exerted by the absorbed gas. The amount of partial coverage of surface quantified at varied pressures and constant temperature results in different adsorption isotherms types. Adsorption isotherm has necessary data to calculate surface areas as well as porosity of samples. Nitrogen is a commonly and conventionally used adsorbate gas (Farahani et al., 2018).

A report by Farahani and co-authors disclosed that addition of Mg to BST through a solid state reaction method has demonstrated the elevation of specific surface area (8.1 m^2/g to 46.2 m^2/g) and pore radius (1.5 nm to 95.3 nm) of BST (Farahani et al., 2018).

2.8.4 Capacitive application studies of the BST samples

Impedance Analyzer is utilized in measuring the impedance of a circuit or a device. It is also used to determine dissipation factor D or quality factor Q or dielectric loss. D is calculated by determining the ratio of actual to the imaginary impedance (called reactance). The inverse of D is Q. Variation of current drives an analogous variation of applied voltage. This characteristic belongs to the inductance of the sample. On the other hand, a sample's capacity to accumulate electrical charge corresponds to capacitance. A potential is allowed to pass via a sample under study, DUT (Device Under Test). Impedance analyzer measures the potential as well as the amount charge per time flowing through the sample. The amount of impedance is then determined by the ratio of voltage to current. It is used in evaluating dissipation factor, inductance, capacitance, resistance, current, voltage, and conductance at known frequencies. These values lead to the determination of dielectric constant and dielectric loss of the samples (Balachandran et al., 2012; Eswaramoorthi et al., 2015; Shahzad et al., 2017). Thus, impedance analyzer has been used to explore the effect of dopant, calcination temperature, and sintering temperature on the dielectric properties of a Fe-doped BST sample. According to the report, addition of Fe to BST at calcination temperature of 800 ^{o}C and sintering temperature of 1200 ^{o}C has shown higher dielectric constant and lower dielectric loss as compared to the undoped BST (Saeed et al., 2015b).

2.9 Application of BST as a capacitor

The BST is a good dielectric material for capacitor applications because it can store more charge due to the significant polarisation that results from this distortion's large dielectric constant. BST in the form of thin film is being widely studied considering its utilization as a capacitor of Dynamic Random Access Memory (DRAM), Magnetic Core Memory (MCM) and Monolithic Microwave Integrated Circuit (MMIC), due to its favourable ferroelectric as well as dielectric properties including polarizability, piezoelectricity, pyroelectricity and electro-optic activity (Jiao et al., 2022; Saeed et al., 2015; M. Zhang et al., 2011). A BST multi-layered capacitor should fulfil the requirements of upper as well as lower conducting electrodes. That is, electrodes must possess high metallic conductivity; they should be chemically inert toward oxidation, having appreciable adhesion and flat interfacial rows that result in enhanced capacitance (F Stemme et al., 2013). This definitely tells that the electrical passage techniques are highly impacted through the interfacial event between BST and the electrode (Chen et al., 2001).

There are many works reporting the application of BST as a capacitor. For instance, a report by R. Balachandran *et al.* explored the phase formation and dielectric parameters of $Ba_{0.5}Sr_{0.5}TiO_3$ synthesized through gradual injection *sol-gel* method. A dielectric constant and dielectric loss have

been found as 1,164 and 0.063 respectively when calcined at 800 ^{o}C and sintered at 1,350 ^{o}C (R Balachandran et al., 2011). Baniecki *et al*. reported BST thin film used as a capacitor in a small inductance decoupling utilization where the capacitance density was reported as 1.2 μF/cm^{2} (Baniecki et al., 2002). A work on BST thin film used as a capacitor for a microwave was reported with a dielectric loss range of 0.003 - 0.009 (Tombak et al., 2002).

CHAPTER 3. MATERIALS AND METHODS

3.1 Chemicals and Instruments

The starting materials used in the synthesis of BST and BST doped with Mo, Se and their composites were barium acetate (99%, Loba Chemie Pvt. Ltd, Mumbai, India), strontium acetate (99.5%, Research-Lab Fine Chem Industries, Mumbai, India), titanium (IV) isopropoxide, TTIP (97%, SRL, Mumbai, India). Molybdenum trioxide (99.5%, Research-Lab Fine Chem Industries, Mumbai, India) and selenium dioxide (99.995%, Research-Lab Fine Chem Industries, Mumbai, India) were used as the dopants. Acetic acid (99%, Loba Chemie Pvt. Ltd, Mumbai, India), diethyl ether (99%, Loba Chemie Pvt. Ltd, Mumbai, India), ammonia solution (25%, Loba Chemie Pvt. Ltd, Mumbai, India) and de-ionized water were used as solvents of the precursors. Acetyl acetone (98%, Alpha Chemika, Mumbai, India) was used as a stabilizing agent. All the chemicals utilized in the experiment were of analytical grade reagent and no extra purifications were done. The instruments TGA/DSC (HCT-3, Beijing Hengjiu Instrument, China), FT-IR (JASCO, FT/IR-6600, Japan), Raman spectroscopy (UniDRON, South Korea), XRD (Shimadzu, XRD-7000, Japan), XPS (Thermo Scientific K-Alpha, USA), SEM-EDS (JEOL, Germany), TEM/HR-TEM (JEM-2100, USA), BET (Quantachrome NovaWin, version 11.0, USA), Impedance Analyzer (Solartron-1260, Switzerland) and DC sputtering (SC500 Bio rad, JEOL Ltd., Japan) were used.

3.2 Experimental Procedures

3.2.1 Synthesis of BST

The complete synthesis steps for all the BST samples have been described in Figure 3.1 where the formation of respective *gel* of the BST samples was followed by the generation of *sols.* The *sols* were dried to produce powders which were used for the characterization of the samples.

For the synthesis of 250.0 mL of 0.1 M $Ba_{0.77}Sr_{0.23}TiO_3$ *sols*, 4.91 g of barium acetate and 1.18 g of strontium acetate granules were measured. The barium acetate and strontium acetate salts were separately dissolved in acetic acid by stirring at a speed of 450 rpm and 60 ^{o}C in 250.0 mL of the solutions. Afterwards, the solutions were mixed by stirring at 450 rpm and 60 ^{o}C for 0.5 h which was finally was made to cool down. 7.4 mL of TTIP was dissolved in 15 mL of diethyl ether (DEE) in which 2.0 mL of acetyl acetone was added to prevent oxidation of TTIP. 200.0 mL of the barium and strontium solutions was mixed with the TTIP solution using a syringe while stirring. To hasten the *gel* formation and stabilise it, 1.0 mL of the acetyl acetone was added after 30 min of heating (Attar et al., 2017; Saeed et al., 2015).

Similar procedures were followed for the synthesis of 250.0 mL of 0.1 M $Ba_{0.6}Sr_{0.4}TiO_3$, except 4.47 g of $Ba(CH_3COO)_2$, 1.54 g of $Sr(CH_3COO)_2$ and 7.1 mL of TTIP were used as precursors.

Parts of the *gels* were taken for TGA/DSC measurement while the remaining amount was allowed to age at room temperature for 3 h which was then heat-treated in an oven at 180 ^oC for 4 h to remove the solvents. To obtain nanocrystalline granules, the samples were calcined in a muffle furnace at 800 ^oC and 900 ^oC with a heat rate of 10 $℃/min$. The nanocrystalline powders were obtained after the granules were ground using mortar and pestle. The BST powders were used for characterization of the nanocrystalline sample using XRD, FT-IR, Raman spectroscopy, XPS, SEM, EDS, TEM/HR-TEM and BET techniques to study their morphological, microstructural and compositional characteristics. The powders were pressed in order to get pellets of 10 mm in diameter with an average thickness of about 2 mm using a pelletizer at 100 MPa pressure in Bharathiar University, PSG College of Technology, Tamil Nadu, India. The samples were placed into the muffle furnace and were sintered at temperatures of 1000 ^oC and 1100 ^oC along with a heating rate of 10 ^oC/min for 2 h. Then, a silver of an estimated thickness 20 Å was applied to both surfaces of the pellets using *DC* sputtering at a voltage of 500 V and current of 1.5 A. Then they were hardened from 200 to 600 °C using a muffle furnace. The pellets with silver electrodes were inserted into a compression jig prior to electrical measurement using an *AC* impedance Analyzer in the temperature range of 10 ^oC to 100 ^oC for the capacitance as well as dielectric constant measurement and from 10 ^oC to 125 ^oC for the dielectric loss determination at an ambient atmosphere (Attar et al., 2017; Saeed et al., 2015a). Sine-wave excitation was used in the capacitance measuring circuit that runs on *AC* power. Using two DDS (direct-digital-synthesiser) integrated circuit chips (AD7008), two 500 kHz sine-wave signals with a peak break down voltage of 18 V/cm were produced. One served as a voltage source for excitation, and the other as a reference signal. Using two latches (74HC273) and a common clock of 50 MHz, the two signal generators were kept in sync. The unknown capacitance received the excitation voltage application. The current was transformed into voltage using a wide bandwidth operational amplifier (LM6263), feedback capacitance and feedback resistance. To accommodate a wide range of capacitance values and to guarantee that the signal to be demodulated was of the order of volts, the signal was further amplified by an *AC* programmable-gain amplifier (PGA) built from operational amplifiers (LM6263) and CMOS switches (ADG201), which provided gains of 10 and 100. If the signal was not of the order of volts, the following circuit was to be resulted in significant noise and errors.

3.2.2 Synthesis of Mo-doped BST

A procedure reported by Sadeghzadeh Attar was applied for the synthesis of 250.0 mL of 0.1 M Mo-doped $Ba_{0.77}Sr_{0.23}TiO_3$ *sols*. Hence 4.91 g of barium acetate and 1.18 g of strontium acetate granules were separately dissolved in acetic acid by stirring at a speed of 450 rpm and 60 ^oC to form 150.0 mL of each clear solution. Subsequently, the two solutions were mixed and stirred at 450 rpm and 60 ^oC for half an hour. The final solution was then allowed to cool down. Afterwards, 0.02 mol (0.07 g), 0.04 mol (0.14 g) and 0.06 mol (0.22 g) of molybdenum trioxide were dissolved in a 60% (v/v) ammonia/de-ionized water solution for the complete dissolution of the MoO_3 powder. In the meantime, 7.1 mL of TTIP was mixed with 15.0 mL of diethyl ether so as to form a solution where 2.0 mL of acetyl acetone was added to it for the purpose of resisting oxidation of TTIP and stabling it. 200.0 mL of the previously prepared mixture of barium and strontium was added to the TTIP solution slowly using a syringe at a rate of 2.0 mL per minute under the continuous stirring. Subsequently, Mo solution was added to the previous solution and it was heated to 110 ^oC. After about 30 min of heating, 1.0 mL of the acetyl acetone was added to speed up the *gel* formation and stabilize it (Attar et al., 2017).

Equivalently, for the purpose of synthesizing 250.0 mL of 0.1 M Mo-doped $Ba_{0.6}Sr_{0.4}TiO_3$, the same steps were adopted except that 4.47g of barium acetate and 1.54 g of strontium acetate, 7.0 mL of TTIP were used as staring materials. Meanwhile, 0.02 mol (0.07 g), 0.04 mol (0.14 g) and 0.06 mol (0.22 g) of molybdenum trioxide dissolved in 60% (v/v) ammonia/de-ionized water solution were used as dopants (Attar et al., 2017).

The same procedure applied during the synthesis of the pristine BST was followed after the formation of the *gel*s. Likewise, the same characterization techniques and dielectric properties measurements were also used.

3.2.3 Synthesis of Se-doped BST

250.0 mL of 0.1 M Se-doped $Ba_{0.77}Sr_{0.23}TiO_3$ *sols* were prepared through the liquefying of 4.92 g barium acetate along with 1.44 g strontium acetate granules in acetic acid by stirring them at a speed of 450 rpm and 60 ^oC so that 150.0 mL of each clear solution was formed. Subsequently, the two solutions were mixed and stirred at 450 rpm and 60 ^oC for 30 min. The final solution was then allowed to cool down. 0.02 mol (0.06 g), 0.04 mol (0.11 g) and 0.06 mol (0.17 g) of selenium dioxide were dissolved in de-ionized water at room temperature. In the meantime, 7.4 mL of TTIP was mixed with 15.0 mL of diethyl ether so as to form a solution where 2.0 mL of acetyl acetone was added to it so as to inhibit oxidation of TTIP and make it stable. 200.0 mL of the previously

prepared final solution of barium and strontium was added to the TTIP solution slowly using a syringe at a rate of 2.0 mL per minute under the continuous stirring. Afterwards, all of the selenium solution was then added. Finally, the solution was heated to 110 ^{o}C. After half an hour of heating, 1.0 mL of the acetyl acetone was added to speed up the *gel* formation and stabilize it. The *gel* was then formed (Attar et al., 2017).

Similarly, 4.47 g of barium acetate, 1.54 g of strontium acetate, and 7.2 mL of TTIP were employed as precursors. Meanwhile, 0.02 mol (0.06 g), 0.04 mol (0.11 g) and 0.06 mol (0.17 g) of SeO_2 selenium dioxide were used as dopant to synthesize 250.0 mL of 0.1 M Se-doped $Ba_{0.6}Sr_{0.4}TiO_3$ nanopowder. Exactly the same steps were then followed.

Both *gels* were converted to nanopowders which were later characterized using the same techniques as that of the Mo-doped BST samples. The same capacitance and dielectric properties determination steps and conditions were also employed as that of the Mo-doped BST samples.

3.2.4 Synthesis of (Mo, Se) co-doped BST

Here, only (Mo, Se) co-doped $Ba_{0.6}Sr_{0.4}TiO_3$ nanopowder was synthesised and studied since its microstructural and morphological differences from the doped $Ba_{0.77}Sr_{0.23}TiO_3$ nanopowder has been already observed and discussed in the Mo-doped BST and Se-doped BST nanopowder samples.

For the preparation of 250.0 mL 0.1 M (Mo, Se) co-doped $Ba_{0.6}Sr_{0.4}TiO_3$, 4.47 g barium acetate, 1.44 g strontium acetate and 7.2 mL of TTIP precursors were used. Meanwhile, 0.04 g (0.02 mol) MoO_3, 0.07 g (0.04 mol) MoO_3, 0.11 g (0.06 mol) MoO_3, 0.03 g (0.02 mol) SeO_2, 0.06 g (0.04 mol) SeO_2 and 0.08 g (0.06 mol) SeO_2 were utilized as dopants. Afterwards, exactly the same steps used for the synthesis of the Mo-doped BST and Se-doped BST were followed.

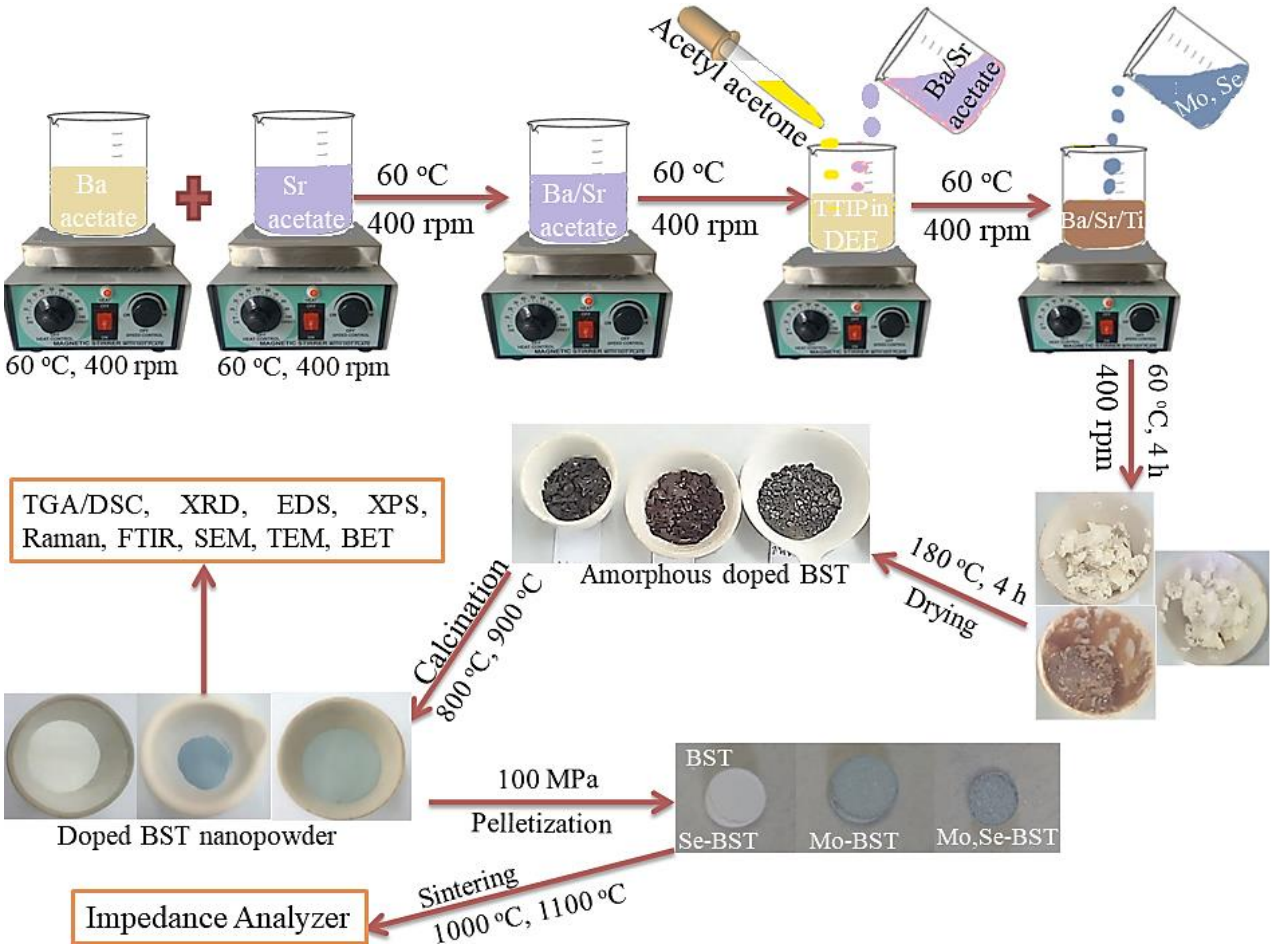

FIGURE 3.1 The slow injection *sol-gel* synthesis and characterization of the BST samples

3.2.5 Characterization of the pristine and doped BST samples

From TGA curves, the percentage of weight loss of the BST and doped BST samples were explored and assessed for their coincidences with the respective heat changes of the DSC peaks. The two curves were utilized to describe the type of species formed and decomposed during the calcination process of the BST and doped BST samples (Eswaramoorthi et al., 2015; A.-C. Ianculescu et al., 2016). The temperature at which no weight loss and no heat change were determined. It was taken as the suitable calcination temperature of the BST samples. Thermal gravimetric analysis and differential scanning calorimetry (HCT-3, Beijing Hengjiu Instrument, China) have been performed using a thermal analyser from 30 ^{o}C to 800 ^{o}C under air flow with a heating rate of 10 ^{o}C/min and hold time of 50 °C min^{-1} at the School of Chemical and Food Engineering, Bahir Dar University, Bahir Dar to determine the temperature at which BST and doped BST were formed. The curves were then drawn using Origin 2021 software.

The FT-IR and Raman spectroscopy spectra have been used to describe the existence of the functional groups before and after doping of BST. All the bands were assigned so to investigate the effects of the dopants on the position of peaks of BST. Any shift of peaks and change of intensity of

the peaks were examined to confirm the effectiveness of doping. The FT-IR (JASCO, FT/IR-6600, Japan) was utilized in the range of 400 - 4000 cm^{-1}. All the BST samples were mixed with KBr powder and around 6 drops of water was added so that respective pellets were prepared using a pelletizer. The thin pellets were placed into the sample holder of the instrument during the measurement which took place in the School of Chemical and Food Engineering, Bahir Dar University, Bahir Dar. The FT-IR curves were then drawn and analyzed using Origin 2021 software.

Raman spectroscopy (UniDRON, Republic of Korea) has also been applied in detecting the formation of BST perovskite structure as well as the extent of doping of BST with the respective dopants within the range of 200 – 1000 cm^{-1} Raman shift. Pellet or powder forms of the respective BST samples were firstly prepared before taking them in to the instrument using a glass. As a result, a laser is used to irradiate the sample, and a spectrograph (dispersive or FT technology) is used to analyse some of the scattered light. Final results include a Raman spectrum that revealed distinctive signals or "bands" for the BST samples. This was performed in Nano-Electrochemistry Laboratory, Department of Chemical Engineering, National Taiwan University of Science and Technology, Taiwan. The Raman spectra were then drawn using Origin 2021 software.

From the XRD patterns, the full widths at half maximum values of the three major peaks were utilized to explore the crystallite size of BST and doped BST samples. The sharpness and width of the peaks were also used to assess the crystallinity of the BST samples. The changes in crystallinity and average crystal size of BST as a result of doping were examined. The corresponding experimentally observed peaks were compared with standard values (from JCPDS/ICDD database) so as to match and identify the BST samples. XRD diffract meter (Shimadzu, XRD-7000, Japan) with a $CuK_{\alpha 1}$ radiation of wavelength 1.5406 Å, a voltage of 40 kV, a current of 30 mA at a scan rate of 3 ^{o}/min, and scan range of 10.00 – 80.00° was employed during the measurement of the BST and doped BST nanopowders at Department of Material Science and Engineering of Adama Science and Technology University. The XRD spectra were then drawn and anayzed using Origin 2021 software so that the crystal size was calculated. QualX software was used to determine the card number and shape of the BST samples.

The SEM images were used to collect information concerning the average grain size, shape and degree of agglomeration of the nanopowders before and after doping of the BST base material. The surface morphology and average grain size of all the BST and doped BST nanopowders were explored by SEM-EDS (JEOL, Germany) at the Department of Chemistry, Chemistry Engineering and Applied Chemistry, Chungnam National University, Republic of Korea. This was done once the

sample has been attached to the sample holder which was later taken in to stage of the instrument. A beam of electrons was allowed to scan the surface the BST nanopowder samples and the secondary electrons were collected for analysis. After wards, the grain sizes were determined using an image j software. In the meantime, the chemical compositions of the samples have been dealt through the use of EDS. The EDS spectra were analysed by simply observing the atomic/weight percentage of occurrence of the respective atoms of both BST and doped BST samples. The most intense peak was supposed to be the one with higher percentage of abundance in the samples (BST and doped BST). From the data, the atomic percentage values were compared with the values utilized during the synthesis.

The XPS data was examined by assigning every peak to the respective ions with specific orbitals. Hence, the existence of all the ions of the BST samples was examined. In a similar way to EDS, the stoichiometric amounts of the atoms and their respective atomic/weight percentage values obtained from the XPS data sheet were compared. XPS (Thermo Scientific K-Alpha, USA) has been used to verify the existence of ions of doped BST nanopowders and the respective dopants so as to confirm the incorporation of the dopant ions to the BST material at Chemistry, Chemistry Engineering and Applied Chemistry, Chungnam National University, Republic of Korea. This has been done by pressing the BST powder in a clean, high purity indium foil. The powder put in the DMSO solvent to dissolve it, and then dropped the cast onto a silicon wafer's clean surface. The powder was sprinkled over a piece of conductive carbon tape that is adhesive. Finally the BST nanopowder samples were radiated using K_{α} X-ray radiation in to where electrons were used for analysis. The XPS spectra were drawn using Origin 2021 software.

The TEM/HR-TEM micrographs were analysed by assessing the particle size, rate of agglomeration, orientation and shape of the particles of the doped BST sample. The shapes of the particles were compared with the one obtained from the XRD data of the doped BST samples. The particle size was examined with the crystal size of the respective sample obtained from XRD for comparison purposes. Images from HR-TEM-SAED were also used to determine the miller indices (*h k l)* of the doped BST samples which were compared with the respective XRD data. From the orientations of the sample obtained, single or poly crystallinity existence of the samples was determined. TEM/HR-TEM (JEM-2100, USA) has been utilized to determine the inner arrangement of particles and grain of the BST samples at Department of Chemistry, Chemistry Engineering and Applied Chemistry, Chungnam National University, Republic of Korea. Here, The BST samples were cut into extremely thin cross-sections. This enabled direct electron through-passage through the BST material. The samples were embedded in hard resin after being cured and dehydrated to make them easier to cut. The samples were then taken in to the TEM where a beam of electrons was

transmitted through the BST nanopowder samples. This was followed by collecting the electrons which provide information about the plan orientation, particle size and shape of the particles. Such informations were obtained using Gatan software.

From the BET, the pore size, surface area and total pore volume values of both BST and doped BST were compared to describe the effect of the dopants on the porosity of BST. The surface area values together with the corresponding average crystal and grain sizes were also utilized to calculate the rate of agglomeration of particles of the BST samples before and after incorporation of the dopants. BET measurement was performed (Quantachrome NovaWin, version 11.0, USA) to determine the textural properties of BST and the doped BST nanopowder samples at the School of Chemical and Food Engineering, Bahir Dar University, Bahir Dar. The BET method calculates a sample's "surface area" by measuring the physisorption of a gas. The measurement covers the entire microscopic surface area of the sample because the gas molecules can penetrate all pores, fissures, and surface roughness in addition to passing through gaps between particles. 0.05 g of each BST sample was utilized for such a measurement. Nitrogen gas has been used as an adsorbate at the surface of the BST samples with an out gas temperature of 300 ^{o}C, bath temperature of 77.3 K and outgas time of 8.0 h. The textural properties of the samples were illustrated through a non-local density functional theory (NLDFT) model. The respective graphs were plotted and analyzed using Origin 2021 software.

The impedance analyzer measurement data was used to examine the dielectric constant and dielectric loss of all the BST samples with reference to temperature. The dielectric constant along with dielectric loss values of the pristine BST were also compared with the doped BST samples. The dielectric property values at different calcination temperature, amount of dopant and sintering temperature were also examined. Ultimately, the effect of the dopants on the capacitive performance of the BST were assessed (Jacob et al., 2015). Impedance analyzer (Solartron-1260, Switzerland) measurements of the respective pellets of the BST samples were performed to determine the dielectric constant, capacitance, and dielectric loss at Universiti Putra Malaysia, Serdang, Malaysia. Initially, the pellets were coated with a 20 Å thick silver using a *DC* sputtering (SC500 Bio rad, Japan) at a voltage of 500 V and a current of 1.5 A. and sandwiched between the electrodes. The silver coated pellets were then attached to the impedance analyzer through copper wire for the measurement to take place. The potential was applied in the randomly selected temperatures within the ranges of 10 ^{o}C to 100 ^{o}C for the capacitance measurement and 10 ^{o}C to 125 ^{o}C for the dielectric loss determination at a frequency of 1 MHz. Then the effect of temperature on the dielectric constant, capacitance, and dielectric loss was explored for the pristine, doped and

co-doped BST samples at calcining and sintering temperature. Finally, the respective graphs were plotted and analyzed using Origin 2021 software.

CHAPTER 4. RESULTS AND DISCUSSION

4.1 Synthesis of the BST, Mo-doped BST, Se-doped BST, and their co-doped BST samples

Figure 4.1 (a-d) portraits the colour of BST, Mo-doped BST, Se-doped BST and their co-doped BST nanopowder samples synthesized through the slow injection *sol-gel* method after calcination. The addition of the dopants to the BST solution resulted in a sample of varied colours. Light yellow coloured *gels* of BST, Mo-doped BST and (Mo, Se) co-doped BST and brown colored Se-BST were initially obtained. This was supposed to be resulted from the occurrence of carbon in the samples as well as the evaporation of water from the *gel*s. The colour was later converted in to brown after drying them in an oven at 180 ^{o}C. This was believed to indicate the existence of carbon still in the BST samples and the removal of water from the *gels*. As a result of calcination of the BST samples at 800 ^{o}C and 900 ^{o}C, the brown colour was changed into white (BST and Se-doped BST), blue grey (Mo-doped BST) and light green (Mo, Se co-doped BST). This colour change was taken as a signal for the removal or minimization of the carbon atoms from the samples even though small amounts of remaining carbon atoms were detected by FT-IR. The uniform colours could be the result of the evenly distributed amount of the dopants in the BST sample. Hence, this was considered to be the first indication of the formation of the (Mo, Se) co-doped BST which was later, credibly, confirmed by the analysis of Raman spectroscopy, XRD, EDX and XPS data.

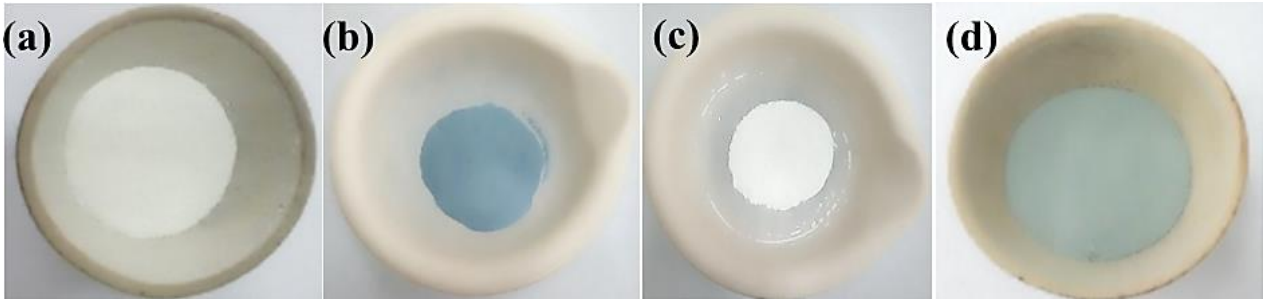

FIGURE 4.1 The visual observation of (a) BST (b) 0.04 mol Mo-doped BST (c) 0.04 mol Se-doped BST, and (d) 0.04 mol (Mo,Se) co-doped BST nanopowders

4.2 Characterization of the BST, Mo-doped BST, Se-doped BST and their co-doped BST Samples

4.2.1 TGA/DSC analysis

The thermal stability of both the pristine and doped BST *gel* samples was studied before calcination. Similar TGA/DSC data has been obtained for both BST-0.6 and BST-0.7 samples. The TGA/DSC data of the samples are indicated at Figure 4.2 (a-c). From the TGA and DSC curves of

the undoped and Mo-doped BST samples (Figure 4.2 a), endothermic peaks have been observed in the temperature range of 80 - 177 ^{o}C with a first weight loss of ~19% for BST and ~74% for the Mo-doped BST samples. These peaks are supposed to be resulted from the evaporation of water and acetic acid. The loss of water has been observed more in the Mo-BST *gel* than the BST *gel* in the region 100 ^{o}C to 250 ^{o}C. This could be due to the hygroscopic nature of Mo that more amount of water was initially composed in the Mo-doped BST *gel* (Ashoka et al., 2010; Attar et al., 2017).

Moreover, the exothermic peak appeared in the range of 400 ^{o}C - 444 ^{o}C revealed the combustion and decomposition of acetic acid and acetyl acetone, organic components of both samples (Somani & Kalita, 2007; Zhao et al., 2008). Such peaks were supported by the 53% weight loss of BST and ~7% weight loss of Mo-BST. The other exothermic peak at 528 ^{o}C belongs to the formation of the BST perovskite structure. The development of amorphous BST perovskite structure has also been confirmed by an exothermic peaks around the regions 612 ^{o}C to 630 ^{o}C (Attar et al., 2017; Hu et al., 2005; Somani & Kalita, 2007; Zhao et al., 2008). The lastly observed peak around 694 ^{o}C was assigned to the polymorphic conversion of the BST and Mo-doped BST samples after which a smooth curve continued up to 800 ^{o}C. Therefore, a stable BST and Mo-doped BST samples were formed, starting around 600 ^{o}C to 800 ^{o}C. Hence, calcination temperatures of 800 ^{o}C and 900 ^{o}C were selected by considering the hygroscopic property of Mo and for the synthesis of relatively pure and crystalline BST and Mo-doped BST nanopowders (Somani & Kalita, 2007). This was supported by the XRD data of the sample calcined at 800 ^{o}C and 900 ^{o}C. Similar findings were reported by Attara (Attar et al., 2017).

Similarly, Figure 4.2 (b) depicted the thermograms of pristine BST-0.6 and Se-doped BST-0.6 which was similar to the thermograms the BST-0.7 samples. From both spectra, an endothermic peaks at 80 ^{o}C, 105 ^{o}C, 109 ^{o}C, 116 ^{o}C and ~130 ^{o}C signified the evaporation of water and acetic acid (Ashoka et al., 2010). This is represented by the respective 19% and 23% weight losses for the BST and Se-doped BST. Other weight losses of 53% and 25% were seen in the BST and Se-doped BST spectra, respectively, between 250 and 411 ^{o}C. These correspond to the decomposition of organic solvent components (Somani & Kalita, 2007; Zhao et al., 2008). Another exothermic peaks observed around 430 ^{o}C and 447 ^{o}C for 20% weight losses described the development of BST perovskite structure of Se-doped BST (Zhou et al., 2009). The evolution of amorphous BST and Se-doped BST was indicated by an exothermic peaks ~ 633 ^{o}C and 644 ^{o}C which confirmed the embodiment of Se^{4+} ions into the perovskite structure (Emadi, et al., 2019; Zhao et al., 2008). Finally, the respective peaks around 701.78 ^{o}C and 728 ^{o}C were used as confirmatory peaks for the polymorphic conversion of the BST and Se-doped BST nanocrystalline (Attar et al., 2017; R Balachandran et al., 2011; Emadi et al., 2019; Mohammadi & Fray, 2011; Wang, 2004). Hence,

synthesizing Se-doped BST nanocrystalline at 800 ^{o}C and 900 ^{o}C was planned to be successful where changes of some properties of BST were obviously expected. Such predictions were later confirmed using the Raman spectroscopy, XRD, EDS and XPS data.

The TGA and DSC curves of the BST-0.6 and 0.04 mol (Mo, Se) co-doped BST-0.6 gels have been presented in the Figure 4.2 (c). From both curves, peaks around 80 ^{o}C, 105 ^{o}C, 109 ^{o}C, 116 ^{o}C and 168 ^{o}C represented endothermic processes with weight loss values of ~ 19% (BST-0.6) and ~ 60% ((Mo, Se) co-doped BST-0.6). These are supposed to be indicators of evaporation of water as well as acetic acid. Higher temperature and larger weight loss values were obtained for the (Mo, Se) co-doped BST-0.6 as compared to BST-0.6 which were supposed to be due to the hygroscopic property of both the Mo and Se dopants (Ashoka et al., 2010; Attar et al., 2017; Zhou et al., 2009). Consequently, more loss of water has been observed in the (Mo, Se) co-doped BST *gel* as to BST *gel* in the region 100 ^{o}C to 250 ^{o}C which is probably attributed to the higher amount of water found in the (Mo, Se) co-doped BST-0.6 *gel*. Still additional weight losses around 53% for BST-0.6 and 9% for (Mo, Se) co-doped BST-0.6 were resulted in the region from 250 ^{o}C to 430 ^{o}C. Such peaks revealed the decomposition of lower boiling point organic components (Somani & Kalita, 2007; Zhao et al., 2008).

An additional exothermic peak was detected around 527 ^{o}C and 594 ^{o}C illustrating the earliest evolution of the (Mo, Se) co-doped BST-0.6 perovskite. The formation of amorphous BST-0.6 perovskite structure has also been verified by an exothermic peak around 633 ^{o}C (Attar et al., 2017; Somani & Kalita, 2007; Zhao et al., 2008; Zhou et al., 2009). Finally, the peak around 693 ^{o}C was taken as an illustrative of the polymorphic crystalline development of the BST-0.6 and (Mo, Se) co-doped BST-0.6 perovskites (Attar et al., 2017; Somani & Kalita, 2007; J. Wang et al., 2004). Therefore, the 800 ^{o}C calcination temperature was considered as a suitable temperature for the complete formation of crystalline (Mo, Se) doped BST-0.6 sample. Subsequently, the prediction was validated using the respective Raman spectroscopy, XRD and EDS results.

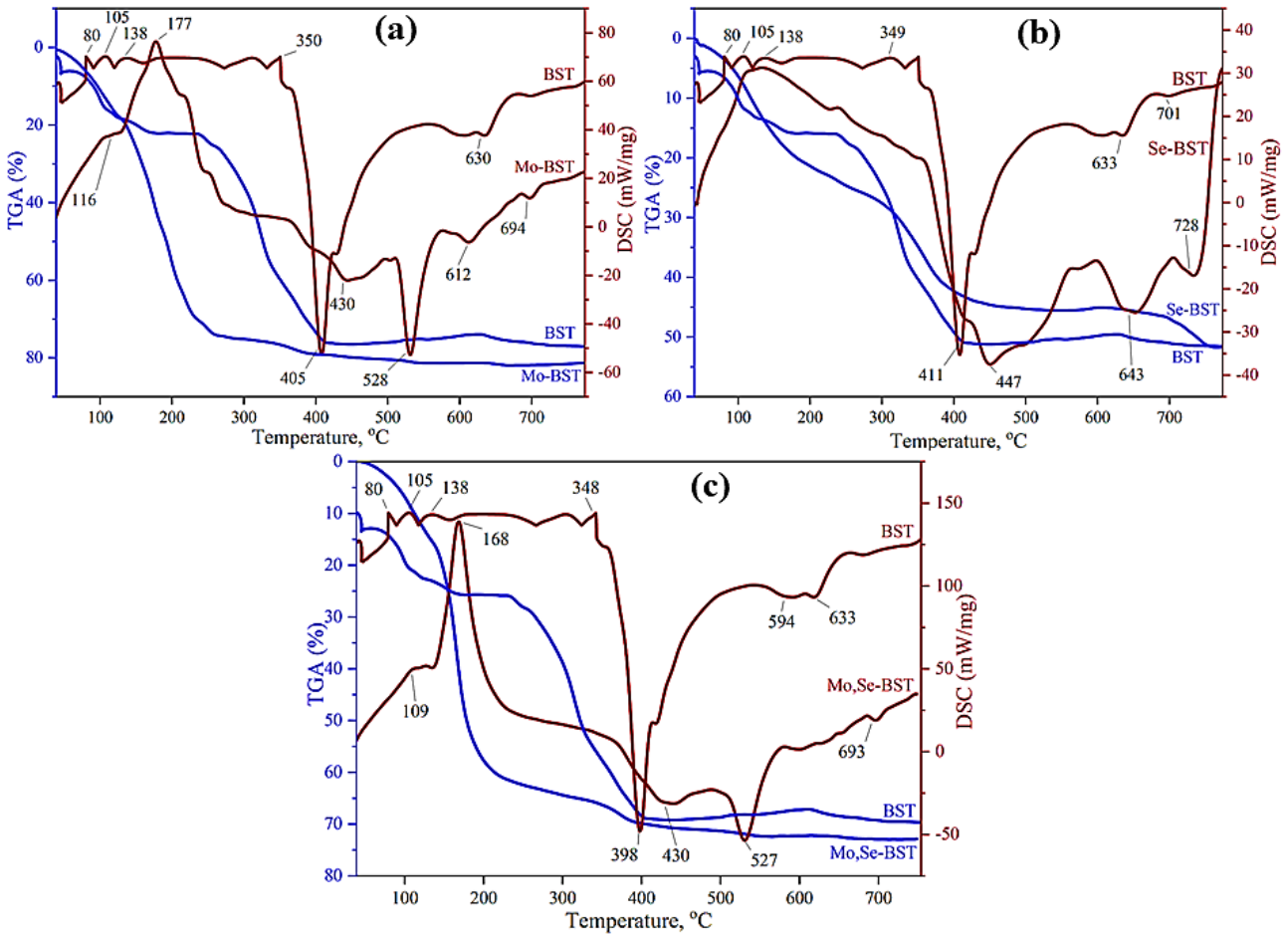

FIGURE 4.2 TGA-DSC curves of the (a) 0.04 mol Mo-doped BST-0.7 (b) 0.04 mol Se-doped BST-0.6 and (c) 0.04 mol (Mo, Se) co-doped BST-0.6 nanopowders

4.2.2 FT-IR analysis

Similar FT-IR data was attained for the BST-0.6 and BST-0.7 of the Mo-doped BST and Se-doped BST samples and hence either of the corresponding samples was discussed.

Figure 4.3 (a, b) described the FT-IR spectra of undoped BST and Mo-doped BST nanopowders calcined at 900 ^{o}C for 2 h. A broad band at 3431 cm^{-1} was clearly observed in the Figure 4.3 (b). It could be due to the existence of an un-removed O-H bond which belongs to the smaller amount of water molecules adsorbed at the surface during the time of measurement accompanied by the highest hygroscopic nature of the Mo dopant (Attar et al., 2017; Emadi et al., 2019). Another band observed at around 1442 cm^{-1} revealed the evolution of Ba-O-Ti bond of the perovskite. The C=O bond of the $BaCO_3$ secondary phase was also noticed at 1640 cm^{-1} which was resulted from the thermal oxidization of barium acetate, since its boiling point (1360 ^{o}C) is greater than the calcination temperature of 900 ^{o}C. The O-H and carbonates are found in very smaller amount that they are not included in the empirical formula of Mo-doped BST (Jiang et al., 2022; Shaban & Bahar, 2017; Shalu & Ghosh, 2019; Simões et al., 2010). Hence, calcining the Mo-doped BST

powder above 800 ^{o}C was expected to be resulted in a more crystalline powder by removing the tiny amounts of the O-H and carbonates. The bands found at ~ 1110 cm^{-1} are possibly assigned to the resonated C-O bonds of the carbonates (Mohammadi & Fray, 2011; Shalu & Ghosh, 2019; Socrates, 1995). Such a bond existed in the BST samples despite their calcination at 900 ^{o}C. This was found similar to Bi-doped BST and Zr-doped BST samples which were composed of O-C bond after they were calcined at 800 ^{o}C and 850 ^{o}C (Attar et al., 2017; Shalu & Ghosh, 2019).

All the unnecessary O-H and carbonates were expected to be completely removed during sintering of the pellets. The bands encompassing 420 cm^{-1}, 440 cm^{-1}, 530 cm^{-1}, 600 cm^{-1} and 832 cm^{-1} were representatives of the M-O bonds (M - metal) such as Ba-O, Sr-O and Ti-O vibrations (Emadi et al., 2019; González, Wu, & Vilarinho, 2006). The FT-IR spectra of Mo-doped BST have shown no unique peak, even though shifting of some peaks have been observed. The distinctive peaks of the Ba-O, Sr-O, Ti-O vibrations shifted towards smaller wave numbers (from 440 cm^{-1}, 534 cm^{-1}, 567 cm^{-1}, 620 cm^{-1}and 878 cm^{-1} towards 421 cm^{-1}, 537 cm^{-1}, 600 cm^{-1}, and 832 cm^{-1}) indicating the incorporation of Mo in to BST. This is the result of weaker interaction found at the B-site ions and O^{2-}, since Mo-O bond (391.6 kJ/mol) possess less intense bond as compared to the Ti-O bond (662.4 kJ/mol) (Luo, 2003). In addition, the Mo-doped BST nanopowder has shown more intense and sharp peaks as compared to the BST nanopowder. This was supposed to be an indication of higher amount of O-H which is caused by the addition of the hygroscopic Mo dopant (Emadi et al., 2019; González et al., 2006). The substitution of Ti^{4+} ions by Mo^{6+} ions was later found in a better matching with the Raman spectroscopy, XRD, EDS, and XPS data outcomes.

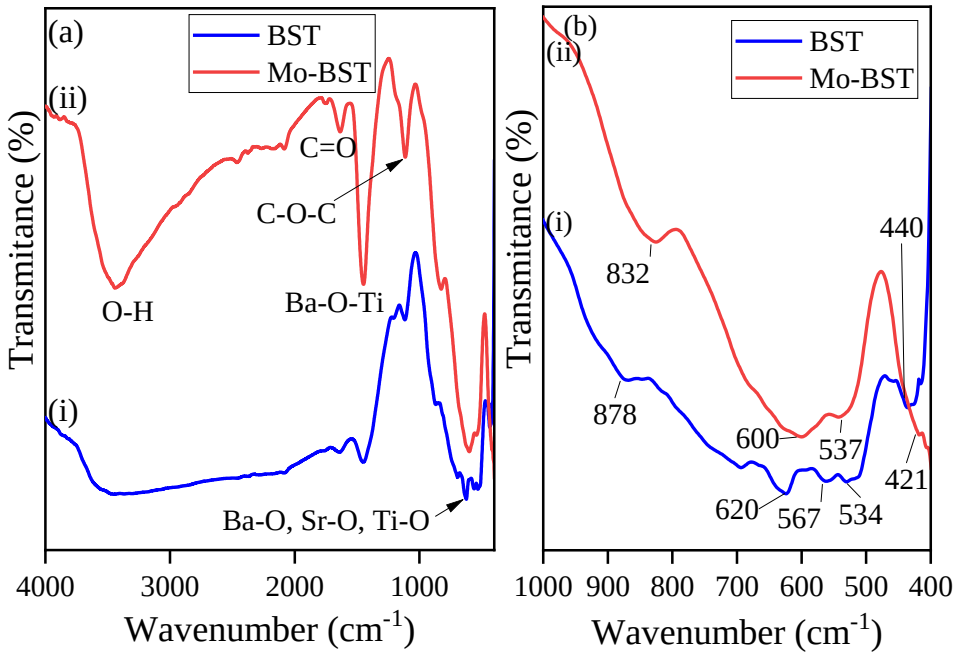

FIGURE 4.3 (a) FT-IR spectra of (i) BST-0.7 and (ii) 0.04 mol Mo-doped BST-0.7 nanopowders calcined at 900 ^{o}C (b) Enlagred version of shifting of peaks after doping

The BST and 0.04 mol Se-doped BST-0.6 nanopowders are presented in Figure 4.4 (a, b). The broader peak at 3432 cm^{-1} represents O-H bonds defining water molecules adsorbed from the surrounding onto the surface of the powder samples during measurement accompanied by the higher hygroscopic property of Se (Emadi et al., 2019). An insignificant amount of C = O bond of the $BaCO_3$ secondary phase was also detected at 1640 cm^{-1}. It is very smaller than that of Mo-doped BST samples. This was apparently caused by the lower number of carbonates attached to Ba. Because some Ba atoms were also attracted to wards Se dopant in the perovskite structure, due to the same electronegativity value of both Se and C atoms (2.55). The band at 1456 cm^{-1} represented the existence of Ba–O–Ti bond (Jiang et al., 2022; Simões et al., 2010). The bands observed around 1116 cm^{-1} are expected to be the respective peaks for the C-O stretching vibrations of the resonated single bond of the $BaCO_3$ (Mohammadi & Fray, 2011; Socrates, 1995). Such a bonds was very small in amount that it was not usually included in the empirical formula of the sample (Attar et al., 2017; Shalu & Ghosh, 2019).

Moreover, as per the TGA-DSC spectra, calcination of the samples above 800 ^{o}C was expected to remove the smaller amount of the O-H and carbon atoms so as to synthesize a more crystalline and uniform Se-doped BST-0.6 nanopowder. Besides, any remaining amounts of them were assumed to be detached while sintering the pellets of the BST-0.6 samples, so that their impacts on the dielectric characteristics of the BST-0.6 samples were minimized.

The bands around 436 cm^{-1}, 448 cm^{-1}, 523 cm^{-1}, 548 cm^{-1}, 564 cm^{-1}, 624 cm^{-1} as well as 635 cm^{-1} were indicators of metal-oxygen bonds such as Sr-O, Ba-O, Ti-O as well as Se-O vibrations of the BST-0.6 perovskite that is caused by evolution of the metal oxide bonds (Chen et al., 2006; Emadi et al., 2019; González et al., 2006; Shalu & Ghosh, 2019).

The FT-IR spectrum of the Se-doped BST-0.6 nanopowder was found with almost the same intensity as that of the pristine BST-0.6 unlike the Mo-doped BST-0.6 nanopowder. This was believed to be due to the lower absorption wave length of Se (260 nm) as compared to the absorption wave length of Mo (650 nm). In addition, the absorption wave length of Se is closer to the respective values for the Sr (~203 nm). of BST-0.6. Hence, less changes in absorbance and transmittance was expected following the incorporation of Se in to the BST-0.6 structure. This might also be the reason why the Se-doped BST-0.6 acquired the same white colour as BST-0.6. The Se-doped BST-0.6 nanopowder has been resulted in the FT-IR spectrum with no additional peaks, but shifting of a few peaks was detected. The characteristic peaks of M-O vibrations slightly shifted to higher wavenumbers (436 cm^{-1}, 513 cm^{-1}, 532 cm^{-1}, 564 cm^{-1} and 626 cm^{-1} to the respective 448 cm^{-1}, 542 cm^{-1}, 580 cm^{-1} and 635 cm^{-1}) after the incorporation of Se to the BST-

0.6 structure. Hence, this was taken as an implication of successful doping of BST base material with Se (Y. Luo, 2003; Shalu & Ghosh, 2019).

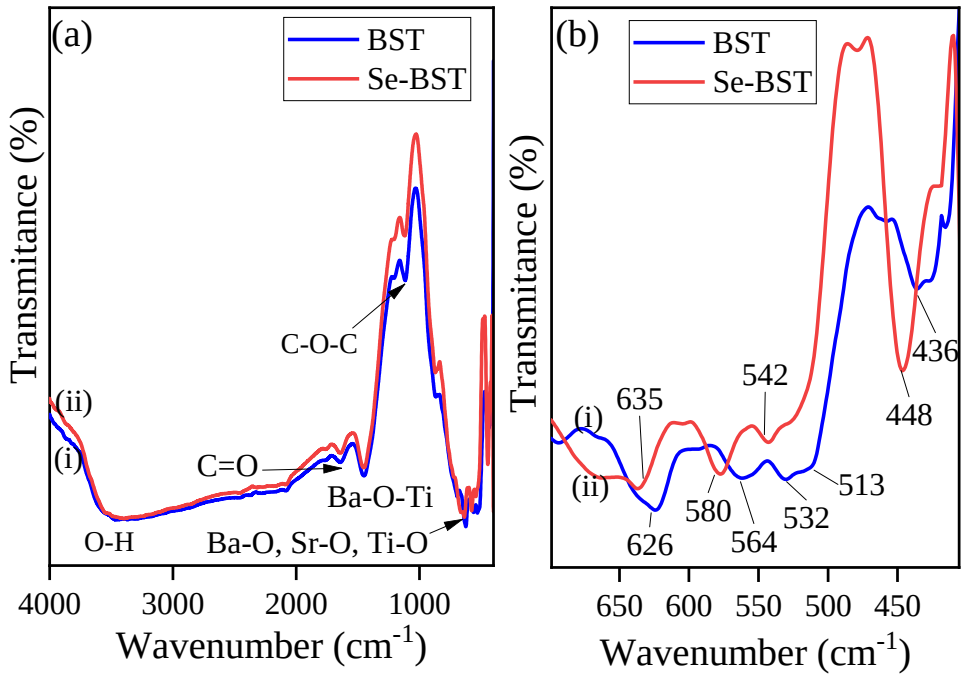

FIGURE 4.4 (a) FT-IR spectra of (i) BST-0.6 and (ii) 0.04 mol Se-doped BST-0.6 nanopowders calcined at 800 ^{o}C for 2 h (b) Enlagred version of shifting of peaks after doping

The FT-IR spectra of BST-0.6 and (Mo, Se) co-doped BST-0.6 nanopowders are shown in Figure 4.5 (a, b). Similar to the Mo-doped BST and Se-doped BST-0.6 spectra, a broader peak appeared around 3464 cm^{-1} revealed the occurrence of O-H stretching due to the adsorbed water molecules on KBr pellets during the FT-IR measurement besides the higher hygroscopic nature of both Mo and Se (Tangwiwat & Milne, 2005). On the other hand, the band around 1640 cm^{-1} expressed the existence of a very low amount of carbonate. The band around 1433 cm^{-1} confirms the appearance of Ba–O–Ti bond (Jiang et al., 2022). The weak bands around 1113 cm^{-1} of the $Ba_{0.6}Sr_{0.4}TiO_3$ peak was associated with the C-O bond of the carbonates which was later broken down by the dopants and remained as a very small amount in the (Mo, Se) co-doped BST-0.6 nanopowder. Such minimization of the carbon content might also be related to the broader and weak C=O bond noticed at the FT-IR spectrum of the (Mo, Se) co-doped BST-0.6 nanopowder in which Se was believed to lower the formation of the $BaCO_3$ by getting attracted towards Ba (Mohammadi & Fray, 2011; Socrates, 1995). That is why the peak which corresponded to the O-C bond almost disappeared in the FT-IR spectrum of the (Mo, Se) co-doped BST-0.6 nanopowder. The existence of the very small amount of O-H and O-C bonds indicated that calcination of the sample above 800 ^{o}C was favourable for the synthesis of more crystalline (Mo, Se) co-doped BST-0.6 nanopowders which was in a good agreement with the TGA-DSC spectra. Further, they were expected to be

minimized or eliminated during sintering of the pellets where their effects on the dielectric properties were minimized.

The three bands observed around 438 cm^{-1}, 529 cm^{-1} and 564 cm^{-1} were treated as representatives of the M-O vibration bands such as Sr-O, Ba-O, Ti-O, Mo-O and Se-O which were possibly due to the development of the metal-oxide bonds of the BST-0.6 perovskite structure (Y.-W. Chen et al., 2006; Emadi et al., 2019; González et al., 2006). Some peaks of the Metal-O bonds (400 – 600 cm^{-1}) that belong to the BST-0.6 spectra could not be found at the respective spectra of the (Mo, Se) co-doped BST-0.6 sample because of the replacement of the A - site and B - site metallic ions by the Mo^{6+} and Se^{4+} ions. Moreover, no unique peak has been obtained for the FT-IR spectra of (Mo, Se) co-doped BST-0.6 nanopowder though a few deviation of some peaks have been resulted. The distinguished peaks at the M-O vibrations has shown little shifting towards higher wavenumbers. This is probably inferred by the weaker interaction of the B - site with O^{2-}, since the Mo-O (607 kJ/mol) and Se-O (423 kJ/mol) bonds involve weaker bonds relative to the Ti-O bonds (662.4 kJ/mol) (Kerr, 1966; Y. Luo, 2003). Therefore, it was evidently confirmed that the co-doped BST sample was composed of the co-dopants Mo and Se which was later validated by XRD and EDS.

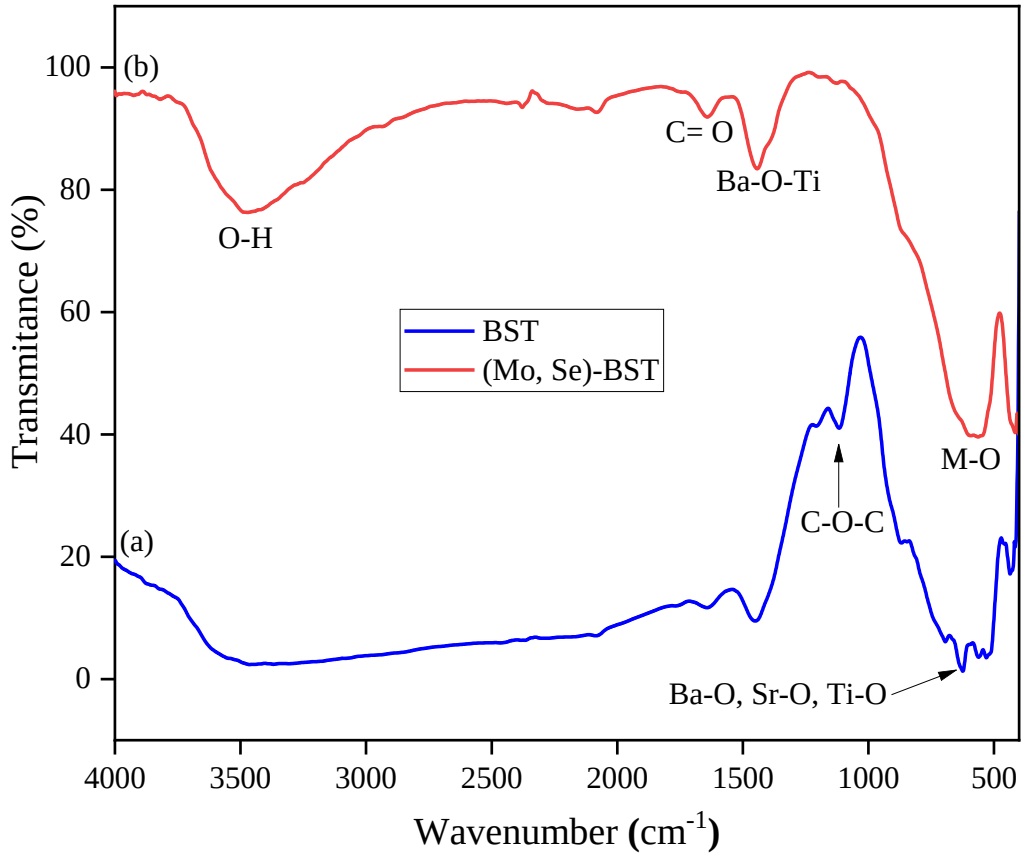

FIGURE 4.5 The FT-IR spectra of (a) BST-0.6 and (b) 0.04 mol (Mo, Se) co-doped BST-0.6 calcined at 800 ^{o}C for 2 h

4.2.3 Raman spectroscopy analysis

Raman spectroscopy is an extremely sensitive spectroscopic method used to further realize the structural and crystalline phases of samples. Raman spectroscopy gives essential data about the impurity, shape, as well as crystal symmetry (Synetos & Tousoulis, 2018). The Raman spectroscopy spectra of both the BST-0.6 and BST-0.7 samples were found similar and compatible to each other. Hence, either of them was explained for the respective Mo-doped BST and Se-doped BST samples.

As can be seen in Figure 4.6 (a-c), Raman bands were observed at 226 cm^{-1}, 303 cm^{-1}, 515 cm^{-1} and 730 cm^{-1} which are represented by their respective vibration modes of A_1(TO), A_1(LO), [A_1, E(TO)] and [A_1, L(TO)] for the undoped and doped BST (Li & Qu, 2009). A_1 (LO) belongs to the longitudinal optical vibration mode of A_1 phonon while A_1 (TO) refers to the transverse optical vibration mode of A_1 phonon. All these bands corresponds to the BST perovskite structure where such results matched with earlier reported works (Balmuchu et al., 2022; Shalu et al., 2022; Venkateswaran et al., 1998; Wang et al., 2006). The weak signal at 303 cm^{-1} is interpreted as the A_1(LO) component, which showed that both samples had a tetragonal structure (Shalu & Dasgupta Ghosh, 2019). The peaks of large frequency at 530 cm^{-1} and 750 cm^{-1} along with the other 170 cm^{-1} peak with small frequency have been obtained representing the (A_{1g} + E_g) and A_1 symmetry of vibrational modes (Bouyanfif et al., 2009; Kuo et al., 2001). The small frequency peaks illustrated the cation ordering, while broadening of the other two peaks represented the effective doping of $Ba_{0.77}Sr_{0.23}TiO_3$ with 0.02 mol and 0.04 mol of Mo.

In 0.02 mol doping of Mo, the Mo^{6+} ions distorted the Ti-O-Ti bond angle and the TiO_6 octahedron which was represented by the (A_{1g} + E_g) mode of vibration where a section of the original BST-0.7 lattice's symmetry is broken (Liu et al., 2016; Pokorný et al., 2011; Yuzyuk et al., 2002). Furthermore, as the amount of Mo added to BST were elevated to 0.04 mol, the prominent phonon peaks of Mo-doped $Ba_{0.77}Sr_{0.23}TiO_3$ at 226 cm^{-1} [A_1(TO)], 515 cm^{-1} [A_1, E(TO)], and 730 cm^{-1}[A_1, L(TO)] shifted towards larger wave numbers (blue shift). Such shifts of the peaks are associated with the alteration of residual stress which was caused by the incorporation of the dopant, Mo, to the BST structure (Chen et al., 2000; Shalu et al., 2022).

The variation of the residual stress was also considered to be the result of elevation of the lattice parameter as well as volume expansion which matched with the XRD data. Such a phenomenon usually occurs due to the difference in ionic radii of Mo^{6+} (0.59 Å) and Ti^{4+} (0.60 Å) as well as the formation of compositional deficiencies including Ba, Sr, and O vacancies (Chang et al., 1999; S. Wang et al., 2006). A_1g octahedral vibration mode representing the Raman band in the vicinity of 800 cm^{-1} and 890 cm^{-1} were detected in the Raman spectrum of Mo-doped BST but not in the

respective spectrum of undoped BST. This demonstrated the existence of a B-site dopant (Mo) in the Mo-doped BST nanopowder (Shalu & Ghosh, 2019; Wang et al., 2006). These explanations were considered as positive indicators of the formation of Mo-doped BST which was subsequently illustrated and sustained by the XRD, EDS and XPS data.

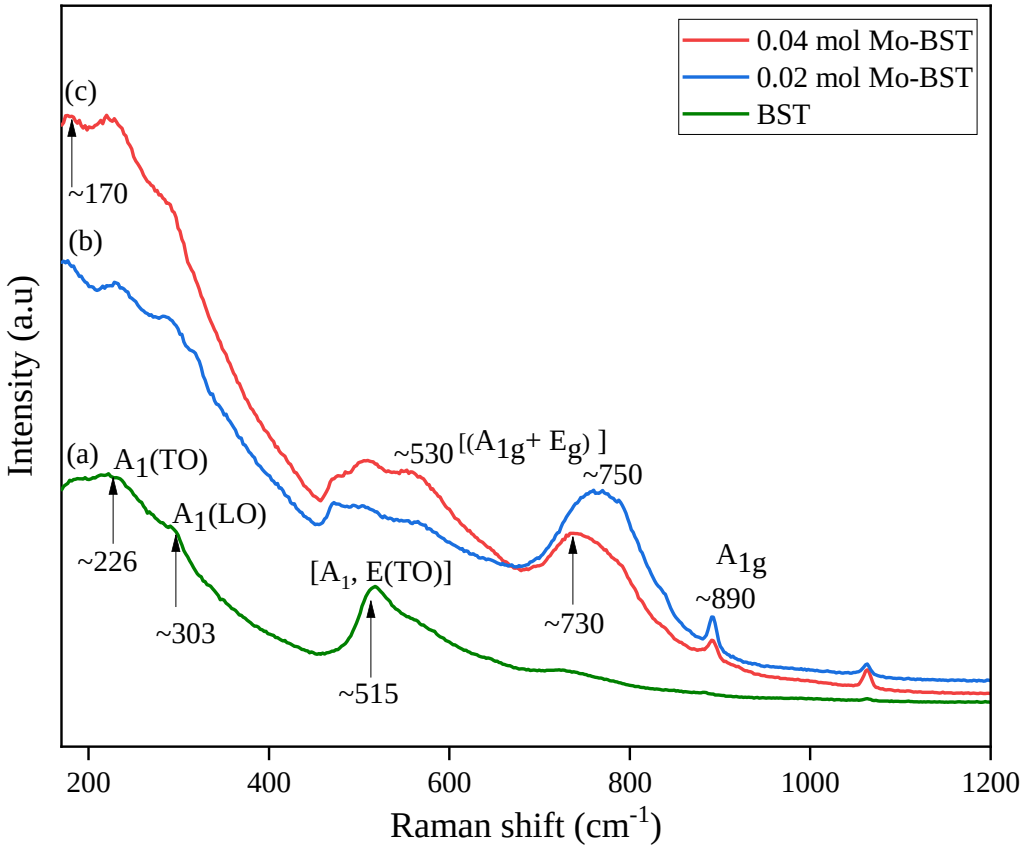

FIGURE 4.6 Raman spectra of (a) BST-0.7 (b) 0.02 mol Mo-doped BST-0.7 and (c) 0.04 mol Mo-doped BST-0.7 nanopowders

As it is clarified in Figure 4.7 (a-c), Raman bands of 226 cm^{-1}, 236 cm^{-1}, 303 cm^{-1}, 515 cm^{-1}, 524 cm^{-1} and 733 cm^{-1} have described the formation of BST-0.6 structure in the doped and undoped nanopowders (Balmuchu et al., 2022; Shaluet al., 2022; Wang et al., 2006). The relatively smaller frequency peaks at 170 cm^{-1} show the (A_1+ E) and A_1 symmetry vibrational modes which described the ordered arrangement of the cation (Bouyanfif et al., 2009; Kuo et al., 2001). It was retained that the Se^{4+} ions distorted the TiO_6 octahedron as well as the Ti-O-Ti bond angle resulting in the alteration of the symmetry of BST-0.6 (Liu et al., 2016; Pokorný et al., 2011; Yuzyuk et al., 2002). Increasing the mass of Se has been resulted in shifting of the above prominent phonon peaks towards 236 cm^{-1} [A_1 (TO)], 524 cm^{-1} [A_1, E (TO)] and 733 cm^{-1} [A_1, E (LO)] to the respective enlarged wavenumbers. Such a phenomenon is related to the change of residual stress after Se^{4+} ion was incorporated in to BST-0.6 (Chen et al., 2000; Shalu et al., 2022). Any difference in the residual stress was expected to have yielded from the change of lattice parameters as well as volume expansion driven by the difference in ionic radii and the deficiencies of vacancies (Chang et al.,

1999; Wang et al., 2006). Such results led to the conclusion that Se-doped BST-0.6 was effectively synthesized. It was later confirmed using the XRD, EDS, and XPS data.

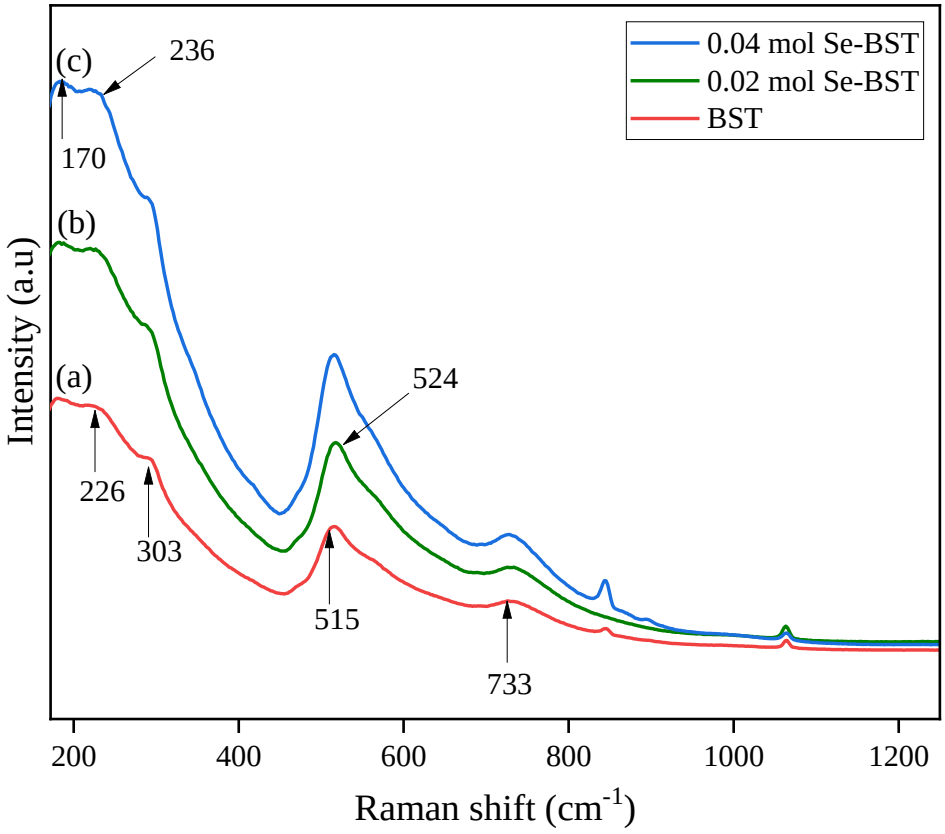

FIGURE 4.7 Raman spectra of (a) BST-0.6 (b) 0.02 mol Se-doped BST-0.6 (c) 0.04 mol Se-doped BST-0.6 calcined at 800 ^{o}C for 2 h

Furthermore, the structural as well as crystalline phases of the BST-0.6 and (Mo, Se) co-doped BST-0.6 perovskites were analysed using the Raman spectroscopy. A very similar Raman spectra with the Se-doped BST-0.6 were obtained for the (Mo, Se) co-doped BST-0.6 Figure 4.8 (a-c). It was clarified that the Raman bands of 236 cm^{-1}, 293 cm^{-1}, 515 cm^{-1} and 733 cm^{-1} are good indicators of the occurrence of a perovskite structured BST-0.6 nanopowder (Balmuchu et al., 2022; Wang et al., 2006). The weak band peaks at 170 cm^{-1} was examined to be the representatives of the (A_1 + E) along with A_1 symmetry of vibrational modes of the BST-0.6 (Bouyanfif et al., 2009; Kuo et al., 2001) that revealed the ordered structure of cations.

Most commonly, broad peaks illustrate the effectiveness of doping of A/B- site of the BST-0.6 perovskite which supported the FT-IR data. Hence, the broad bands at 500 - 700 cm^{-1} of (Mo, Se) co-doped BST-0.6 is weaker than BST-0.6 which is caused by the co-dopants on the TiO_6 octahedra (A_{1g} + E_g mode). The co-dopants distorted the TiO_6 octahedron and the Ti-O-Ti bond angle which later caused the distortion of the symmetry of BST (Liu et al., 2016; Pokorný et al., 2011; Yuzyuk et al., 2002). Elevation of the amount of the co-dopants has caused shifting of the dominant phonon peaks at 236 cm^{-1} [A_1(TO)], 515 cm^{-1} [A_1, E(TO)] and 733 cm^{-1}[A_1, E(LO)] to an increased wave

numbers where the residual stress was altered due to the addition of the co-dopant ions in to BST (Chen et al., 2000; Shalu et al., 2022). The variation of the residual stress was considered to be resulted from the elevation of the lattice parameters as well as the volume expansion (Chang et al., 1999; S. Wang et al., 2006). Such explanations supported the conclusion that (Mo, Se) co-doped BST-0.6 was excellently synthesized which was confirmed by the XRD and EDS data.

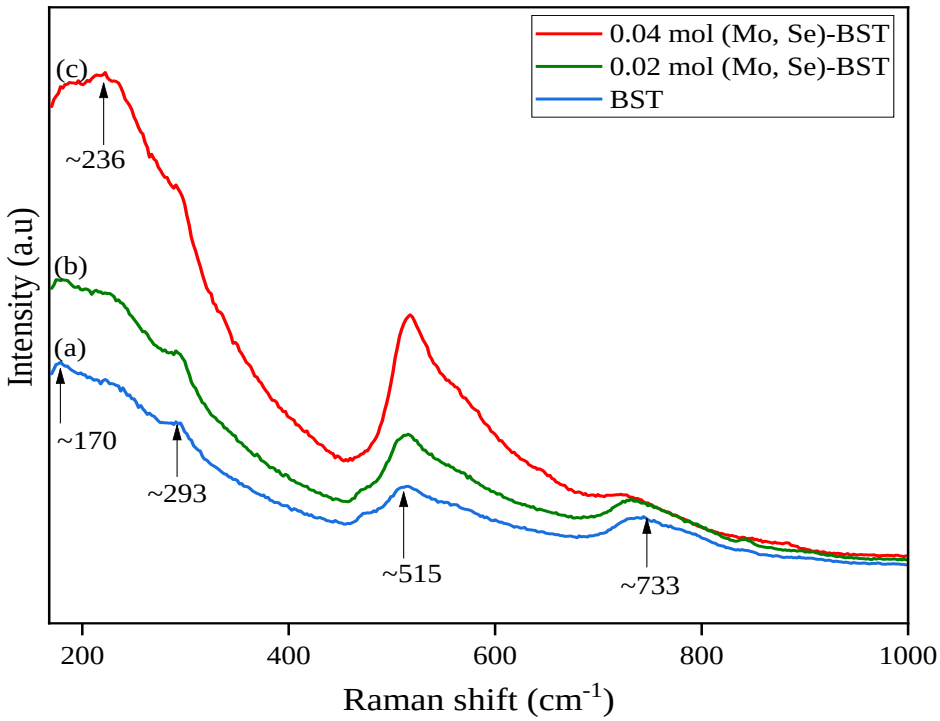

FIGURE 4.8 Raman spectra of (a) BST-0.6 (b) 0.02 mol (Mo, Se) co-doped BST-0.6 and (c) 0.04 mol (Mo, Se) co-doped BST-0.6 calcined at 800 ^{o}C for 2 h

4.2.4 XRD analysis

Varied crystalline structures with different average crystalline sizes were observed in the XRD data of the BST-0.6 and BST-0.7 samples. Thus, it was important to discuss both samples separately.

For the BST-0.6 samples, the XRD spectra of the Mo-doped BST-0.6, Se-doped BST-0.6 and (Mo, Se) co-doped BST-0.6 are described at Figure 4.9, 4.10, and 4.11 respectively. Hence, the formation of cubic shaped BST-0.6 nanopowder (JCPDS # 00-034-0411 index file) calcined at 900 ^{o}C has been confirmed by the appearance of peaks with planes of (100), (110), (111), (200), (210), (211), (220), (300) and (310) in all of the three BST samples (Figure 4.9 (a)). The weak peaks defined by the planes (020) and (040) indicated the appearance of small amount of $BaCO_3$ and MoO_3 phases respectively where the later became more intense as the concentration of Mo^{4+} added to the host (*i.e*. BST), was increased from 0.02 mol to 0.06 mol (Abboudi et al., 2018; Batttisha et al., 2014). The calcination temperature is selected from the TGS/DSC data analysis and previously reported works of the same ratio of Ba to Sr with a B-site dopant (Chou *et al.*, 2007; Jiwei et al., 2002; Paul et al., 2009). Moreover, the sharp peaks revealed the powder (amorphous phase) was fully changed

to the crystalline state at this calcined temperature. The diffraction angles has also been shifted towards higher and lower degrees due to the increased cation-cation repulsion and lower ionic radius of Mo^{6+} ion as compared to Ti^{4+} (Figure 4.9 (b)).

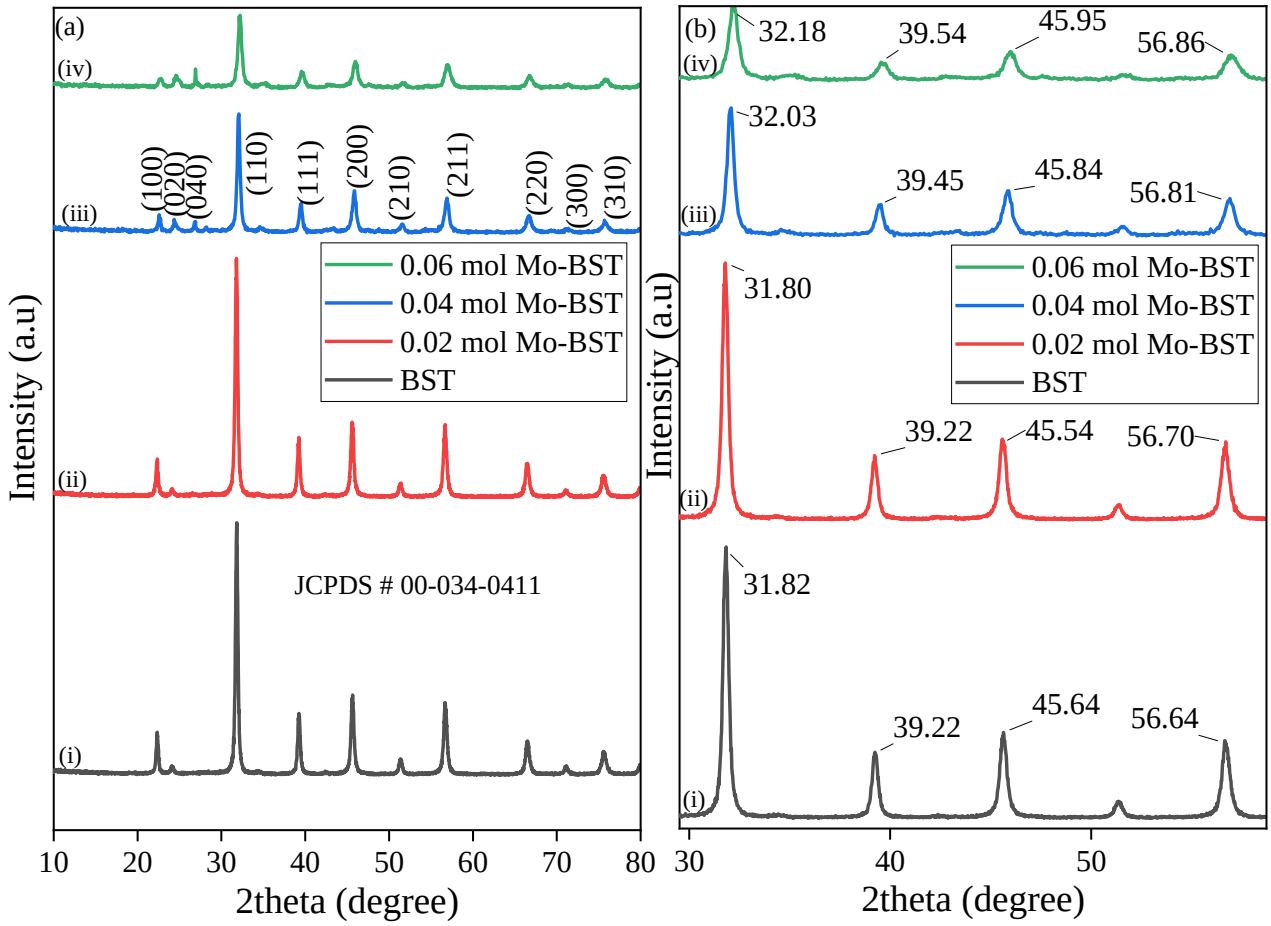

FIGURE 4.9 (a) The XRD spectra of (i) BST-0.6 (ii) 0.02 mol Mo-doped BST-0.6 (iii) 0.04 mol Mo-doped BST-0.6 (iv) 0.06 mol Mo-doped BST-0.6 nanopowders synthesized at a calcination temperature of 900 ^{o}C for 2 h (b). Enlarged version of peak shifts due to incorporation of Mo to BST

Figure 4.10 (a, b) discribed the XRD spectra of the BST-0.6 and (0.02 – 0.06) mol Se-doped BST-0.6 nanopowders calcined at 800 ^{o}C for 2 h as well as the shifting of peaks after BST was doped with Se^{4+}. Moreover, the typical peaks of BST-0.6 shifted to lower angles (except 0.02 mol Se-doped BST) due to the ionic radius difference between Se^{4+} and Sr^{2+} ions and higher charge of Se^{4+} ion as compared to Sr^{2+} ion, which led to the increment of B-O bond lengths of the Se-doped BST-0.6. It implied that Se has brought about significant changes on the microstructure of the BST-0.6 base material. Ultimately, the lower ionic radius of Se^{4+} has been resulted in the reduction of lattice parameters of BST-0.6 (Kakumani et al., 2016a; Kakumani et al., 2016c; Shalu & Ghosh, 2019). The incorporation of Se to BST-0.6 by replacing Sr component of the BST-0.6 perovskite structure has been later confirmed by the EDS and XPS data. Even though Se^{4+} ion has similar ionic radii

with Ti^{4+} ion, the ***t-factor*** value became the dominant factor. Substitition of Ti^{4+} ion by Se^{4+} ion provided a value (1.55) out of the allowed ***t-factor*** range but when Se^{4+} ion replaced the Sr^{2+} ion the respective value lies in the permitted range (0.77 – 1.1). From the XRD spectra, it was described that after the addition of Se^{4+} into BST structure, there was almost no carbonate impurities matching with the predication made by the FT-IR spectra. Most of the cabon atoms were suspected to be removed during calcination of the Se-doped BST-0.6 samples. The carbon atoms found in the form of $BaCO_3$ were minimized since there was a possibility for Ba to be attached towards Se intead of carbon.

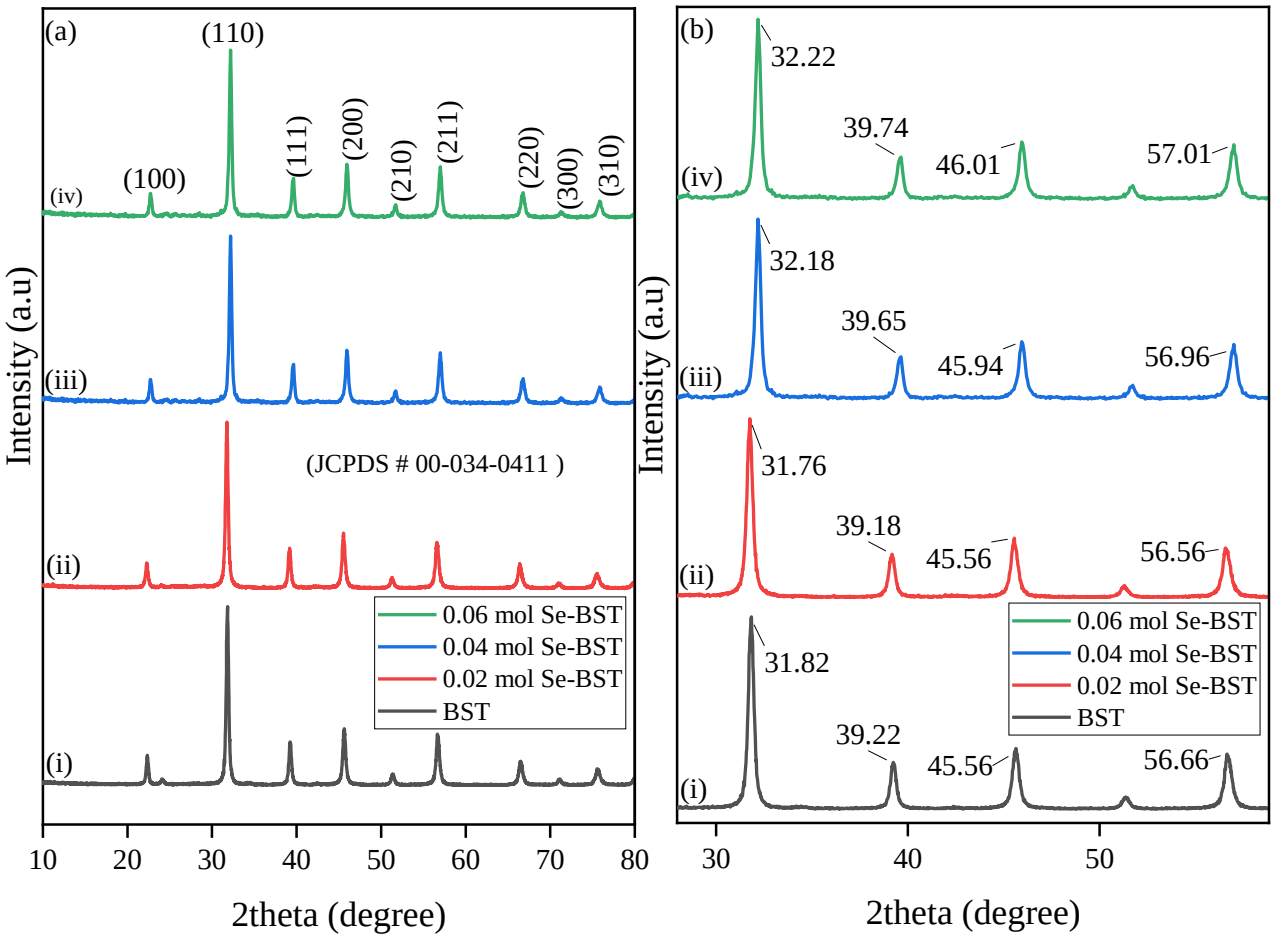

FIGURE 4.10 (a) The XRD patterns of (i) BST-0.6 (ii) 0.02 mol Se-doped BST-0.6 (iii) 0.04 mol Se-doped BST-0.6 (iv) 0.06 mol Se-doped BST-0.6 nanopowders synthesized at a calcination temperature of 800 ^{o}C for 2 h and (b) Enlarged version of the shifting of peaks after doping

Figure 4.11 (a) shows the XRD spectra of BST-0.6 and (0.02 – 0.06) mol (Mo, Se) co-doped BST-0.6 powders which were calcined at 800 ^{o}C for 2 h. Figure 4.11 (b) illustrated the XRD spectra with shifting of peaks due to the incorporation of the dopants Mo^{6+} and Se^{4+} ions in to BST-0.6. The new major peaks with respective *(h k l)* values of (202), (333), (004), (044) and (404) expressed the existence of the Mo and Se co-dopants in the BST-0.6 and in the form of secondary phases such as $Mo_9Se_{11}Ti_2$ (Gougeon et al., 2010; Valencia-Gálvez et al., 2022). These peaks became more intense

as the concentration of the Mo^{6+} ions added to the BST base material was increased from 0.02 mol to 0.06 mol. In a similar way to the Mo-doped BST, some weak diffraction peaks with planes of (020) and (040) were observed which were possibly associated to the occurrence of $BaCO_3$ and MoO_3, respectively, matched with FT-IR data (Abboudi et al., 2018; Attar et al., 2017). The co-doped BST has also been resulted in the peaks with 2θ values shifted towards the lower degrees (Figure 4.48 (b)).

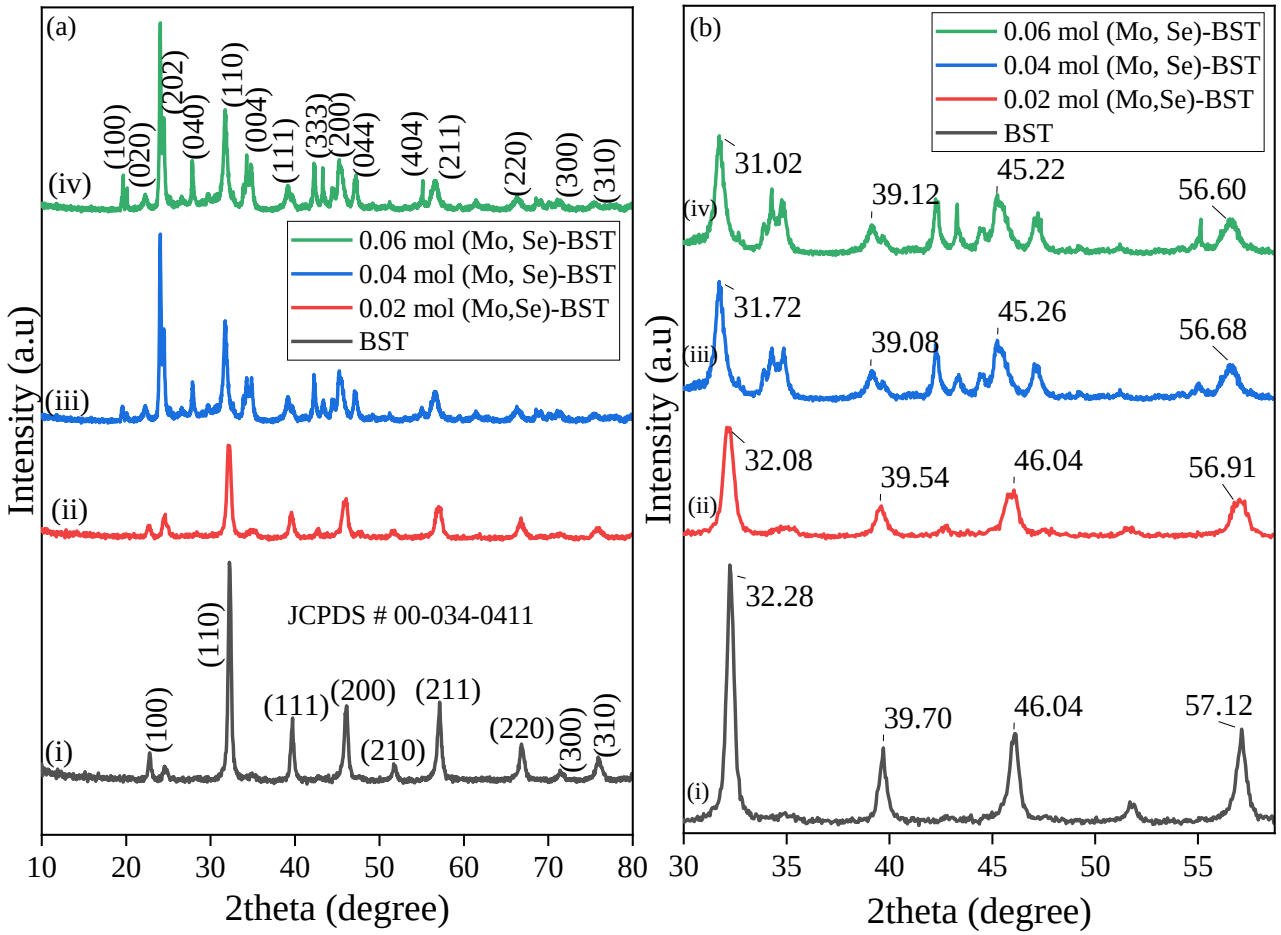

FIGURE 4.11 (a) The XRD patterns of (i) BST-0.6 (ii) 0.02 mol (Mo, Se) co-doped BST-0.6 (iii) 0.04 mol (Mo, Se) co-doped BST-0.6 (iv) 0.06 mol (Mo, Se) co-doped BST-0.6 nanopowders calcined at 800 ^{o}C for 2 h (b) Enlarged version of the shifting of peaks after doping

The mean crystallite sizes of the BST nanopowder samples were calculated through the use of *Debye-Scherrer's* (Equation 4.1) which was derived from Equation 2.7 (Shalu et al., 2022).

$$D = \frac{0.89\,\lambda}{\beta\cos\theta} \quad \text{.....4. 1}$$

Where, D is average crystallite size (nm), λ is wavelength of CuK_{α} (0.154 nm), β is full width at half maximum intensity (FWHM) in *radians* and θ is Bragg angle in *radians*.

The FWHM, lattice parameter and crystal size values of the all the BST-0.6 samples were summarized in Table 4.1. By increasing the amount of Mo and Se dopants, there is an increase in FWHM and hence there is a correspondingly shift of the angles towards lower degree which ultimately resulted in lowering of the average crystal size of BST-0.6. The initial elevation of the lattice parameters was caused by the higher charge of Mo^{6+} and Se^{4+} ions than Ti^{4+} and Sr^{2+} ions of BST-0.6 that expanded the unit cells by creating cation-cation repulsion after substitution (Lumpkin & Ribbe, 1983). Afterwards, the ultimate reduction of the lattice parameters was the result of the relatively lower ionic radius of the Mo^{6+} ion (0.59 Å) and Se^{4+} (0.5 Å) ions as compared to Ti^{4+} ion (0.63 Å) and Sr^{2+} (1.18 Å) ions. The reduction of average crystal size of $Ba_{0.6}Sr_{0.4}TiO_3$ after addition of the dopants was most probably caused by the lesser diffusion rate of the Mo^{6+} and Se^{4+} ions and smaller growth rate of their crystals. This phenomenon was backed by the broadening of the major peaks (Chen et al., 2007a; Shalu & Ghosh, 2019).

The FWHM of the (Mo, Se) co-doped BST-0.6 was obtained being lower than BST-0.6. Meanwhile, the lattice parameters were enlarged as amounts of the dopants were elevated from 0.02 mol to 0.06 mol following the higher charge of the Mo^{6+} and Se^{4+} ions as compared to the Ti^{4+} and Sr^{2+} ions of BST-0.6. This initiated the cation-cation repulsion which at last increased the lattice parameters (Deepthi et al., 2014; Kim et al., 2014; Lumpkin & Ribbe, 1983). Thus, the calculated average crystal size of the (Mo, Se) co-doped BST-0.6 nanopowder was greater than the pristine BST nanopowder (Table 4.1). These trends agreed with a report by Zhou (Zhou et al., 2009). Hence, such microstructural variations were caused by the incorporation of Mo^{6+} and Se^{4+} ions in to the BST-0.6 structure through the concurrent substitution of Ti^{4+} and Sr^{2+} ions of the BST-0.6 host dielectric material (Fan et al., 2010; Shalu & Ghosh, 2019).

Figure 4.12 and 4.13 illustrated the XRD spectra of the Mo-doped BST-0.7, and Se-doped BST-0.7 samples. Figure 4.12 (a) described the XRD spectra analysis of BST-0.7 and (0.02 - 0.06) mol Mo-doped BST-0.7 nanopowders synthesized at a calcination temperature of 800 ^{o}C for 2 h. The 800 ^{o}C calcination temperature was selected after considering the TGA-DSC and FT-IR data about the hygroscopic nature of Mo and the existence of carbonate impurities in the Mo-doped BST-0.7 sample. The formation of a tetragonal shaped (P4mm space group) Mo-doped BST-0.7 nanopowder (JCPDS # 00-044-0093 index file) has been confirmed by the appearance of peaks with (*h k l*) values of (100), (101), (111), (002), (201), (211), (202), (300), and (310).

Table 4.1 - The XRD crystallite size analysis of the BST-0.6 (BST) and (0.02 – 0.06) mol Mo, Se and their co-doped BST-0.6 nanopowders

Sample	*a* (lattice parameter), *nm*	FWHM, *radian*	*D* (crystallite size), *nm*	Calcination temperature, ^{o}C
BST	0.3925	0.3771	19.35	900
0.02 mol Mo-BST	0.3975	0.3921	18.31	
0.04 mol Mo-BST	0.3956	0.4001	17.84	
0.06 mol Mo-BST-0.6	0.3935	0.5783	15.17	
BST	0.2139	0.3771	23.97	800
0.02 mol Se-BST	0.4033	0.3980	22.38	
0.04 mol Se-BST	0.4387	0.3903	20.68	
0.06 mol Se- BST-0.6	0.3998	0.4087	18.89	
0.02 mol (Mo, Se)-BST	0.2054	0.3455	24.93	
0.04 mol (Mo, Se)-BST	0.3379	0.3029	26.18	
0.06 mol (Mo, Se)-BST	0.3398	0.3009	28.36	

The less intense peaks around 2theta of 20^{o} ((020)) was believed to be caused by the existence of higher boiling point of $BaCO_3$ (1,360 °C) that were obtained from the combustion of acetic acid which agreed with the FT-IR data (Batttisha et al., 2014). The other weak peak around 26^{o} which corresponds to (040) represented the occurrence of MoO_3 formed after calcining the Mo-doped BST-0.7 nanopowder at 800 ^{o}C (Abboudi et al., 2018). Its intensity increased with the concentration of the Mo^{4+} incorporated to the BST base material. Figure 4.12 (b) described the enlarged version of peaks after doping. It was found that slight shifting of the three major peaks of BST-0.7 to higher degrees were obtained which could be due to the difference of ionic radius between Mo^{6+} and Ti^{4+} ions of BST-0.7. This led to the elongation of the Ti-O bond lengths and distortion of the Mo-doped BST-0.7 lattice. Consequently, the expansion of cell volume and enlargement of lattice parameters of BST-0.7 were followed (Dong et al., 2020; Fan, Yu, Sun, Li, Yin, & Du, 2010; Kakumani et al., 2016a). The above effects of incorporation of Mo^{6+} (0.59 Å) to BST-0.7 were expected to occur through the replacement of Ti^{4+} (0.63 Å) by the Mo^{6+} ions (Attar et al., 2017; Fan et al.,2010; Shalu & Ghosh, 2019; Ye & Guo, 2009).

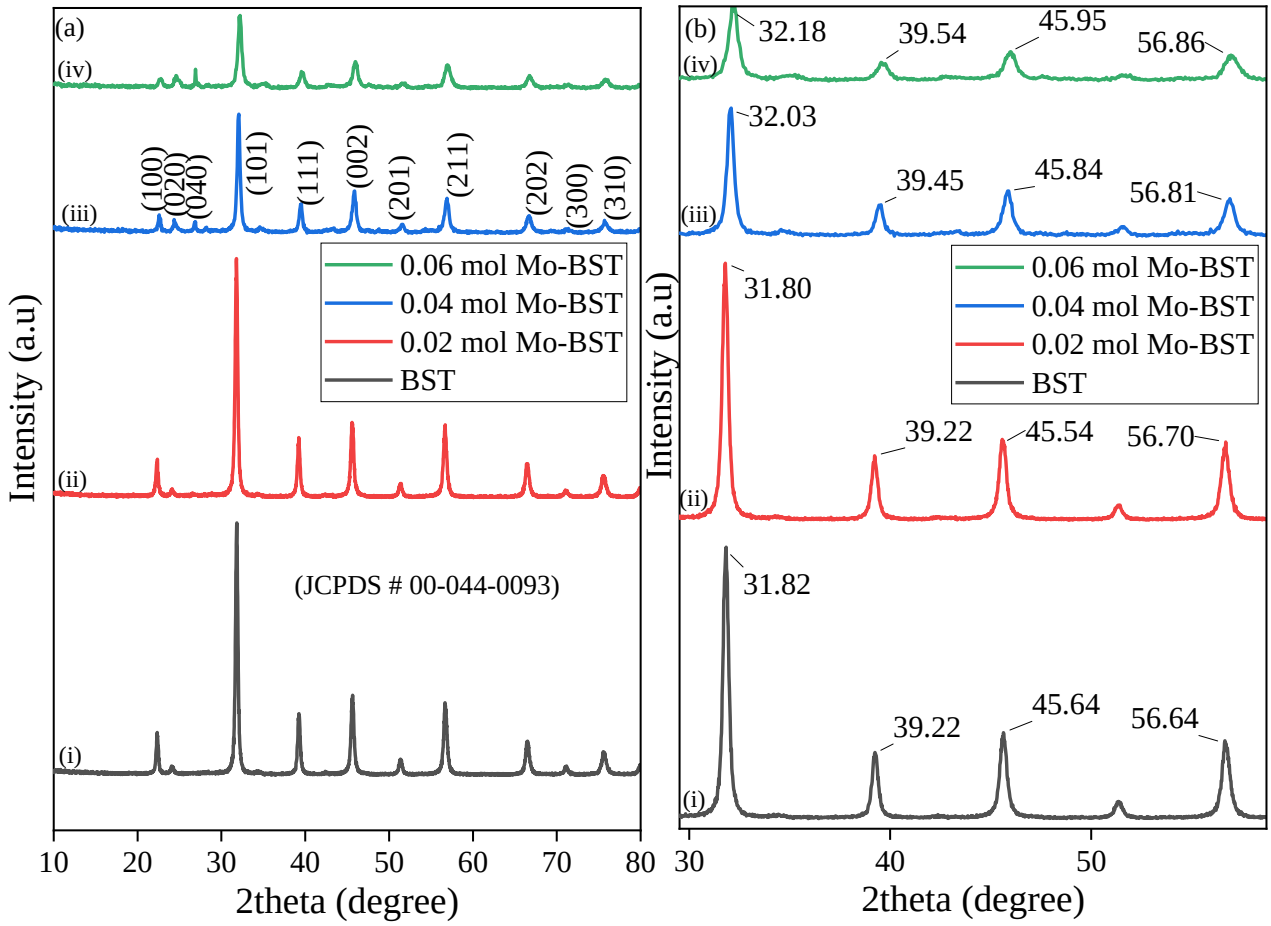

FIGURE 4.12 (a) The XRD patterns of (i) BST-0.7 (ii) 0.02 mol Mo-doped BST-0.7 (iii) 0.04 mol Mo-doped BST-0.7 (iv) 0.06 mol Mo-doped BST-0.7 nanopowders synthesized at a calcination temperature of 800 ^{o}C for 2 h (b) Enlarged version of the shifting of peaks after doping

Remarkably, the Se-doped BST-0.7 nanopowder synthesized at a calcination temperature of 900 ^{o}C has shown different trend from the Se-doped BST-0.6. Here, the calcination temperature is choosen from some prevously reported works on BST-0.7 containing an acceptor dopant (Li & Dou, 2013; Pookmanee & Phanichphant, 2010). Figure 4.13 (a, b) revealed that a tetragonal shaped $Ba_{0.77}Sr_{0.23}TiO_3$ nanopowder (JCPDS # 00-034-0493 index file) was firmly established through the existence of all planes observed at the Mo- BST-0.7 except the (040). The plane around 20^{o} ((020)) has been observed diminished as the concentration of Se^{4+} ions added to the BST-0.7 which was in a good agrreement with the FT-IR data.

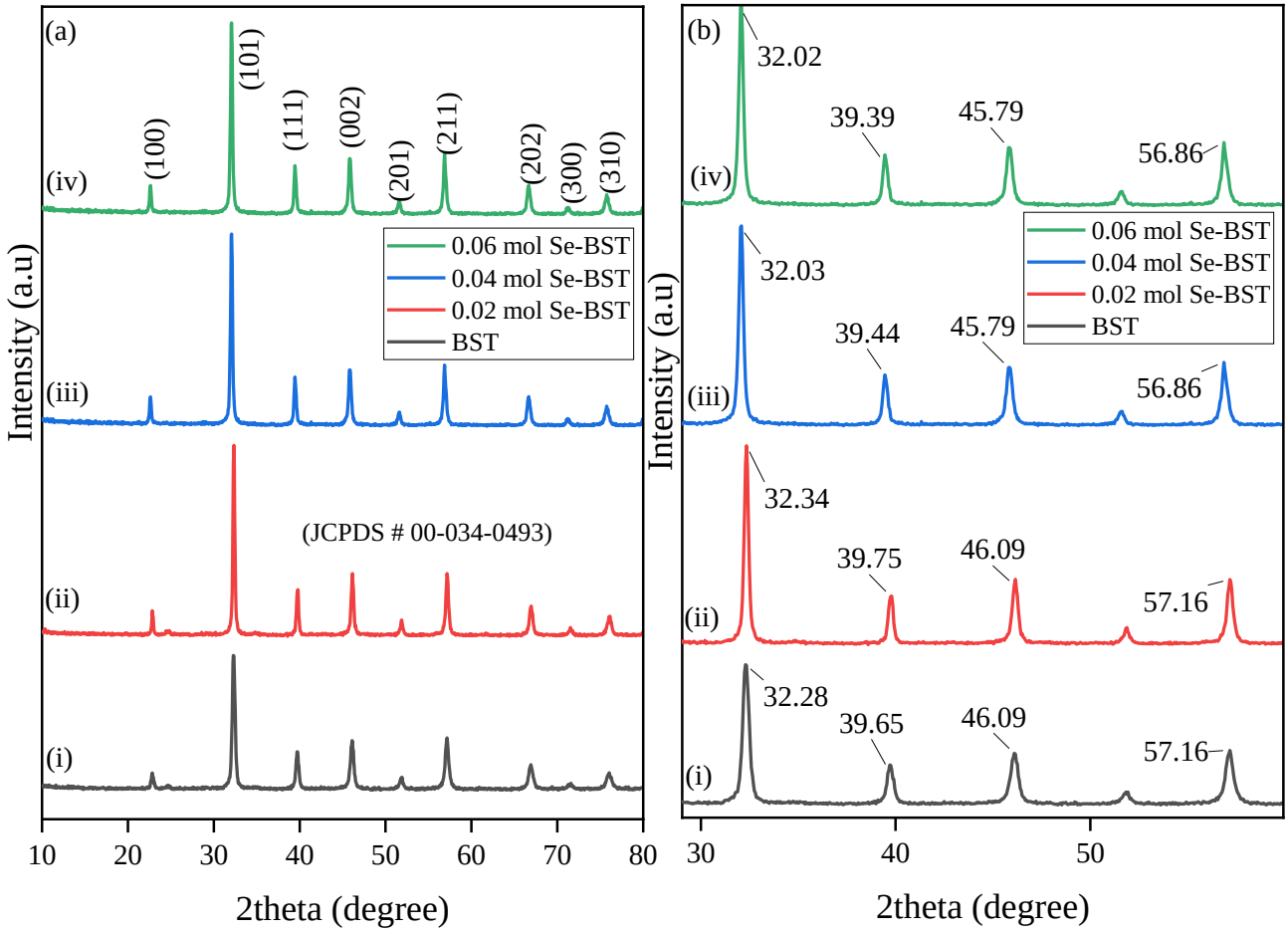

FIGURE 4.13 (a) The XRD patterns of (i) BST-0.7 (ii) 0.02 mol Se-doped BST-0.7 (iii) 0.04 mol Se-doped BST-0.7 (iv) 0.06 mol Se-doped BST-0.7 nanopowders synthesized at a calcination temperature of 900 ^{o}C for 2 h and (b) Enlarged version of the shifting of peaks after doping

Table 4.2 discussed the elevation and lowering of full width at half maximum (FWHM) and the lattice parameters of BST-0.7 as the amount of Mo and Se were enlarged to 0.06 mol. Analogous to the BST-0.6 nanopowders, the initial elevation of the lattice parameters was caused by the higher charge of Mo^{6+} than Ti^{4+} that expanded the unit cells by creating cation-cation repulsion (Lumpkin & Ribbe, 1983). Afterwards, the ultimate reduction of the lattice parameters was initiated by the relatively lower ionic radius of the Mo^{6+} ion (0.59 Å) as compared to Ti^{4+} ion (0.63 Å). As a result, the average crystallite size of BST-0.7 decreased after the addition of 0.06 mol of Mo dopant. This trend is most probably due to the low diffusion rate of the dopant ions and lower growth rate of the crystals. This is also supported by the broadening of the major peaks (Chen et al., 2007; Shalu & Ghosh, 2019). These results do agree with a report by Shalu and Ghosh (Shalu & Ghosh, 2019). Therefore, varying the dopant and calcination temperature of the BST host material resulted in varied crystalline properties.

Table 4.2 also showed a slight reduction of the full width at half maximum (FWHM) of the Se-doped BST-0.7 nanopowder. Likewise, the lattice parameters decreased at first due to the smaller ionic radius of the Se^{4+} (0.5 Å) ions as compared to Sr^{2+} (1.18 Å) ions of the BST base material and shifting of 2theta towards higher degrees (Fan, Yu, Sun, Li, Yin, & Du, 2010; Kakumani et al., 2016a; Shalu & Dasgupta Ghosh, 2019). Afterwards, the angles shifted towards lower degrees. As the same time, the higher charge of Se^{4+} ion than Sr^{2+} ion forms a larger cation-cation repulsion. The mixed effect of both the phenomenon triggered the elevation of Ti-O bond lengths, which is why the lattice parameters of BST increased (Lumpkin & Ribbe, 1983). Unlike the Mo-doped BST-0.7 and Se-doped BST-0.6, the average crystal size of BST-0.7 was enlarged from 19.41 nm to 30.03 nm after the incorporation of the Se^{4+} ion dopant. The higher diffusion rate of the Se^{4+} ions and higher growth rate of the Se-doped BST-0.7 crystals at higher calcination temperature were also supposed to be the other driving force for such a trend (Z. Chen et al., 2007a; Shalu & Dasgupta Ghosh, 2019).

Table 4.2 - The XRD crystallite size analysis of BST-0.7 (BST) and (0.02 – 0.06) mol Mo and Se doped BST-0.7 nanopowders

Sample	Lattice parameters, *nm*		FWHM, *radian*	*D* (crystallite size), *nm*	Calcination temperature, ^oC
	a	*c*			
BST	0.3910	0.3959	0.4696	23.97	800
0.02 mol Mo-BST	0.3921	0.3963	0.5009	18.30	
0.04 mol Mo-BST	0.3928	0.3924	0.5183	17.83	
0.06 mol Mo-BST	0.3911	0.3924	0.5196	14.46	
BST	0.3995	0.3967	0.4663	19.41	900
0.02 mol Se-BST	0.3987	0.3955	0.3487	26.41	
0.04 mol Se-BST	0.3992	0.3971	0.3222	28.02	
0.06 mol Se-BST	0.3997	0.3986	0.3007	30.03	

4.2.5 SEM image analysis

The SEM images were utilized to assess the grain size, shape and rate of agglomeration of the BST nanoparticles. In complementary way to the XRD data, the morphologies of both BST-0.6 and BST-0.7 samples were different.

The Mo-doped BST-0.7 nanopowder synthesized at a calcination temperature of 900 ^{o}C has shown different morphology from the Mo-doped BST-0.7 samples. Figure 4.14 illustrated the SEM image of Mo-doped BST-0.6 where the Mo- BST-0.6 nanopowder was observed to be cubic shaped, dense and less agglomerated nanomaterial with porous grains. The average grain size, D_{SEM}, of BST-0.6 decreased following the incorporation of (0.02 - 0.06) mol Mo^{6+} (Table 4.3). This matched with the trend of the average crystallite size obtained from the XRD data where the lower crystal sized crystals form reduced grain sizes. Such a variation of average grain size was believed to be the result of slower growth rates of the particles. The alteration of the average grain size was verified to be comparable to Y. Fan's report (Fan et al., 2010).

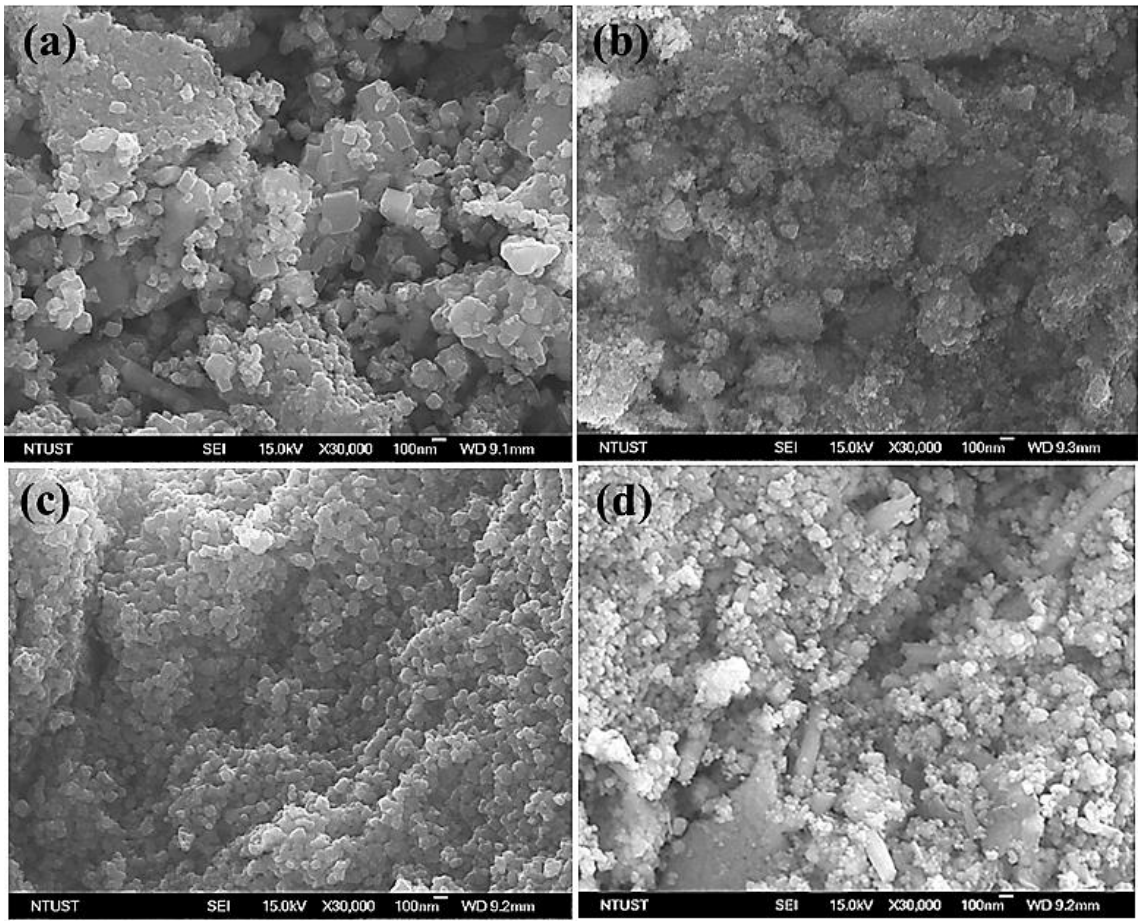

FIGURE 4.14 The SEM images of the (a) BST-0.6 (b) 0.02 mol Mo-doped BST-0.6 (c) 0.04 mol Mo-doped BST-0.6 and (d) 0.06 mol Mo-doped BST-0.6 nanopowders calcined at 900 ^{o}C for 2 h

Figure 4.15 (a, b) demonstrated the morphological property of BST-0.6 and (0.02 – 0.06) mol Se-doped BST-0.6 nanopowders calcined at 800 ^{o}C. The images described that increase in the amount of Se dopant acquired surface morphologies with uniform, well-crystallized, porous and less agglomerated arrangements of fine grains. Like the Mo-BST-0.6 nanopowder, the average grain size of BST has been lowered as a result of the introduction of the Se^{4+} dopant into BST-0.6, which is supported by the XRD results (Table 4.3). This alteration of the grain size was also affected by the

lower growth rates of the Se-doped BST-0.6 grain as compared to the pristine BST-0.6. These results were similar to a report by Attar (Attar et al., 2017).

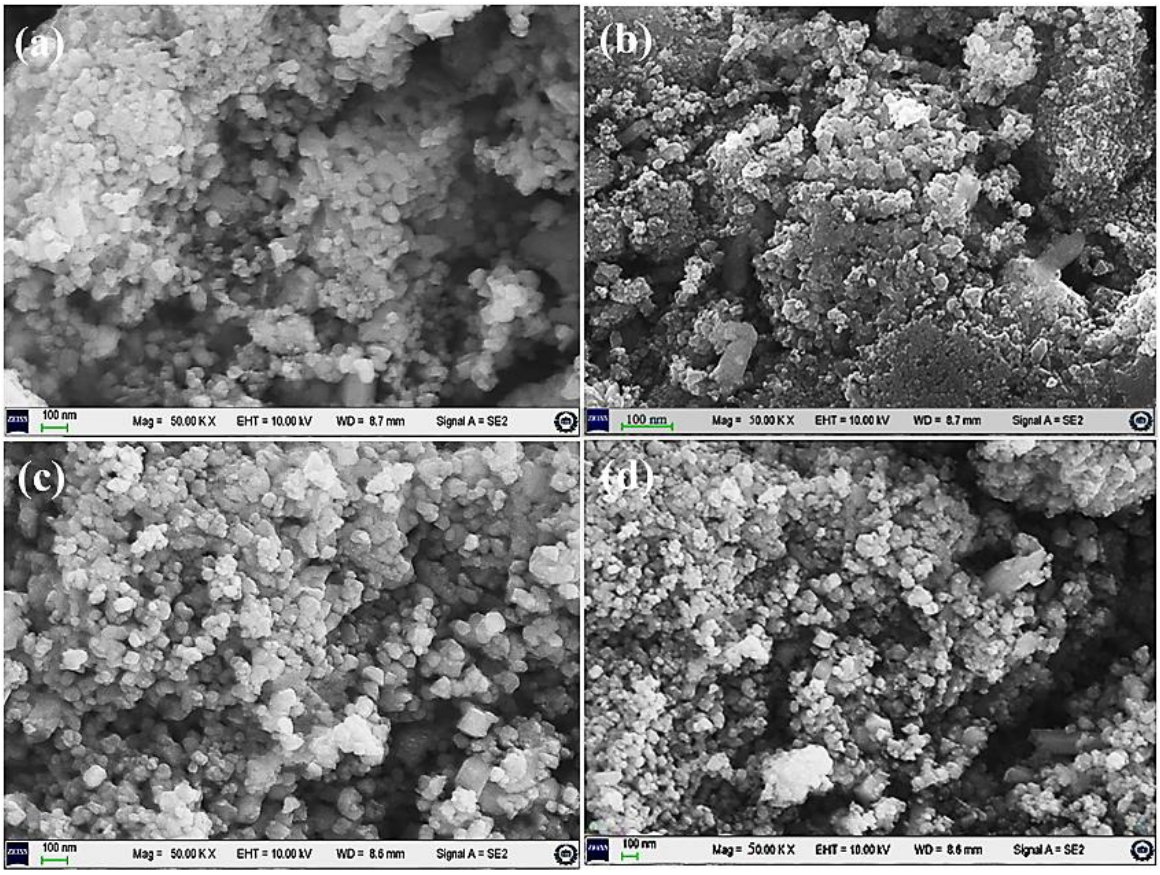

FIGURE 4.15 The SEM images of (a) BST-0.6 (b) 0.02 mol Se-doped BST-0.6 (c) 0.04 mol Se-doped BST-0.6 (d) 0.06 mol Se-doped BST-0.6 nanopowders calcined at 800 ^{o}C for 2 h

Figure 4.16 (a) and (b) illustrate the respective morphology of BST-0.6 and (0.02 – 0.06) mol (Mo, Se) co-doped BST-0.6 nanopowders where the (Mo, Se) co-doped BST-0.6 nanopowders possessed porous and agglomerated morphology with cubic shaped particles. On the contrary to the Mo-doped BST-0.6 and Se-doped BST-0.6 nanopowders, embodiment of (0.02 - 0.06) mol (Mo + Se) co-dopants to the BST-0.6 host material gave rise to elevation of the average grain sizes (Table 4.3). This was in a similar agreement with the XRD data. Such change in the mean grain sizes of the BST-0.6 samples were assumed to be caused by variation in the respective growth rates. Hence, the grain size of BST-0.6 has been influenced by the addition of the co-dopants Mo and Se (Attar et al., 2017). Therefore, it was observed that the mean grain size has been increased as the co-dopants Mo and Se were incorporated into BST-0.6, where such a trend was similarly reported by Deepthi (Deepthi et al., 2014).

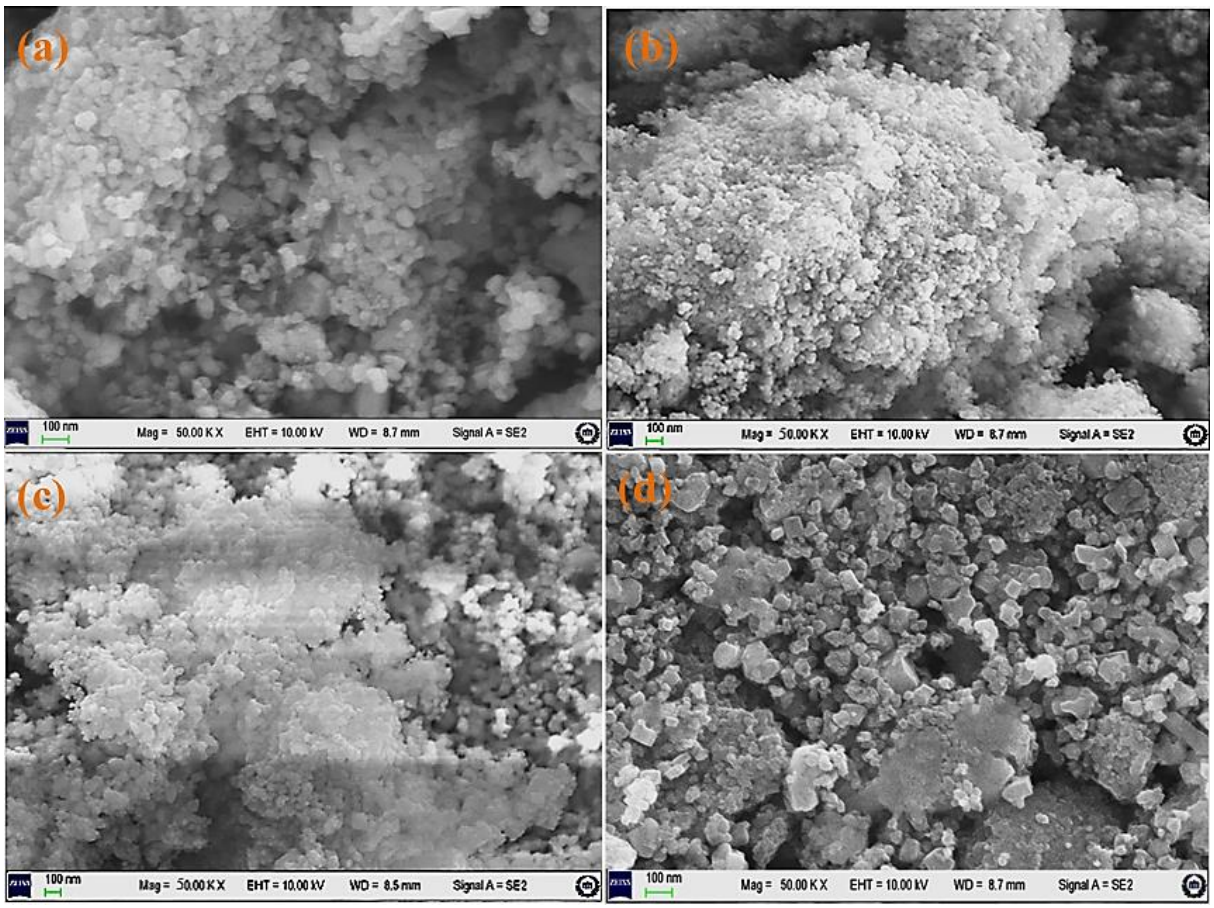

FIGURE 4.16 The SEM images of the (a) BST-0.6 (b) 0.02 mol (Mo, Se) co-doped BST-0.6 (c) 0.04 mol (Mo, Se) co-doped BST-0.6 (d) 0.06 mol (Mo, Se) co-doped BST-0.6 nanopowders synthesized at a calcination temperature of 800 ^{o}C for 2 h

Table 4.3 - The grain sizes of BST-0.6 (BST) as well as (0.02 – 0.06) mol Mo, Se and their co-doped BST-0.6 nanopowders

Samples	D_{SEM} (Grain size), *nm*	Calcination temperature, ^{o}C
BST	26.02	900
0.02 mol Mo-BST	21.43	
0.04 mol Mo-BST	18.58	
0.06 mol Mo-BST	16.40	
BST	40.13	800
0.02 mol Se-BST	28.73	
0.04 mol Se-BST	16.81	
0.06 mol Se-BST	12.43	
0.02 mol (Mo, Se)-BST	45.10	
0.04 mol (Mo, Se)-BST	53.27	
0.06 mol (Mo, Se)-BST	62.51	

The varied XRD data of the BST-0.7 samples from the BST-0.6 samples administered the expectation that they possess varied SEM image parameters. And this was clearly noticed at their respective SEM images. Figure 4.17 (a) and (b) displayed the morphological aspects of BST-0.7 and (0.02 - 0.06) mol Mo-doped BST-0.7 nanopowders synthesized at a calcination temperature of 800 ^{o}C. The SEM images clarified that the tetragonal shaped Mo- BST-0.7 nanopowder was composed of dense, agglomerated and porous grains which were backed by the BET analysis. The average grain sizes of (0.02 - 0.06) mol Mo-doped BST-0.7 nanopowders were obtained lower than the value for BST (Table 4.4) in a similar way to the Mo-doped BST-0.6. This matched with the trend of the average crystallite size obtained from the XRD data. Such alteration of the grain size was believed to be inferred by the slower growth rates of the particles which was found to be similar to a report by Fan (Fan et al., 2010).

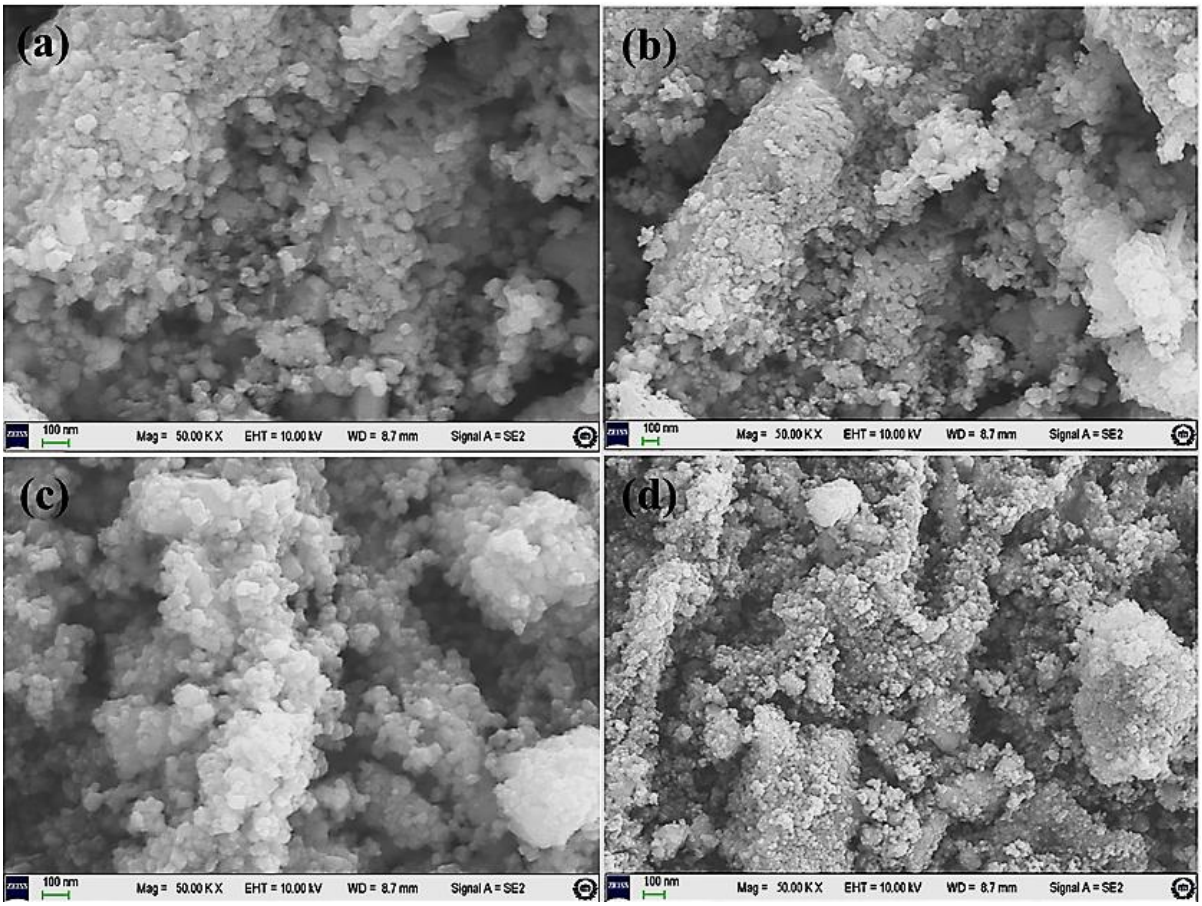

FIGURE 4.17 The SEM images of the (a) BST-0.7 (b) 0.02 mol Mo-doped BST-0.7 (c) 0.04 mol Mo-doped BST-0.7 and (d) 0.06 mol Mo-doped BST-0.7 nanopowders calcined at 800 ^{o}C for 2 h

However, more reduction of grain size was observed for the Mo-doped BST-0.6 nanopowder which was calcined at higher temperature than the Mo-doped BST-0.6. Furthermore, elevation of the calcination temperature of the BST samples resulted in lower grain size which is possibly owing to the lower number of agglomerated BST crystallites on a grain at the higher calcination temperature.

This could also be due to the differences in crystallinity and particular arrangement as a result of the varied calcination temperature and the ratio of Ba to Sr (Fan et al., 2010).

Figure 4.18 displayed the surface morphology of BST-0.7 together with (0.02 – 0.06) mol Se-doped BST-0.7 nanopowder synthesized at a calcination temperature of 900 ^{o}C showing opposite results from the Se-doped BST-0.6 and Mo-doped BST-0.7 nanopowders. From the images, it was observed that incorporation of the Se^{4+} ions in to the BST-0.7 base material initiated the formation of uniform and more-crystallized Se-doped BST grains with lower porosity and decreased agglomerates. Besides, the image demonstrated that the BST-0.7 samples contain tetragonal shaped particles. The average grain size of BST elevated after the addition of (0.02 - 0.06) mol Se^{4+} ions. It was believed that the increase in the crystal sizes in the XRD data of the Se-doped BST-0.7 nanopowder gave rise to the elevation of the average grain size of the Se-doped BST-0.7 sample (Shalu & Dasgupta Ghosh, 2019). Such a change of grain size is believed to be affected by the higher growth rate as explained at the XRD data. These results followed the same trend with a report by Liu (Liu et al., 2019). In a similar way with the XRD, variation of the Ba to Sr ratio and calcination temperature has been resulted in different morphology and grain size of the BST samples.

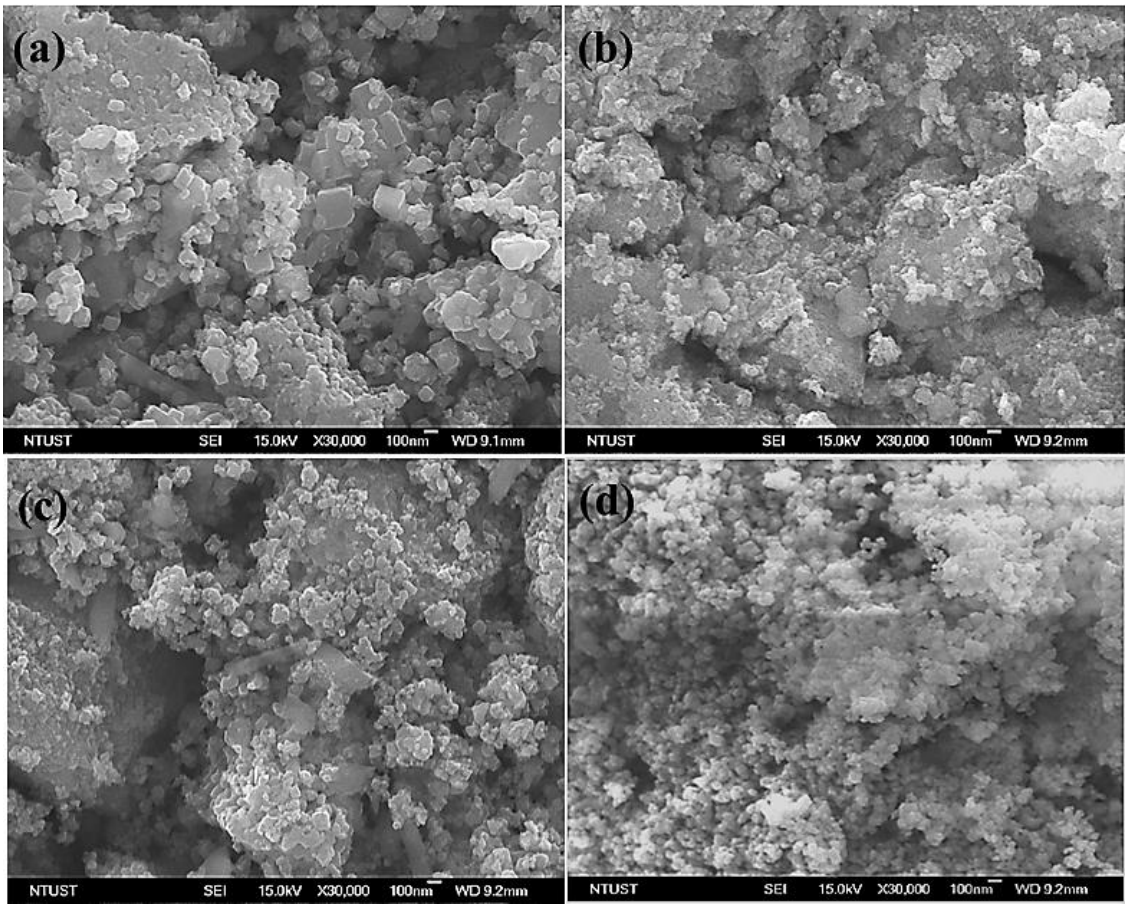

FIGURE 4.18 The SEM images of the (a) BST-0.7 and (b) 0.02 mol Se-doped BST-0.7 (c) 0.04 mol Se-doped BST-0.7 (d) 0.06 mol Se-doped BST-0.7 nanopowders calcined at 900 ^{o}C for 2 h

Table 4.4 - The grain sizes of BST-0.7 (BST) as well as (0.02 – 0.06) mol Mo and Se doped BST-0.7 nanopowders

Samples	D_{SEM} (Grain size), *nm*	Calcination temperature, ^{o}C
BST	40.13	800
0.02 mol Mo-BST	32.45	
0.04 mol Mo-BST	27.00	
0.06 mol Mo-BST	23.35	
BST	26.02	900
0.02 mol Se-BST	30.84	
0.04 mol Se-BST	32.26	
0.06 mol Se-BST	35.45	

4.2.6 EDS analysis

The EDS data for both BST-0.6 and BST-0.7 samples were the same where they were effective in indicating the existence all the atoms found in the BST samples. The EDS spectra of BST-0.7 and 0.04 mol Mo-doped BST-0.7 samples are described in Figure 4.19 (a) and (b) respectively. The effectiveness of doping has also been observed through the appearance of Ba, Sr, Ti, O and Mo on the EDS spectra of 0.04 mol Mo-doped BST-0.7 sample. Besides, the un-assigned EDS peaks of BST-0.7 and Mo-doped BST-0.7 around 0.15 keV were believed to represent the carbon impurity found in both BST samples (Fan, Yu, et al., 2010b; Marzeddu et al., 2022) which agreed with the FT-IR spectrum. Hence, these EDS data have been considered as one of the appropriate indicators of the synthesis of Mo-doped BST-0.7 nanopowder.

Table 4.5 described that the incorporation of Mo^{6+} ions to the BST-0.7 base material has been firmly established using the atomic percentage composition of the atoms existing in the 0.04 mol Mo-doped BST-0.7 nanopowder. It was observed that the atomic percentage values obtained from the stoichiometric equation and EDS data are comparable to each other with smaller variation. This difference is possibly resulted from the loss of few amounts of the ions, addition of extra oxygen atoms from the atmosphere and the existence of impurities such as carbonates in the 0.04 mol Mo-doped BST-0.7 nanopowder. The remaining atomic percentage obtained from EDS (~ 0.85%) was occupied by the carbon impurity.

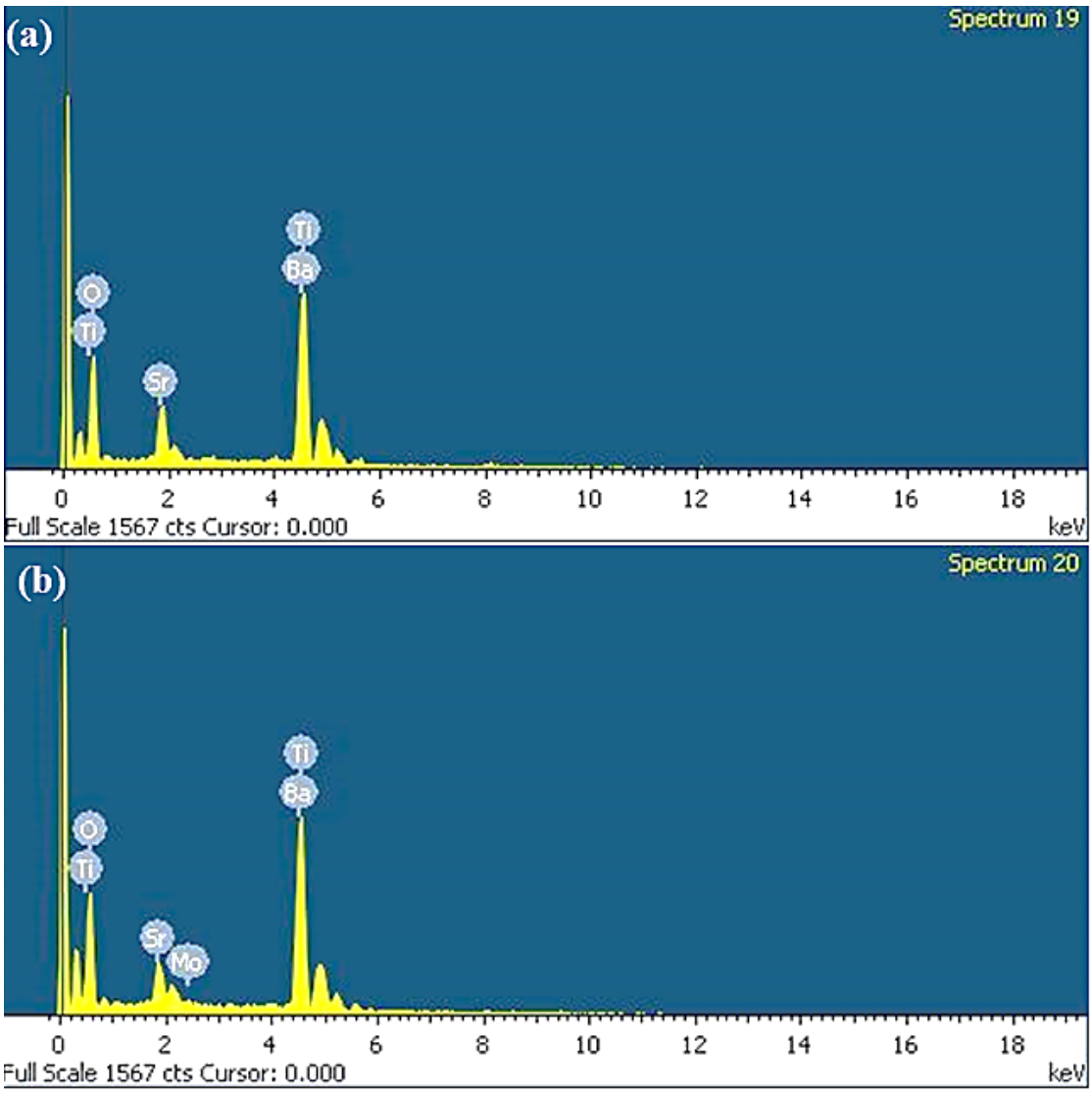

FIGURE 4.19 The EDS spectra of the (a) BST-0.7 and (b) 0.04 mol Mo-doped BST-0.7 nanopowders calcined at 800 ^{o}C for 2 h

Table 4.5 - The stoichiometric and EDS atomic percentage compositions of the 0.04 mol Mo-doped BST-0.7 nanopowders

Elements	Starting stoichiometric atomic percentage composition	Atomic percentage composition from EDS
O *K*	60.00	60.55
Ti *K*	19.20	18.66
Sr *L*	04.60	4.52
Mo *L*	00.80	0.71
Ba *L*	15.40	14.71
Total	100.00	99.15

As can be observed in Figure 4.20 (a) and (b), the EDS spectra of BST-0.6 and 0.04 mol Se-doped BST-0.6 samples were respectively illustrated. Hence, the elemental content of the BST was found as Ba, Sr, Ti, O, and Se. Additionally, it was considered that the unassigned EDS peaks of BST and Se-doped BST at about 0.15 keV corresponded to the carbon impurity that was detected in both BST samples which was in good agreement with the FT-IR spectra (Fan, Yu, et al., 2010b; Marzeddu et al., 2022). The extent of doping BST with Se was possibly proved through the existence of Se on the EDS spectra of 0.04 mol Se-doped BST-0.6. This was why the microstructural, morphological and dielectric property changes of BST were observed.

The EDS data was also used as a useful confirmatory method for the formation of $Ba_{0.6}Sr_{0.4-x}Se_xTiO_3$ nanopowder. As given in the Table 4.6, the EDS percentage composition of most of the elements have been found comparable with stoichiometrically predicted amounts where few of them were found lower than the expected amounts. This was believed to be caused by the loss and evaporation of few amounts of the elements during synthesis and the occurrence of the carbon impurities. Oxygen was found higher than the expected amounts as the occurrence of some additional oxygen atoms from the environment (Wang et al., 2020). The carbon impurity composed the 0.40% of remaining atomic percentage found in the EDS data. This was smaller than the carbon atomic composition detected in the 0.04 mol Mo-doped BST-0.7 nanopowder due to the similar electronegativity of Se and C, matching with the FT-IR and XRD spectra. The 0.04 mol doped Se-doped BST-0.7 nanopowder had shown the same EDS data with the Se-doped BST-0.6 samples.

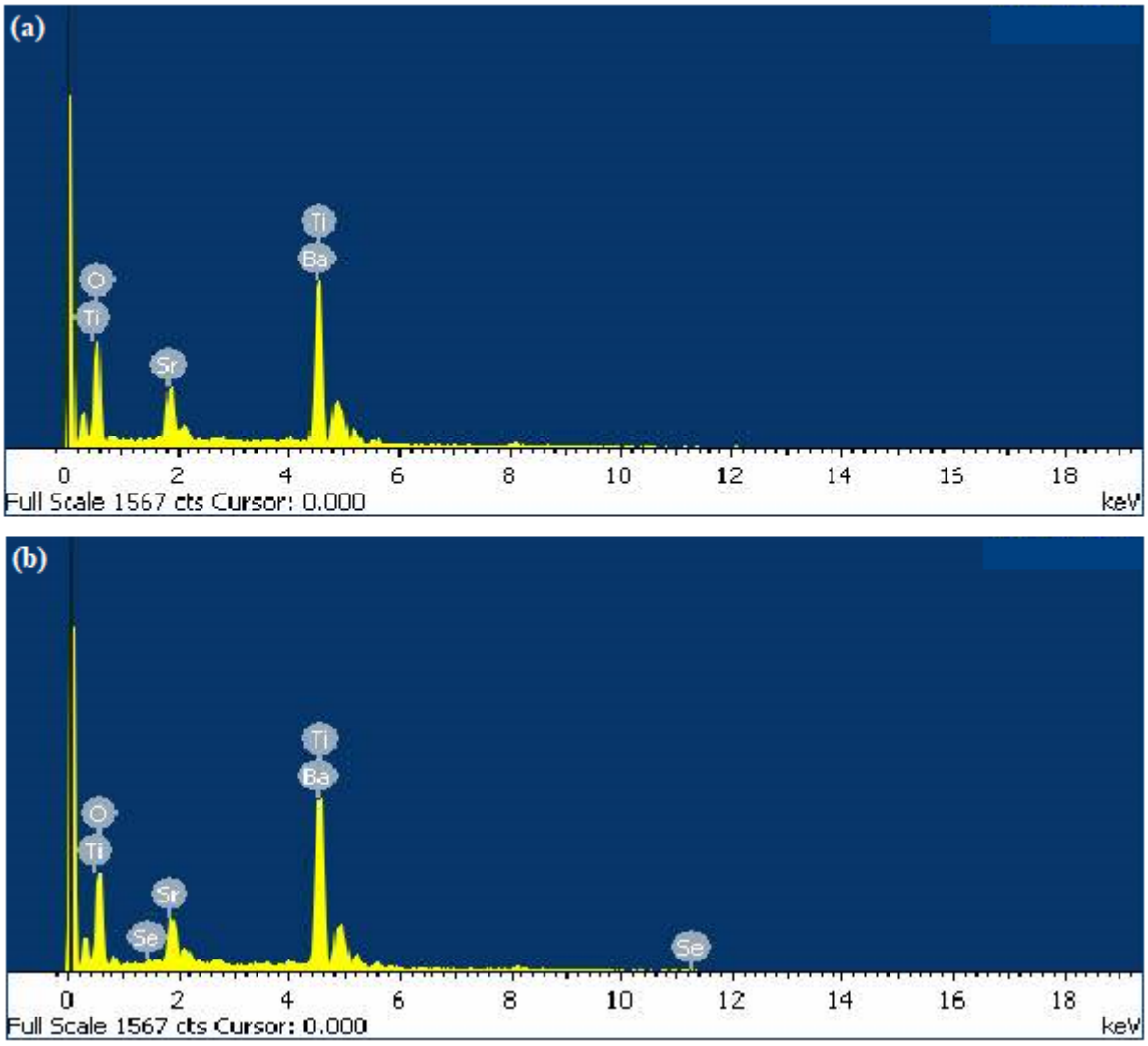

FIGURE 4.20 The EDS spectra of the (a) BST-0.6 and (b) 0.04 mol Se-doped BST-0.6 nanopowders calcined at 800 ^{o}C for 2 h

Table 4.6 - The stoichiometric and EDS atomic percentage compositions of the 0.04 mol Se-doped BST-0.6 nanopowders

Elements	Atomic percentage composition from stoichiometry	Atomic percentage composition from EDS
Ba *L*	12.00	11.95
Sr *L*	07.20	6.52
Ti *K*	20.00	19.50
Se *L*	00.80	0.69
O *K*	60.00	60.94
Total	100.00	99.60

Figure 4.21 described the EDS spectra of 0.04 mol (Mo, Se) co-doped BST-0.6 nanopowders. The EDS spectrum has shown the elements (Ba, Sr, Ti, and O) with an expected weight percentage values are found in the BST nanopowder. The effectiveness of co-doping of BST was also confirmed by the appearance of Mo and Se, in addition to the basic components of BST at the EDS spectra of the (Mo, Se) co-doped BST-0.6.

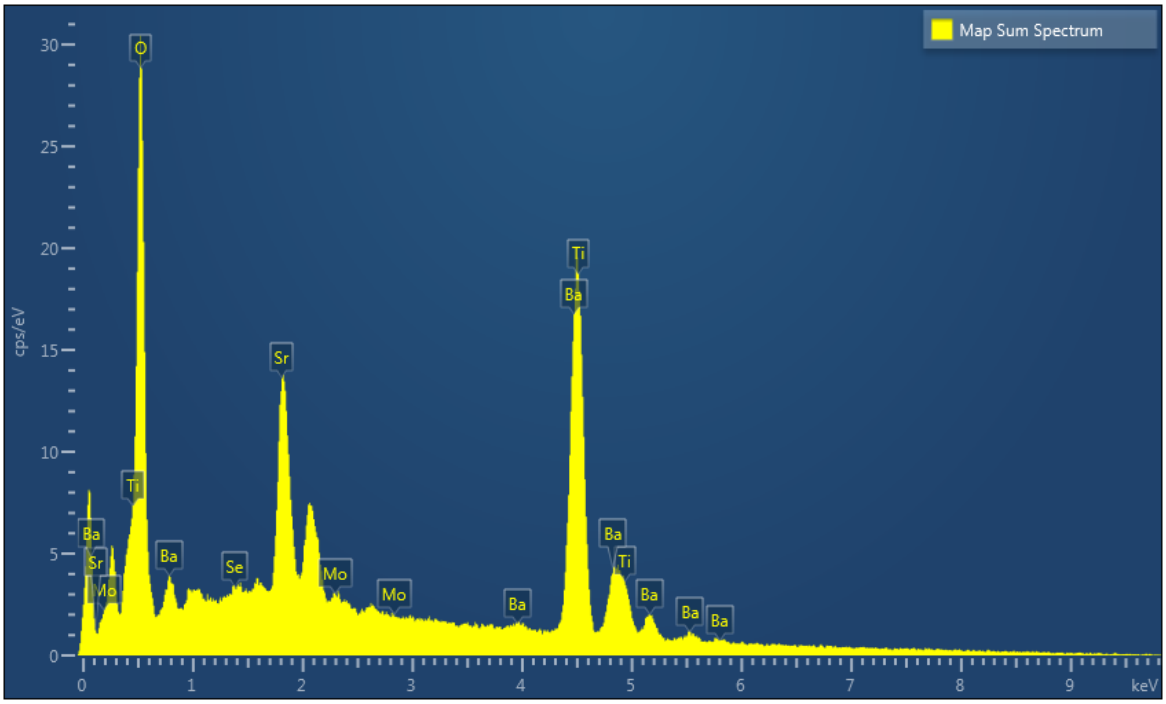

FIGURE 4.21 The EDS spectra of 0.04 mol (Mo, Se) co-doped BST-0.6 nanopowders calcined at 800 ^{o}C for 2 h

The EDS data has also been used to quantitatively express (Table 4.7) the addition of the Mo^{6+} and Se^{4+} ions to the BST-0.6 base material where most of the weight percentage values attained from the stoichiometry (Mo, Se) co-doped BST-0.6 and EDS data matched to each other with small differences. The variation was believed to be caused by the loss of few amounts of the components and the addition of extra oxygen atoms from the environment in to the BST sample. When the carbon content was considered, some deviations of the weight percentage composition were realized. In such a case the remaining 0.44% weight percentage belonged to the carbon impurity. This agreed with the FT-IR and XRD spectra which indicated the existence of the carbonate impurities. Therefore, the EDS data of the BST samples has shown the effective incorporation of uni-dopants and co-dopants to the BST host material where the existence of carbon impurity in the calcined BST samples was also described.

Table 4.7 - The weight percentage values of the stoichiometry and EDS data of 0.04 mol (Mo, Se) co-doped BST-0.6 nanopowders

Elements	Weight percentage from stoichiometry	Weight percentage from EDS
O *K*	20.42	21.11
Ti *K*	24.92	24.62
Se *L*	00.34	00.28
Sr *L*	09.55	09.06
Mo *L*	00.90	0.86
Ba *L*	43.87	43.63
Total	100.00	99.56

4.2.7 XPS analysis

Similar XPS results were obtained for both the BST-0.6 and BST-0.7 nanopowder samples. As can be observed in Figure 4.22 and Figure 4.23(a-e), the compositional existences of all the ions in 0.04 mol Mo-BST-0.7 nanopowders have been confirmed using XPS. The formation of Mo-doped BST has also been confirmed by the occurrence of each ion of the perovskite sample through their respective binding energies. For instance, Ba^{2+} $3d_{5/2}$ was detected in the sample (Figure 4.23 (a)) at a binding energy of 778.9 eV (Allen et al., 1973; Fowler & Miller, 1992) while another peak at 794 eV was considered to be a representative of Ba^{2+} found at the surface of the sample (F. Stemme et al., 2013). Figure 4.23 (b) described that Sr^{2+} $3d_{5/2}$ and Sr^{2+} $3d_{3/2}$ were observed at 132.9 eV and 134.4 eV respectively ((Gopinath, Subramanian, Huth, & Adrian, 1994). After the replacement of some Ti^{4+} ions by the Mo^{6+} ions, Ti^{4+} $2p_{1/2}$ along with Ti^{4+} $2p_{3/2}$ were detected at 463.8 eV and 458.6 eV in the Mo-BST (Figure 4.23 (c)) (Fan et al., 2010; Gonbeau et al., 1991; Netterfield et al., 1989). O*1s* of the Mo-BST was obtained at 530.2 eV (Figure 4.23 (d)) (Garbassi et al., 1995). The band overlaps at the Mo *3d* peaks have been fixed using the Gaussian curves fitting process. The respective Mo*3d* peak has split forming two peaks that correspond to Mo^{6+} $3d_{5/2}$ (232 eV) as well as Mo^{6+} $3d_{3/2}$ (235 eV) (Figure 4.23 (e)), based on the handbook of XPS (Anwar et al., 1990; Chastain & King Jr, 1992). This led to the conclusion that Mo has been incorporated in to BST by replacing some Ti of BST. The Mo^{6+} $3d_{5/2}$/Mo^{6+} $3d_{3/2}$ peaks of the Mo-doped BST nanopowders have shown smaller binding energies as a result of alteration of lattice parameters driven by the added Mo dopant. This is in a good agreement with the XRD data (Fan et al., 2010). Besides, carbon (C *1s*) has been found as an impurity at a 284.8 eV of the XPS survey (Figure 4.22) of the Mo-doped BST-

0.7 (Wang et al., 2022). This supported the FT-IR, XRD and EDS spectra of the BST samples which described the existence of few carbon impurities.

The XPS data have also been used to verify the empirical formula of the *sol-gel* synthesized $Ba_{0.77}Sr_{0.23}Mo_xTi_{1-x}O_3$ nanopowder. Table 4.8 explored the atomic percentage compositions of every element in the nanopowder. It is found that almost all of the atomic percentage compositions obtained from the XPS data matched with the starting compositions of an empirical formula of 0.04 mol Mo-doped BST-0.6 ($Ba_{0.6}Sr_{0.4}Mo_{0.04}Ti_{0.96}O_3$). The small variations were believed to be caused by the loss of some amount of the ions during synthesis and the formation of side products, such as carbonates (~0.87%). This revealed the successful synthesis of the Mo-doped BST nanopowder using a slow injection *sol-gel* method at a calcination temperature of 800 ^oC.

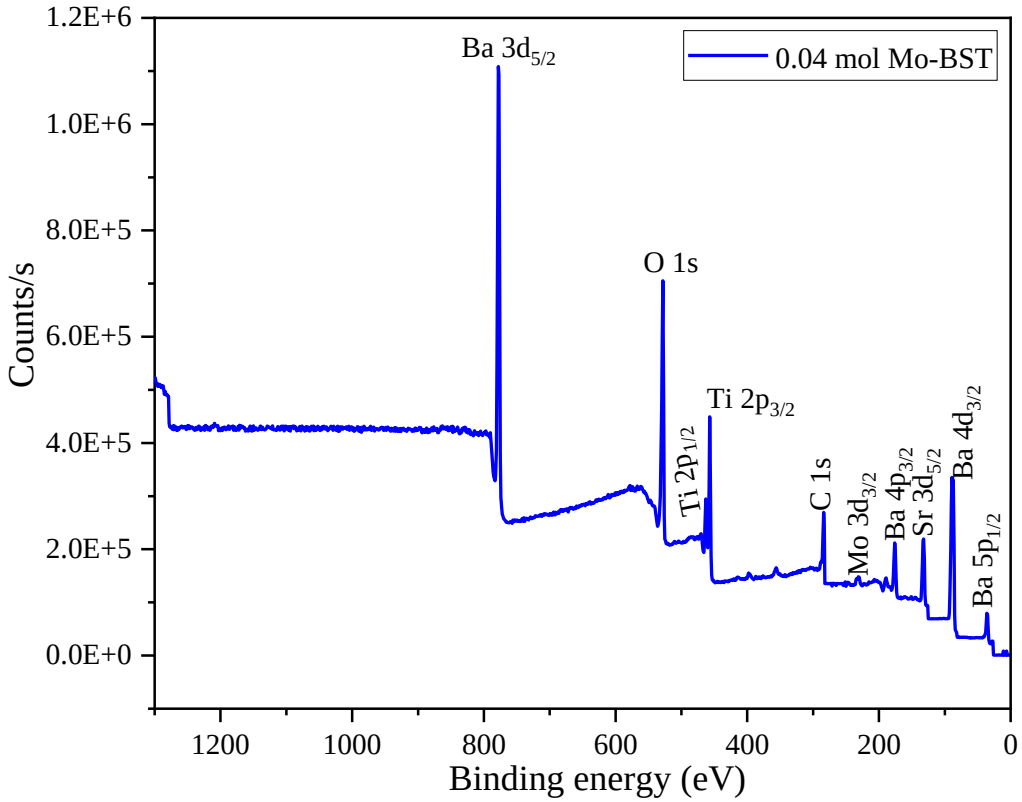

FIGURE 4.22 The XPS survey of 0.04 mol Mo-doped BST-0.7 nanopowder calcined at 800 ^oC for 2 h

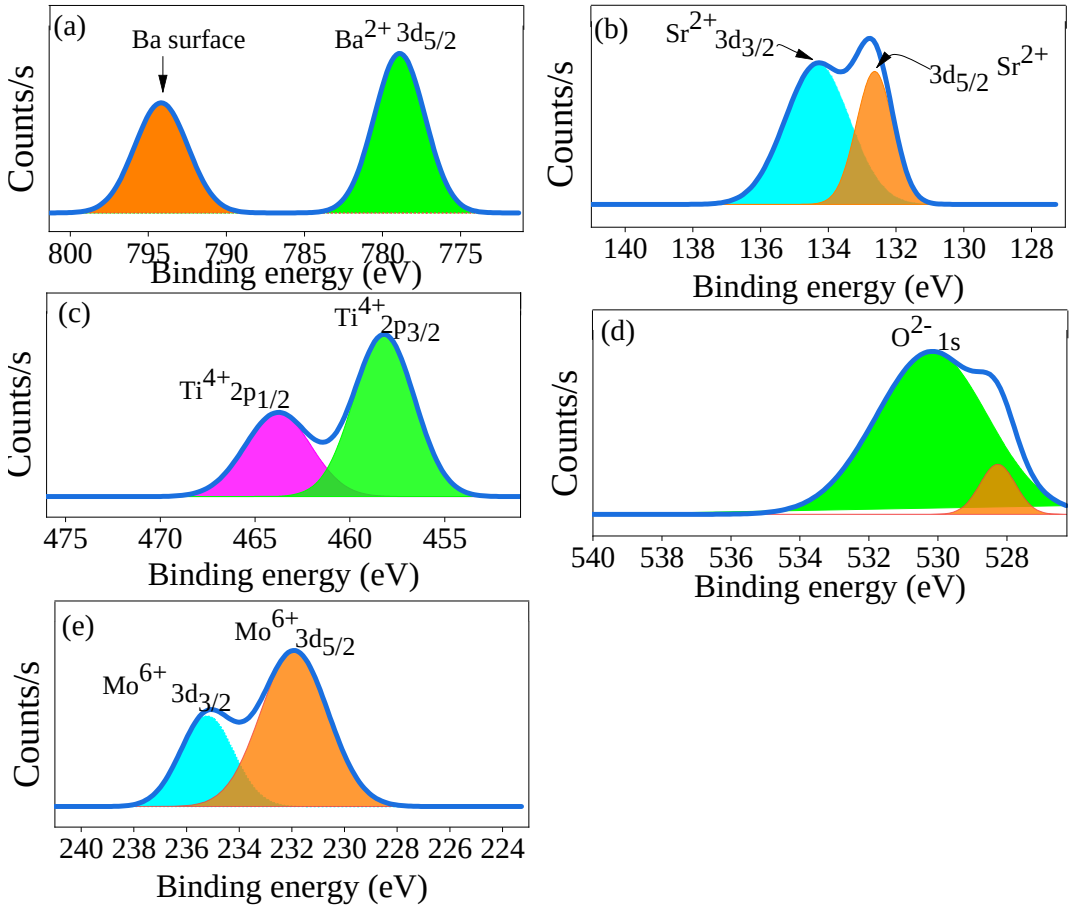

FIGURE 4.23 The XPS spectra of (a) Ba^{2+} ion (b) Sr^{2+} ion (c) Ti^{4+} ion (d) O^{2-} ion and (e) Mo^{6+} ion in Mo-doped BST-0.7 nanopowders

Table 4.8 - The stoichiometric and XPS atomic percentage compositions of the 0.04 mol Mo-doped BST-0.7 nanopowder

Name	Stoichiometric composition (atomic %)	Composition from XPS (atomic %)
Ba*3d*	15.40	15.11
Sr*3d*	4.60	4.53
Ti*2p*	19.20	18.97
Mo*3d*	0.80	0.75
O*1s*	60.00	59.77
Total	100.00	99.13

Figure 4.24 (a-e) illustrated the occurrence of Se^{4+} ion in 0.04 mol Se-doped BST-0.6 nanopowders using XPS. One of the main reasons why XPS was needed in characterizing the Se-doped BST-0.6 was its effectiveness in exploring the incorporation of Se^{4+} ion dopant into the BST-0.6

perovskite structure. $Ba^{2+}3d_{5/2}$ existed in the sample (Figure 4.24 (a)) at 779.1 eV (Doveren & Verhoeven, 1980; Nefedov et al., 1982). While Sr was detected as $Sr^{2+}3d_{5/2}$ at 133.1 eV as well as $Sr^{2+}3d_{3/2}$ at 134.7 eV (Figure 4.24 (b)) (Ohbayashi et al., 1992; Srivastava et al., 1994). $Ti^{4+}2p_{1/2}$ and $Ti^{4+}2p_{3/2}$ were detected at 463.9 eV and 458.6 eV, respectively (Figure 4.24 (c)) (Ikawa et al., 1991; Netterfield et al., 1989). Likewise, $O^{2-}1s$ was observed at 531.8 eV and 529.8 eV (Figure 4.24 (d)) (Castner & Ratner, 1990; Folkesson & Sundberg, 1987). Besides, Se^{4+} $3d_{5/2}$ was found with a binding energy of 61.0 eV (Figure 4.24 (e)) according to the handbooks of XPS agreeing with the EDS spectra (Chastain & King Jr, 1992; Weser et al., 1977; Yu et al., 1991). The existence of all the atoms of the Se-doped BST-0.6 nanopowder is indicated in the XPS survey (Figure 4.25). All the above XPS data were taken as a signal of the formation of Se-doped BST-0.6 nanopowder. Furthermore, carbon (C 1s) was detected as an impurity in the Se-doped BST-0.6 at a 284.8 eV (Wang et al., 2022) of the XPS survey (Figure 4.25). This matched with the BST samples' FT-IR, XRD and EDS spectra, which described the existence of a small amount of carbon impurity. In addition, the Se-doped BST-0.7 nanopowder samples produced exactly the same XPS survey data with the Se-doped BST-0.6 nanopowders.

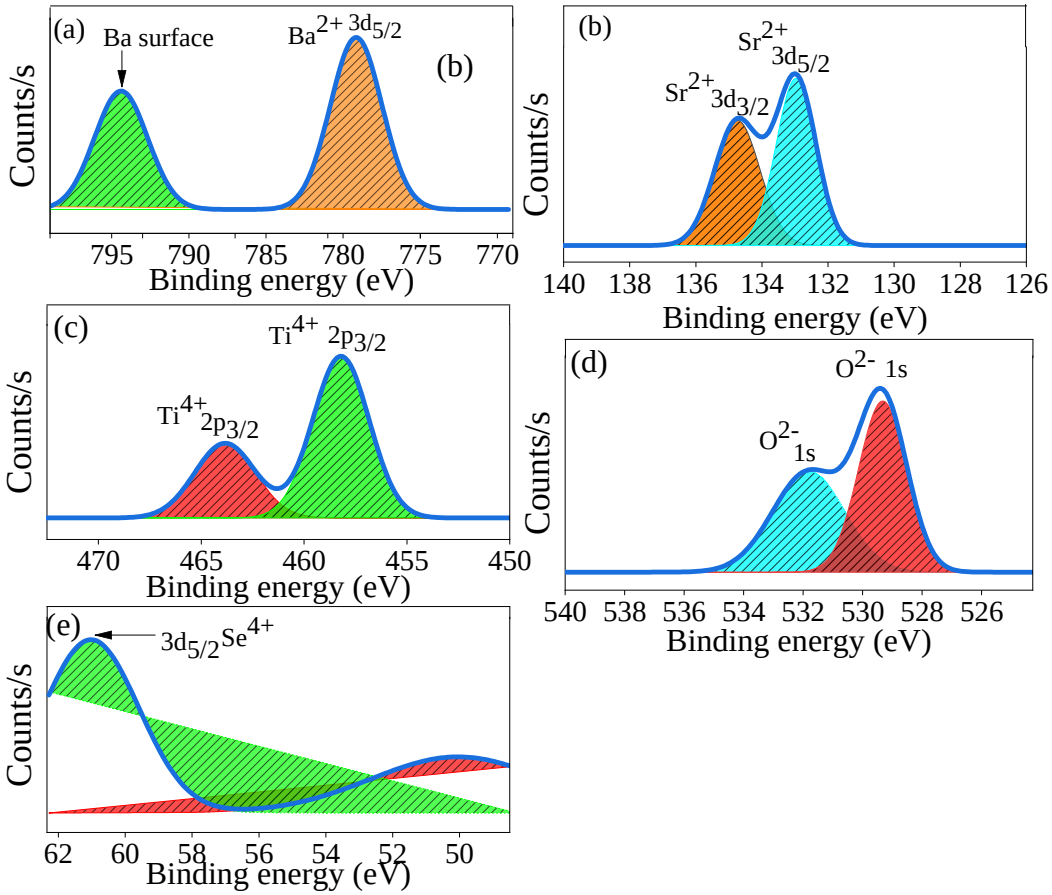

FIGURE 4.24 The XPS spectra of (a) Ba^{2+} ion (b) Sr^{2+} ion (c) Ti^{4+} ion (d) O^{2-} ion (e) Se^{4+} ion in 0.04 mol Se-doped BST-0.6 nanopowder

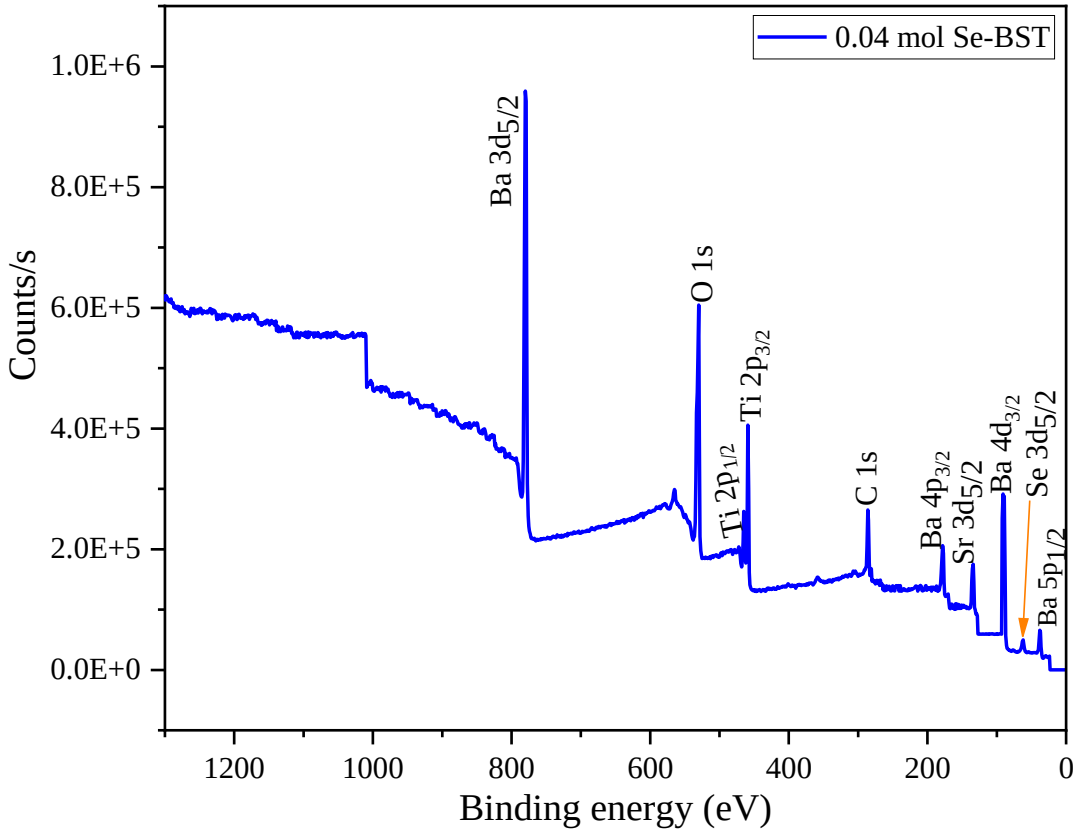

FIGURE 4.25 The XPS survey of 0.04 mol Se-doped BST-0.6 nanopowder calcined at 800 ^{o}C for 2 h

Moreover, the amount of each ion found in the 0.04 mol Se-doped BST-0.6 ($Ba_{0.6}Sr_{0.36}Se_{0.04}TiO_3$) has also been quantitatively determined from the XPS data as described in Table 4.9. Hence, most of the atomic percentages of the ions obtained from the XPS data matched with the stoichiometrically calculated and used during the synthesis of the 0.04 mol Se-doped BST-0.6 sample. There are few variations due to the loss of some amount of the ions during the *sol-gel* synthesis and addition of small amount of extra oxygen atoms from the atmosphere as well as the appearance of few carbon containing impurities. The remaining atomic percentage of ~ 0.45% corresponded to the carbon impurities.

The XPS data of the BST samples efficiently described the existence of all the ions of the pristine and doped BST samples which could be taken as the perfect indicators of the formation of the BST samples.

Table 4.9 - The stoichiometric atomic percentage and the XPS atomic percentage composition of 0.04 mol Se-doped BST-0.6

Name	stoichiometric atomic percentage composition	Atomic percentage composition from XPS
Sr3*d*	7.20	6.79
Ti*2p*	20.00	19.86
O*1s*	60.00	60.17
Ba*3d*	12.00	11.96
Se*3d*	0.80	0.77
Total	100.00	99.55

4.2.8 TEM analysis

Since distinct crystal and grain structures were obtained for the doped BST-0.6 and doped BST-0.7 nanopowders, the TEM micrograph data of 0.04 mol Mo-BST-0.6 and 0.04 mol Mo-doped BST-0.7 nanopowders were found a little bit different from each other.

The respective TEM micrographs, High resolution TEM (HR-TEM) image, Fast Fourier Transform (FFT) of the HR-TEM image and the particle size distribution of the 0.04 mol Mo-doped BST-0.6 were shown in Figure 4.26 (a-d). The cubic shaped nanopowders were found to have agglomerates within the dispersed solution and some irregular shapes. This supported the result obtained from the XRD data. It was shown that the nanopowders possessed uniform morphologies with some irregularities (Figure 4.26 (a)). A characteristic *d*-spacing of 0.1946 nm was computed from the HR-TEM (Figure 4.26 (b)) FFT model which belonged to one of the plane of the cubic BST-0.6 nanopowder, *i.e*. (200). Moreover, the three planes (200), (310) and (111) observed at the FFT of the HR-TEM of the 0.04 mol Mo-doped BST-0.6 (Figure 4.26 (c)) expressed the characteristic miler indices values of the BST-0.6 sample with the respective 0.1946 nm, 0.1220 nm and 0.2190 nm. The TEM micrograph of the 0.04 mol Mo-doped BST-0.6 nanopowders demonstrated a mean particle size of 20.92 nm with standard deviation (SD) of 5.68 (Figure 4.26 (d)). Hence, the Mo-doped BST-0.6 nanopowder was composed of smaller particles with varied particle sizes. This was found in a good agreement with the crystal size and grain size of the Mo-doped BST-0.6 samples obtained from the XRD and SEM image data.

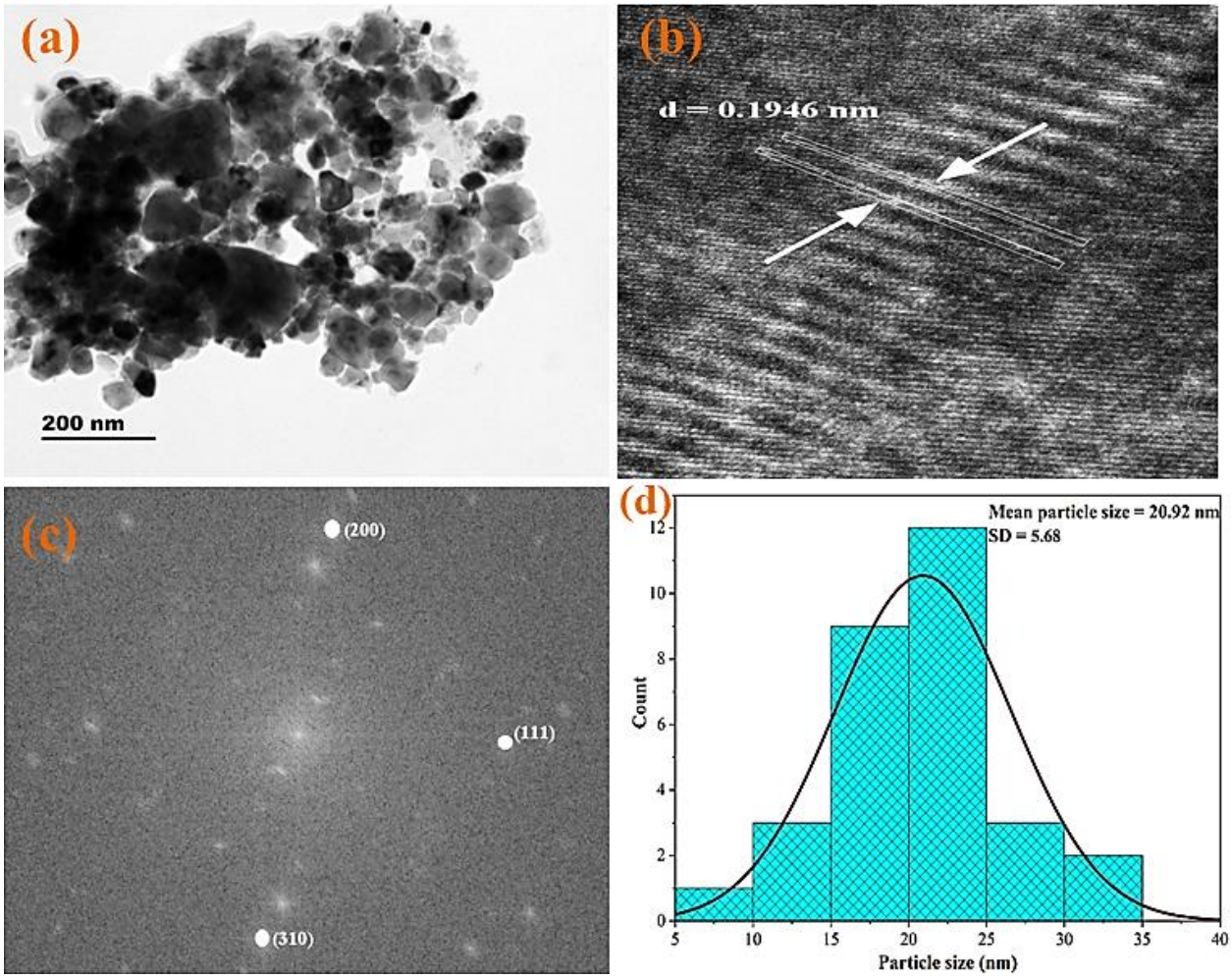

FIGURE 4.26 (a) TEM image (b) HRTEM image and (c) FFT of the HRTEM image (d) particle size distribution of 0.04 mol Mo-doped BST-0.6 nanopowders synthesized at calcination temperature of 900 ^{o}C for 2 h

The TEM micrograph of 0.04 mol Se-doped BST-0.6 nanopowder, calcined at 800 ^{o}C for 2 h, was shown in the Figure 4.27 (a-d). The 0.04 mol Se-doped BST-0.6 nanopowder contains agglomerated particles having an average particle size of 27.08 nm which was higher than the Mo-doped BST-0.6 (Figure 4.27 (a)). This matched with XRD data. The 0.04 mol Se-doped BST-0.6 was mostly composed of cubic shaped particles with few irregularities which supported the prediction made using the XRD data. Moreover, Figure 4.27 (b) clarified the HR-TEM image of the Se-doped BST-0.6 nanopowder where lattice fringes with a lattice distance of 0.285 nm were displayed. This lattice distance belongs to one of the miller indices of the Se-doped BST-0.6 nanopowder resulted from the XRD spectra, (101) where more of them have been explored at the selected area electron diffraction (SAED) image. Figure 4.27 (c) revealed that the SAED image of Se-doped BST-0.6 has shown well-defined rings revealing a crystalline structure with polycrystalline phase. It is matched with the sharp XRD peaks. The (*h k l)* values of Se-doped BST nanopowder determined using SAED have exactly matched with the XRD spectra. Figure 4.27 (d)

has shown narrow particle size distribution with a SD of 0.488 and dominant particle size of 19.21 nm. The Se-doped BST-0.6 possessed uniformly distributed arrangement of nanoparticles that has been supported by the respective SEM image. This acquired the improvement of the dielectric attainment of Se-doped BST-0.6 sample, according to a report by Ianculescu (Ianculescu et al., 2007). Besides, the porous appearance is believed to be a driving force for the enhancement of the respective energy storing capacity of materials made up of the Se-doped BST-0.6 nanopowder (Zhang et al., 2021).

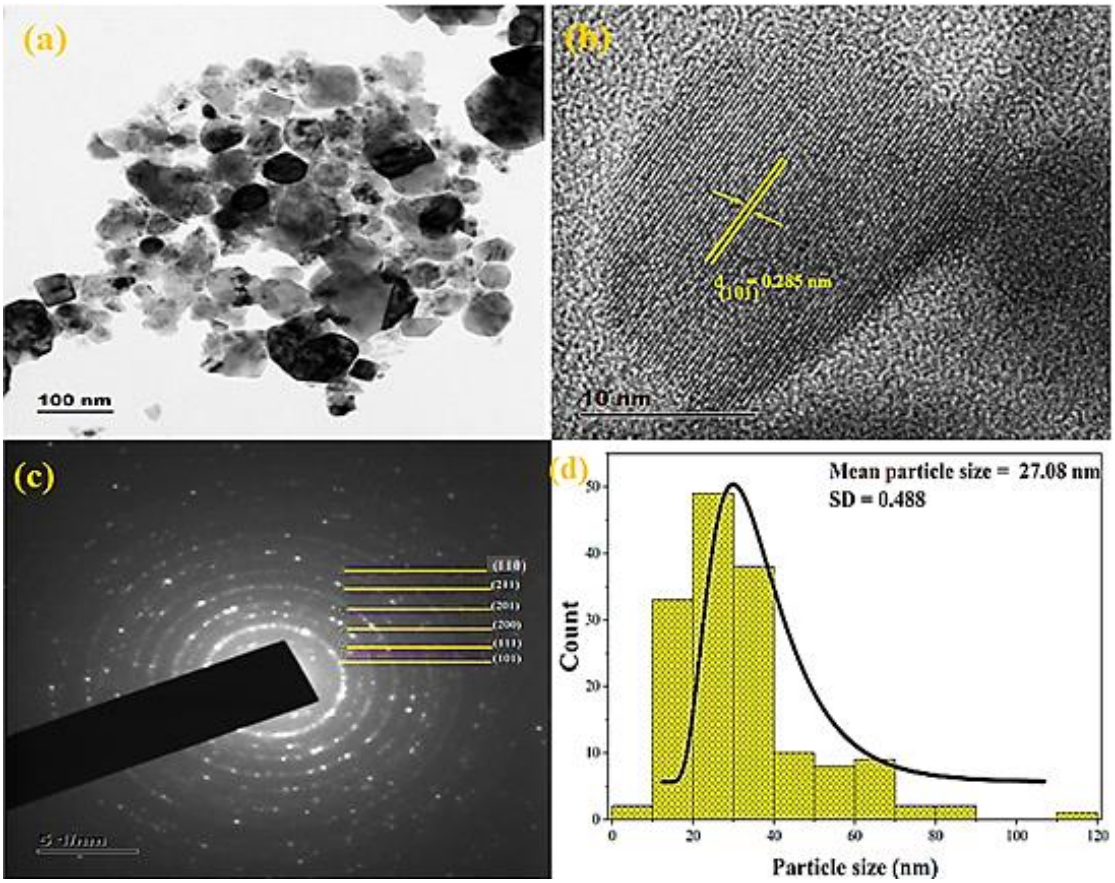

FIGURE 4.27 (a) The TEM (b) HRTEM (c) SAED images and (d) particle size distribution of 0.04 mol Se-doped BST-0.6 nanopowder calcined at 800 ^{o}C for 2 h

Similarly, Figure 4.28 (a-d) illustrated the TEM micrograph of the 0.04 mol (Mo, Se) co-doped BST-0.6 nanopowder calcined at 800 ^{o}C for 2 h. It has been shown that the nanopowder was composed of porous and agglomerated particles with average particle size of 20.22 nm. This was comparable with the respective particle size of the Mo-doped BST-0.6 nanopowder. (Mo, Se) co-doped BST-0.6 contains cubic shaped particles with few irregularities that have endorsed the prediction made using the XRD data (Figure 4.28 (a)).

From the HR-TEM as shown in Figure 4.28 (b), lattice fringes having a lattice distance of 0.312 nm has been observed. This corresponds to the respective miller indices, (100). It was one of the characteristic (*h k l)* values of the (Mo, Se) co-doped BST-0.6 nanopowder obtained from the XRD

data. Furthermore, other (*h k l)* values were determined from the SAED image (Figure 4.28 (c)). All the (*h k l)* values of (Mo, Se) co-doped BST-0.6 nanopowder were found matching with the XRD data. The SAED pattern has also clarified the formation of polycrystalline (Mo, Se) co-doped BST-0.6 phase. This was in a good agreement with the sharp XRD peaks and the polymorphism stage at the TGA/DSC spectrum.

The (Mo, Se) co-doped BST-0.6 possessed a narrow particle size distribution (Figure 4.28 (d)) described by the lower SD of 5.15. This projected the uniform arrangement of (Mo, Se) co-doped BST-0.6 nanoparticles agreeing with the SEM results. Such a porous nanostructure of (Mo, Se) co-doped BST-0.6 nanomaterial was expected to enhance the energy storage application (dielectric activity) of the (Mo, Se) co-doped BST-0.6 nanopowder (Ianculescu et al., 2007; Zhang et al., 2021).

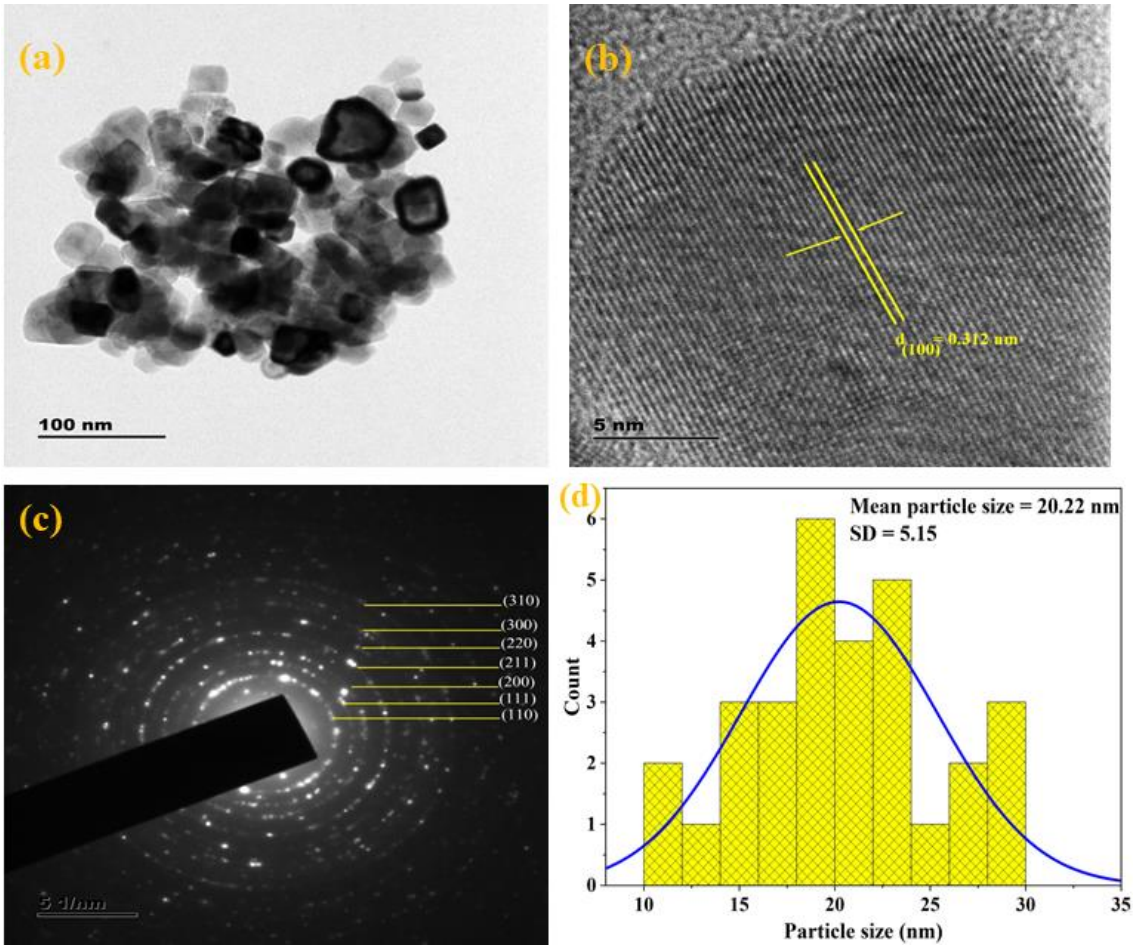

FIGURE 4.28 (a) TEM (b) HRTEM (c) SAED images and (d) Particle size distribution of 0.04 mol (Mo, Se) co-doped BST-0.6 nanopowder calcined at 800 ^{o}C for 2 h

The TEM micrograph of the 0.04 mol Mo-doped BST-0.7 nanopowder displayed at Figure 4.29 (a-d) demonstrated similar result with the 0.04 mol Mo-doped BST-0.6 despite different particle size and particle size distribution values. The tetragonal shaped nanopowders were found to have

agglomerates within the dispersed solution and some irregular shapes. This supported the result obtained from the XRD data. It was shown that the nanopowders possess uniform morphologies with some irregularities (Figure 4.29 (a)). The Mo-doped BST nanopowder is composed of particles with FFT model computed typical *d*-spacing such as 0.3440 nm, 0.2740 nm, 0.1220 nm and 0.2190 nm which belong to the respective miller indices of the major peaks; (200), (110), (310) and (111) (Figure 4.29 (b, c)). A typical *d*-spacing has been assigned at the HR-TEM that belongs to plane (200). This indicated that the TEM results are in compliance with the XRD data for the confirmation of the formation of Mo-doped BST nanopowder. The average particle size of 0.04 mol Mo- BST-0.7 nanopowder was found to be 24.60 nm. This was comparable with a report by Batttisha (Batttisha et al., 2014).

The Mo- BST-0.7 nanopowder is composed of particles with a narrow size distribution expressed by the lower standard deviation of 0.35 indicating that they are uniformly distributed throughout the powder (Figure 4.29 (d)). This was believed to have a direct impact on the microstructure and enhancement of the dielectric characteristics of the Mo-doped BST sample (Ianculescu et al., 2007).

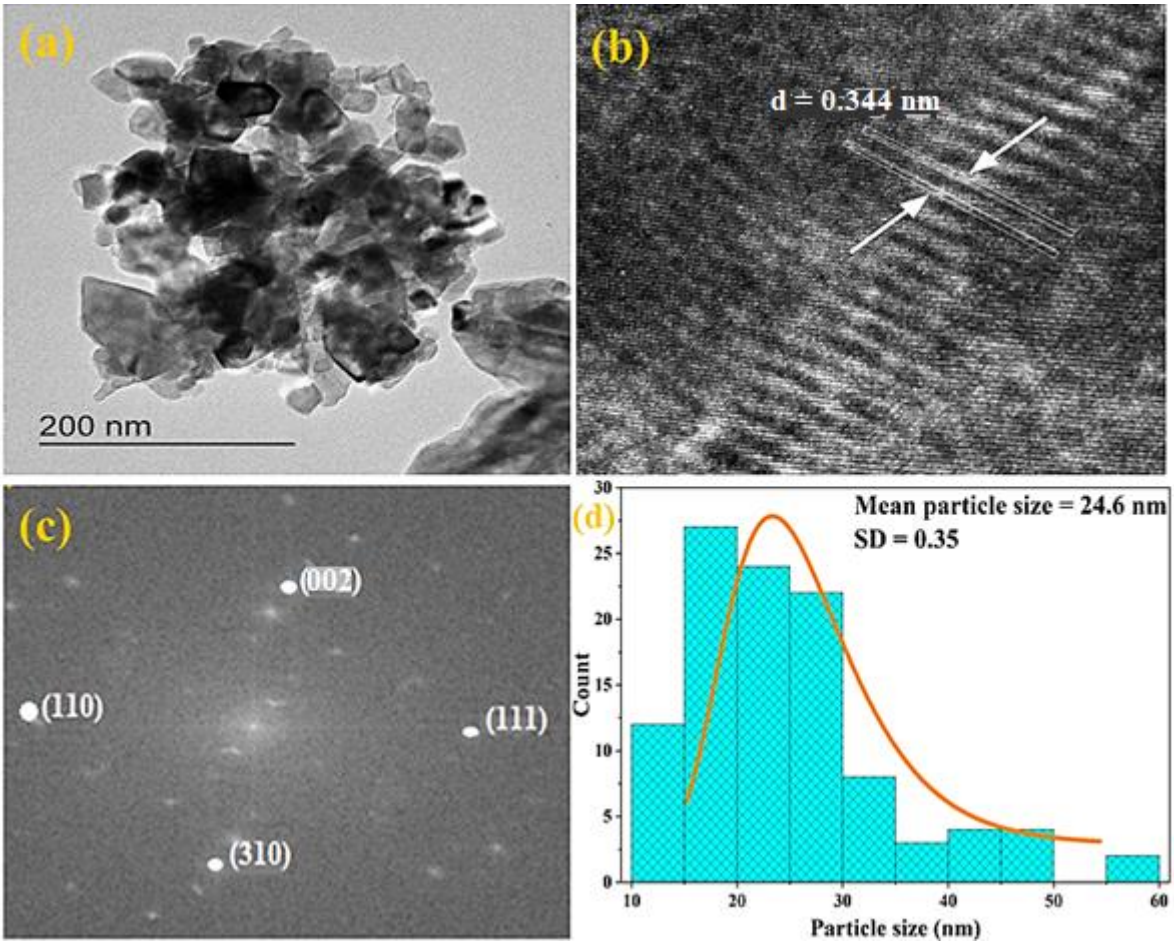

FIGURE 4.29 (a) The TEM image (b) HR-TEM image and (c) FFT of the HR-TEM image (d) particle size distribution of 0.04 mol Mo-doped BST-0.7 nanopowders synthesized at calcination temperature of 800 ^{o}C for 2 h

A similar TEM micrograph outcome with the 0.04 mol Se-doped BST-0.6 was attained for 0.04 mol Se-doped BST-0.7 nanopowder, as shown in Figure 4.30 (a-d). Porous and agglomerated particles of the Se-doped BST-0.7 nanopowder was observed at the TEM micrograph data (Figure 4.30 a).

Using the HR-TEM and SAED data, the respective planes of the tetragonal shaped Se-doped BST-0.7 (Figure 4.30 (b, c)) was found in consistent with those obtained from the XRD spectra. The mean particle size of 0.04 mol Se-doped BST-0.7 nanopowder was obtained as 28.34 nm with SD of 9.29 (Figure 4.30 d). Hence, in comparison to Se-doped BST-0.7, the Se-doped BST-0.6 nanopowder contains smaller particles of extremely variable particle sizes. Such a phenomenon was found in consistent with the XRD and SEM data for the Se-doped BST-0.7 and Se-doped BST-0.6 samples. Its particle size was higher than any of the doped BST samples with the highest variation of the particles sizes.

As the XRD and SEM data do, the TEM data shown that variation of the Ba:Sr ratio resulted in varied arrangement of particles and particles sizes of the BST samples where the particles size values were found closer to the crystal sizes of the BST samples.

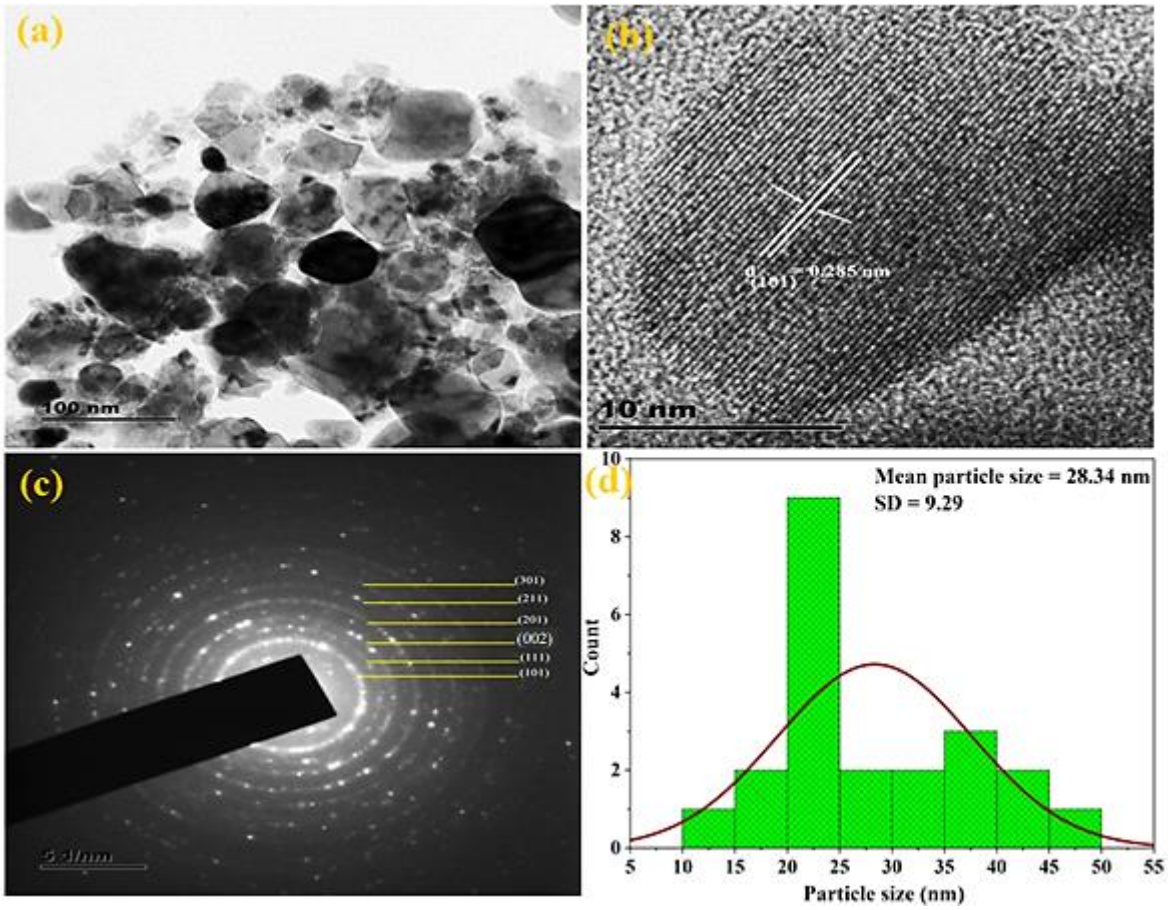

FIGURE 4.30 (a) The TEM (b) HRTEM (c) SAED images and (d) Particle size distribution of 0.04 mol Se-doped BST-0.7 nanopowder calcined at 900 ^{o}C for 2 h

4.2.9 The BET analysis

The BET data is treated according to a BET adsorption isotherm linear equation (Equation 4.2).

$$\frac{P/P_O}{W(1-P/P_O)} = \frac{1}{C \times W_{ml}} + \left(\frac{C-1}{C \times W_{ml}}\right) P/P_O \quad \text{.....4.2}$$

Where, P_o is the saturated vapor pressure of N_2 gas in *Pa*; P is the partial vapor pressure of N_2 gas in *Pa*; W is the mass of N_2 gas at standard temperature and pressure (*STP*); W_{ml} is the appropriate mass of N_2 gas forming a complete monolayer adsorbed on the BST sample (the BET monolayer capacity); and C is a dimensionless constant related to the enthalpy of N_2 gas adsorption on the BST samples (Bardestani et al., 2019).

A graph of $\frac{1}{W((P_O/P)-1)}$ vs P/P_O was plotted (Figure 4.31) to resolve W_{ml}. It is calculated from the intercept and slope of the graph using equation 4.3 (Bardestani et al., 2019).

$$W_{ml} = \frac{1}{Slope + Intercept} \quad \text{.....4.3}$$

The linear plots of equation 4.2 should provide a straight line in the relative pressure range of 0.05 - 0.3. Furthermore, the linear regression value (R^2) is allowed when it is ≥ 0.995 (Boningari et al., 2018; Raghupathi et al., 2011). Both BST-0.7 and the 0.04 mol Mo-doped BST-0.7 samples fulfilled the two requirements accordingly (Figure 4.31 (a, b) and Table 4.10).

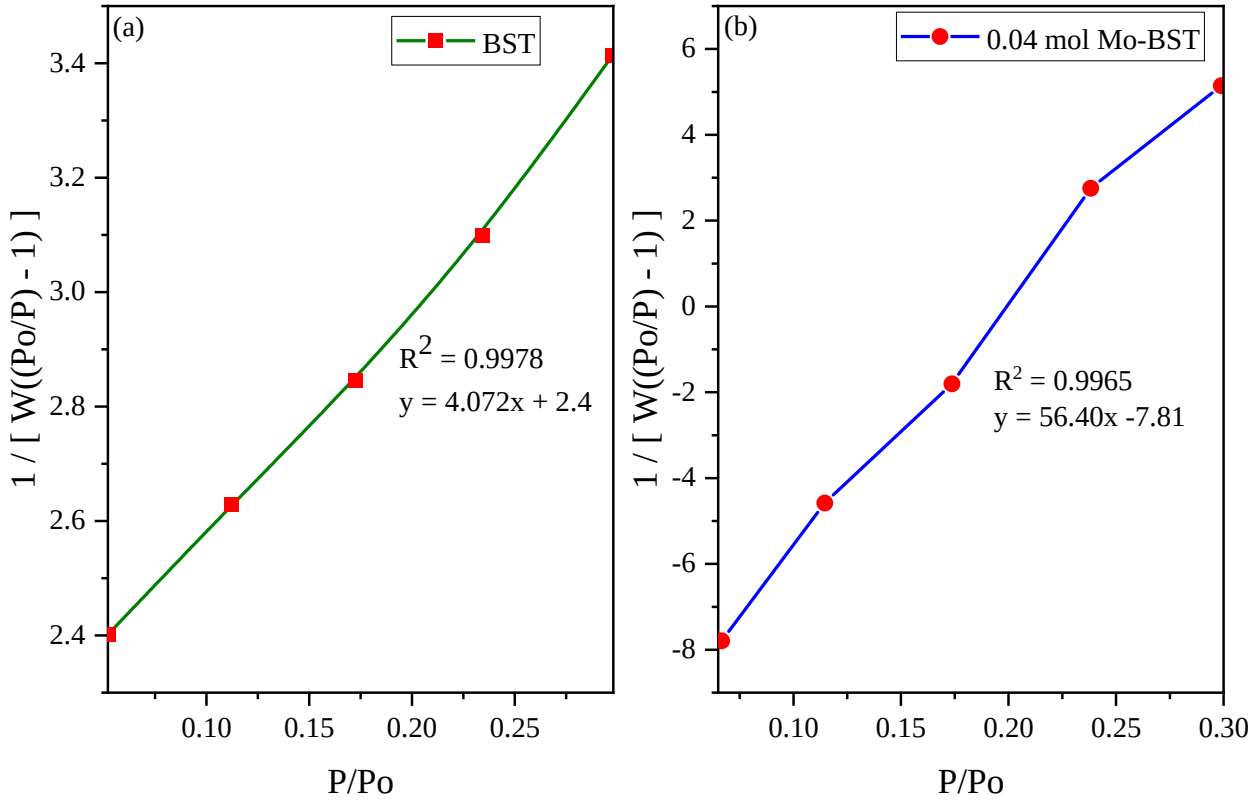

FIGURE 4.31 The linear BET plot of (a) BST-0.7 (b) 0.04 mol Mo- BST-0.7 nanopowders

The respective specific surface area (SSA) in m^2g^{-1} of the BST samples were then computed using their respective W_{ml} values (Equation 4.4).

$$SSA = \frac{W_{ml}}{M \times m} \times N \times A \quad \text{.....4.4}$$

Where, M is the molar mass of nitrogen at *STP*; m is the mass of the BST samples in g; A is the cross sectional area occupied by N_2 gas molecule in the complete monolayer (0.162 nm^2); and N is Avogadro's number (6.022×10^{23} mol^{-1}) (Bardestani et al., 2019).

Subsequently, the non-local density function theory (NLDFT) method was employed to determine the pore size and pore volume of the BST-0.7 (BST) samples. Hence, incorporation of Mo to BST-0.7 resulted in elevation of the SSA, pore size as well as pore volume of BST-0.7 (BST) (Table 4.10). Since the pore sizes of the samples are < 2 nm, the samples are supposed to be composed of micropores (Rouquerol et al., 1994). The Mo-doped BST-0.7 is less porous as compared to the BST-0.7 nanopowder. This is to mean that the decreased pore volume of the Mo-doped BST-0.7 nanopowder was probably caused by the lower number of agglomerates per BST-0.7 grain after doping of the BST-0.7 with Mo (Zhou et al., 2009). The same data with negligible difference has been obtained for the $Ba_{0.6}Sr_{0.4}TiO_3$ and 0.04 mol Mo-doped BST-0.6 nanopowders.

The 0.04 mol Se-doped BST-0.6 and 0.04 mol Se-doped BST-0.7 nanopowders produced identical BET results. The BET data of 0.04 mol Se-doped BST-0.6 was analysed using the equations 4.2, 4.3, and 4.4 supported by the BET plots of both BST-0.6 and Se-doped BST-0.6 nanopowders (Figure 4.32 (a, b)). Accordingly, the 0.04 mol Se-doped BST-0.6 nanopowder resulted in lower SSA, pore size and pore volume as compared to the undoped BST-0.6 (Table 4.10). This was found similar to the Mo-doped BST-0.6 nanopowders. However, the Se-doped BST-0.6 nanopowder was obtained as more porous in relative to the Mo-doped BST-0.6 nanopowder. The pore sizes of both the samples are < 2 nm indicating that their respective pores are dominantly micropores (Rouquerol et al., 1994). Hence, incorporation of Se ion into BST-0.6 caused the particles to be less porous with higher agglomerates. Such results were in consistent with the uniformly arranged particles observed at the SEM image of the 0.04 mol Se-doped BST-0.6.

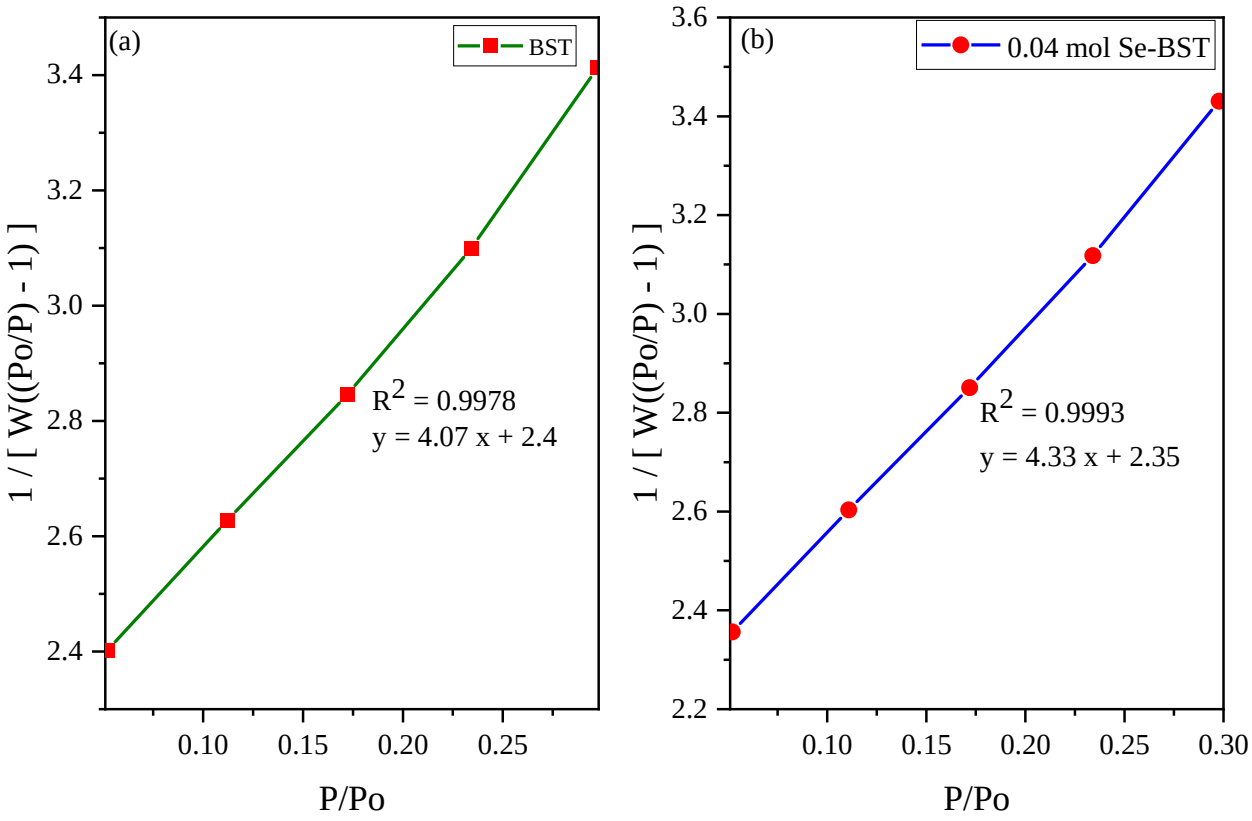

FIGURE 4.32 The linear BET plot of (a) BST-0.6 (B) 0.04 mol Se-BST-0.6 nanopowders

Figures 4.33 (a, b) described the slope and y-intercept values of the graph $\frac{1}{W((P_O/P)-1)}$ vs P/P_O for both BST-0.6 and 0.04 mol (Mo, Se) co-doped BST-0.6 nanopowders. Hence, the SSA, pore size and pore volume values BST decreased following the addition of 0.04 mol of both Mo^{6+} and Se^{4+} ions to BST through a slow injection *sol-gel* method (Table 4.10) in a similar way with the Mo-doped BST-0.6 and Se-doped BST-0.6 nanopowders. Besides, such a trend was found to be comparable with the lowering of agglomerates per SEM particles (Table 4.16). Therefore, the 0.04 mol (Mo, Se) co-doped BST-0.6 nanopowder was found slightly less porous as compared to BST-0.6. Meanwhile, the pore sizes of both the undoped and doped BST-0.6 nanopowders were found to be < 2 nm. This makes the samples to possess a predominant micropores (Rouquerol et al., 1994).

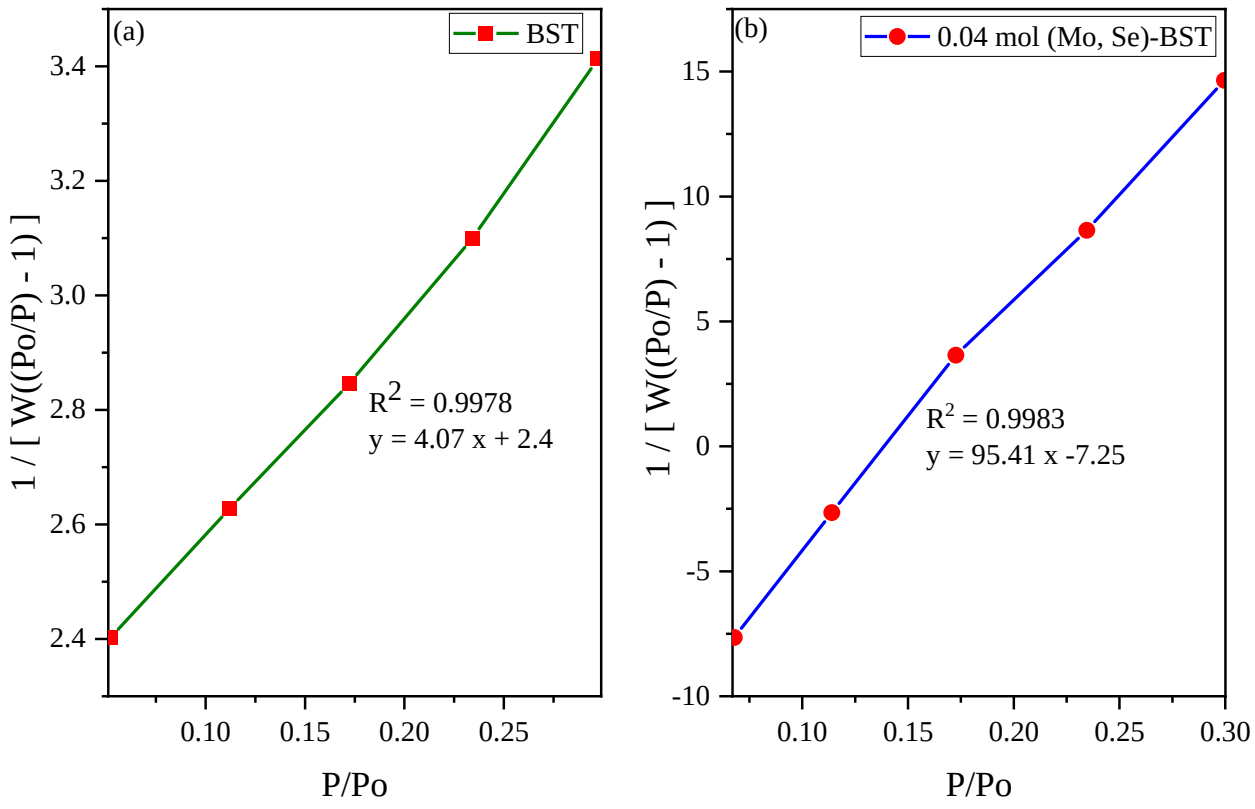

FIGURE 4.33 The linear BET plot of (a) BST-0.6 (B) 0.04 mol (Mo, Se) co-doped BST-0.6 nanopowders

Table 4.10 - The BET textural data of pure BST as well as Mo, Se and their co-doped BST nanopowders calcined at 800 ^{o}C for 2 h

Measurement	BST	0.04 mol Mo-doped BST	0.04 mol Se -doped BST	0.04 mol (Mo, Se) co-doped BST
Weight (g)	0.0500	0.0500	0.0500	0.0500
Slope	4.0700	56.4000	4.3300	95.4100
Intercept	2.1700	-11.3100	2.1200	-13.0000
R^2	0.9978	0.9965	0.9993	0.9983
C	2.8760	-4.1060	3.0440	- 4.1030
SSA (m^2/g)	557.8880	54.2340	539.5080	52.9600
Pore size (nm)	1.3240	1.3230	1.1560	1.2650
Pore volume (cc/g)	0.1400	0.0990	0.1083	0.0975

The mean BET grain diameter (D_{BET}) of the nanopowders serves as a rough estimate of the powders' principal particle size. The D_{BET} (*nm*) is calculated from the experimentally obtained

specific surface area, SSA ($m^2\ g^{-1}$), as well as the known theoretical density, ρ (5.69 g/cm^3), through equation 4.5, (Zhou et al., 2010);

$$D_{BET} = \frac{6 \times 10^3}{\rho \times SSA} \text{.....4.5}$$

Doping of BST-0.6 with Mo resulted in the lowering of the SSA of $Ba_{0.6}Sr_{0.4}TiO_3$. Consequently, the D_{BET} value of Mo-doped BST nanopowder was found to be higher than the undoped BST-0.6. The increase of D_{BET} due to Mo doping was similar to a research work reported by X. Zhou (Zhou et al., 2010). Meanwhile, when BST-0.6 was doped with Mo the average number of crystallites per SEM particles $(D_{SEM}/D_\beta)^3$ decreased which revealed that the particles observed in the SEM image of the Mo-doped BST-0.6 are in a mono coherent diffracting scope. This is believed to be the cause for the grain size of Mo-doped BST-0.6 nanopowder to be lower than that of the BST-0.6 as illustrated by the SEM image (Zhou et al., 2009).

The volume-weighted diameters of crystallites, D_β, has been determined using the apparent crystallite sizes, ϵ_β, through the relation, $D_\beta = \frac{4}{3}\ \varepsilon_\beta$ (Audebrand, Bourgel, & Louër, 2006). The D_β values of both BST-0.6 samples are comparable with the respective grain seizes (D_{SEM}) in a similar way with a previously reported work (Zhou et al., 2010). On the other hand, the Mo-doped BST-0.6 nanopowder possessed higher number of crystallites agglomerated per BET grain, $(D_{BET}/D_\beta)^3$, as compared to an undoped BST-0.6. This is believed to be the cause for the dense and reduced the average crystal size of Mo-doped BST-0.6 nanopowder, as already illustrated by the XRD data (Zhou et al., 2010).

Table 4.11 - The BET surface analysis of BST-0.6 (BST) and 0.04 mol Mo-doped BST-0.6

Nanopowders	ϵ_β (nm)	D_β (nm)	D_{SEM} (nm)	D^3_{SEM}/D^3_β	D_{BET} (nm)	D^3_{BET}/D^3_β
BST	19.35	25.80	26.02	1.02	1.89	0.0002
0.04 mol Mo-BST	17.84	23.78	18.58	0.47	19.46	0.5470

The BST-0.7 samples possessed higher ϵ_β and D_{SEM} values from the BST-0.6 samples indicating the BST-0.7 and the 0.04 mol Mo-doped BST-0.7 nanopowders to have higher $(D_{SEM}/D_\beta)^3$, as compared to the BST-0.6 and the 0.04 mol Mo-doped the BST-0.6 (Table 4.12).

Table 4.12 - The BET surface analysis of BST-0.7 (BST) and 0.04 mol Mo-doped BST-0.7

Nanopowders	ϵ_β (nm)	D_β (nm)	D_{SEM} (nm)	D^3_{SEM}/D^3_β	D_{BET} (nm)	D^3_{BET}/D^3_β
BST	23.97	31.96	40.12	1.98	1.89	0.0002
0.04 mol Mo-BST	17.84	23.78	27.00	1.46	19.46	0.5470

Table 4.13 summarized the BET surface analysis of BST-0.6 and 0.04 mol Se-doped BST-0.6 samples. Incorporation of Se^{4+} ion into BST through a slow injection *sol-gel* method resulted in reduction of the respective SSA value of BST-0.6. Thereupon, the D_{BET} value of BST was found to be higher than the Se-doped BST nanopowder which was similar to the Mo-doped BST. This trend was found similar to a previously reported research work by Zhou (Zhou et al., 2010). Moreover, the average amount of crystals agglomerated inside a BET grain, $[(D_{BET}/D_{\beta})^3]$, of BST-0.6 increased when doped with Se complementing the Mo-doped BST. This is supposed to be resulted in a more dense and higher average crystal size of the Se-doped BST-0.6 nanopowder calcined at 800 ^{o}C, as illustrated by the XRD data (Zhou et al., 2010). On the other hand, the average number of $Ba_{0.6}Sr_{0.4}TiO_3$ crystallites per SEM particle, $[(D_{SEM}/D_{\beta})^3]$, decreased with the incorporation of Se as that of Mo- doped BST-0.6 nanopowder.

Table 4.13 - The BET surface analysis of BST-0.6 (BST) and 0.04 mol Se-doped BST-0.6

Nanopowders	ϵ_{β} (nm)	D_{β} (nm)	D_{SEM} (nm)	D^3_{SEM}/D^3_{β}	D_{BET} (nm)	D^3_{BET}/D^3_{β}
BST	23.97	31.96	40.125	1.97	2.757	0.0006
0.04 mol Se-BST	20.68	27.57	16.806	0.23	2.850	0.0011

Moreover, form the XRD and SEM data, the ϵ_{β} and D_{SEM} values of the BST-0.6 samples were different from those of the BST-0.7 samples. This brought about variation in the number of crystallites per SEM particle between the BST-0.7 and the BST-0.6 nanopowder samples (Table 4.14). But the same trend of the number of crystalites agglomorated were obtained.

Table 4.14 - The BET surface analysis of BST-0.7 (BST) and 0.04 mol Se-doped BST-0.7

Nanopowders	ϵ_{β} (nm)	D_{β} (nm)	D_{SEM} (nm)	D^3_{SEM}/D^3_{β}	D_{BET} (nm)	D^3_{BET}/D^3_{β}
BST	19.41	25.88	26.02	1.02	2.757	0.0006
0.04 mol Se-BST	28.02	37.36	32.26	0.64	2.850	0.0011

The BET surface analysis of BST-0.6 and 0.04 mol (Mo, Se) co-doped BST-0.6 were summarized in Table 4.15. BST-0.6 was found with lower D_{BET} value as compared to the (Mo, Se) co-doped BST-0.6 nanopowder due to the reduction of SSA after the addition of the co-dopants. The average number of agglomerated crystallites in a grain per SEM particles of (Mo, Se) co-doped BST nanopowder, $(D_{SEM}/D_{\beta})^3$, was larger than that of the undoped BST in Hence, more compacted agglomerates together with the closed pores have been obtained for the (Mo, Se) co-doped BST nanopowders. Meanwhile, the average number of agglomerated crystallites in a grain per BET particles, $(D_{BET}/D_{\beta})^3$ was also elevated, agreeing with the SEM and TEM micrographs. This result

was similar to a research reported by X. Zhou (Zhou et al., 2010). All the data were analogous with the Mo-doped BST and Se-doped BST nanopowders.

Table 4.15 - BET surface analysis of BST-0.6 (BST) and 0.04 mol (Mo, Se) co-doped BST-0.6

Nanopowders	ϵ_β (nm)	D_β (nm)	D_{SEM} (nm)	D^3_{SEM}/D^3_β	D_{BET} (nm)	D^3_{BET}/D^3_β
BST	23.97	31.96	40.13	1.98	1.89	0.0004
0.04 mol (Mo, Se) co-doped BST	26.18	34.91	53.27	3.55	19.90	0.2670

4.3 Dielectric Properties and Capacitive application of the BST, Mo-doped BST, Se-doped BST and their co-doped BST samples

For the purpose of exploring the effect of the dopants on the capacitive application of BST, one typical BST host material (BST-0.6) was selected. BST-0.6 is one of the most commonly utilized BST-0.6 samples for a capacitor application with expanded and optimized lattice volume which readily accommodate the dopants (Chou et al., 2007; Jiwei et al., 2002; Paul et al., 2009).

4.3.1 Dielectric constant and capacitance analysis

Dielectric constant is the ratio of capacitance of a unit volume per unit potential elevation. It is influenced by the microstructure, grain structure, and grain size of ceramics. There is a time where one dominates the other factors in determining the dielectric constant of samples (Kim & Kim, 2005). Four representative measuring temperatures of 10 ^oC, 25 ^oC, 50 ^oC and 100 ^oC were randomly selected to measure the dielectric constant and capacitance of all the pristine BST-0.6, Mo-doped BST-0.6, Se-doped BST-0.6 and (Mo, Se) co-doped BST-0.6 samples.

Figure 4.34 described the dielectric constant of BST-0.6 and Mo-doped BST-0.6 nanopowder which was calcined at 900 ^oC as well as sintered at 1000 ^oC. The respective maximum dielectric constant values of BST-0.6 increased after the addition of 0.02 - 0.06 mol of Mo^{6+}ions at a frequency of 1 MHz (Table 4.16). The pattern was found to be similar to previously reported works (Alkathy et al., 2016; Wang et al., 2004). The maximum dielectric constant values of the BST samples reported here are greater than some formerly disclosed woks (table 4.16). The increase in dielectric constant within the range 10 ^oC – 100 ^oC is caused by the formation of extrinsic oxygen vacancies (Equation 4.6) and space charge polarization which are resulted from the structural and microstructural impacts of Mo^{6+} on BST (Liao et al., 2014; Lv et al., 2022b; Yang et al., 2023). The temperature for the respective highest dielectric constant values of the samples known as Curie temperature, T_c, was found to be 25 ^oC.

$$BaO + MoO_3 \rightarrow Ba_{Ba} + Mo_{Ti} + 4\ O_O + V_O'' \text{.....4.6}$$

V_O'' - is an extrinsic oxygen vacancy controlled by the Mo content.

Elevation of the temperature *T* of the measurement decreases the effect of the electric field (voltage) leading to the reduction of dielectric constant, ε_r, according to the Curie-Weiss law (Equation 4.7) (Zhang, 2012).

$$\varepsilon_r = \frac{k}{T - T_0} \text{.....4.7}$$

Where, *k* is the Curie constant ($10.48\times 10^4 K$) and T_0 is the Curie-Weiss temperature ($1.50\times 10^6 K$).

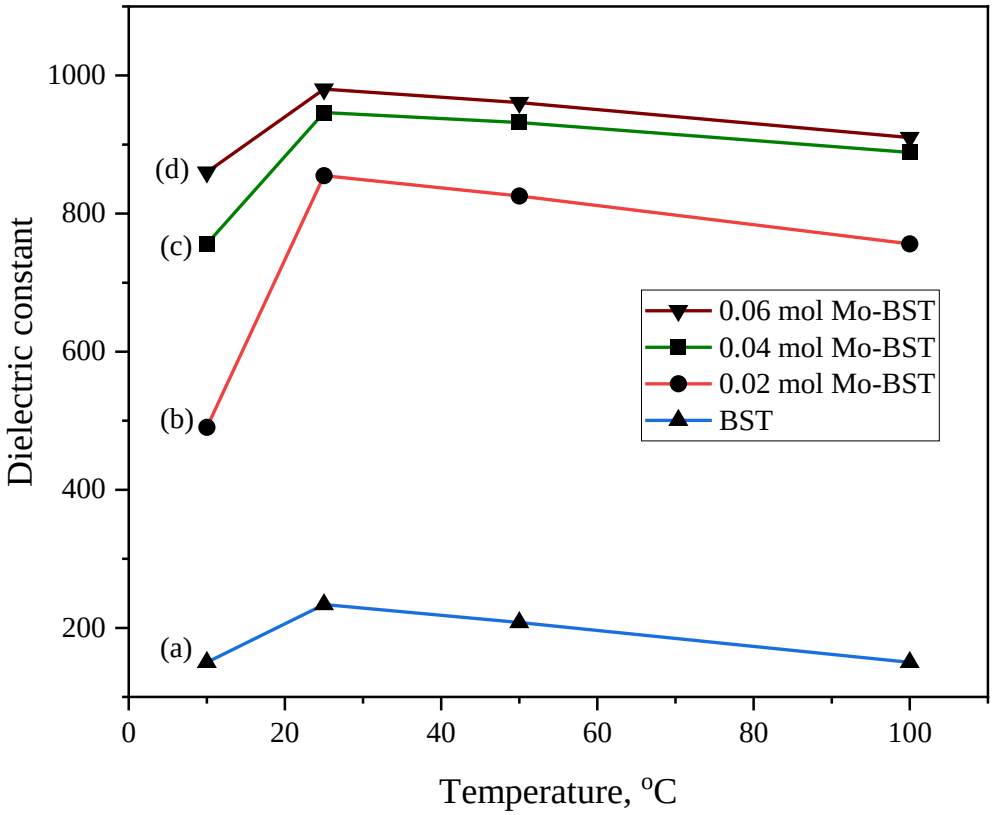

FIGURE 4.34 The dielectric constant as a function of temperature for (a) BST-0.6 (b) 0.02 mol Mo-doped BST-0.6 (c) 0.04 mol Mo-doped BST-0.6 (d) 0.06 mol Mo-doped BST-0.6 calcined at 900 °C and sintered at 1000 °C.

Figure 4.35 discussed the dielectric constant of BST-0.6 and Se-doped BST-0.6 nanopowder calcined at 800 °C as well as sintered at 1000 °C. Elevated dielectric constants of BST-0.6 were resulted following the incorporation of 0.02 - 0.06 mol Se^{4+}, at a frequency of 1 MHz. The T_c value for all the sample was recorded as 25 °C (Table 4.16). From Table 4.18, the highest dielectric constant resulted for the 0.06 mol Se-doped BST-0.6 pellet was reportedly higher than some already described works on BST (Das et al., 2022; Jaidka et al., 2022). It was also greater than the respective value for the 0.06 mol Mo-doped BST-0.6 pellet. The increasing of dielectric constant of BST-0.6, within the test temperature of 10 °C to 100 °C, primarily came from the lattice

deformation along with inner stress which led to the structural and microstructural changes. This was then followed by the increment of space charge polarization (Zhang et al., 2017). In order to balance the charge mismatch induced by the tetravalent Se^{4+} ions which replaced the divalent Sr^{2+} ions, it was proposed that Se^{4+} ions were positioned at off-centre positions of the Sr^{2+} sites. As a result, Sr vacancies might appear in the Se-doped BST to balance out the charge difference. Consequently, local electric fields were generated via the formation of dipoles by the off-centre Se^{4+} ions and Se^{4+}-Sr vacancy centres. This was followed by the elevated polarization and hence increased dielectric constant (Attar et al., 2017). The dielectric constant of the Se-doped BST-0.6 samples maintained stability at higher temperature, which is consistent with a report by Zhou (Zhou et al., 2009).

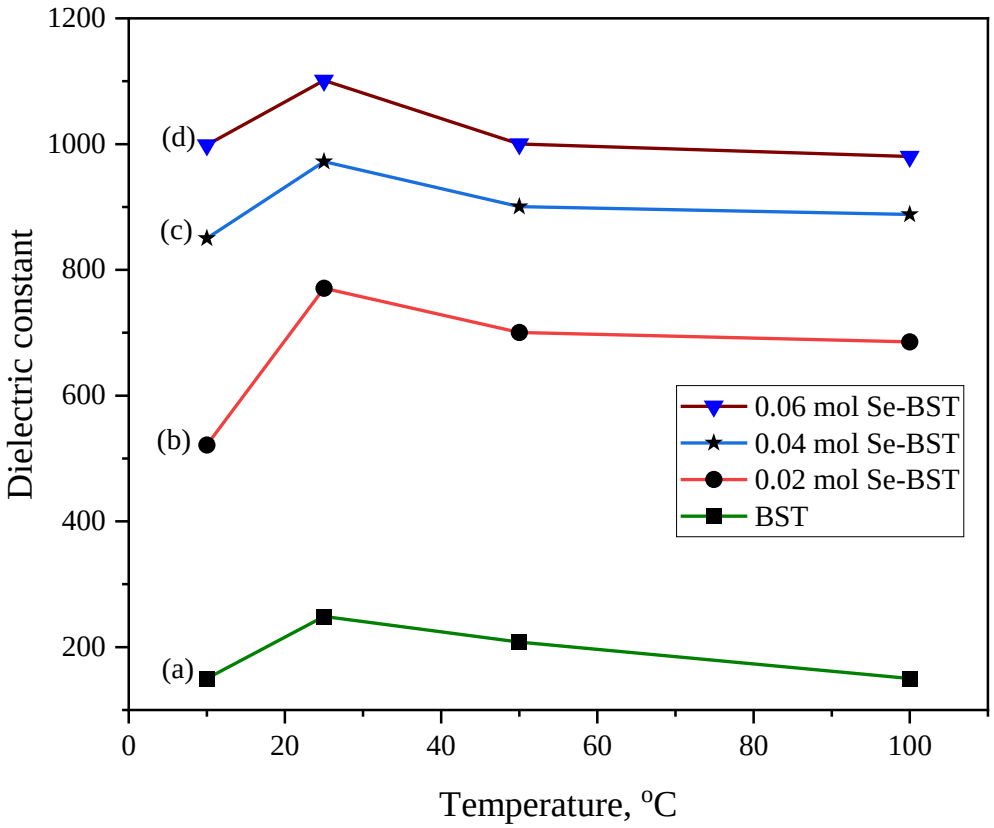

FIGURE 4.35 The dielectric constant as a function of temperature for (a) BST-0.6 (b) 0.02 mol Se-doped BST-0.6 (c) 0.04 mol Se-doped BST-0.6 (d) 0.06 mol Se-doped BST-0.6 calcined at 800 °C and sintered at 1000 °C

The dielectric constant of BST-0.6 and (Mo, Se) co-doped BST-0.6 calcined and sintered at 800 °C and 1000 °C respectively were presented in Figure 4.36. The respective dielectric constant values of the (0.02 - 0.06) mol (Mo, Se) co-doped BST-0.6 were found greater than the $Ba_{0.6}Sr_{0.4}TiO_3$ sample (Table 4.16) at a frequency of 1 MHz with a T_c value of 25 °C. The T_c value was not changed with amount of the co-dopants added to the BST host material. The maximum dielectric constant recorded for the 0.06 mol (Mo, Se) co-doped BST-0.6 pellets and also higher than the respective

values for the 0.06 mol Mo-doped BST-0.6 and Se-doped BST-0.6 pellets. The elevation of the dielectric constant was due to the increased concentration of Mo^{6+} and Se^{4+} which led to the increment of oxygen vacancies and space charge polarization which was caused by the structural as well as microstructural effects of the co-dopants on BST. On the other hand, it is usually reported that higher grain size leads to higher polarization which gives rise to the higher amount of active polarisation types particularly; atomic, ionic, and electronic polarisations (Cole et al., 2002; Fan et al., 2010a; Saeed et al., 2015a; Shalu & Ghosh, 2019). Thus, the higher grain sizes of the (Mo, Se) co-doped BST-0.6 samples as compared to the $Ba_{0.6}Sr_{0.4}TiO_3$ acquired elevated dielectric constant values.

The highest dielectric constant value recorded for the 0.06 mol (Mo, Se) co-doped BST-0.6 was greater than some already reported values (Das et al., 2022; Jaidka et al., 2022). It was also larger than the respective value for the Mo-doped BST-0.6 and Se-doped BST-0.6 samples (Table 4.16). The dielectric constants of the (Mo, Se) co-doped BST-0.6 samples decreased at higher temperature obeying the Curie-Weiss law. This trend of the dielectric constant was similar with a report by Zhou (Zhou et al., 2009). Moreover, addition of the Mo^{6+} and Se^{4+} dopants to the BST host material afforded increased amount of polarization where higher number of dipoles and hence charges were readily generated. Subsequently, lower voltage was needed for the dipoles to be formed. Ultimately, the capacitance of BST elevated after the incorporation of the dopants (Table 4.17).

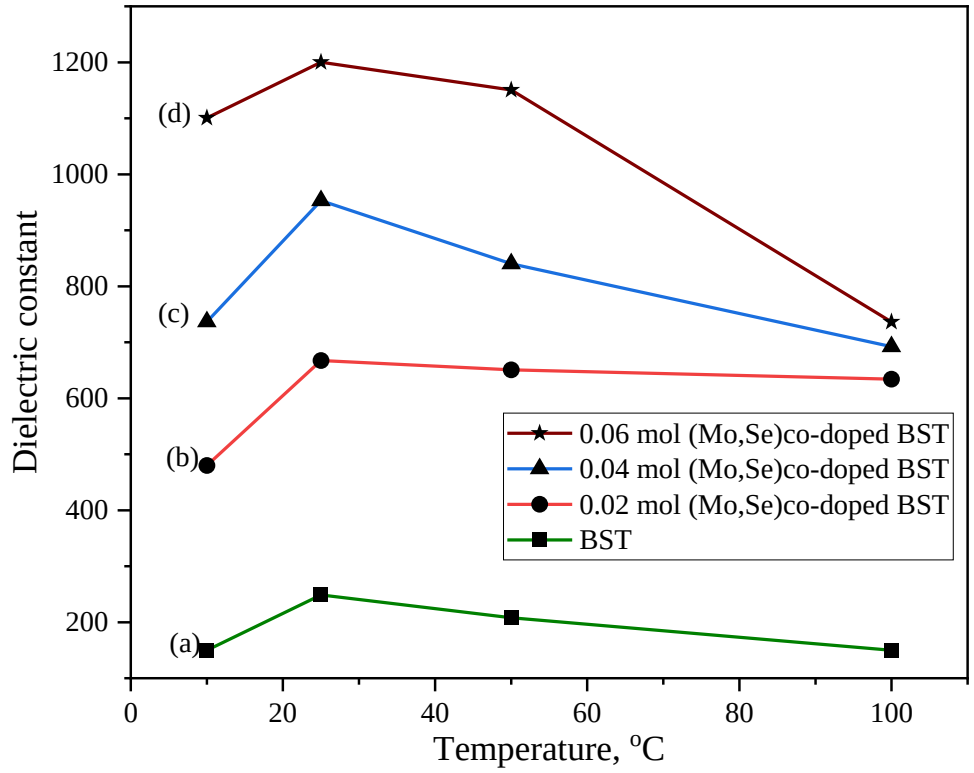

FIGURE 4.36 The dielectric constant as a function of temperature for (a) BST-0.6 (b) 0.02 mol (Mo, Se) co-doped BST-0.6 (c) 0.04 mol (Mo, Se) co-doped BST-0.6 (d) 0.06 mol (Mo, Se) co-doped BST-0.6 calcined at 800 °C and sintered at 1000 °C

Table 4.16 - The maximum dielectric constants of undoped as well as Mo, Se and their co-doped BST-0.6 (BST) samples

Samples	Calcination temperature (^oC)	Sintering temperature (^oC)	Maximum dielectric constant after addition of dopants				Reported maximum dielectric constant from reference	Reference
			0.00 mol	0.02 mol	0.04 mol	0.06 mol		
BST	800	1000	248.8	-	-	-	241	(S.-X. Wang et al., 2007)
	900	1000	233.8	-	-	-	232	(Qin et al., 2007)
Mo-BST	900	1000	233.8	854.6	946.3	980.3	923	(Ha et al., 2006)
Se-BST	800	1000	248.8	770.7	972.3	1101.4	603	(Liao et al., 2014)
(Mo, Se)-BST	800	1000	248.8	667.4	953.0	1200.2	433	(Tkach et al., 2005)

Figure 4.37 presented that the addition of Mo to BST has been resulted in increment of the maximum capacitance of BST base nanomaterial. The capacitance of the 0.06 mol Mo-doped BST-0.6 was found larger than other reported works (Shalu et al., 2022). Such a value was also greater than the minimum requirement for the Mo-doped BST-0.6 to be applied as a capacitor (25 *fF*) (Nagaraj et al., 1999). As the temperature of the measurement was increased, the amount of diploes formed from the BST samples was diminished. Furthermore, dopants might sometimes neutralize the applied voltage and decrease the capacitance to a value lower than the base material. Such a phenomenon was observed here around 100 ^oC (Zhang & Qu, 2012). Therefore, the doped BST samples possessed better capacitive application at lower measuring temperature.

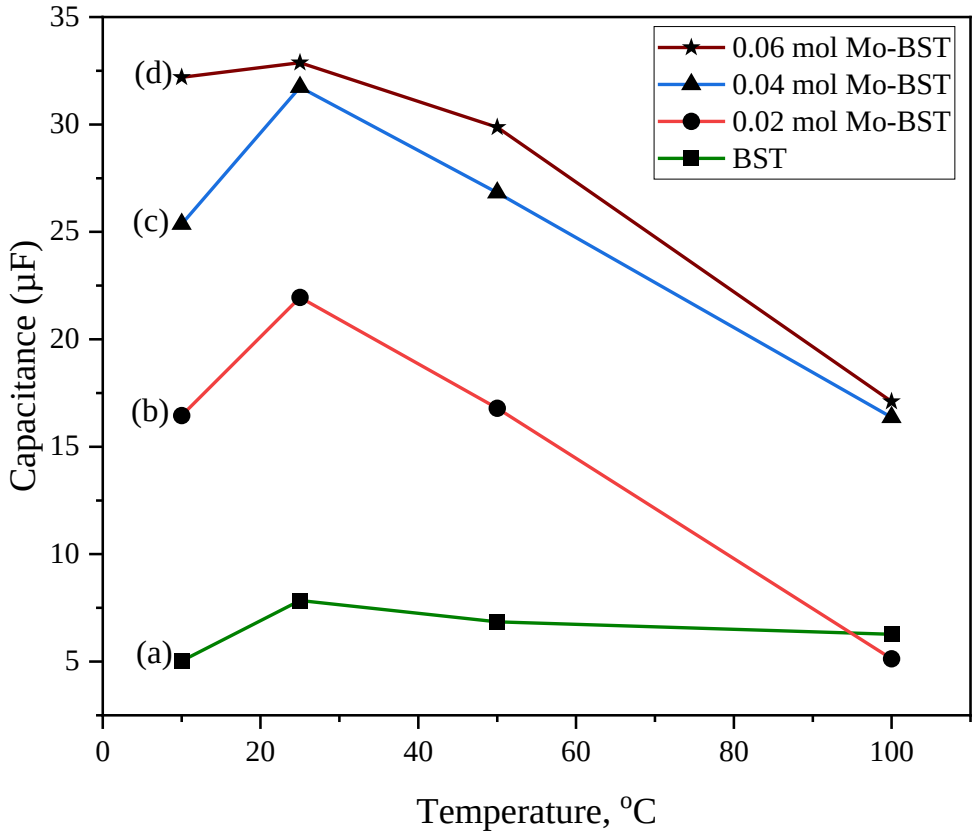

FIGURE 4.37 The capacitance as a function of temperature for (a) BST-0.6 (b) 0.02 mol Mo-doped BST-0.6 (c) 0.04 mol Mo-doped BST-0.6 and (d) 0.06 mol Mo-doped BST-0.6 calcined at 900 ^{o}C and sintered at 1000 ^{o}C

The maximum capacitance of BST-0.6 has been elevated following the addition of 0.06 mol Se^{4+} ions (Figure 4.38). This value surpassed the corresponding value for the 0.06 mol Mo- BST-0.6 (Table 4.17). Further, the maximum capacitance of the Se-doped BST-0.6 was found being higher than previously reported works (Shalu et al., 2022; Wang et al., 2022). As a result, the Se-doped BST-0.6 fulfilled the minimum requirement (25 *fF*) for it to be utilized in a capacitor (Nagaraj et al., 1999). Such data was considered as the first indicator for the Se-doped BST-0.6 to be applied in capacitors. Therefore, the Se-doped BST-0.6 sample could be utilized as a component of a capacitor in devices.

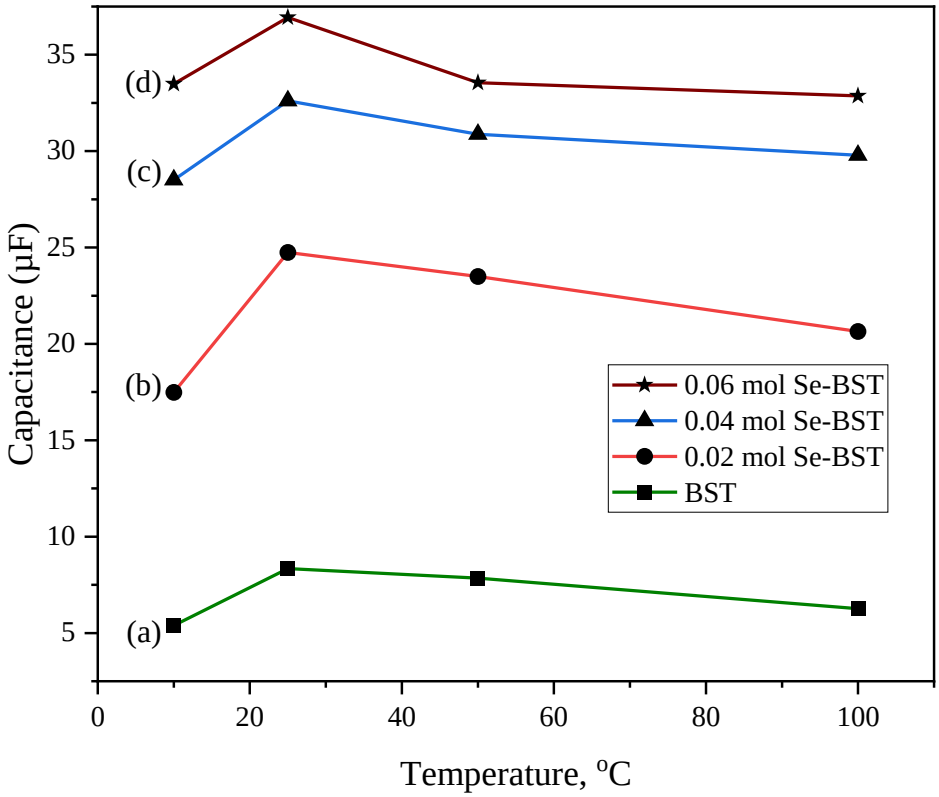

FIGURE 4.38 The capacitance as a function of temperature for (a) BST-0.6 (b) 0.02 mol Se-doped BST-0.6 (c) 0.04 mol Se-doped BST-0.6 (d) 0.06 mol Se-doped BST-0.6 calcined at 800 ^{o}C and sintered at 1000 ^{o}C

The enhancement of the dielectric constant of the BST base material due to the combined effect of the Mo^{6+} and Se^{4+} dopants brought about the elevation of the charge storing capacity of the material viz. capacitance. This has been illustrated in the Figure 4.39. The maximum capacitance recorded by the 0.06 mol (Mo, Se) co-doped BST-0.6 sample was greater than the uni-doped BST samples which was caused by the joined outcome of the Mo^{6+} and Se^{4+} ions (Table 4.17). The capacitance of the BST-0.6 and (Mo, Se) co-doped BST-0.6 was obtained larger than some heretofore previously reported works (Liu et al., 2022). Hence, the maximum capacitance of 0.06 mol (Mo, Se) co-doped BST-0.6 (40.25 μF) enables the (Mo, Se) co-doped BST-0.6 sample met the least requirement (25 fF) for the (Mo, Se) co-doped BST-0.6 to be used in a capacitor (Nagaraj et al., 1999).

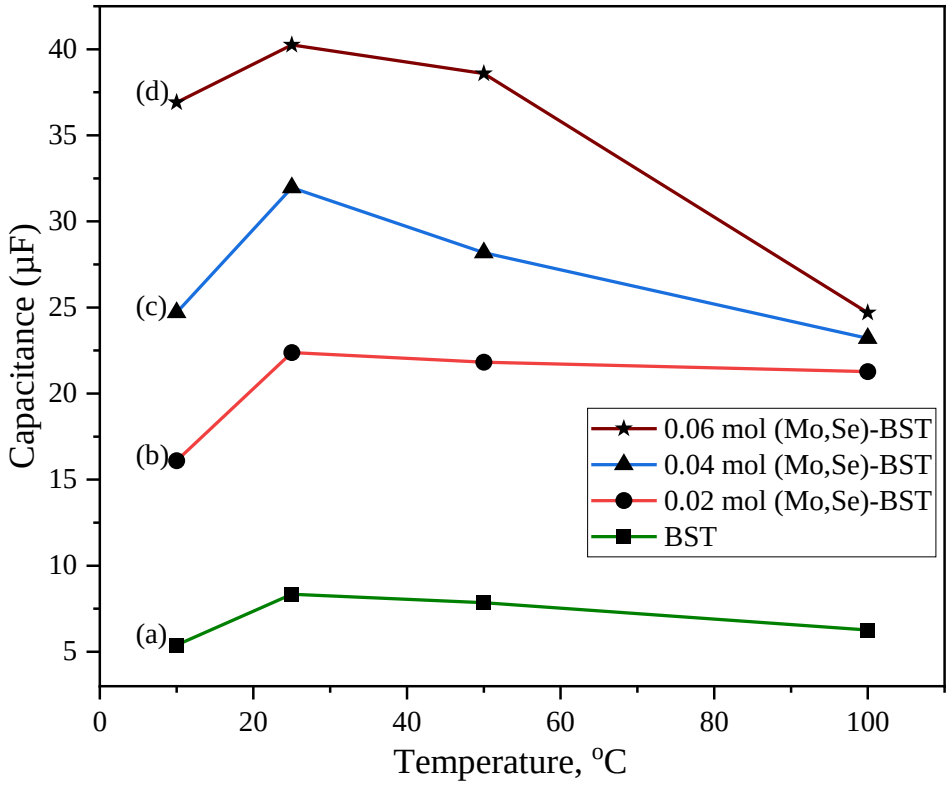

FIGURE 4.39 The capacitance as a function of temperature for (a) BST-0.6 (b) 0.02 mol (Mo, Se) co-doped BST-0.6 (c) 0.04 mol (Mo, Se) co-doped BST-0.6 (d) 0.06 mol (Mo, Se) co-doped BST-0.6 calcined at 800 °C and sintered at 1000 °C

Table 4.17 - The maximum capacitance of prestine BST-0.6 (BST), Mo, Se and their co-doped BST-0.6 samples

Samples	Calcination temperature (°C)	Sintering temperature (°C)	Maximum capacitance after addition of dopants (µF)			
			0.00 mol	0.02 mol	0.04 mol	0.06 mol
BST	800	1000	8.34	-	-	-
	900	1000	7.84	-	-	-
Mo-BST	900	1000	7.84	21.95	31.73	32.87
Se-BST	800	1000	8.34	24.74	32.61	36.94
(Mo, Se)-BST	800	1000	8.34	22.38	31.96	40.25

The dielectric constant of all the BST samples has also been affected by the variation in the calcination temperature in a similar way to previously reported works (Attar et al., 2017). For such a purpose, two ideal calcination temperatures (800 ^{o}C and 900 ^{o}C) and one BST sample (0.04 mol Mo-doped BST-0.6) were used. Increasing the calcination temperature form 800 ^{o}C to 900 ^{o}C resulted in lowering of the dielectric constant of 0.04 mol Mo-doped BST-0.6 in a similar trend with a report by Saeed (Saeed et al., 2015) where no shifting of the T_c value of the samples were observed (Figure 4.40 (i) and Table 4.18). This indicated that elevation of the calcination temperature of the 0.04 mol Mo-doped BST-0.6 nanopowder was not higher enough to lower or increase the T_c value of the BST samples. Such a trend was believed to be caused by the dragging of the formation of dipoles, elevation of grain boundary thickness and reduction of grain size after most of the solvent molecules and other impurities were removed (Rahman et al., 2016; Saeed et al., 2015a). This is usually illustrated using the Internal Barrier Layer Capacitor (IBLC) model for perovskites showing reduction of dielectric constant with elevation of calcination temperature (Equation 4.8).

$$\varepsilon_r = \varepsilon_{\mathrm{gb}} \left(\frac{d_{\mathrm{g}}}{d_{\mathrm{gb}}}\right) \ldots\ldots\ldots\ldots\ldots\ldots\ldots\ldots\ldots\ldots \quad 4.8$$

Where $\varepsilon_{\mathrm{gb}}$ represents dielectric constant of the insulating grain boundaries, d_{g} refers to the mean grain size and d_{gb} is the mean grain boundary thickness (Rahman et al., 2016)

The elevation of calcination temperature resulted in the lowering of the respective polarization leading to the descending of the capacitance of the 0.04 mol Mo-doped BST-0.6 ((Figure 4.40 (ii) and Table 4.18). The enlargement of the grain boundary thickness supposedly suppressed the movement of the particles between the grains of 0.04 mol Mo-doped BST-0.6 pellets and hence the effect of the applied voltage was lowered. As a result, the BST sample demanded increased voltage for it to be polarized and generate the charges, hence, the capacitance decreased. Thus, for a Mo-doped BST-0.6 nanopowder samples to be applied as a dielectric material of a capacitor with elevated capacitance, lower calcination temperature was believed to be the convenient temperature. Such a phenomenon applies when the Internal Barrier Layer Capacitor (IBLC) model for perovskites is taken in to account (Rahman et al., 2016).

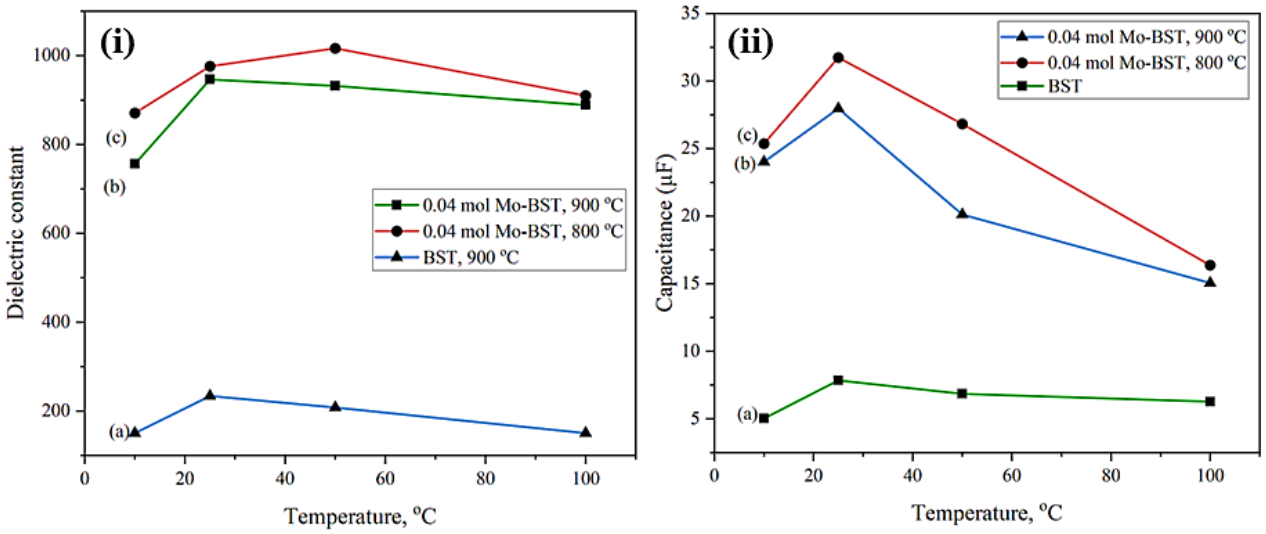

FIGURE 4.40 (i) The dielectric constant and (ii) capacitance as a function of temperature for (a) BST-0.6 calcined at 900 °C (b) 0.04 mol Mo-doped BST-0.6 calcined at 900 °C (c) 0.04 mol Mo-doped BST-0.6 calcined at 800 °C, all sintered at 1000 °C

The variation of calcination temperature form 800 °C to 900 °C has also been resulted in elevation of dielectric constant of 0.04 mol Se-doped BST-0.6 at a frequency of 1 MHz (Figure 4.41 (i)). This was in opposite to the 0.04 mol Mo-doped $Ba_{0.6}Sr_{0.4}TiO_3$ sample (Table 4.18). Such a change is believed to occur following the increased average crystal size, crystallinity and uniformity of the particles of the 0.04 mol Se-doped BST-0.6 after most of the solvent molecules and other impurities were removed during sintering (H. Xu et al., 2022).

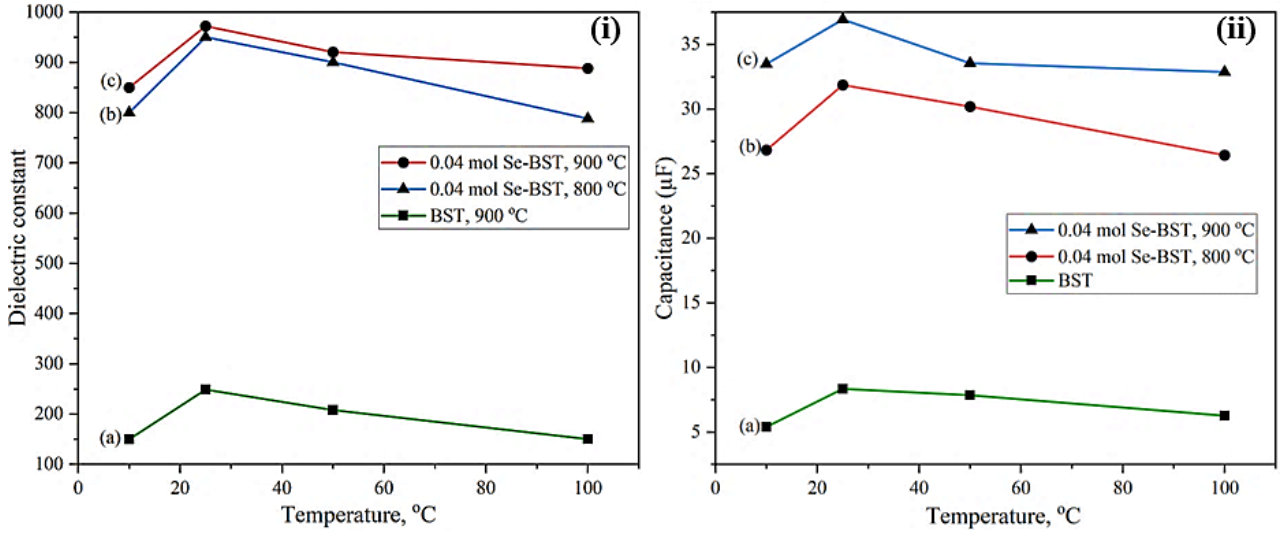

FIGURE 4.41 The (i) The dielectric constant and (ii) capacitance as a function of temperature for (a) BST-0.6 (b) 0.04 mol Se-doped BST-0.6 calcined at 800 °C (c) 0.04 mol Se-doped BST-0.6 calcined at 900 °C and sintered at 1000 °C

The capacitance of the 0.04 mol Se-doped BST-0.6 increased as the calcination temperature was changed from 800 °C to 900 °C (Figure 4.41 (ii)) unlike the 0.04 mol Mo-doped BST-0.6 sample

(Table 4.18). Here, it was expected that more removal of impurities and enhancement of crystallinity was followed as the calcination temperature was elevated from 800 ^{o}C to 900 ^{o}C. Such phenomenon was supposed to be followed by the readily available dipoles and hence more charges were stored at a minimized voltage. Afterwards, an eventual increase in capacitance of the 0.04 mol Se-doped BST-0.6 was noticed with alteration of the calcination temperature from 800 ^{o}C to 900 ^{o}C.

Increasing the calcination temperature from 800 ^{o}C to 900 ^{o}C brought about an increase in the dielectric constant of 0.04 mol (Mo, Se) co-doped BST-0.6 at a frequency of 1 MHz (Figure 4.42 (i)). Such an increase in dielectric constant was analogous with the Se-doped BST-0.6 (Table 4.18) but opposite to the Mo-doped BST-0.6 sample. This trend was believed to be caused by the increased uniformity of the arrangement of the particles after the solvent molecules and other impurities were minimized to a higher extent. It might also be due to the lowering of the grain boundary sizes as the calcination temperature altered from 800 ^{o}C to 900 ^{o}C. Thus, altering the calcination temperature to a higher amount for a (Mo, Se) co-doped BST-0.6 nanopowder was advised to be proper in utilizing it as a part of a capacitor with higher dielectric constant value.

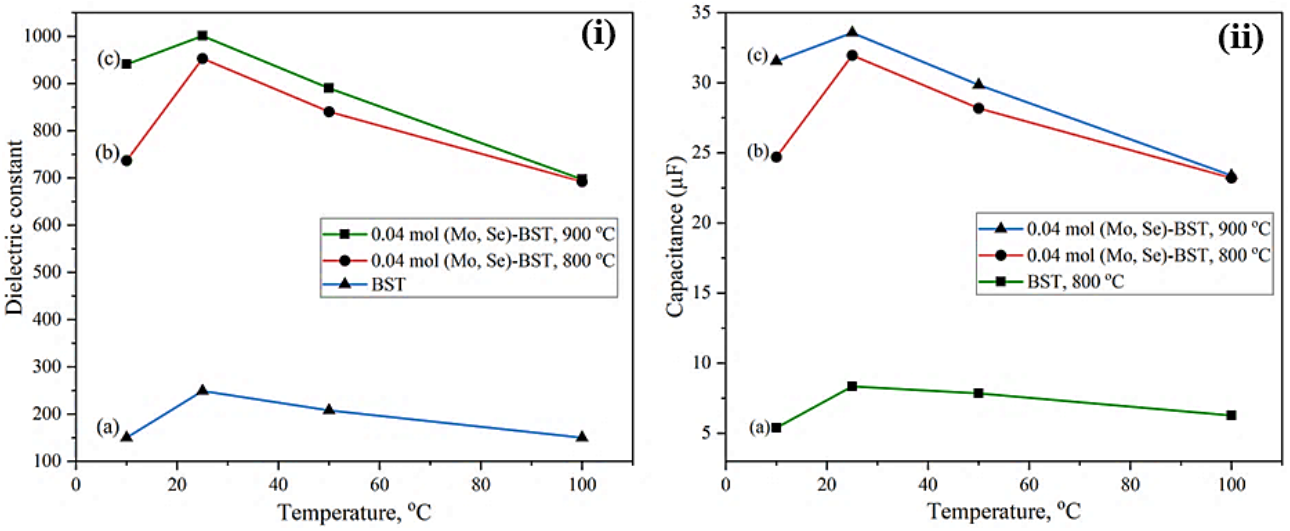

FIGURE 4.42 The (i) dielectric constant and (ii) capacitance as a function of temperature for (a) BST-0.6 (b) 0.04 mol (Mo, Se) co-doped BST-0.6 calcined at 800 ^{o}C (c) 0.04 mol (Mo, Se) co-doped BST-0.6 calcined at 900 ^{o}C and sintered at 1000 ^{o}C

Elevation of the calcination temperature had a positive influence on the extent of polarization which led to the elevated capacitance (Figure 4.42 (ii)) of the BST-0.6 nanomaterial following the simultaneous addition of the 0.04 mol of Mo^{6+} and 0.04 mol of Se^{4+} ions to the BST-0.6 base material. This was emerged as a complementary trend with the Se- BST-0.6 samples (Table 4.18). The increment in calcination temperature from 800 ^{o}C to 900 ^{o}C of the 0.04 mol (Mo, Se) co-doped BST-0.6 nanopowder caused the removal impurities and enhancement of the crystallinity of the

sample. Hence, the formation of dipoles became easy through the application of lower voltage which ultimately increased the capacitance of the 0.04 mol (Mo, Se) co-doped BST-0.6 pellets sintered at 1000 ^{o}C as compared to the BST-0.6 base material.

Two representative sintering temperatures (1000 ^{o}C and 1100 ^{o}C) and one depictive doped BST sample (0.04 mol doped BST-0.6) were employed to evaluate the impact of sintering temperature variation on the dielectric constant and capacitance of the BST samples. All the Mo-doped BST-0.6 and Se-doped BST-0.6, and their co-doped BST-0.6 samples possessed enhanced dielectric constant and capacitance as sintering temperatures was altered from 1000 ^{o}C to 1100 ^{o}C. Change of the sintering temperature of the 0.04 mol Mo-doped BST-0.6 pellets from 1000 ^{o}C to 1100 ^{o}C driven an elevated dielectric constant due to the increased density and reduction of cracks which directed to the evolution of more oxygen vacancies and space charge polarization (Figure 4.43 (i), Table 4.18). By accumulating charges at the insulating grain boundary, the space charge polarization produced by applying the electric field increased the dielectric constant. Furthermore, the loss of oxygen causes the generation of oxygen vacancies at high sintering temperatures leading to elevated dielectric constant. This has proved the assumption that the change of sintering temperature of the pellets alters the dielectric properties of BST perovskite samples (Balachandran et al., 2011; Tick et al., 2008).

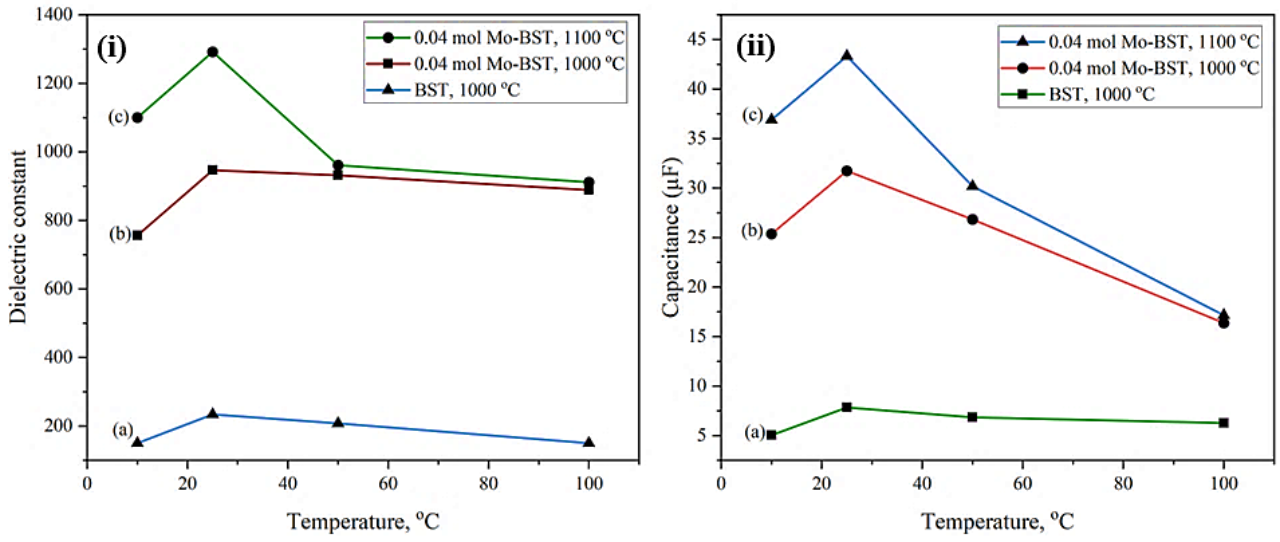

FIGURE 4.43 The (i) dielectric constant and (ii) capacitance as a function of temperature for (a) BST-0.6 sintered at 1000 ^{o}C (b) 0.04 mol Mo-doped BST-0.6 sintered at 1000 ^{o}C and (c) 0.04 mol Mo-doped BST-0.6 sintered at 1100 ^{o}C and calcined at 900 ^{o}C

The elevation of the dielectric constant with sintering temperature became a driving force for the increase in capacitance of the 0.04 mol Mo-doped BST-0.6 (Figure 4.43 (ii), Table 4.18). This is mainly due to the increase in the amount of accumulated charges as a result of enhanced

polarization of the 0.04 mol Mo-doped BST-0.6 pellets. The reduced cracks and higher density of the 0.04 mol Mo-doped BST-0.6 at the higher sintering temperature apparently afforded simple and enhanced generation of more charges. The elevated sintering temperature of the 0.04 mol Mo-doped BST-0.6 pellets caused easy and simultaneous movements of higher number of dipoles requiring lower amount of voltage. Thus, the number of charges accumulated in the 0.04 mol Mo-doped BST-0.6 pellets at larger sintering temperature was higher which finally brought about an elevated capacitance. Therefore, in good agreement with many other doped BST samples, sintering the Mo-doped BST-0.6 pellets at increased temperature was treated as desirable for the BST sample to be applied as a dielectric component of capacitors of enhanced capacitance. This was found in a similar trend with previously disclosed works (Balachandran et al., 2011; Tick et al., 2008).

The change of sintering temperature of the 0.04 mol Se-doped BST-0.6 pellets from 1000 to 1100 ^{o}C derived an elevated dielectric constant (Figure 4.44 (i)) due to the increased density as well as crystallinity accompanied by the reduction of cracks and defects that elevated the rate of polarization (Arya et al., 2003; Balachandran et al., 2011). Here, more dipoles were able to be formed at a time at a relatively increased sintering temperature. Consequently, higher sintering temperature of the 0.04 mol Se-doped BST-0.6 pellets resulted in the larger amount of charges stored in the 0.04 mol Se-doped BST-0.6 samples which brought about increased capacitance (Figure 4.44 (ii)). Such a result matched with many other doped BST samples of varied sintering temperature (Table 4.18).

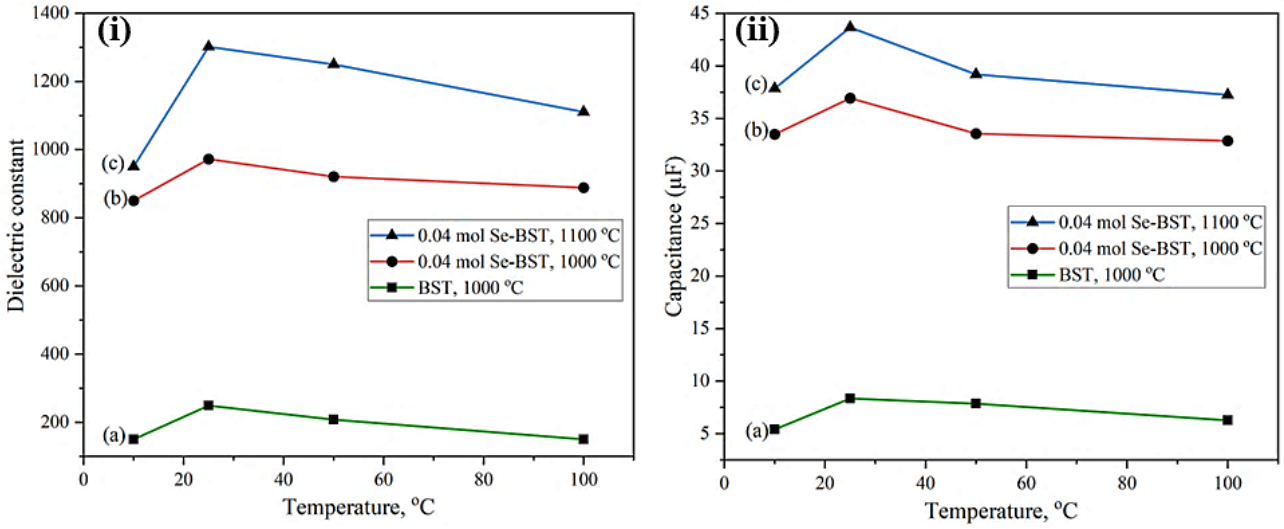

FIGURE 4.44 The (i) dielectric constant and (ii) capacitance as a function of temperature for (a) BST-0.6 sintered at 1000 ^{o}C (b) 0.04 mol Se-doped BST-0.6 sintered at 1000 ^{o}C (c) 0.04 mol Se-doped BST-0.6 sintered at 1100 ^{o}C and calcined at 800 ^{o}C

A change in the sintering temperature of the 0.04 mol (Mo, Se) co-doped BST-0.6 pellets from 1000 ℃ to 1100 ℃ provided an elevated maximum dielectric constant (Figure 4.45 (i)) due to the

greater crystallinity, increased density, and reduction of cracks (Balachandran et al., 2011; Gatea & Naji, 2018) in the same way as the 0.04 mol Mo-doped BST-0.6 0.04 mol Se-doped BST-0.6 (Table 4.18). The joined effect of both Mo^{6+} and Se^{4+} ions on the dielectric constant became more significant where the highest value was obtained for the (Mo, Se) co-doped BST-0.6 pellets sintered at 1100 ^{o}C (Table 4.18).

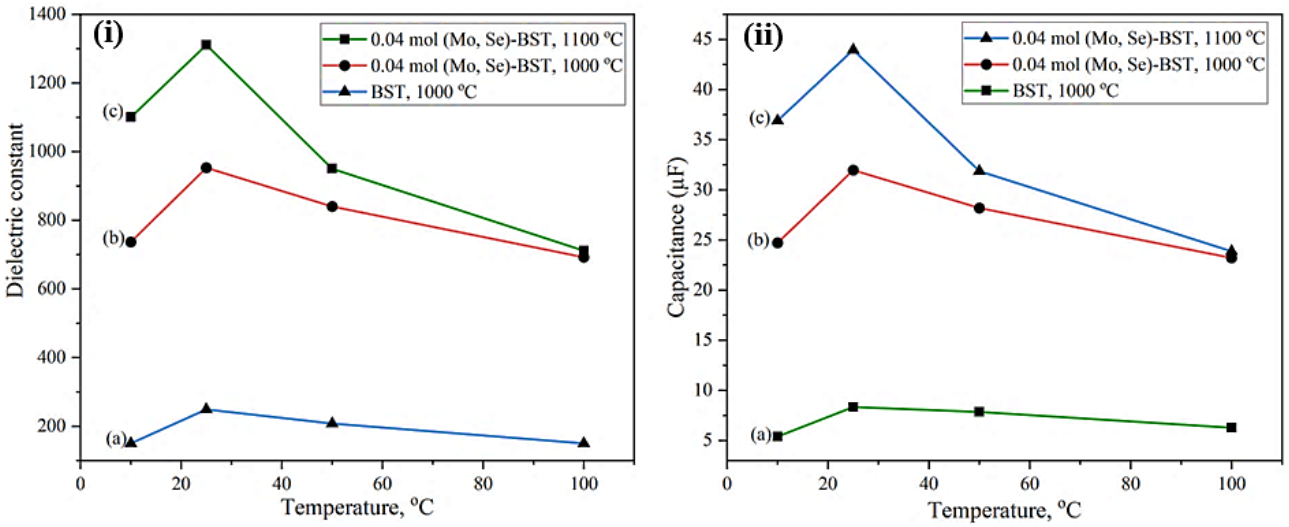

FIGURE 4.45 The (i) dielectric constant and (ii) capacitance as a function of temperature for (a) BST-0.6 sintered at 1000 ^{o}C (b) 0.04 mol (Mo, Se) co-doped BST-0.6 sintered at 1000 ^{o}C and (c) 0.04 mol (Mo, Se) co-doped BST-0.6 sintered at 1100 ^{o}C and calcined at 800 ^{o}C

As a result, the increase in dielectric constant with the sintering temperature resulted in increased capacitance of the 0.04 mol (Mo, Se) co-doped BST-0.6 pellets with higher sintering temperature as compared to the 0.04 mol (Mo, Se) co-doped BST-0.6 sintered at lower temperature and the pristine BST-0.6 pellets (Figure 4.45 (ii)). This is mainly due to the combined effect of both Mo^{6+} and Se^{4+} ions on the BST host material. A maximum capacitance was acquired for the 0.04 mol (Mo, Se) co-doped BST-0.6 in relative to the corresponding values of the Mo-doped BST-0.6 and Se-doped BST-0.6 samples (Table 4.18).

Table 4.18 - The effect of altering calcination temperature and sintering temperature on the dielectric constant and capacitance of the BST-0.6 (BST) samples

Samples	Calcination temperature (^oC)	Sintering temperature (^oC)	Maximum dielectric constant	Maximum capacitance (μF)	Reported Maximum dielectric constant from reference	Reference
BST	800	1000	248.80	8.34	130	(Upadhyay et al., 2015)
		1100	253.45	9.21	232	(Qin et al., 2007)
	900	1000	233.80	7.84		
0.04 mol Mo-BST	800	1000	1016.40	31.73	870	(Chong et al., 2004)
		1100	1291.95	43.32		
	900	1000	946.30	27.96		
0.04 mol Se-BST	800	1000	950.31	31.86	486	(Luo et al., 2016)
		1100	1301.95	43.66		
	900	1000	972.29	36.93		
0.04 mol (Mo, Se)-BST	800	1000	953.00	31.95	630	(Zhang et al., 2009)
		1100	1311.00	43.96		
	900	1000	1000.89	33.56		

4.3.2 Dielectric loss analysis

The dielectric loss values of the BST samples were studied within the test temperatures of 10 ^oC to 125 ^oC where a common lowering of the values has been obtained after the incorporation of the dopants in to BST-0.6 nanomaterial and at elevated sintering temperature (Table 4.19). For instance, Mo^{6+} ions resisted the reduction of Ti^{4+} to Ti^{3+} through neutralization of the donor activity of the oxygen vacancies. The Mo^{6+} ions carry extra positive charges which counterbalanced the negative charges of the oxygen vacancies after the Ti^{4+} ions of BST were substituted in the ABO_3 perovskite structure. Besides, Mo^{6+} is an acceptor dopant where it was expected to lower the dielectric loss of BST as other such dopants do (Zhou et al., 2010). This caused the lowering of mobile electrons which could be the reason for the minimum dielectric loss of the 0.06 mol Mo-doped BST-0.6 to be smaller than the BST-0.6 with the elevation of the amount of Mo^{6+} ions (Table 4.19). This phenomenon is clearly observed in Figure 4.46 where the respective least dielectric loss values of the BST samples were obtained at 100 ^oC.

Thus, at 100 ^oC the conductivity loss of the BST-0.6 samples was lower and hence the resistivity was higher. This was supported by the fact that the number of charges was decreased at higher temperature which was indicated by the reduced dielectric constant of the BST-0.6 samples at the higher temperature. Such a trend of lowering of dielectric loss was consistent with the previously

reported works (Joshi & Cole, 2000; Khardazi et al., 2022; Eswaramoorthi, 2015). Moreover, the minimum dielectric loss of the Mo-doped BST-0.6 attained here is smaller than that of announced work (Shalu et al., 2022). It has also met the demand for the Mo-doped BST-0.6 to be used in a capacitor (dielectric loss < 0.1).

The dielectric loss of BST-0.6 decreased at higher temperature due to the decreased number of extra electrons as a result of lowering of conductivity agreeing with a previously reported work on Al_2O_3 doped BST-0.6 (Liang, 2003). Ultimately, increase in dielectric loss at higher temperature was observed due to the increment of conductivity and hence conductivity loss of the BST samples.

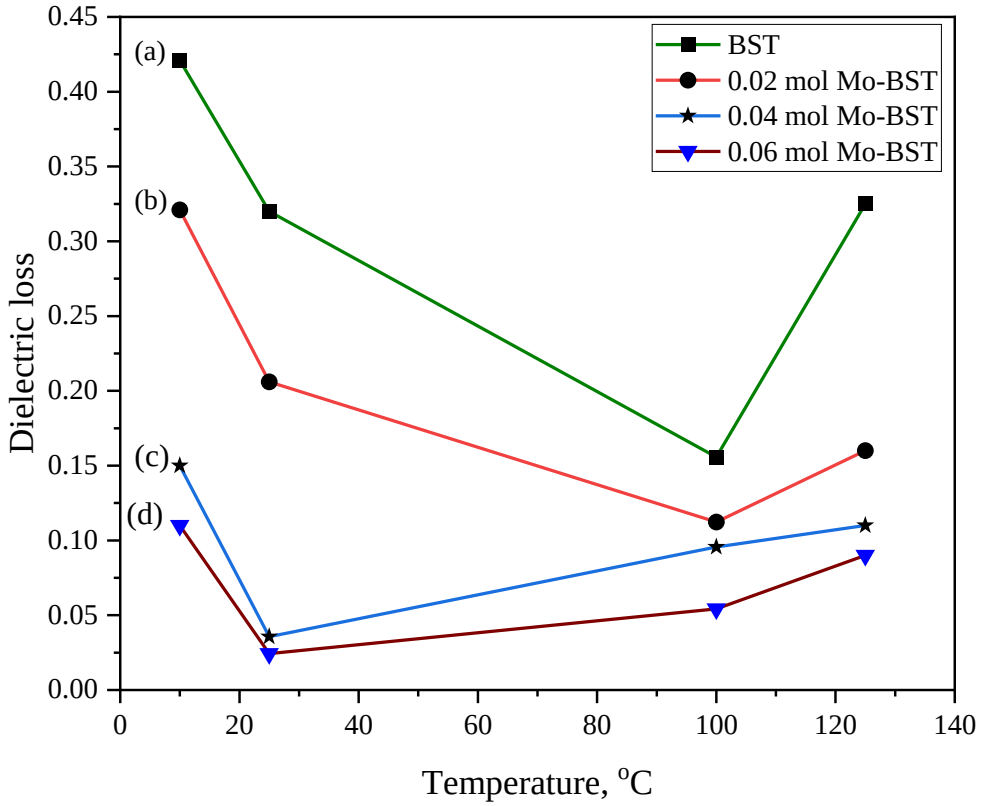

FIGURE 4.46 The dielectric loss as a function of temperature for (a) BST-0.6 (b) 0.02 mol Mo-doped BST-0.6 (c) 0.04 mol Mo-doped BST-0.6 (d) 0.06 mol Mo-doped BST-0.6 calcined at 900 ^oC and sintered at 1000 ^oC

The Se^{4+} ions carry extra positive charges that counter balance negative charges of the oxygen vacancies after Sr^{2+} ions of BST-0.6 were substituted by Se^{4+} ions in the ABO_3 perovskite structure. Moreover, the excess positive charges of Se^{4+} ions counter balance and block the movement of the extra electrons obtained from the distortion of the TiO_6 octahedral arrangement. This resulted in the reduction of extra electrons causing the minimum dielectric loss (Figure 4.47) for the 0.02 mol, 0.04 mol and 0.06 mol Se-doped BST-0.6 to be smaller than the undoped BST and the Mo-doped BST-0.6 (Table 4.19). This was found in a similar fashion with the previously reported woks (Joshi &

Cole, 2000; Khardazi et al., 2022; Eswaramoorthi, 2015; Xiao et al., 2011). The least dielectric loss value of the 0.06 mol Se-doped BST is lower than some formerly announced works (Fan et al., 2010; Qian et al., 2018). Besides, it met the requirement of the Se-doped BST-0.6 to be utilized in a capacitor application where the dielectric loss needs to be less than 0.1 (Nagaraj et al., 1999). Furthermore, the increase in dielectric loss with temperature is attributed to the elevation in the conductivity at higher temperature that directed the larger dielectric loss (Chen et al., 2015).

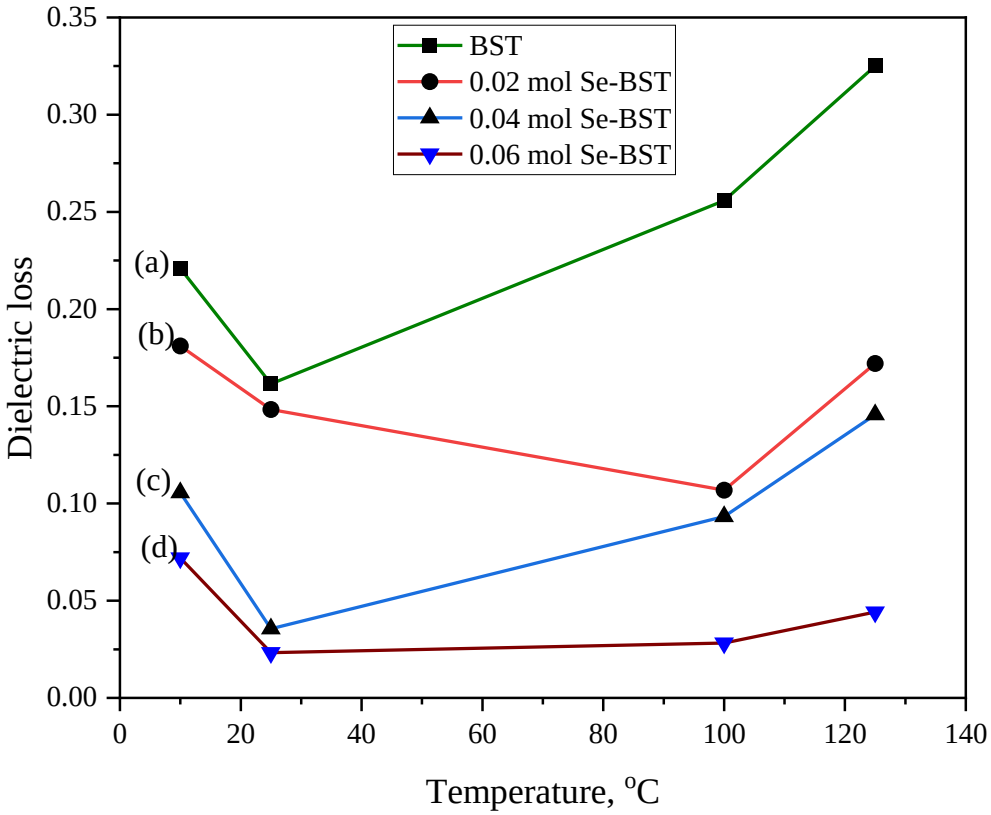

FIGURE 4.47 The dielectric loss as a function of temperature for (a) BST-0.6 (b) 0.02 mol mol Se-doped BST-0.6 (c) 0.04 mol Se-doped BST-0.6 (d) 0.06 mol Se-doped BST-0.6 calcined at 800 ^{o}C and sintered at 1000 ^{o}C

The simultaneous addition of the Mo^{6+} and Se^{4+} co-dopants affected the dielectric loss of BST. They became the major driving forces for acquiring the smallest dielectric loss value of the 0.06 mol (Mo, Se) co-doped BST-0.6 as compared to BST-0.6 (Figure 4.48, Table 4.19). The Mo^{6+} prohibited the reduction of Ti^{4+} to Ti^{3+} through the neutralization of the donor activity of the oxygen vacancies. Moreover, the Mo^{6+} ions have excess positive charges and balance the negative charges of the oxygen vacancies leading to the lowering of electrons (Xiao et al., 2011). The Mo^{6+} ions were believed to pin the oxygen vacancies which forces the dielectric loss to be reduced (Qiu et al., 2022).

The Mo^{6+} and Se^{2+} ions were also believed to captivate and counter balance the mobile electrons among the Ti^{4+} ions after replacing the Ti^{4+} ions of the ABO_3 perovskite structure which resulted in the diminished dielectric loss. The Se^{4+} donor dopant was also expected to minimize the impact of oxygen vacancies on the dielectric loss by prohibiting the formation of new defects in the crystal structure of the (Mo, Se) co-doped BST samples (Zhou et al., 2009). This matched with the previously reported works (Joshi & Cole, 2000; Khardazi et al., 2022; Eswaramoorthi, 2015).

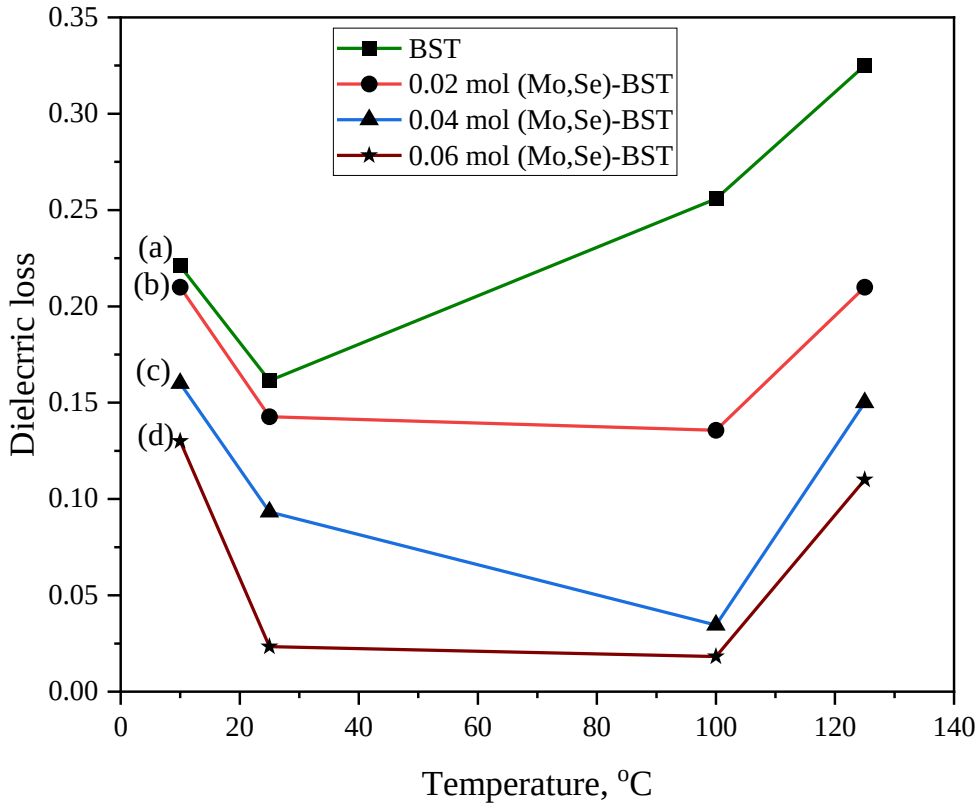

FIGURE 4.48 The dielectric loss as a function of temperature for (a) BST-0.6 (b) 0.02 mol (Mo, Se) co-doped BST-0.6 (c) 0.04 mol (Mo, Se) co-doped BST-0.6 (d) 0.06 mol (Mo, Se) co-doped BST-0.6 calcined at 800 ^{o}C and sintered at 1000 ^{o}C

The minimum dielectric loss value of the 0.06 mol (Mo, Se) co-doped BST-0.6 was found to be smaller (Table 4.19) as to some already disclosed works (Jaidka et al., 2022; Xinxin Liu et al., 2022; Qian et al., 2018). This value was also lower than the minimum dielectric loss value of 0.06 mol Mo-doped BST-0.6 and 0.06 mol Se-doped BST-0.6 samples (Table 4.19). Such a trend was analogous with the respective dielectric constant and capacitance of the BST-0.6 samples. Further, the 0.06 mol (Mo, Se) co-doped BST-0.6 satisfied the requirement for the (Mo, Se) co-doped BST-0.6 to be applied in a capacitor (dielectric loss < 0.1) (Nagaraj et al., 1999). This was taken as an additional confirmatory data to the dielectric constant and capacitance of the Mo, Se) co-doped

BST-0.6 sample so that the sample was validated to be utilized as a convenient component of a capacitor.

Table 4.19 - The minimum dielectric loss of undoped as well as Mo, Se and their co-doped BST-0.6 (BST) samples

Samples	Calcination temperature (^oC)	Sintering temperature (^oC)	Minimum dielectric loss after addition of dopants				Reported minimum dielectric loss (reference)	Reference
			0.00 mol	0.02 mol	0.04 mol	0.06 mol		
BST	800	1000	0.1614	-	-	-	0.1700	(Xiao et al. , 2011)
	900	1000	0.1557	-	-	-		
Mo-BST	900	1000	0.1557	0.1600	0.0356	0.0243	0.0380	(Liu et al., 2012)
Se-BST	800	1000	0.1614	0.1068	0.0356	0.0232	0.0320	(Qin et al., 2007)
Mo, Se-BST	800	1000	0.1614	0.1357	0.0346	0.0182	0.0300	(Oh et al., 2010)

Altering calcination temperature of the BST samples changed the respective dielectric loss of the samples. Increasing calcination temperature from 800 ^oC to 900 ^oC has increased the dielectric loss of 0.04 mol Mo-doped BST-0.6 at higher temperature (Figure 4.49). This was mainly due to the formation of dislocation as well as defects at the higher temperature in between the grains of the 0.04 mol Mo-doped BST-0.6 (Xu et al., 2022). The increment of dielectric loss with the calcination temperature has been correlated with the lowering of dielectric constant for the Mo-doped BST-0.6. Similar trend of elevation of the dielectric loss of Mo-doped BST as a result of increase in the calcination temperature has been reported by Balachandran (R. Balachandran et al., 2011).

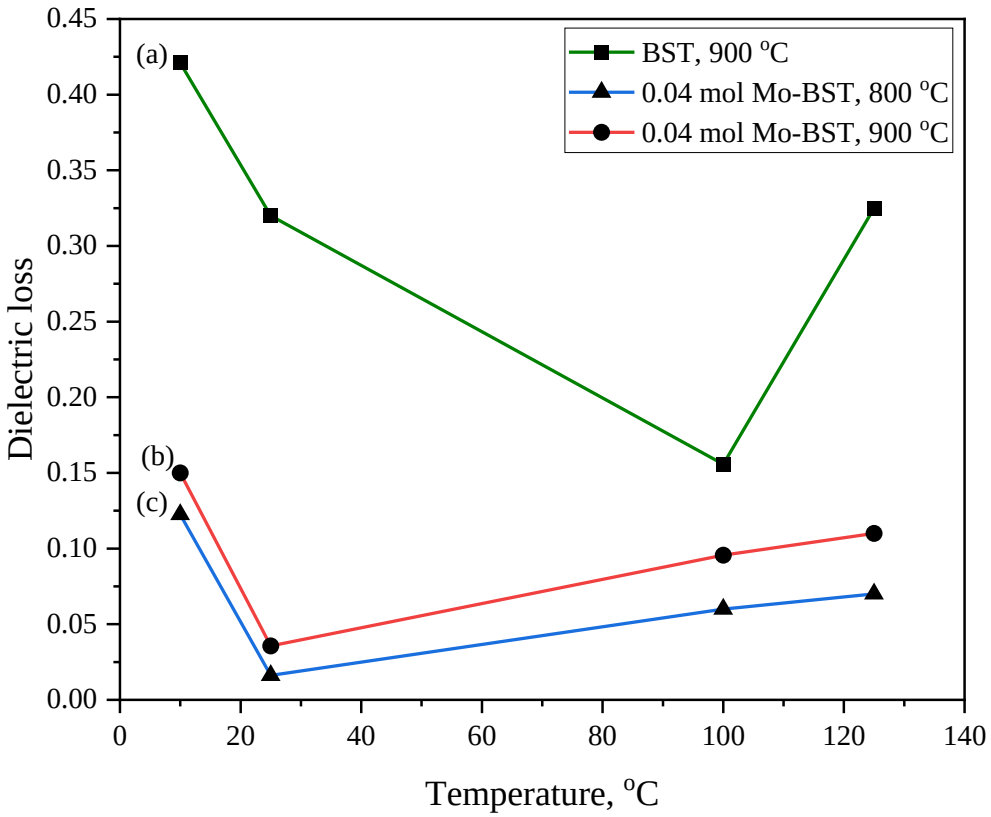

FIGURE 4.49 The dielectric loss as a function of temperature for (a) BST-0.6 (b) 0.04 mol Mo-doped BST-0.6 calcined at 900 °C (c) 0.04 mol Mo-doped BST-0.6 calcined at 800 °C and sintered at 1000 °C

Increasing the calcination temperature of the process from 800 °C to 900 °C has resulted in the reduction of the dielectric loss of 0.04 mol Se-doped BST-0.6 (Figure 4.50, Table 4.20) to a stable minimum value possible. Such a change of the dielectric loss was driven by the increased movement of Se^{4+} at higher temperature which led to a higher extent of trapping of the extra electrons. This agreed with elevation of the dielectric constant at higher calcination temperature which led to the conclusion that the Se-doped BST-0.6 nanopowder synthesized at a relatively higher calcination temperature is preferably selected so as to enhance the capacitive application of the material. Such an aspect could also be caused by the elevation of resistivity and lowering of the conductivity loss of the Se-doped BST-0.6 nanopowder at a comparably increased calcination temperature. The reduction of dielectric loss following the increment in calcination temperature was analogous with a previously reported work (Kakumani et al., 2016b).

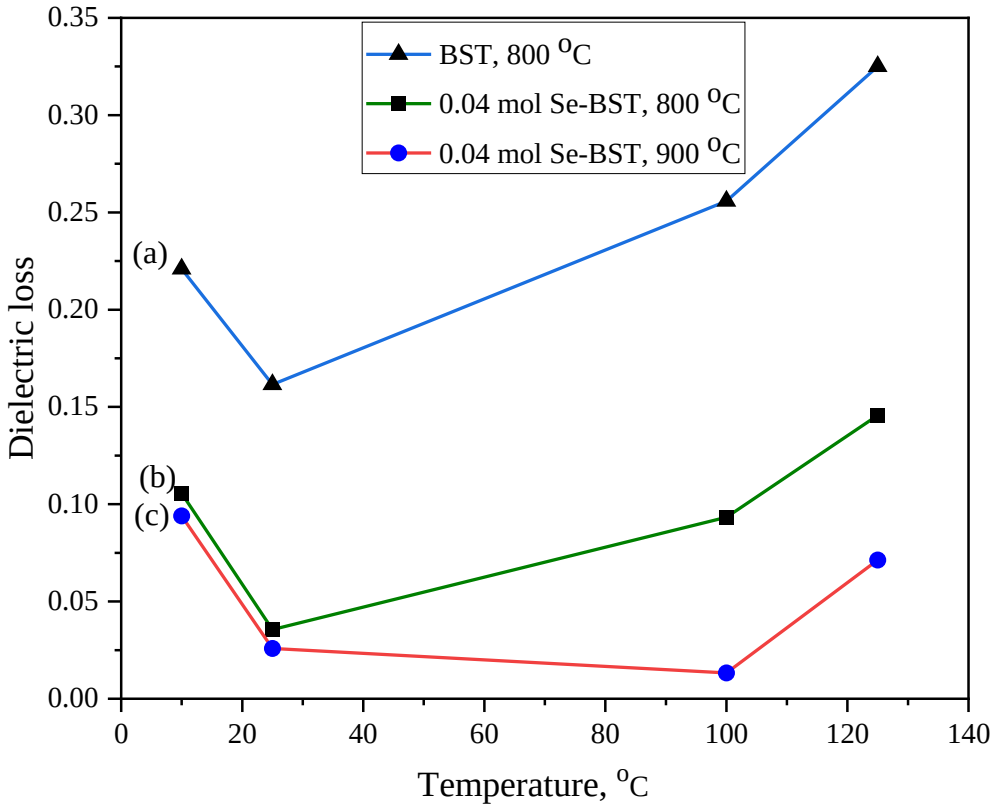

FIGURE 4.50 The dielectric loss as a function of temperature for (a) BST-0.6 (b) 0.04 mol Se-doped BST-0.6 calcined at 800 °C (c) 0.04 mol Se-doped BST-0.6 calcined at 900 °C and sintered at 1000 °C

Varying the calcination temperature of 0.04 mol (Mo, Se) co-doped BST-0.6 samples from 800 °C to 900 °C made the respective dielectric loss to be lowered (Figure 4.51, Table 4.20) which could be due to the lowering of defects and hence supported the increment of the dielectric constant. It was considered as the summed effects of altering calcination temperatures of both 0.04 mol Mo-doped BST-0.6 and Se-doped BST-0.6 pellet samples. Besides, intrinsic oxygen vacancies are produced in the 0.04 mol (Mo, Se) co-doped BST after high-temperature calcination in air (Equation 4.9). Afterwards, the concentration of free carriers (electrons) was decreased, because the dopant ions have additional negative charges that balance out the positive charge of the oxygen vacancies. Finally, lower dielectric loss resulted from the reduction in electron concentration (Attar et al., 2017). This has been found in a similar trend with a previously reported work (Kakumani et al., 2016).

$$O_0 \rightarrow V_O^{\bullet\bullet} + 2e + {}^1/_2\, O_2 \uparrow \quad \text{..... 4.9}$$

Where $V_O^{\bullet\bullet}$ represented the intrinsic oxygen vacancies

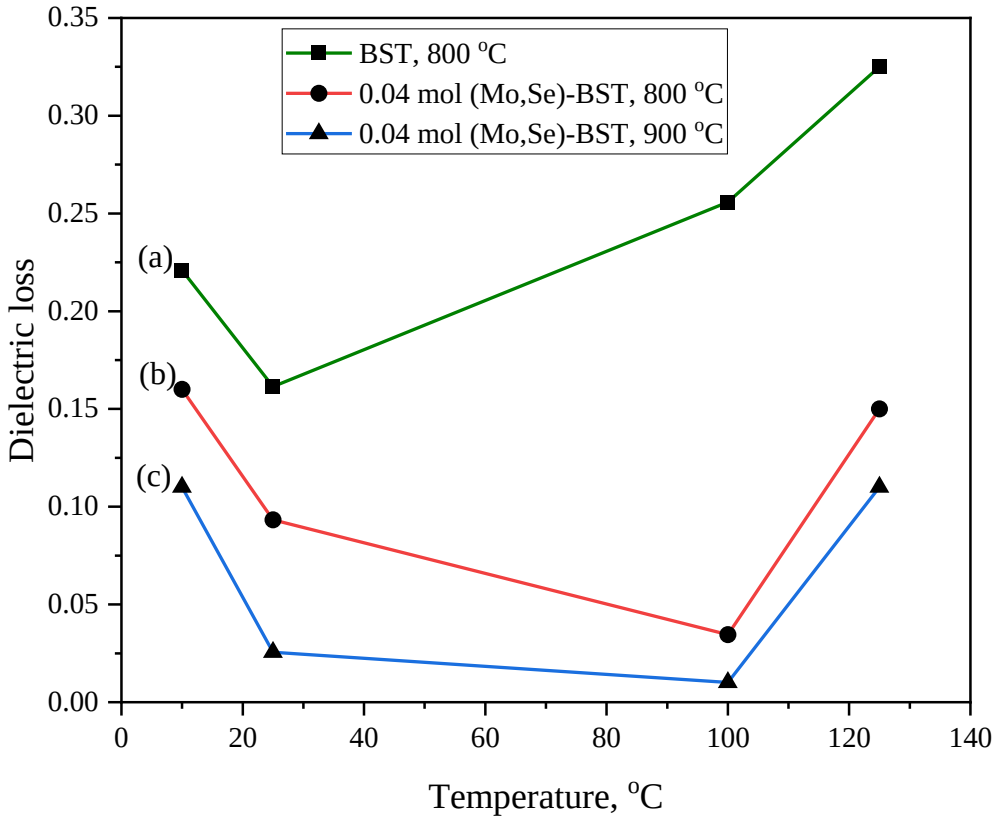

FIGURE 4.51 The dielectric loss as a function of temperature for (a) BST-0.6 (b) 0.04 mol (Mo, Se) co-doped BST-0.6 calcined at 800 °C and (c) 0.04 mol (Mo, Se) co-doped BST-0.6 calcined at 900 °C and sintered at 1000 °C

To study the effect of variation of sintering temperature on the dielectric loss of the BST samples, two representative temperatures (1000 °C and 1100 °C) and one depictive doped BST sample (0.04 mol) were adopted. Thus, complementing the effect of sintering temperature on the dielectric constant of the Mo-doped BST-0.6, Se-doped BST-0.6 and (Mo, Se) co-doped BST-0.6 samples, increasing sintering temperature of the BST pellets caused lowering of their respective dielectric loss values (Table 4.20). Hence, the dielectric loss decreased as the sintering temperature was increased. It was resulted from the smaller conduction loss and higher resistivity of the Mo-doped BST-0.6 BST pellets (Figure 4.52) (Mao et al., 2011). Therefore the higher sintering temperature results in an improved dielectric properties or capacitive application of the Mo-doped BST-0.6 perovskite material (Balachandran et al., 2011).

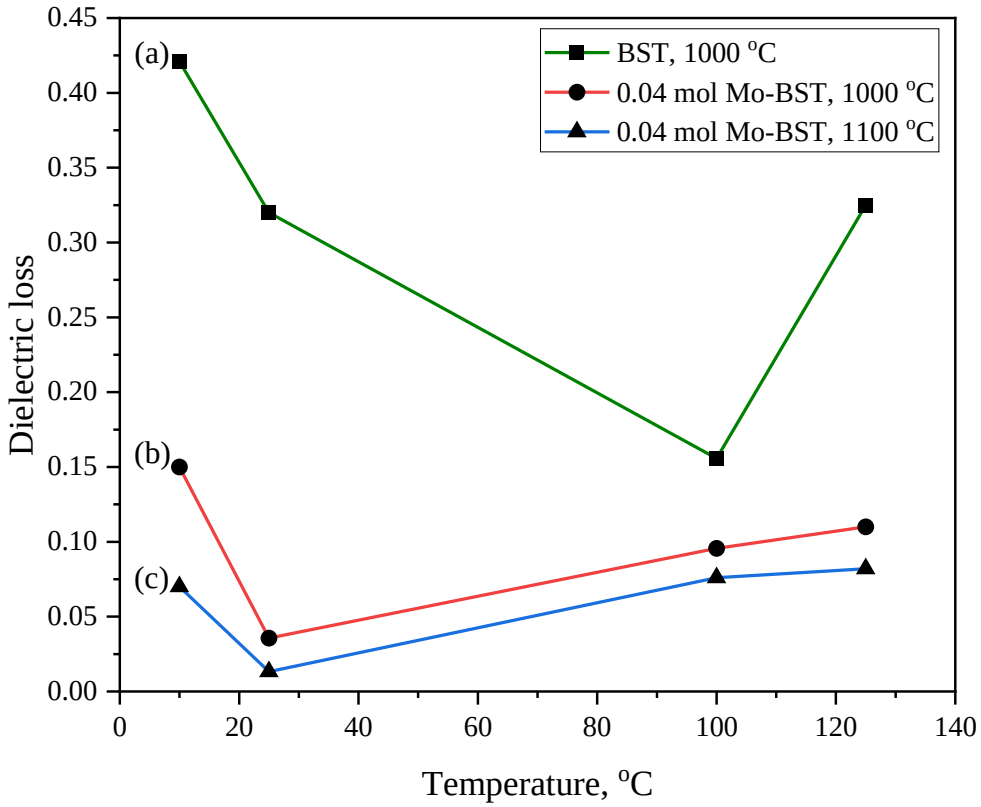

FIGURE 4.52 The dielectric loss as a function of temperature for (a) BST-0.6 sintered at 1000 °C (b) 0.04 mol Mo-doped BST-0.6 sintered at 1000 °C and (c) 0.04 mol Mo-doped BST-0.6 sintered at 1100 °C and calcined at 900 °C

Changing the sintering temperature of the 0.04 mol Se-doped BST-0.6 sample pellets from 1000 °C to 1100 °C has been resulted in the reduction of dielectric loss (Figure 4.53) due to the increased density and reduction of cracks and defects, supporting the elevation of the respective dielectric constant values. At the elevated sintering temperature, the impurities were supposed to be reduced more where conductivity loss were diminished with elevated resistivity. Such a phenomenon was in a good agreement with the FT-IR and XRD data of the 0.04 mol Se-doped BST-0.6 nanopowder. The increase in the dielectric loss with the higher measuring temperature was mainly due to thermal effect on the conductivity of the pellets where increase in temperature results in the elevated conductivity and dielectric loss (Balachandran et al., 2011). The minimum dielectric loss value of the 0.04 mol Se-doped BST-0.6 pellets noted at a sintering temperature of 1100 °C was lower than the corresponding value of the 0.04 mol Mo-doped BST-0.6 pellets but higher than the value for the (Mo, Se) co-doped BST-0.6 pellets (Table 4.20).

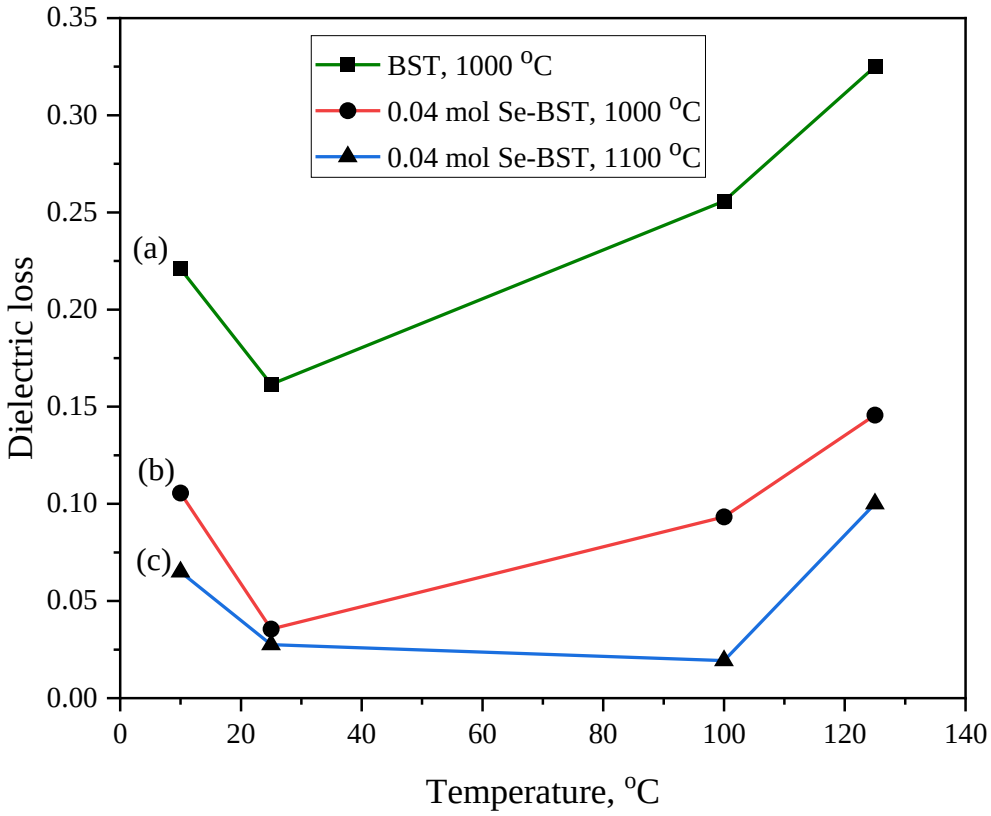

FIGURE 4.53 The dielectric loss as a function of temperature for (a) BST-0.6 sintered at 1000 °C (b) 0.04 mol Se-doped BST-0.6 sintered at 1000 °C (c) 0.04 mol Se-doped BST-0.6 sintered at 1100 °C and calcined at 800 °C

Increasing the sintering temperature of the 0.04 mol (Mo, Se) co-doped BST-0.6 sample pellets from 1000 °C to 1100 °C caused the lowering of the respective dielectric loss (Figure 4.54) in the same manner as the Mo-doped BST-0.6 pellets and the Se-doped BST-0.6 pellets (Table 4.20). This could be motivated by the elevation of density, decreasing of cracks and increasing of resistivity of the (Mo, Se) co-doped BST-0.6 (Balachandran et al., 2011). It was also supposed to be resulted from the reduction of secondary phase components which were minimized at higher temperature agreeing with the FT-IR and XRD data (Teoh et al., 2009). This might be possibly the reason why the 0.04 mol (Mo, Se) co-doped BST-0.6 pellets have shown the least dielectric loss value as compared to the Mo-doped BST-0.6 and Se-doped BST-0.6 pellets which were sintered at the same temperature with (Mo, Se) co-doped BST-0.6 pellets (Table 4.20).

Therefore, higher sintering temperature was supposed to be a favourable condition for the enhancement of the capacitive application of the Mo-doped BST, Se-doped BST and their composite co-doped BST samples.

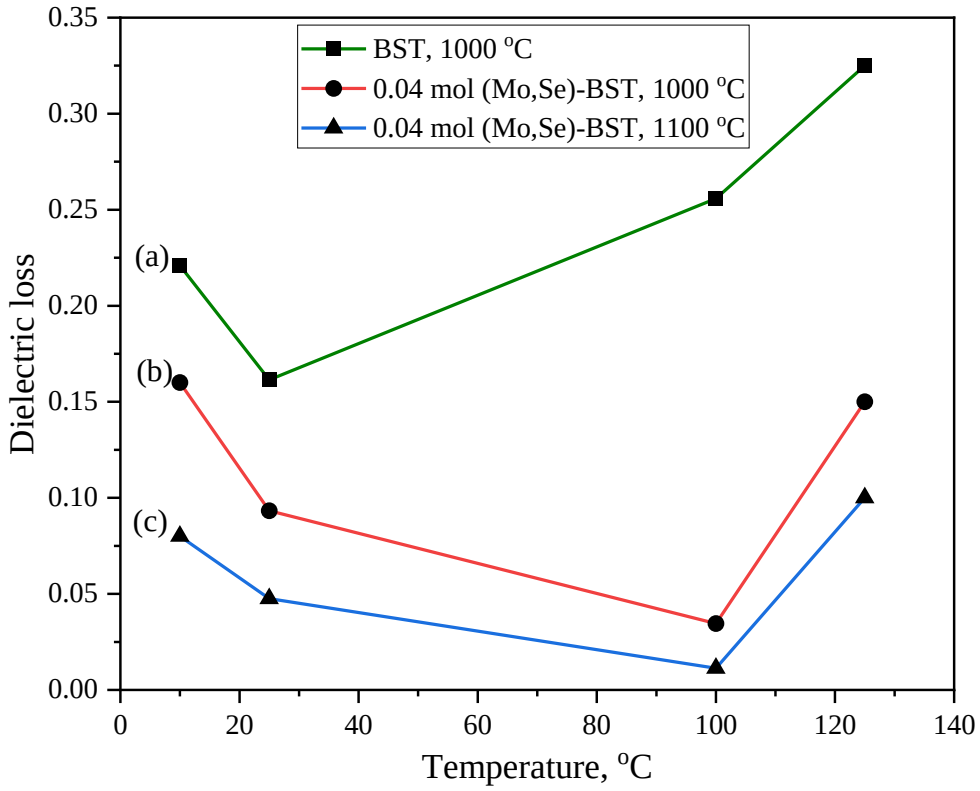

FIGURE 4.54 The dielectric loss of (a) BST-0.6 sintered at 1000 °C (b) 0.04 mol (Mo, Se) co-doped BST-0.6 sintered at 1000 °C (c) 0.04 mol (Mo, Se) co-doped BST-0.6 sintered at 1100 °C and calcined at 800 °C

Table 4.20 - The effect of altering calcination temperature and sintering temperature on the dielectric loss of the BST-0.6 (BST) samples

Samples	Calcination temperature (°C)	Sintering temperature (°C)	Minimum dielectric loss	Reported minimum dielectric loss (reference)	Reference
BST	800	1000	0.1614	0.1700	(Xiao et al., 2011)
		1100	0.1423		
	900	1000	0.1557		
0.04 mol Mo-BST	800	1000	0.0162	0.0190	(Cole et al., 2001)
		1100	0.0132		
	900	1000	0.0356	-	-
0.04 mol Se-BST	800	1000	0.0356	-	-
		1100	0.0193	0.0210	(Kim et al., 2014)
	900	1000	0.0132	0.0136	(Gao et al., 2008)
(Mo, Se)-BST	800	1000	0.0346	0.0410	(Oh et al., 2010)
		1100	0.0113	0.0250	(Zhang et al., 2009)
	900	1000	0.0100	0.0170	(Song et al., 2014)

5. CONCLUSIONS AND RECOMMENDATIONS

5.1 Conclusions

A slow rate injection *sol-gel* method was effective in synthesizing the Mo, Se and their co-doped BST nanopowders at calcination temperatures of 800 ^{o}C and 900 ^{o}C which were identified from the respective TGA-DSC data of the BST samples. The formation of cubic shaped doped $Ba_{0.6}Sr_{0.4}TiO_3$ and tetragonal shaped doped $Ba_{0.77}Sr_{0.23}TiO_3$ samples have been confirmed using XRD, Raman spectroscopy, EDS, and XPS. Both possessed varied morphological and microstructural properties. Incorporation of Mo to BST caused lowering of the average crystal size and average grain size accompanied by the formation of agglomerates and more porous surface while the addition of Se has resulted in the reduction and elevation of both the average crystal size and average grain size with the agglomerated arrangement of particles and less porous surface. Furthermore, (Mo, Se) co-doped BST has shown higher average crystal size and increased average grain size as well as less porous surface with agglomerated particles, as compared to the pristine BST.

All the dopants have yielded varied microstructural and morphological properties of BST which ultimately resulted in elevated dielectric constant and capacitance along with lowered dielectric loss values of BST. Hence, the doped BST has shown enhanced capacitive performance compared to BST. Elevation of sintering temperature was resulted in the increased dielectric constant and capacitance as well as reduced dielectric loss of all the BST samples due to the removal of cracks and impurities accompanied by the formation of denser arrangement of particles of BST. The (Mo, Se) co-doped BST has shown the highest average dielectric constant and capacitance values as compared to the Mo-doped BST and Se-doped BST samples. It has also the least dielectric loss values as compared to the other doped BST samples. Hence, the (Mo, Se) co-doped BST samples were believed to be the better options for the capacitor application as compared to the Mo-doped BST and Se-doped BST nanomaterials.

5.2 Recommendations

No optimization was done for the amount of dopants, calcination temperature, and sintering temperature. Therefore, it is very important to find the best conditions for the BST samples to perform well as a dielectric component of the capacitor. On the other hand, leakage current density is an additional property of a dielectric material where doping should be resulted in lower leakage current density value. Hence, measuring the leakage current density of the pristine BST and doped BST samples so as to quantify any wasted amount of current/charge in unknown pathways is also

recommended as a future work. In addition, the dielectric strength of the pristine and doped BST samples shall also be determined so as to know the maximum voltage needed to polarize the materials. Finally, this research was aimed at preparing and testing the capacitors using undoped and doped BST pellets, it is recommended to go for the large scale production of such capacitors to be used in any of the devices. This helps to transform the laboratory level technology to an industry level.

REFERENCES

Abboudi, M., Oudghiri-Hassani, H., Al Wadaani, F., Rakass, S., Al Ghamdi, A., & Messali, M. (2018). Enhanced catalytic reduction of para-nitrophenol using α-MoO_3 molybdenum oxide nanorods and stacked nanoplates as catalysts prepared from different precursors. *Journal of Taibah University for Science, 12*(2), 133-137.

Abd Mutalib, M., Rahman, M. A., Othman, M. H. D., Ismail, A. F., & Jaafar, J. (2017). Scanning Electron Microscopy (SEM) and Energy-Dispersive X-Ray (EDX) Spectroscopy. 161-179.

Abdel Maksoud, M. I. A., Fahim, R. A., Shalan, A. E., Abd Elkodous, M., Olojede, S. O., Osman, A. I., Rooney, D. W. (2021). *Advanced materials and technologies for supercapacitors used in energy conversion and storage: a review* (Vol. 19): Springer International Publishing.

Aguadero, A., Pérez-Coll, D., Alonso, J. A., Skinner, S. J., & Kilner, J. (2012). A new family of Mo-doped srcoo 3-delta; Perovskites for application in reversible solid state electrochemical cells. *Chemistry of Materials, 24*(14), 2655-2663.

Ahmed, A., Goldthorpe, I. A., & Khandani, A. K. (2015). Electrically tunable materials for microwave applications. *Applied Physics Reviews, 2*(1), 011302.

Alkathy, M. S., Joseph, A., & Raju, K. J. (2016). Dielectric properties of Zr substituted barium strontium titanate. *Materials Today: Proceedings, 3*(6), 2321-2328.

Alkathy, M. S., Raju, K. J., & Eiras, J. (2021). Colossal dielectric permittivity and high energy storage efficiency in barium strontium titanate ceramics co-doped with bismuth and lithium. *Journal of Physics D: Applied Physics, 54*(12), 125501.

Allen, G. C., Curtis, M. T., Hooper, A. J., & Tucker, P. M. (1973). X-ray photoelectron spectroscopy of chromium–oxygen systems. *Journal of the Chemical Society, Dalton Transactionsb*(16), 1675-1683.

Anwar, M., Hogarth, C., & Bulpett, R. (1990). An XPS study of amorphous MoO_3/SiO films deposited by co-evaporation. *Journal of materials science, 25*(3), 1784-1788.

Arita, M., Kaji, H., Fujii, T., & Takahashi, Y. (2012). Resistance switching properties of molybdenum oxide films. *Thin Solid Films, 520*(14), 4762-4767.

Arya, P. R., Jha, P., & Ganguli, A. K. (2003). Synthesis, characterization and dielectric properties of nanometer-sized barium strontium titanates prepared by the polymeric citrate precursor method. *Journal of Materials Chemistry, 13*(2), 415-423.

Asa Deepthi, K., Balachandran, R., Ong, B. H., Wong, H. Y., Tan, K., Yow, H., & Daud, Z. (2014). Phase formation and surface morphology of nickel doped Ba_{1-x} Sr_x TiO_3 ceramics prepared by *sol–gel* technique. *Materials Research Innovations, 18*(sup6), S6-453-S456-456.

Ashoka, S., Chithaiah, P., & Chandrappa, G. (2010). Studies on the synthesis of $CdCO_3$ nanowires and porous CdO powder. *Materials Letters, 64*(2), 173-176.

Assadi, M. H. N., Li, S., & Yu, A. (2013). Selecting the suitable dopants: electronic structures of transition metal and rare earth doped thermoelectric sodium cobaltate. *RSC Advances, 3*(5), 1442-1449.

Attar, A. S., Sichani, E. S., & Sharafi, S. (2017). Structural and dielectric properties of Bi-doped barium strontium titanate nanopowders synthesized by *sol–gel* method. *Journal of materials research and technology, 6*(2), 108-115.

Audebrand, N., Bourgel, C., & Louër, D. (2006). Ex-oxalate magnesium oxide, a strain-free nanopowder studied with diffraction line profile analysis. *Powder diffraction, 21*(3), 190-199.

Auromun, K., & Choudhary, R. (2020). Structural, dielectric, and electrical characteristics of selenium-modified $BiFeO_3$–$(BaSr)TiO_3$ ceramics. *Journal of Materials Science: Materials in Electronics, 31*(16), 13415-13433.

Balachandran, R., Ong, B., Wong, H., Tan, K., & Rasat, M. M. (2012). Dielectric characteristics of barium strontium titanate based metal insulator metal capacitor for dynamic random access memory cell. *Int. J. Electrochem. Sci, 7*(12), 11895.

Balachandran, R., Yow, H., Ong, B., Tan, K., Anuar, K., Teoh, W., Swaminathan, V. (2011). Phase formation and dielectric properties of $Ba_{0.5}Sr_{0.5}TiO_3$ by slow injection *sol–gel* technique. *Journal of materials science, 46*(6), 1806-1813.

Baniecki, J., Laibowitz, R., Shaw, T., Parks, C., Lian, J., Xu, H., & Ma, Q. (2001). Hydrogen induced tunnel emission in Pt/$(Ba_x Sr_{1-x}) Ti_{1+y} O_{3+z}$/Pt thin film capacitors. *Journal of Applied Physics, 89*(5), 2873-2885.

Baniecki, J., Shioga, T., & Kurihara, K. (2002). Barium strontium titanate thin film capacitors for low inductance decoupling applications. *MRS Online Proceedings Library (OPL), 748*.

Bao, Q., Wu, J., Fan, L., Ge, J., Dong, J., Jia, J., Lin, J. (2017). Electrodeposited $NiSe_2$ on carbon fiber cloth as a flexible electrode for high-performance supercapacitors. *Journal of energy chemistry, 26*(6), 1252-1259.

Bardestani, R., Patience, G. S., & Kaliaguine, S. (2019). Experimental methods in chemical engineering: specific surface area and pore size distribution measurements—BET, BJH, and DFT. *The Canadian Journal of Chemical Engineering, 97*(11), 2781-2791.

Barrett, R. L. (1962). Electronegativity chart. *Journal of Chemical Education, 39*(5), 251.

Batttisha, I. K., Farag, I. S. A., Kamal, M., Ahmed, M. A., Girgis, E., El Meleegi, H. A., & El Desouky, F. G. (2014). Structural, magnetic and dielectric properties of Fe-Co Co-doped $Ba_{0.9} Sr_{0.1} TiO_3$ prepared by *sol-gel* technique. *New Journal of Glass and Ceramics, 2014*.

Behrens, R. G., Lemons, R. S., & Rosenblatt, G. M. (1974). Vapor pressure and thermodynamics of selenium dioxide. The enthalpy of atomization of SeO_2 (g). *The Journal of Chemical Thermodynamics, 6*(5), 457-466.

Boningari, T., Inturi, S. N. R., Suidan, M., & Smirniotis, P. G. (2018). Novel one-step synthesis of nitrogen-doped TiO_2 by flame aerosol technique for visible-light photocatalysis: Effect of synthesis parameters and secondary nitrogen (N) source. *Chemical Engineering Journal, 350*, 324-334.

Bouyanfif, H., Wolfman, J., El Marssi, M., Yuzyuk, Y., Bodeux, R., Gervais, M., & Gervais, F. (2009). Combinatorial (Ba, Sr) TiO_3 thin film growth: X-ray diffraction and Raman spectroscopy. *Journal of applied physics, 106*(3), 034108.

Capsoni, D., Bini, M., Massarotti, V., Chiodelli, G., Mozzatic, M., & Azzoni, C. (2004). Role of doping and CuO segregation in improving the giant permittivity of $CaCu_3Ti_4O_{12}$. *Journal of Solid State Chemistry, 177*(12), 4494-4500.

Carlson, C., Rivkin, T., Parilla, P., Perkins, J., Ginley, D., Kozyrev, A., Pavlov, A. (2000). Large dielectric constant (ε/ε 0> 6000) $Ba_{0.4}$ $Sr_{0.6}$ TiO_3 thin films for high-performance microwave phase shifters. *Applied Physics Letters, 76*(14), 1920-1922.

Castner, D. G., & Ratner, B. D. (1990). Surface characterization of butyl methacrylate polymers by XPS and static SIMS. *Surface and interface analysis, 15*(8), 479-486.

Chang, W., Horwitz, J. S., Carter, A. C., Pond, J. M., Kirchoefer, S. W., Gilmore, C. M., & Chrisey, D. B. (1999). The effect of annealing on the microwave properties of $Ba_{0.5}$ $Sr_{0.5}$ TiO_3 thin films. *Applied Physics Letters, 74*(7), 1033-1035.

Chastain, J., & King Jr, R. C. (1992). Handbook of X-ray photoelectron spectroscopy. *Perkin-Elmer Corporation, 40*, 221.

Chen, C., Zhuang, H., Zhu, X., Zhang, D., Zhou, K., & Yan, H. (2015). Effect of Ca substitution sites on dielectric properties and relaxor behavior of Ca doped barium strontium titanate ceramics. *Journal of Materials Science: Materials in Electronics, 26*(4), 2486-2492.

Chen, M., Shen, Z., Tang, S., Shi, W., Cui, D., & Chen, Z. (2000). Stress effect on Raman spectra of Ce-doped BaTiO3 films. *Journal of Physics: Condensed Matter, 12*(31), 7013.

Chen, S.-Y., Wang, H.-W., & Huang, L.-C. (2001). Electrical properties of Mg/La, Mg/Nb co-doped ($Ba_{0.7}Sr_{0.3}$) TiO_3 thin films prepared by metallo-organic deposition method. *Japanese Journal of Applied Physics, 40*(8R), 4974.

Chen, Y.-W., Li, L., D'Ulivo, A., & Belzile, N. (2006). Extraction and determination of elemental selenium in sediments—A comparative study. *Analytica Chimica Acta, 577*(1), 126-133.

Chen, Z., Xinyou, H., Hao, G., & Chunhua, G. (2007a). Effect of Y_2O_3 and Dy_2O_3 on Dielectric Properties of $Ba_{0.7}$ $Sr_{0.3}$ TiO_3 Series Capacitor Ceramics. *Journal of Rare Earths, 25*, 197-200.

Chinnathambi, M., Sakthisabarimoorthi, A., Jose, M., & Robert, R. (2021). Study of the Electrical and Dielectric behaviour of selenium doped CCTO ceramics prepared by a facile *sol-gel* route. *Materials Chemistry and Physics, 272*, 124970.

Chong, K., Kong, L., Chen, L., Yan, L., Tan, C., Yang, T., Osipowicz, T. (2004). Improvement of dielectric loss tangent of Al_2O_3 doped $Ba_{0.5}Sr_{0.5}TiO_3$ thin films for tunable microwave devices. *Journal of Applied Physics, 95*(3), 1416-1419.

Chou, X., Zhai, J., Sun, J., & Yao, X. (2007). Dielectric properties of Mg-doped $Ba_{0.6}Sr_{0.4}TiO_3$ ceramic sintered at a low temperature with Li_2O additve. *Ferroelectrics, 356*(1), 13-18.

Chu, A., & Braatz, P. (2002). Comparison of commercial supercapacitors and high-power lithium-ion batteries for power-assist applications in hybrid electric vehicles: I. Initial characterization. *Journal of Power Sources, 112*(1), 236-246.

Ćirković, J., Vojisavljević, K., Nikolić, N., Vulić, P., Branković, Z., Srećković, T., & Branković, G. (2015). Dielectric and ferroelectric properties of BST ceramics obtained by a hydrothermally assisted complex polymerization method. *Ceramics International, 41*(9), 11306-11313.

Cole, M., Hubbard, C., Ngo, E., Ervin, M., Wood, M., & Geyer, R. (2002). Structure–property relationships in pure and acceptor-doped Ba_{1-x} Sr_x TiO_3 thin films for tunable microwave device applications. *Journal of applied physics, 92*(1), 475-483.

Cole, M., Joshi, P., & Ervin, M. (2001). La doped Ba_{1-x} Sr_xTiO_3 thin films for tunable device applications. *Journal of Applied Physics, 89*(11), 6336-6340.

Cole, M., Joshi, P., Ervin, M., Wood, M., & Pfeffer, R. (2000). The influence of Mg doping on the materials properties of $Ba_{1-x}Sr_xTiO_3$ thin films for tunable device applications. *Thin Solid Films, 374*(1), 34-41.

Das, A., Saxena, V., Bhardwaj, A., Rabha, S., Pandey, L. M., & Dobbidi, P. (2022). Microstructural, interfacial, biological and electrical activity in sputtered Hydroxyapatite-Barium strontium titanate bilayered thin films. *Surfaces and Interfaces, 31*, 102063.

Datta, R., Haque, F., Mohiuddin, M., Carey, B., Syed, N., Zavabeti, A., Ou, J. (2017). Highly active two dimensional α-MoO_{3-x} for the electrocatalytic hydrogen evolution reaction. *Journal of Materials Chemistry A, 5*(46), 24223-24231.

Deb, B., & Ghosh, A. (2012). Correlation of structure and dielectric properties of silver selenomolybdate glasses. *Journal of Applied Physics, 112*(2), 024102.

Dong, W., Liu, J., Li, S., Bi, K., Gu, M., Yuan, H., & Luo, Y. (2020). The dielectric and flexoelectric properties of Mg^{2+}/K^{+} doped BST films. *Ceramics International, 46*(16), 25164-25170.

Doveren, H. v., & Verhoeven, J. T. (1980). XPS spectra of Ca, Sr, Ba and their oxides. *Journal of Electron Spectroscopy and Related Phenomena, 21*(3), 265-273.

Emadi, F., Nemati, A., Hinterstein, M., & Adabifiroozjaei, E. (2019). Microstructural, optical, and electrical characteristics of Ni/C doped BST thin films. *Ceramics International, 45*(5), 5503-5510.

Eswaramoorthi, V., Sebastian, S., & Williams, R. V. (2015). Influence of Ga doping on the structural, optical and electrical properties of $Ba_{0.6}Sr_{0.4}TiO_3$ thin films. *International Research Journal of Science and Technology, 4*, 86-91.

Fan, Y., Yu, S., Sun, R., Li, L., Yin, Y., & Du, R. (2010). Microstructure and electrical properties of $Ba_{0.7}Sr_{0.3}(Ti_{1-x}Zr_x)O_3$ thin films prepared on copper foils with *sol–gel* method. *Thin Solid Films, 518*(14), 3610-3614.

Fan, Y., Yu, S., Sun, R., Li, L., Yin, Y., Wong, K.-W., & Du, R. (2010a). Microstructure and electrical properties of Mn-doped barium strontium titanate thin films prepared on copper foils. *Applied Surface Science, 256*(22), 6531-6535.

Farahani, H., Wagiran, R., Yurchenko, O., & Urban, G. A. (2018). Barium Strontium Titanate Humidity Sensor: Impact of Doping on the Structural and Electrical Properties. *Proceedings, 2*(13), 1007-1007.

Folkesson, B., & Sundberg, P. (1987). A reinvestigation of the binding energy versus atomic charge relation for oxygen from X-ray photoelectron spectroscopy. *Spectroscopy letters, 20*(3), 193-200.

Fowler, D., & Miller, D. (1992). Orthorhombic $YBa_2Cu_3O_7$ Cleaved Single Crystal by XPS. *Surface Science Spectra, 1*(4), 381-392.

Gaabour, L. (2020). Effect of selenium oxide nanofiller on the structural, thermal and dielectric properties of CMC/PVP nanocomposites. *Journal of Materials Research and Technology, 9*(3), 4319-4325.

Gao, L., Guan, Z., Huang, S., Liang, K., Chen, H., & Zhang, J. (2019). Enhanced dielectric properties of barium strontium titanate thin films by doping modification. *Journal of Materials Science: Materials in Electronics, 30*(14), 12821-12839.

Gao, L., Yang, X., Zhang, L., & Yao, X. (2008). Structure and dielectric properties of Ca-doped ($Ba_{0.7}Sr_{0.3}$) TiO_3 thin films fabricated by *sol–gel* method. *Journal of Electroceramics, 21*, 645-648.

Garbassi, F., Gila, L., & Proto, A. (1995). XPS study of metallocene based catalysts for the polymerization of ethylene. *Journal of Molecular Catalysis A: Chemical, 101*(3), 199-209.

Gatea, H., & Naji, I. (2018). Impact of sintering temperature on structural and dielectric properties of barium strontium titanate prepared by *sol-gel* method. *Journal of Ovonic Research Vol, 14*(6), 467-474.

Giridharan, N., Jayavel, R., & Ramasamy, P. (2001). Structural, Morphological and Electrical Studies on Barium Strontium Titanate Thin Films Prepared by *Sol-Gel* Technique. *Crystal Research and Technology: Journal of Experimental and Industrial Crystallography, 36*(1), 65-72.

Godara, S. K., Kaur, V., Chuchra, K., Narang, S., Singh, G., Verma, S., Sood, A. K. (2021). Impact of Zn^{2+}-Zr^{4+} substitution on M-type Barium Strontium Hexaferrite's structural, surface morphology, dielectric and magnetic properties. *Results in Physics, 22*, 103892.

Gonbeau, D., Guimon, C., Pfister-Guillouzo, G., Levasseur, A., Meunier, G., & Dormoy, R. (1991). XPS study of thin films of titanium oxysulfides. *Surface Science, 254*(1-3), 81-89.

González, M. B., Wu, A., & Vilarinho, P. M. (2006). Influence of Solvents on the Microstructure and dielectric properties of $Ba_{0.5}Sr_{0.5}TiO_3$ thin films prepared by a diol-based *sol−gel* process. *Chemistry of materials, 18*(7), 1737-1744.

Gopinath, C., Subramanian, S., Huth, M., & Adrian, H. (1994). Comparative photoemission studies of $Bi_{2-x}Pb_xSr_2Ca_{n-1}Cu_nO_{2n+4+y}$ (n= 2, 3). *Journal of Electron Spectroscopy and Related Phenomena, 70*(1), 61-71.

Goswami, D. Y., & Kreith, F. (2007). *Energy conversion*: CRC press.

Gougeon, P., Gall, P., & Potel, M. (2010). $Tl_2Mo_9Se_{11}$. *Acta Crystallographica Section E: Structure Reports Online, 66*(8), i56-i56.

Ha, T., Kim, J., Kim, S., & Kim, W.-J. (2006). Enhanced tunability and electrical properties of $Ba_{0.7}Sr_{0.3}TiO_3$ thin films by Cu doping. *Integrated Ferroelectrics, 86*(1), 77-84.

Han, F., Meng, G., Zhou, F., Song, L., Li, X., Hu, X., Wei, B. (2015). Dielectric capacitors with three-dimensional nanoscale interdigital electrodes for energy storage. *Science advances, 1*(9), e1500605.

Hofman, W., Hoffmann, S., & Waser, R. (1997). Dopant influence on dielectric losses, leakage behaviour, and resistance degradation of $SrTiO_3$ thin films. *Thin Solid Films, 305*(1-2), 66-73.

Hu, W., Yang, C., Zhang, W., & Qiu, Y. (2005). Dielectric Characteristics of *Sol-Gel*-Derived BST/BSLaT/BST Multilayer. *Journal of Sol-Gel Science and Technology, 36*(3), 249-255.

Ianculescu, A.-C., Vasilescu, C.-A., Trupina, L., Vasile, B. S., Trusca, R., Cernea, M., Nicoară, A. (2016). Characteristics of Ce^{3+}-doped barium titanate nanoshell tubes prepared by template-mediated colloidal chemistry. *Journal of the European Ceramic Society, 36*(7), 1633-1642.

Ianculescu, A., Berger, D., Viviani, M., Ciomaga, C. E., Mitoseriu, L., Vasile, E., Crişan, D. (2007). Investigation of $Ba_{1-x}Sr_xTiO_3$ ceramics prepared from powders synthesized by the modified Pechini route. *Journal of the European Ceramic Society, 27*(13-15), 3655-3658.

Ikawa, H., Yamada, T., Kojima, K., & Matsumoto, S. (1991). X-ray photoelectron spectroscopy study of high-and low-temperature forms of zirconium titanate. *Journal of the American Ceramic Society, 74*(6), 1459-1462.

Iro, Z. S., Subramani, C., & Dash, S. (2016). A brief review on electrode materials for supercapacitor. *Int. J. Electrochem. Sci, 11*(12), 10628-10643.

Itoh, T., Tashiro, S., & Igarashi, H. (1993). Fabrication of multilayer barrier layer capacitors with semiconducting (Ba, Sr) TiO_3 ceramics. *Japanese journal of applied physics, 32*(9S), 4261.

Jacob, R., Nair, H. G., & Isac, J. (2015). Impedance spectroscopy and dielectric studies of nanocrystalline iron doped barium strontium titanate ceramics. *Processing and Application of Ceramics, 9*(2), 73-79.

Jaidka, S., Aggarwal, A., Chopra, S., & Singh, D. P. (2022). Significantly Enhanced Dielectric Behavior of Polyvinylidene Fluoride-Barium Strontium Titanate Flexible Nanocomposite Thick Films: Role of Electric Field-Induced Effects. *Journal of Electronic Materials, 51*(9), 5429-5439.

Jiang, F., Yin, L., Feng, G., Wu, C., Tan, J., Wu, Q., Jiang, W. (2022). Ultrasonic-driven polycondensation nonaqueous precipitation synthesis of $Ba_{0.7}Sr_{0.3}TiO_3$ ceramics. *Ceramics International, 48*(6), 8721-8725.

Jiao, T., You, C., Tian, N., Ma, L., Duan, Z., Yan, F., Zhao, G. (2022). High tunability and low loss via establishing an internal electric field in $LiFe_5O_8/Ba_{0.6}Sr_{0.4}TiO_3$ composite films using chemical solution deposition method. *Applied Surface Science, 590*, 153112.

Jiwei, Z., Xi, Y., Xiaogang, C., Liangying, Z., & Chen, H. (2002). Direct-current field dependence of dielectric properties in B_2O_3-SiO_2 glass doped $Ba_{0.6}$ $Sr_{0.4}$ TiO_3 ceramics. *Journal of Materials Science, 37*, 3739-3745.

Joshi, P., & Cole, M. (2000). Mg-doped $Ba_{0.6}$ $Sr_{0.4}$ TiO_3 thin films for tunable microwave applications. *Applied Physics Letters, 77*(2), 289-291.

Kakumani, A. D., Ruthramurthy, B., Wong, H. Y., Ong, B. H., Tan, K.-B., & Yow, H. K. (2016a). Microstructure and Dielectric Properties of Nickel-Doped $Ba_{0.7}Sr_{0.3}TiO_3$ Ceramics Fabricated by *Sol-gel* Method. *International Journal of Applied Ceramic Technology, 13*(1), 177-184.

Kathait, G. S., Rohilla, V., Thapliyal, P., Biswas, D., & Singh, S. (2017). Effect of different strontium content on dielectric properties of barium strontium titanate ceramic. *Int. J. Latest Technol. Eng. Manage. Appl. Sci*, *6*, 75.

Kerr, J. (1966). Bond dissociation energies by kinetic methods. *Chemical reviews*, *66*(5), 465-500.

Khardazi, S., Zaitouni, H., Asbani, B., Mezzane, D., Amjoud, M., Choukri, E., Gagou, Y. (2022). Structural, dielectric, ferroelectric and electrical properties of lead-free $Ba_{0.9}Sr_{0.1}Ti_{0.9}Sn_{0.1}O_3$ ceramic prepared by *sol–gel* method. *Materials Today: Proceedings*, *51*, 2059-2065.

Khardazi, S., Zaitouni, H., Belkhadir, S., Mezzane, D., Amjoud, M., Gagou, Y., Terenchuk, S. (2022). Improvement of the electrocaloric effect and energy storage performances in Pb-free ferroelectric $Ba_{0.9}Sr_{0.1}Ti_{0.9}Sn_{0.1}O_3$ ceramic near room temperature. *Journal of Solid State Chemistry*, *311*, 123112.

Kim, K.-T., & Kim, C.-I. (2005). The effect of Cr doping on the microstructural and dielectric properties of (Ba0. 6Sr0. 4) TiO3 thin films. *Thin Solid Films*, *472*(1-2), 26-30.

Kim, K.-T., Kim, C., Senior, D. E., Kim, D., & Yoon, Y.-K. (2014). Microwave characteristics of *sol-gel* based Ag-doped $(Ba_{0.6}Sr_{0.4})TiO_3$ thin films. *Thin Solid Films*, *565*, 172-178.

Kongtaweelert, S., Sinclair, D., & Panichphant, S. (2006). Phase and morphology investigation of $Ba_xSr_{1-x}TiO_3$ (x= 0.6, 0.7 and 0.8) powders. *Current Applied Physics*, *6*(3), 474-477.

Kostopoulou, A., Brintakis, K., Nasikas, N. K., & Stratakis, E. (2019). Perovskite nanocrystals for energy conversion and storage. *Nanophotonics*, *8*(10), 1607-1640.

Kuo, S.-Y., Liao, W.-Y., & Hsieh, W.-F. (2001). Structural ordering transition and repulsion of the giant LO-TO splitting in polycrystalline $Ba_x Sr_{1-x} TiO_3$. *Physical Review B*, *64*(22), 224103.

Leese, H. S., Tejkl, M., Vilar, L., Georgi, L., Yau, H. C., Rubio, N., Shaffer, M. S. P. (2022). High-k dielectric screen-printed inks for mechanical energy harvesting devices. *Materials Advances*, *3*(3), 1780-1790.

Li, B., Wang, C., Dou, G., Wang, Z., & Fei, W. (2017). Crystallized $Bi_{0.9}La_{0.1}Fe_{0.95}Mn_{0.05}O_3/Ba_{0.7}Sr_{0.3}Ti_{0.95}Co_{0.05}O_3$ bilayer thin films with enhanced multiferroic properties. *Applied Surface Science*, *404*, 162-167.

Li, Y., & Dou, G. (2013). Towards the implementation of memristor: A study of the electric properties of $Ba_{0.77}$ $Sr_{0.23}$ TiO_3 material. *International Journal of Bifurcation and Chaos*, *23*(12), 1350204.

Li, Y., & Qu, Y. (2009). Dielectric properties and substitution mechanism of samarium-doped Ba0.68Sr0.32TiO3 ceramics. *Materials Research Bulletin*, *44*(1), 82-85.

Liang, X.-F., Wu, W.-B., & MENG, Z.-Y. (2003). Microstructure and dielectric tunable properties of Al_2O_3-doped barium strontium titanate in the paraelectric state. *Chin. J. Inorg. Mater*, *18*(6), 1240-1244.

Liang, X., Wu, W., & Meng, Z. (2003). Dielectric and tunable characteristics of barium strontium titanate modified with Al_2O_3 addition. *Materials Science and Engineering: B, 99*(1-3), 366-369.

Liao, J., Wei, X., Xu, Z., & Wang, P. (2014). Effect of potassium-doped concentration on structures and dielectric performance of barium-strontium-titanate films. *Vacuum, 107*, 291-296.

Liu, B., Huang, Y. H., Hu, C. C., Song, K. X., & Wu, Y. J. (2019). Colossal dielectric permittivity in (Al+ Nb) co-doped $Ba_{0.4}Sr_{0.6}TiO_3$ ceramics. *Ceramics International, 45*(11), 14263-14269.

Liu, B., Li, L., Liu, X. Q., & Chen, X. M. (2016). Structural evolution of $SrLaAl_{1-x}(Zn_{0.5}Ti_{0.5})_xO_4$ ceramics and effects on their microwave dielectric properties. *Journal of Materials Chemistry C, 4*(21), 4684-4691.

Liu, H., Zhu, J., Chen, Q., Yu, P., & Xiao, D. (2012). Enhanced ferroelectric properties of Mg doped (Ba, Sr) TiO_3 thick films grown on (001) $SrTiO_3$ substrates. *Thin Solid Films, 520*(9), 3429-3432.

Liu, J., Wei, A., Zhao, X., & Zhang, H. (2011). Structural and electrical properties of Ta_2O_5 thin films prepared by photo-induced CVD. *Bulletin of Materials Science, 34*(3), 443-446.

Liu, N., Liang, R., Zhou, Z., & Dong, X. (2018). Designing lead-free bismuth ferrite-based ceramics learning from relaxor ferroelectric behavior for simultaneous high energy density and efficiency under low electric field. *Journal of Materials Chemistry C, 6*(38), 10211-10217.

Liu, X., Yuan, Y., Cao, L., Li, E., & Zhang, S. (2022). Enhanced energy storage properties with excellent stability in BST-BLZS relaxor ceramics. *Ceramics International, 48*(13), 19382-19391.

Liu, X., Zhai, Y., Xie, X., Zhou, R., Li, X., & Liu, S. (2022). Relaxation dielectric enhancement of barium strontium titanate ceramics by trace doping sodium niobate. *Materials Technology, 37*(12), 2049-2055.

Liu, Y., Nagra, A. S., Erker, E. G., Periaswamy, P., Taylor, T. R., Speck, J., & York, R. A. (2000). BaSrTiO/sub 3/interdigitated capacitors for distributed phase shifter applications. *IEEE microwave and guided wave letters, 10*(11), 448-450.

Lumpkin, G. R., & Ribbe, P. H. (1983). Composition, order-disorder and lattice parameters of olivines; relationships in silicate, germanate, beryllate, phosphate and borate olivines. *American Mineralogist, 68*(1-2), 164-176.

Luo, W., Chen, X., Fan, J., Hu, Y., Zheng, Z., & Fu, Q. (2016). Effect of Rb-doping on the dielectric and tunable properties of $Ba_{0.6}Sr_{0.4}TiO_3$ thin films prepared by *sol-gel*. *Ceramics International, 42*(15), 17229-17236.

Luo, Y. (2003). Handbook of Bond Dissociation Energies in Organic Compounds CRC. *New York*, 61.

Lv, F., Jiang, X., Zhou, L., Hong, Z., Wu, Y., & Huang, Y. (2022). Enhanced energy storage performance and theoretical understanding of the dielectric breakdown behavior for $Ba_{0.4}Sr_{0.6}TiO_3/Al_2O_3$ ceramics. *Journal of Alloys and Compounds, 923*, 166344.

Mao, C., Cao, S., Yao, C., Cao, F., Li, K., Liu, W., Reece, M. J. (2011). Effect of Sintering Atmosphere on the Microstructure and Electrical Properties of Donor-Doped Barium Strontium Calcium Titanate Pyroelectric Ceramics. *Journal of the American Ceramic Society, 94*(7), 2003-2006.

Marzeddu, S., Decima, M. A., Camilli, L., Bracciale, M. P., Genova, V., Paglia, L., oni, M. R. (2022). Physical-Chemical Characterization of Different Carbon-Based Sorbents for Environmental Applications. *Materials (Basel), 15*(20).

Masrul, M., Suprayogi, T., Diantoro, M., Fuad, A., Latifah, E., & Hidayat, A. (2019). *The effect of light irradiation on performance of photo-supercapacitor of FTO/TiO_2-ZnO-β Carotene-Quercetin/Carbon/Al/PVDF-$BaTiO_3$/Al.* Paper presented at the IOP Conference Series: Materials Science and Engineering.

Mather, R. R. (2009). Surface modification of textiles by plasma treatments. 296-317.

Mikolajick, T., Slesazeck, S., Park, M. H., & Schroeder, U. (2018). Ferroelectric hafnium oxide for ferroelectric random-access memories and ferroelectric field-effect transistors. *MRS Bulletin, 43*(5), 340-346.

Miller, J. R., & Burke, A. (2008). Electrochemical capacitors: challenges and opportunities for real-world applications. *The electrochemical society interface, 17*(1), 53.

Miller, J. R., & Simon, P. (2008). Electrochemical capacitors for energy management. *Science Magazine, 321*(5889), 651-652.

Mohamed Shameer, P., & Mohamed Nishath, P. (2019). Exploration and enhancement on fuel stability of biodiesel. 181-213.

Mohammadi, M. R., & Fray, D. J. (2011). *Sol–gel* derived nanocrystalline and mesoporous barium strontium titanate prepared at room temperature. *Particuology, 9*(3), 235-242.

Mohammadian, N., Moshaii, A., Alizadeh, A., Gharibzadeh, S., & Mohammadpour, R. (2016). Influence of perovskite morphology on slow and fast charge transport and hysteresis in the perovskite solar cells. *The journal of physical chemistry letters, 7*(22), 4614-4621.

Moon, S. E., Ryu, H. C., Kwak, M. H., Kim, Y. T., Lee, S. J., & Kang, K. Y. (2005). X-Band Phased Array Antenna Using Ferroelectric (Ba, Sr) TiO_3 Coplanar Waveguide Phase Shifter. *ETRI journal, 27*(6), 677-684.

Mustikasari, A. A., Diantoro, M., Mufti, N., & Suryana, R. (2018). The Effect Of Nano ZnO Morphology on Structure, Dielectric Constant, and Dissipation Factor Of CA-Nano ZnO/ITO Films. *Jurnal Neutrino: Jurnal Fisika dan Aplikasinya*, *10*(2), 59-68.

Nagaraj, B., Sawhney, T., Perusse, S., Aggarwal, S., Ramesh, R., Kaushik, V., Balu, V. (1999). (Ba, Sr) TiO_3 thin films with conducting perovskite electrodes for dynamic random access memory applications. *Applied Physics Letters, 74*(21), 3194-3196.

Nan, H.-s., Hu, X.-y., & Tian, H.-w. (2019). Recent advances in perovskite oxides for anion-intercalation supercapacitor: a review. *Materials Science in Semiconductor Processing, 94*, 35-50.

Nandanwar, S., Lee, M. W., Borkar, S., Cho, J. H., Tarte, N. H., & Kim, H. J. (2020). Synthesis, Characterization, and Anti-Algal Activity of Molybdenum-Doped Metal Oxides. *Catalysts, 10*(7), 805.

Nefedov, V., Firsov, M., & Shaplygin, I. (1982). Electronic structures of $MRhO_2$, MRh_2O_4, $RhMO_4$ and Rh_2MO_6 on the basis of X-ray spectroscopy and ESCA data. *Journal of Electron Spectroscopy and Related Phenomena, 26*(1), 65-78.

Netterfield, R. P., Martin, P., Pacey, C., Sainty, W., McKenzie, D., & Auchterlonie, G. (1989). Ion-assisted deposition of mixed TiO_2-SiO_2 films. *Journal of applied physics, 66*(4), 1805-1809.

Novianty, I., Seminar, K. B., Irzaman, & Budiastra, I. W. (2018). Analysis of saturation currents and barrier height of Ta_2O_5 doped based on $Ba_{0.5}Sr_{0.5}TiO_3$ photodiode. *Integrated Ferroelectrics, 192*(1), 164-177.

Oh, J., Delprat, S., Ismail, M., Chaker, M., Djoumessi, E. E., & Wu, K. (2010). Improvement of $Ba_{0.\ 5}Sr_{0.\ 5}TiO_3$ thin films microwave properties using codoping with Mg-W and Al-W. *Integrated Ferroelectrics, 112*(1), 24-32.

Ohbayashi, K., Yoshida, K., Anma, M., Takai, Y., & Hayakawa, H. (1992). Bismuth valence studies of as-grown superconducting Bi-Sr-Ca-Cu-O thin films with Tc (zero) from 98 K to 66 K. *Japanese journal of applied physics, 31*(7B), L953.

Padmini, E., & Ramachandran, K. (2019). Electrical properties of Mo-doped $SrTiO_3$ prepared by solid state reaction method. *Materials Research Express, 6*(11), 115919.

Pandolfo, A. G., & Hollenkamp, A. F. (2006). Carbon properties and their role in supercapacitors. *Journal of Power Sources, 157*(1), 11-27.

Paul, F., Binder, J., Gesswein, H., Ritzhaupt-Kleissl, H.-J., & Hausselt, J. (2009). Synthesis of doped $Ba_{0.6}Sr_{0.4}TiO_3$ ceramic powder via a *sol*–freeze-granulation and freeze-drying process. *Ceramics International, 35*(1), 479-486.

Petrov, M., Lovchinov, K., Valkov, S., & Tyutyundzhiev, N. (2020). *Soot as electrode coating for supercapacitor prototypes.* Paper presented at the Journal of Physics: Conference Series.

Pohl, R., Gilman, R., Miller, G. A., & Pachucki, K. (2013). Muonic hydrogen and the proton radius puzzle. *Annual Review of Nuclear and Particle Science, 63*, 175-204.

Pokorný, J., Pasha, U., Ben, L., Thakur, O., Sinclair, D., & Reaney, I. (2011). Use of Raman spectroscopy to determine the site occupancy of dopants in BaTiO3. *Journal of applied physics, 109*(11), 114110.

Pookmanee, P., & Phanichphant, S. (2010). Characterisation of $Ba_{0.77}Sr_{0.23}TiO_3$ powder prepared from an oxalate co-precipitation and an impregnation method. *Journal of Ceramic Processing Research, 11*(3), 384-387.

Priya Balmuchu, S., Mangalampalli, S. R. N. K., & Dobbidi, P. (2022). Dielectric spectroscopy and ferroelectric studies of multiferroic bismuth ferrite modified barium titanate ceramics for energy storage capacitor applications. *Materials Science and Engineering: B, 282*, 115791.

Puli, V. S., Pradhan, D. K., Adireddy, S., Chrisey, D. B., & Katiyar, R. S. (2017). Electric field induced weak ferroelectricity in $Ba_{0.70}Sr_{0.30}TiO_3$, ceramics capacitors. *Ferroelectrics, 516*(1), 133-139.

Qian, J., Yang, C., Han, Y., Sun, X., & Chen, L. (2018). Reduced leakage current, enhanced energy storage and dielectric properties in (Ce, Mn)-codoped $Ba_{0.6}Sr_{0.4}TiO_3$ thin film. *Ceramics International, 44*(17), 20808-20813.

Qin, W., Zhu, J., Xiong, J., Tang, J., Jie, W., Wei, X., Li, Y. (2007). Electrical behavior of Y-doped $Ba_{0.6}$ $Sr_{0.4}$ TiO_3 thin films. *Journal of Materials Science: Materials in Electronics, 18*, 1217-1220.

Qiu, J., Liu, G., Wolfman, J., & Xing, J. (2022). Electrical property modulation of $Au/Ba_{0.6}Sr_{0.4}TiO_3/La_{0.7}Sr_{0.3}MnO_3$ structure by continuous composition spread Mn doping. *Ceramics International, 48*(8), 11786-11792.

Raghupathi, K. R., Koodali, R. T., & Manna, A. C. (2011). Size-dependent bacterial growth inhibition and mechanism of antibacterial activity of zinc oxide nanoparticles. *Langmuir, 27*(7), 4020-4028.

Rahman, M. F. A., Abu, M. J., Ain, M. F., Mohamed, J. J., & Ahmad, Z. A. (2016). Effect of Calcination Temperature on Dielectric Properties of $CaCu_3Ti_4O_{12}$ Ceramics. *Procedia Chemistry, 19*, 910-915.

Rallapalli, R., Kalimi, M. R., Nirlakalla, R., & Reniguntla, P. S. (2022). Niobium oxide-activated yttrium barium titanate nanorod structured ceramics for energy storage applications. *International Journal of Applied Ceramic Technology, 19*(4), 2053-2063.

Ramana, C., Atuchin, V., Pokrovsky, L., Becker, U., & Julien, C. (2007). Structure and chemical properties of molybdenum oxide thin films. *Journal of Vacuum Science & Technology A: Vacuum, Surfaces, and Films, 25*(4), 1166-1171.

Raval, N., Maheshwari, R., Kalyane, D., Youngren-Ortiz, S. R., Chougule, M. B., & Tekade, R. K. (2019). Importance of Physicochemical Characterization of Nanoparticles in Pharmaceutical Product Development. 369-400.

Reisinger, H., & Stengl, R. (2000). *Fundamental scaling laws of DRAM dielectrics.* Paper presented at the Proceedings of the 2000 Third IEEE International Caracas Conference on Devices, Circuits and Systems (Cat. No. 00TH8474).

Rizwan, S., Umar, M., Babar, Z. U. D., Awan, S. U., & ur Rehman, M. A. (2019). Selenium-enriched flower-like of bismuth ferrite nanosheets assembly with associated magnetic properties. *AIP Advances*, *9*(5), 055025.

Rouquerol, J., Avnir, D., Everett, D., Fairbridge, C., Haynes, M., Pernicone, N., Unger, K. (1994). Guidelines for the characterization of porous solids *Studies in surface science and catalysis* (Vol. 87, pp. 1-9): Elsevier.

Saeed, A., Ruthramurthy, B., Yong, W. H., Hoong, O. B., Ban, T. K., & Kwang, Y. H. (2015a). Structural and dielectric properties of iron doped barium strontium titanate for storage applications. *Journal of Materials Science: Materials in Electronics*, *26*(12), 9859-9864.

Sawitri, R. A., Suryanti, L., Zuhri, F. U., & Diantoro, M. (2019). *Dielectric Properties of Dirt Sugarcane Sediment (DSS) Extract-$BaTiO_3$ for Organic Supercapacitors.* Paper presented at the IOP Conference Series: Materials Science and Engineering.

Shaban, N., & Bahar, M. (2017). Synthesis and Characterization of Fe and Ni Co-Doped $Ba_{0.6}Sr_{0.4}TiO_3$ Prepared by *Sol-Gel* Technique. *Journal of Theoretical and Computational Science*, *04*(02).

Shahid, M., Rasheed, M., Fatima, K., Maryam, A., Malik, F., Asghar, M., & Warsi, M. (2017). Synthesis, characterization and evaluation of ferroelectric and dielectric behavior of Ni-doped $Ba_{0.7}Sr_{0.3}TiO_3$ thin films prepared via *sol-gel* route. *Digest Journal of Nanomaterials & Biostructures (DJNB)*, *12*(4).

Shahzad, M. A., Shahid, M., Bibi, I., Khan, M. A., Nawaz, M. A., Aboud, M. F. A., Warsi, M. F. (2017). The effect of rare earth Dy^{3+} ions on structural, dielectric and electrical behavior of new nanocrystalline $PbZrO_3$ perovskites. *Ceramics International*, *43*(1), 1073-1079.

Shalu, S., & Dasgupta Ghosh, B. (2019). Synthesis, characterisation and dielectric properties of low-loss Zr-doped barium strontium titanate materials. *Advances in Applied Ceramics*, *118*(8), 451-457.

Shalu, S., Roy, S., Mukherjee, A., Bal, T., Rout, S. K., & Dasgupta Ghosh, B. (2022). Effect of Mn-doping on the morphological and electrical properties of $(Ba_{0.7}Sr_{0.3})$ $(Mn_xTi_{1-x})O_3$ materials for energy storage application. *Ceramics International*, *48*(18), 25816-25825.

Shannon, R. D. (1976). Revised effective ionic radii and systematic studies of interatomic distances in halides and chalcogenides. *Acta crystallographica section A: crystal physics, diffraction, theoretical and general crystallography, 32*(5), 751-767.

Sharma, K., Arora, A., & Tripathi, S. K. (2019). Review of supercapacitors: Materials and devices. *Journal of Energy Storage, 21*, 801-825.

Sharma, K. G., & Singh, N. R. (2013). Synthesis and luminescence properties of $CaMO_4$: Dy^{3+}(M= W, Mo) nanoparticles prepared via an ethylene glycol route. *New Journal of Chemistry, 37*(9), 2784-2791.

Sharma, P., & Bhatti, T. (2010). A review on electrochemical double-layer capacitors. *Energy Conversion and Management, 51*(12), 2901-2912.

Shkuratov, S. I., & Lynch, C. S. (2022). A review of ferroelectric materials for high power devices. *Journal of Materiomics, 8*(4), 739-752.

Simões, A. Z., Moura, F., Onofre, T., Ramirez, M., Varela, J. A., & Longo, E. (2010). Microwave-hydrothermal synthesis of barium strontium titanate nanoparticles. *Journal of Alloys and Compounds, 508*(2), 620-624.

Socrates, G. (1995). Infrared characteristic group frequencies, Tables and charts. *Journal of the American Chemical Society, 117*(5), 1671-1671.

Somani, V., & Kalita, S. J. (2007). Synthesis and characterization of nanocrystalline Barium Strontium Titanate powder via *sol-gel* processing. *Journal of Electroceramics, 18*(1-2), 57-65.

Song, L., Chen, Y., Wang, G., Yang, L., Li, T., Gao, F., & Dong, X. (2014). Dielectric properties of La/Mn codoped $Ba_{0.63}Sr_{0.37}TiO_3$ thin films prepared by RF magnetron sputtering. *Ceramics International, 40*(8), 12573-12577.

Srivastava, P., Saini, N., Sekhar, B., & Garg, K. (1994). Core-level photoemission study on a Bi-2212 single crystal. *Materials Science and Engineering: B, 22*(2-3), 217-221.

Stemme, F., Bruns, M., Geßwein, H., Schroeder, M., Sazegar, M., Drahus, M., Binder, J. (2013). Fabrication and characterization of iron and fluorine co-doped BST thin films for microwave applications. *Journal of Materials Science, 48*(9), 3586-3596.

Sun, Y.-F., Zhang, Y.-Q., Hua, B., Behnamian, Y., Li, J., Cui, S.-H., Luo, J.-L. (2016). Molybdenum doped $Pr_{0.5}Ba_{0.5}MnO_{3-\delta}$ (Mo-PBMO) double perovskite as a potential solid oxide fuel cell anode material. *Journal of Power Sources, 301*, 237-241.

Susarla, S., Chilkoor, G., Kalimuthu, J. R., Saadi, M., Cui, Y., Arif, T., Jasthi, B. (2021). Corrosion Resistance of Sulfur–Selenium Alloy Coatings. *Advanced Materials, 33*(51), 2104467.

Synetos, A., & Tousoulis, D. (2018). Invasive Imaging Techniques. 359-376.

Tangwiwat, S., & Milne, S. J. (2005). Barium titanate *sol*s prepared by a diol-based *sol–gel* route. *Journal of non-crystalline solids, 351*(12-13), 976-980.

Teoh, L. G., Lee, Y.-C., Huang, Y.-L., Huang, H.-H., & Shieu, F.-S. (2009). Influence of 4ZnO-B_2O_3 Addition on Dielectric Properties and Microstructures of Barium Strontium Titanate. *International Journal of Applied Ceramic Technology, 7*, E71-E79.

Tick, T., Peräntie, J., Jantunen, H., & Uusimäki, A. (2008). Screen printed low-sintering-temperature barium strontium titanate (BST) thick films. *Journal of the European Ceramic Society, 28*(4), 837-842.

Tkach, A., Vilarinho, P. M., & Kholkin, A. L. (2005). Structure–microstructure–dielectric tunability relationship in Mn-doped strontium titanate ceramics. *Acta Materialia, 53*(19), 5061-5069.

Tomar, A. K., Singh, G., & Sharma, R. K. (2018). Fabrication of a Mo-doped strontium cobaltite perovskite hybrid supercapacitor cell with high energy density and excellent cycling life. *ChemSusChem, 11*(23), 4123-4130.

Tombak, A., Maria, J.-P., Ayguavives, F., Jin, Z., Stauf, G. T., Kingon, A. I., & Mortazawi, A. (2002). Tunable barium strontium titanate thin film capacitors for RF and microwave applications. *Ieee Microwave and Wireless Components Letters, 12*(1), 3-5.

Tong, S., Ma, B., Narayanan, M., Liu, S., Koritala, R., Balachandran, U., & Shi, D. (2013). Lead lanthanum zirconate titanate ceramic thin films for energy storage. *ACS applied materials & interfaces, 5*(4), 1474-1480.

Upadhyay, R., Annam, S., Patel, M., & Joshi, U. (2015). Influence of aliovalent doping on dielectric properties of $Ba_{0.6}Sr_{0.4}TiO_3$ thin film for voltage tunable applications. *Integrated Ferroelectrics, 167*(1), 184-191.

V. Eswaramoorthi, S. S., R. Victor Williams. (AUGUST 2015). Influence of Ga doping on the structural, optical and electrical properties of $Ba_{0.6}Sr_{0.4}TiO_3$ Thin Films. *international journal of Scientific & technology research, 4*(08), 86-91.

Valencia-Gálvez, P., Aravena, D., Barahona, P., Moris, S., & Galdámez, A. (2022). Effects of Tin and Sulfur Chemical Substitution on the Structural and Electrical Properties of $CuCr_2Se_4$ Selenospinel. *Applied Sciences, 12*(3), 1586.

Van Erp, T. S., & Martens, J. A. (2011). A standardization for BET fitting of adsorption isotherms. *Microporous and Mesoporous Materials, 145*(1-3), 188-193.

Van Hest, M., Dabney, M., Perkins, J., & Ginley, D. (2006). High-mobility molybdenum doped indium oxide. *Thin Solid Films, 496*(1), 70-74.

Venkateswaran, U. D., Naik, V. M., & Naik, R. (1998). High-pressure Raman studies of polycrystalline $BaTiO_3$. *Physical Review B, 58*(21), 14256.

Wang, H.-W., Nien, S.-W., Lee, K.-C., & Wu, M.-C. (2005). Improvement in crystallization and electrical properties of barium strontium titanate thin films by gold doping using metal-organic deposition method. *Thin Solid Films, 489*(1-2), 31-36.

Wang, J., Yao, X., & Zhang, L. (2004). Preparation and dielectric properties of barium strontium titanate glass-ceramics sintered from *sol–gel*-derived powders. *Ceramics International, 30*(7), 1749-1752.

Wang, L., Zhu, M., Shao, Y., Zhao, Y., Wei, C., Gao, L., & Bao, Y. (2022). Smart Sensing Multifunctionalities Based on Barium Strontium Titanate Thin Films. *Sensors (Basel), 22*(19).

Wang, Q., Wang, T., Zhang, L., Liu, Z., Guo, K., Lu, J., & Xie, B. (2022). High energy-storage performance of lead-free $Ba_{0.4}Sr_{0.6}TiO_3$–$Sr_{0.7}Bi_{0.2}TiO_3$ relaxor-ferroelectric ceramics with ultrafine grain size. *Ceramics International, 48*(2), 2068-2074.

Wang, S.-X., Guo, M.-S., Liu, T., Guo, S.-s., Li, M.-Y., & Zhao, X.-Z. (2007). Effect of K-doping on the dielectric and tunable properties of $Ba_{0.6}Sr_{0.4}TiO_3$ thin films prepared by RF magnetron sputtering. *Journal of Crystal Growth, 306*(1), 22-26.

Wang, S., Cheng, B., Wang, C., Dai, S., Jin, K., Zhou, Y., Yang, G. (2006). Raman spectroscopy studies of Ce-doping effects on $Ba_{0.5}$ $Sr_{0.5}$ TiO_3 thin films. *Journal of applied physics, 99*(1), 013504.

Wang, Z., Guo, X., Montoya, J., & Nørskov, J. K. (2020). Predicting aqueous stability of solid with computed Pourbaix diagram using SCAN functional. *npj Computational Materials, 6*(1), 1-7.

Wei, J., Yang, T., & Wang, H. (2019). Excellent energy storage and charge-discharge performances in $PbHfO_3$ antiferroelectric ceramics. *Journal of the European Ceramic Society, 39*(2-3), 624-630.

Weser, U., Sokolowski, G., & Pilz, W. (1977). Reaction of selenite with biochemically active thiols: An X-ray photoelectron spectroscopic study. *Journal of Electron Spectroscopy and Related Phenomena, 10*(4), 429-439.

Wu, Y., Fan, Y., Liu, N., Peng, P., Zhou, M., Yan, S., Wang, G. (2019). Enhanced energy storage properties in sodium bismuth titanate-based ceramics for dielectric capacitor applications. *Journal of Materials Chemistry C, 7*(21), 6222-6230.

Xiao, L., Choy, K.-L., & Harrison, I. (2011). Co-doped BST thin films for tunable microwave applications. *Surface and Coatings Technology, 205*(8-9), 2989-2993.

Xiao, M., Zhou, Z., Gu, Q., Zhao, Y., Lan, K., & Zhang, P. (2017). Influence of molybdenum substitution on the microwave dielectric properties of $CaWO_4$ ceramic. *Journal of Materials Science: Materials in Electronics, 28*(14), 10343-10348.

Xiao, S. H., Jiang, W. F., Luo, K., Xia, J. H., & Zhang, L. (2011). Structure and ferroelectric properties of barium titanate films synthesized by *sol–gel* method. *Materials Chemistry and Physics, 127*(3), 420-425.

Xu, H., Hao, H., Xie, Y., Wang, X., Geng, J., Cao, M., Liu, H. (2022). Microcrystalline structure modulation and energy storage properties of $BaZr_{0.25}Ti_{0.75}O_3$ thin films. *Journal of Alloys and Compounds, 907*, 164236.

Xu, Z., Yan, D., Xiao, D., Yu, P., & Zhu, J. (2013). Dielectric enhancement of $BaSrTi_{1.1}O_3/BaSrTi_{1.05}O_3/BaSrTiO_3$ multilayer thin films prepared by RF magnetron sputtering. *Ceramics International, 39*(2), 1639-1643.

Yang, J., Wang, Z., Feng, H., Wei, Y., Li, G., Zhu, Y., . . . Li, S. (2023). Effect of barium strontium titanate modification on the dielectric-breakdown properties of phenyl-vinyl binary composite silicone rubber. *Ceramics International*.

Ye, Y., & Guo, T. (2009). Dielectric properties of Fe-doped $Ba_{0.65}Sr_{0.35}TiO_3$ thin films fabricated by the *sol–gel* method. *Ceramics International, 35*(7), 2761-2765.

Yu, E., Phillips, M., McCaldin, J., & McGill, T. (1991). Measurement of the CdSe/ZnTe valence band offset by x-ray photoelectron spectroscopy. *Journal of Vacuum Science & Technology B: Microelectronics and Nanometer Structures Processing, Measurement, and Phenomena, 9*(4), 2233-2237.

Yuan, Q., Li, G., Yao, F.-Z., Cheng, S.-D., Wang, Y., Ma, R.,Li, J.-F. (2018). Simultaneously achieved temperature-insensitive high energy density and efficiency in domain engineered $BaTiO_3$-Bi $(Mg_{0.5}Zr_{0.5})O_3$ lead-free relaxor ferroelectrics. *Nano Energy, 52*, 203-210.

Yun, S., Wang, X., Li, B., & Xu, D. (2007). Dielectric properties Ca-substituted barium strontium titanate ferroelectric ceramics. *Solid State Communications, 143*(10), 461-465.

Yuzyuk, Y. I., Alyoshin, V., Zakharchenko, I., Sviridov, E., Almeida, A., & Chaves, M. (2002). Polarization-dependent Raman spectra of heteroepitaxial (Ba, Sr) TiO_3/MgO thin films. *Physical Review B, 65*(13), 134107.

Zeng, Y., Zhang, H., Jiang, S., Shi, M., & Lu, W. (2006). Fabrication and characteristics of Pb doped BST ferroelectric thin films for uncooled infrared focal plane arrays. *Integrated Ferroelectrics, 82*(1), 91-99.

Zhang, B., Liu, P., Li, Z., & Song, X. (2021). Synthesis of two-dimensional Sr-doped $LaNiO_3$ nanosheets with improved electrochemical performance for energy storage. *Nanomaterials, 11*(1), 155.

Zhang, C., Ling, Z. x., Jian, G., & Chen, F. x. (2017). Dielectric properties and point defect behavior of antimony oxide doped Ti deficient barium strontium titanate ceramics. *Transactions of Nonferrous Metals Society of China (English Edition), 27*(12), 2656-2662.

Zhang, C., & Qu, Y.-f. (2012). Dielectric properties and phase transitions of La_2O_3-and Sb_2O_3-doped barium strontium titanate ceramics. *Transactions of Nonferrous Metals Society of China, 22*(11), 2742-2748.

Zhang, K., Zheng, P., Zhang, H., Niu, Z., Luo, C., Bai, W., Zhang, Y. (2022). Excellent energy storage performance of paraelectric $Ba_{0.4}Sr_{0.6}TiO_3$ based ceramics through induction of polar nano-regions. *Ceramics International, 48*(14), 19864-19873. 1

Zhang, M., Zhai, J., Shen, B., & Yao, X. (2011). The effect of transition metal oxides on the tunablility and microwave dielectric properties of $Ba_{0.5}Sr_{0.5}TiO_3$–$BaWO_4$ composite ceramics. *Materials Chemistry and Physics, 128*(3), 525-529.

Zhang, Y., Wang, G., Chen, Y., Cao, F., Yang, L., & Dong, X. (2009). Effect of donor, acceptor, and donor–acceptor codoping on the electrical properties of $Ba_{0.6}Sr_{0.4}TiO_3$ thin films for tunable device applications. *Journal of the American Ceramic Society, 92*(11), 2759-2761.

Zhao, M., Yao, X., Shi, P., Wei, X., Wu, X., Ren, W., & Lin, P. (2008). Effect of poly (vinyl acetate) on structure and property of bismuth-doped strontium titanate thin films derived by *sol–gel* method. *Ceramics International, 34*(4), 997-1001.

Zhou, X., Geßwein, H., Sazegar, M., Giere, A., Paul, F., Jakoby, R., Haußelt, J. (2009). Characterization of metal (Fe, Co, Ni, Cu) and fluorine codoped barium strontium titanate thick-films for microwave applications. *Journal of Electroceramics, 24*(4), 345-354.

LIST OF PUBLISHED PAPERS (Related to Dissertation)

1. Kiflom Gebremedhn Kelele, H. C. Ananda Murthy, Ruthramurthy Balachandran, Aschalew Tadesse, Yosef Nikodimos, Lemma Teshome Tufa, Jaebeom Lee (2022). The microstructural and morphological effects of doping barium strontium titanate nanocrystalline with selenium. *Inorganic Chemistry Communications*, *145*, 1387 – 7003, **Elsevier**. (Impact factor = 3.428, **Q1** Journal, Scopus and SCI indexed). https://doi.org/10.1016/j.inoche.2022.109954
2. Kiflom Gebremedhn Kelele, H.C. Ananda Murthy, Ruthramurthy Balachandran, Aschalew Tadesse & K.B. Tan (2022) Microstructural and dielectric properties of Mo-doped barium strontium titanate nanopowders, *Materials Technology*, *37*(14), 3241 - 3246, **Taylor and Francis**. (Impact factor = 3.846, **Q1** Journal, Scopus and SCIE indexed). https://doi.org/10.1080/10667857.2022.2151685
3. Kiflom Gebremedhn Kelele, H. C. Ananda Murthy, Ruthramurthy Balachandran, Aschalew Tadesse, Yosef Nikodimos, Lemma Teshome Tufa, Jaebeom Lee (2022). Synthesis and characterization of Mo-doped barium strontium titanate nanopowder via slow injection *sol–gel* processing. *Chemical Papers.* **Springer**. (Impact factor = 2.146, **Q2** Journal, Scopus, SCI and SCIE indexed). https://doi.org/10.1007/s11696-022-02458-9
4. Kiflom Gebremedhn Kelele, H.C. Ananda Murthy, Ruthramurthy Balachandran, Aschalew Tadesse & K.B. Tan (2023). Microstructural, morphological and dielectric properties of Mo, Se co-doped $Ba_{0.6}Sr_{0.4}TiO_3$ perovskites. *Materials Science for Energy Technologies*, 6, 310 – 317, **KeAi and Elsevier**. (Impact factor = 7.63, **Q1** Journal, Scopus indexed). https://doi.org/10.1016/j.mset.2023.02.005
5. Kiflom Gebremedhn Kelele, Aschalew Tadesse, Tegene Desalegn, Suresh Ghotekar, Ruthramurthy Balachandran, Hanabe Chowdapp, Ananda Murthy. Synthesis and characterizations of metal ions doped barium strontium titanate (BST) nanomaterials for photocatalytic and electrical applications: A mini review (2021). *International Journal of Materials Research*, *112* (8), 665 - 677. **De Gruyter**. (Impact factor = 0.678, **Q3** Journal, Scopus and WoS indexed). https://doi.org/10.1515/ijmr-2020-8149
6. Ruthramurthy Balachandran, Kiflom Gebremedhn Kelele, H.C. Ananda Murthy, Tan Kar Ban, Chan Kah Yoong, Dhanalakshmi Muniswamy, Aschalew Tadesse, Suresh Ghotekar (2023). Multi-element doped barium strontium titanate nanomaterial as capacitors: A Mini Review. *Journal of chemistry*, ***Hindawi***. (Impact factor = 3.241, **Q2** Journal, Scopus, SCIE and WoS indexed). https://doi.org/10.1155/2023/6338649

OTHER PUBLICATIONS

1. H.C. Ananda Murthy, Kiflom Gebremedhn Kelele, C.R. Ravikumar, H.P. Nagaswarup, Aschalew Tadesse, Tegene Desalegn (2021). Graphene-supported nanomaterials as electrochemical sensors: A mini review. *Results in Chemistry, 3*, 100131, **Elsevier** (Impact factor = 2.21, **Q3** Journal, Scopus indexed).
   https://doi.org/10.1016/j.rechem.2021.100131
2. H.C. Ananda Murthy, Tanima Bhattacharya, Kiflom Gebremedhn Kelele, Abbay Gebretsadik, Atinafu Abayneh (2023). Biobased materials in sustainable development of catalysis: Food, Biomedical, and Environmental Applications. *Advanced Applications of Biobased Materials*: **Elsevier,** 699 - 715.
   https://doi.org/10.1016/B978-0-323-91677-6.00017-9

APPENDIX

1. Determination of amount of precursors of the $Ba_{0.77}Sr_{0.23}TiO_3$

Different forms of BSTs are composed of different ratios of the metals Ba and Sr according to the general formula of $Ba_xSr_{1-x}TiO_3$. For instance, for the synthesis of $Ba_{0.77}Sr_{0.23}TiO_3$, the amounts of precursors were calculated based on the required stoichiometric ratio of BST samples. They were calculated from the molecular weights of starting materials viz., barium acetate, strontium acetate and titanium (IV) iso-propoxide. For instance, to synthesize 6.74 g of $Ba_{0.77}Sr_{0.23}TiO_3$, 4.91 g of barium acetate, 1.18 g of strontium acetate and 7.09 g (7.2 mL) of titanium (IV) iso-propoxide were required. Similarly, for the synthesis of 5.33 g $Ba_{0.6}Sr_{0.4}TiO_3$, 4.47 g of barium acetate, 1.54 g of strontium acetate and 6.88 g (7.0 mL) of titanium (IV) iso-propoxide were used as precursors (R. Balachandran et al., 2011). The detailed calculations are found at the Appendix.

2. Sample calculation of amount of precursors used in the synthesis of pristine and doped $Ba_{0.77}Sr_{0.23}TiO_3$ nano powders

During the synthesis of doped $Ba_{0.77}Sr_{0.23}TiO_3$ nanopowder the calculations below were used to determine the amount of precursors used.

- ► Barium acetate $Ba[CH_3CO_2]_2$ and its molecular weight = 255.43 g
- ► Strontium acetate $Sr[C_2H_2O_2]_2$ and its molecular weight = 205.74 g
- ► Titanium [IV] Iso-propoxide $Ti[OCH[CH_3]_2]_4$ and its molecular weight = 284.26 g

Density = $\frac{\text{Weight}}{\text{Volume}}$, Weight (g) = Density *x* Volume

Molar concentration = $\frac{\text{Mole}}{\text{Volume}}$

Molecular weight of $Ba_{0.77}Sr_{0.23}TiO_3$ = [0.77 *x* molecular mass of Ba] + [0.23 *x* molecular mass of Sr] + [1 *x* molecular mass of Ti] + [3 *x* molecular mass of oxygen]

= [0.77 *x* 137.33] g + [0.23 x 87.62] g + [1 *x* 47.87] g + [3 *x* 16] g = 269.81 g

0.77 mol of barium acetate = 0.77 *x* 255.43 = 196.65 g produces 269.81 g of $Ba_{0.77}Sr_{0.23}TiO_3$

► To produce 6.74 g of $Ba_{0.77}Sr_{0.23}TiO_3$, we need = 6.74 x $\frac{196.65}{269.81}$ = 4.916 g of barium acetate

0.23 mol of strontium acetate = 0.23 x 205.74 = 47.32 g produces 269.81 g of $Ba_{0.77}Sr_{0.23}TiO_3$

► To produce 6.74 g of $Ba_{0.77}Sr_{0.23}TiO_3$, 6.74 x $\frac{47.32}{269.81}$ = 1.18 g of strontium acetate was needed

1 mol of titanium [IV] iso-propoxide = 1 *x* 284.26 g = 284.26g produces 269.81 g of $Ba_{0.77}Sr_{0.23}TiO_3$

► To produce 6.74 g of $Ba_{0.77}Sr_{0.23}TiO_3$, 6.74 g $x \frac{284.26}{269.81} = 7.09$ g of titanium [IV] iso-propoxide powder or $\frac{7.09}{0.962} = 7.37$ mL of titanium [IV] isopropoxide liquid is needed

Likewise, for the synthesis of 0.04 mol doped $Ba_{0.77}Sr_{0.23}TiO_3$, the following calculation steps were used to determine the amount of precursors.

Molecular weight of 0.04 mol doped $Ba_{0.77}Sr_{0.23}TiO_3$ ($Ba_{0.77}Sr_{0.23}Mo_{0.04}Ti_{0.96}O_3$) = [0.77 *x* molecular mass of Ba] + [0.23 *x* molecular mass of Sr] + [0.04 *x* molecular mass of Mo] + [0.96 *x* molecular mass of Ti] + [3 *x* molecular mass of oxygen]

= [0.77 *x* 137.33] g + [0.23 *x* 87.62] g + [0.04 *x* 95.9] g + [0.96 *x* 47.87] g + [3 *x* 16] g = 225.6 g

For 0.1 M $Ba_{0.77}Sr_{0.23}Mo_{0.04}Ti_{0.96}O_3$, 22.56g/1000 mL = 11.28g/500 mL = 5.64g/250 mL was used

Molecular mass of MoO_3 = 143.94 g/mol , 0.04 mol MoO_3 = 5.76 g

Therefore, to prepare 5.64 g $Ba_{0.77}Sr_{0.23}Mo_{0.04}Ti_{0.96}O_3$ nanopowder;

5.64 g $x \frac{196.65\ g}{225.6\ g/mol} = 4.91$ g of Barium acetate

5.64 g $x \frac{47.3\ g}{225.6\ g/mol} = 1.18$ g of Strontium acetate

5.64 g $x \frac{5.76\ g}{225.6\ g/mol} = 0.14$ g of Molybdenum trioxide

5.64 g $x \frac{272.85\ g}{225.6\ g/mol} = 6.82$ g (7.10 mL) of Titanium tetra iso-propoxide were used in 250 mL of the solutions were used as precursors.

Besides, to synthesize 0.04 mol Se-doped $Ba_{0.77}Sr_{0.23}TiO_3$ ($Ba_{0.77}Sr_{0.19}Se_{0.04}TiO_3$), the following calculation steps were used to determine the amount of precursors used.

Molecular weight of $Ba_{0.77}Sr_{0.19}Se_{0.04}TiO_3$ = 221.39 g

Molecular weight of SeO_2 = 110.96 g/mol , 0.04 mol SeO_2 = 4.44 g

0.19 mol barium acetate = 0.19 mol *x* 205.74 g/mol = 39.09 g

For 0.1 M $Ba_{0.77}Sr_{0.19}Se_{0.04}TiO_3$, 22.14g/1000 mL = 11.07g/500 mL = 5.54 g/250 mL;

5.54 g $x \frac{196.65\ g}{221.39\ g/mol} = 4.92$ g of Barium acetate in 250 mL of the solution

5.54 g $x \frac{39.09\ g}{221.39\ g/mol} = 0.98$ g of Strontium acetate in 250 mL of the solution

5.54 g $x \frac{4.44\ g}{221.39\ g/mol} = 0.111$ g of Selenium dioxide in 250 mL of the solution

5.54 g $x \frac{284.22\ g}{221.39\ g/mol} = 7.1$ g (7.4 mL) of Titanium tetra iso-propoxide were used in 250 mL of the solution

Similarly, the mass of the precursors of the 0.04 mol (Mo, Se) co-doped $Ba_{0.77}Sr_{0.23}TiO_3$ ($Ba_{0.77}Sr_{0.19}Se_{0.02}$ $Mo_{0.02}TiO_3$) were determined through the same methods for the respective uni-doped $Ba_{0.77}Sr_{0.23}TiO_3$ nanopowders.

Molecular weight of $Ba_{0.77}Sr_{0.19}Se_{0.02}$ $Mo_{0.02}TiO_3$ = 222.53 g

For 0.1 M $Ba_{0.77}Sr_{0.19}Se_{0.02}$ $Mo_{0.02}TiO_3$, 22.25g/1000 mL = 11.13g/500 mL = 5.56 g/250 mL;

$5.56\ g\ x\ \frac{196.65\ g}{222.53\ g/mol} = 4.900$ g of Barium acetate in 250 mL of the solution

$5.56\ g\ x\ \frac{39.09\ g}{222.53\ g/mol} = 1.079$ g of Strontium acetate in 250 mL of the solution

$5.56\ g\ x\ \frac{4.44\ g}{222.53\ g/mol} = 0.055$ g of Selenium dioxide in 250 mL of the solution

$5.56\ g\ x\ \frac{5.76\ g}{222.53\ g/mol} = 0.072$ g of Molybdenum trioxide

$5.56\ g\ x\ \frac{284.22\ g}{222.53\ g/mol} = 6.96$ g (7.25 mL) of Titanium tetra iso-propoxide were used in 250 mL of the solution

The same way of calculation steps were followed for the determination of the amount of the precursors for the doped $Ba_{0.6}Sr_{0.4}TiO_3$ samples, the only difference was the molecular mass of the BST samples utilized.